# Integrated Optical Filters using Bragg Gratings and Resonators

by

## Mohammad Jalal Khan

Submitted to the Department of Electrical Engineering and Computer Science
in partial fulfillment of the requirements for the degree of
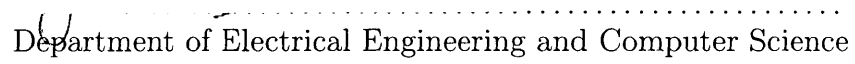
Doctor of Philosophy

at the

MASSACHUSETTS INSTITUTE OF TECHNOLOGY

February 2002

Author . . . . . . . .
Department of Electrical Engineering and Computer Science
February 4, 2002

Certified by . . . . . . . . . . . . . . . . . . . . . . . . . . . . . . . . . . . . . . . . . . . . . . . . . . . . . .
Hermann A. Haus
Institute Professor Emeritus
Thesis Supervisor

Accepted by . . . . . . . . . . . . . . . . . . . . . . . . . . . . . . . . . . . . . . . . . . . . . . . . . . . . . .
Arthur C. Smith
Chairman, Department Committee on Graduate Students
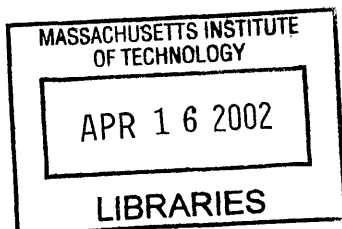
# Integrated Optical Filters using Bragg Gratings and Resonators

by

Mohammad Jalal Khan

Submitted to the Department of Electrical Engineering and Computer Science
on February 4, 2002, in partial fulfillment of the
requirements for the degree of
Doctor of Philosophy

## Abstract

This thesis provides an in-depth study of optical filters made using integrated Bragg gratings and Bragg resonators. Various topologies for making add/drop filters using integrated gratings are outlined. Each class of devices is studied in detail and the theoretical tools needed for designing the add/drop are developed. First-order filters using Bragg resonators do not meet WDM add/drop filter specifications. Consequently, schemes to design higher-order filters are derived. The relative advantages and disadvantages of the various possiblities are outlined. Preliminary integrated Bragg grating devices, in InP, were designed using the tools developed. The fabricated devices were measured. The measurements revealed low-loss structures with $\alpha < 0.1$ cm$^{-1}$ and high-Q Bragg resonators with $Q > 40,000$. Measurements on higher-order inline coupled Bragg resonator filters showed flat-top and fast roll-offs. The results of the measurements and comparison with the theory are presented for the various devices. The results reveal that Bragg grating based devices offer tremendous potential for use as add/drop filters in WDM systems.

Thesis Supervisor: Hermann A. Haus
Title: Institute Professor Emeritus

# Acknowledgments

From the time of walking in as a freshman to the completion of my doctorate degree, my MIT journey has been long, at times wavering, arduous, and yet very fulfilling. There are many many people to whom I owe tremendous thanks, without whose help and support this journey would not have reached its destination. MIT provides a top-class education but what I owe most to MIT has been the people that it gave me an opportunity to meet, befriend, get inspired by, and learn from; the richness they added to my experience has been invaluable. An acknowledgement that does justice to the contribution of these people would constitute a thesis by itself. Unfortunately, this acknowledgement must be brief and by its very nature cannot be complete.

I would like to start by thanking my thesis advisor Prof. Haus for providing me with opportunity to be a part of his research group. Prof. Haus' guidance, enthusiasm, encouragement and support have been invaluable. His keen intuition and mental faculties never cease to amaze me. Prof. Haus' enthusiasm for his work, his child-like curiousity, and his relentless pursuit for greater understanding of the world around us have been truly inspirational. Above all, Prof. Haus' understanding and support in times of difficulty, and his allowing me to take a semester off at the time of my father's surgery will always be deeply appreciated.

I am deeply grateful to Prof. Hank Smith for providing me with an opportunity to collaborate closely with NSL. Prof. Smith's guidance, help and continual drive to supplement theoretical pursuits with practical implementations enabled this thesis to include measurements on fabricated, real devices. Prof. Smith's ability to manage a large and diverse research group and his commitment to facilitate and enable research by his students are difficult to match. His care for detail, particularly in presentations, helped improve my presentation skills. Of course, a special thanks goes out for the caribou dinner and the graduation party !!

While working at NSL I had the opportunity to work closely with a lot of students and staff. I would like to thank Mike Lim for his tenacity to see through the fabrication of the devices, his beautiful Adobe Illustrator figures - and his maybe not-so-well-known culinary skills. Tom Murphy's willingness to sacrifice his time to help others with virtually anything are truly a rare trait. Even after, he became Dr. T.E Murphy and left campus, he could not escape my calls for help and he always delivered. Juan Ferrara's ability to spend countless hours writing the X-ray masks made the quarter-wave shifted devices possible. His friendly demeanor and pleasant personality made it delightful to work with him. I would like to acknowledge the help of Dr. C. Joyner, then at Lucent, in helping with the fabrication effort and performing overgrowth of the top InP cladding for the devices. I would also like to thank Todd Hastings and other members of the "Optics Group" for their fruitful discussion and good company. Minghao's help in dealing with computer problems was greatly appreciated. I will fondly remember discussions of cricket and sub-continent culture with Mark Mondol. Finally, I would like to thank all members of the NSL for making my research and social experience more enjoyable.

During most of my PhD years, I had the pleasure to share an office with Christina Manolatou. Other than our collaboration on research projects, Christina and I shared many enjoyable discussions ranging from research woes to swimming at Walden Pond. Milos Popovic who has been my more recent office mate has been an excellent 'comrade-in-arms' in

our theses writing endevours. His healthy skeptsicm and inquisitive mind leave no place for complacency and have forced me to constantly think through old and new concepts. Charles Yu, my office-mate of long-standing and fellow MIT undergrad and who much against my wishes graduated before me, provided me with much encouragement to become the first PhD in my family. I would also like to thank Cindy Kopf for her patience in dealing with my multiple latex questions and helping out with everything, including my thesis defense presentation.

During the course of my many years at MIT, I have made excellent friends. Ammar Al-Nahwi's ability to bring out the best in others by inspiring people to goodness; his kindness and his consideration make him a friend whose company will be missed sorely. I will fondly remember our "early" morning breakfast meetings intended to give us a head-start to the day. Farhan, has been an excellent friend since we entered MIT as freshmen. He helped me endure and persist through my time at MIT, quitely encouraging and trusting me to achieve the best I could. We have shared many experiences together and I will never be able to forget our time in music class. Kashif Khan and I had been roomates for many years. His willingness to leave his own work aside and spend hours helping others is admirable and helped me many times, particularly during last minute preparation for presentations. His cooking is responsible for my weight gain. Ayman Shabra, another one of my roomates, exemplifies good behavior and kindness to others. Extremely patient and always willing to lend a sympathetic ear, Ayman has been an excellent friend and roomate. Asim Khwaja - a true 'MIT-ian' and now professor at a small neighboring university (Harvard) - and I shared a great time together during our undergrad years at MIT. He continues to be an excellent friend. Mohammad Saeed's sincere friendship and genuine concern for the well-being of others make him an invaluable friend. His superb culinary skills helped offset the trauma induced by MIT food services. Also, I hope that he can continue to provide excellent 're-search retreats' at the Cape Cod location using his HP-Agilent-Philips connections. Gassan Al-Kibsi has been most responsible for injecting fun into our MIT lives. From movies to automobile test drives, to foliage trips to simply wasting time, Gassan's company has always been enjoyable. I indebted to him for causing me to meet a very special person in my life. Babak Ayazifar's desire to do achieve perfection in his endevours and avoid cutting corners are worthy of emulation and I hope to learn from them. Samir Nayfeh's self-motivation and drive for his work are inspiring. I hope that our shared passion for soccer will motivate us to start playing again. Osamah's seemingly quiet demeanor belie his excellent sense of humor. I am grateful to him for his consideration and reassurance in coping with the vicissitudes of life. I would also like to thank the MBC-2 crowd, Ihsan Djomehri, Hasan Nayfeh and Belal Helal for their great company and many shared dinners. Ahmed Ghezala has been always willing to accompany me to Walden pond for swims even when everyone else thought that it was too cold and has been a great friend. Farhan Khursheed has always been an older brother to me in Boston and I appreciate his always being there. I will miss my old friends from MIT, Yassir Elley, Asad Naqvi, Aamer "Manjoo" Manzoor who made my years at MIT a treat.

A special note of thanks to my BU friends, Arshad Ashraf, Ali Ata, Asif Jan and Milton Masud who impressed upon me the value of life outside of MIT. Their friendship and support has been most invaluable to me. They also helped arrange for some of the most fun I had while in Boston. We need to do another camping trip to Maine !!

I would like to take a moment to thank a person who is very dear and special to me. I

met Eli a year and half ago and since then she's added immense joy and happiness to my life. Her love, support, infinite patience, quite encouragement, and full trust in me were instrumental in helping me get through. I cannot thank her enough for everything !!

Finally, I would like to thank my family for their continual support and endless love. My uncles, PM, Abba, Aziz Chacha and Baba have always been there for me and my family. They have taught me the value of hard work and persistence. My late grandmother's love will always be missed. My cousin, Lisa Apa, reminded me how our student years were some of the best part of our lives and trusted that I would succeed. My brothers, Sikander and Akbar have been constant pillars of support in my life; they have continually provided help and encouragement and have been there whenever I needed them. My sister, Dimple's love and care; her constant mailings of baked goodies which left the post-office wondering what an amazing sister I have, are deeply appreciated. My beautiful darling neace and nephew, Alaina and Ali that she's provided the family and whom I love a lot, have infintely enriched our lives. I hope to have much more time to be with them and enjoy their terrific company. Jeff and Tina, have been a wonderful brother and sister to me.

At the end, none of this work would have been possible without my parents whose unconditional love and countless sacrifices for their children cannot even be expressed in words, let alone be thanked. I will never forget the happiness that my successful defense brought to my father and mother and I would gladly go through my PhD years all over again to bring them that moment of joy. Their prayers and their love have been the single-most important factor in my life and to them I dedicate this thesis and my PhD. Ammi and Abbu, thank you for everything !!

M. Jalal Khan

*All Praise belongs to Allah, Lord of the Worlds.*

**8**

# Contents

# List of Figures

# List of Tables

# Chapter 1

# Introduction

## 1.1 Evolution of Optical Networks

The last decade has seen an explosive growth in network traffic fuelled largely by the development and rapid expansion of the internet. As the numbers of users and services offered on the internet has continued to grow exponentially, data-traffic has exceeded voice-traffic and continues to increase at a large rate [1]. The need to provide end users with fast access to data has been forcing telecom service providers to upgrade the capacity and transmission speeds of networks. Optical networks are the network of choice and enormous amounts of new fiber have been installed both terresterially and under-sea. Optical fibers are an excellent transmission medium with incredibly low loss, 0.2 dB/km, and huge bandwidth in excess of 50 THz [2]. Since maximum electronic rates are limited to 40 GBits/s, efficient use of fibers requires concurrent transmission of independent data streams.

Wavelength division multiplexing (WDM) has become the de facto method of accessing the enormous bandwidth of existing fiber optic networks, enabling dramatic increases of aggregate transmission speeds. WDM achieves this by multiplexing n independent channels operating at distinct wavelengths and modulated with their own data, on to a single fiber, thereby giving an n-fold increase in throughput of data. The channel wavelengths and the spacing between them have been defined by the International Telecommunion Union [3] and lie on what is referred to as the ITU grid. Channel spacings for most existing systems are 200 GHz and 100 GHz. However, there has been a push toward 50 GHz-spaced WDM systems [4]. WDM channel counts have progressively increased with 16, 32 and 64 channels systems commercially available. Typically, the bit-rates of the individual channels
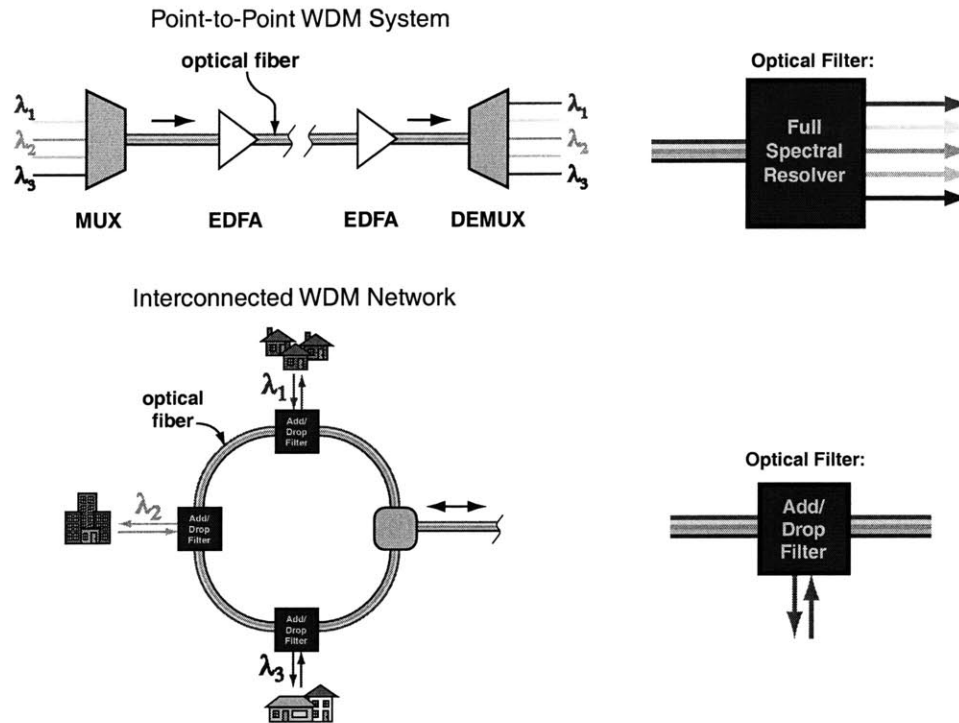
**Figure 1-1:** Evolution of optical networks from linear topologies to more networked architectures. Linear topologies use full-spectral resolvers Add/drop filters that select a single WDM channel are more useful devices for ne tworked architectures

are maintained at the peak speeds possible. Systems at 2.5 Gbits/s (OC-48) and 10 Gbits/s (OC-192) are available, with 40 Gbits/s (OC-768) under development [1]. Whereas other multiplexing technologies such as time division multiplexing and code division multiplexing do exist, they are somewhat futuristic and WDM remains the dominant technology [2].

Most WDM systems to date have been long-haul point-to-point links (see Fig. 1-1). The long-haul networks form the backbone communication layer connecting smaller networks across geographies. The constituent channels are multiplexed at the transmitting end and then completely separated at the receiving end by terminal equipment employing full spectral resolving optical Mux/DeMux filters. There is, however, a trend towards more sophisticated network architectures driven in part by the need for regional and metropolitan optical networks [5, 6]. These networks typically consist of multiple interconnected nodes in various topologies. Figure (1-1) shows a ring-topology but the most general case would consist of a arbitrary meshed network of interconnected nodes. At each node one or more data channel may be accessed and processed or re-routed, allowing architects the flexibility they need in designing regional access networks.
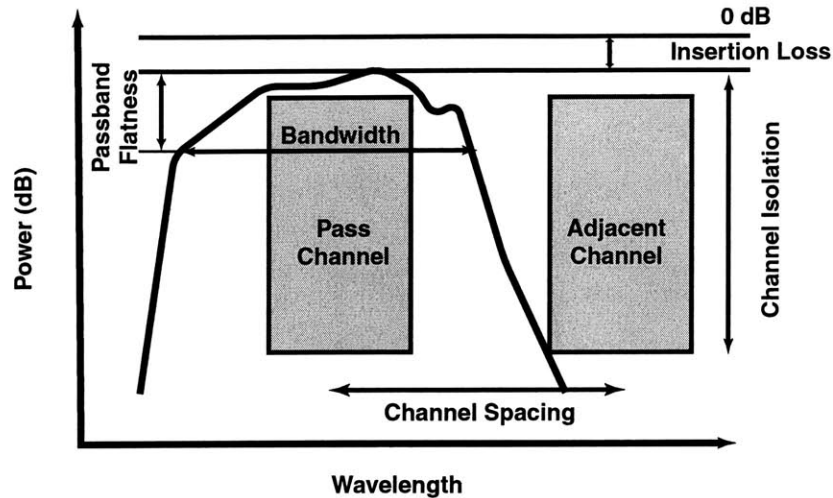
**Figure 1-2:** Generalized spectrum of an add/drop filter defining the various figures-of-merit used to gauge performance.

## 1.2 Add/Drop Filters

A key component needed for WDM regional networks is the Add/Drop filter. Unlike a full spectral resolver, the add/drop filter enables the extraction or addition of a single channel from a stream of WDM channels propagating on a fiber, without disrupting any of the other channels. Figure (1-2) shows the spectrum of a general add/drop filter and defines the various figures-of-merit used to gauge its performance. The specifications of an add/drop filter are determined by its intended use. Since any attenuation of signals degrades performance a minimum insertion loss is preferred. Another key requirement of add/drops is that the dropped signal be restricted to the desired drop channel; contribution from additional channels not only disturbs the on-going signals but more importantly acts as noise source for the selected channel. Consequently, cross-talk should be minimized or alternately add/drop filters must have high channel isolation. Most systems require a channels isolation in excess of 25 dB. This channel isolation must be achieved within the channel spacing that can typically be 200, 100 or 50 GHz. Of course as the channel spacings get narrower the cross-talk or channel isolation requirement becomes more challenging to achieve. The passband width of add/drop filters is typically defined as the frequency separation between the 0.5 dB, 1 dB or 3 dB points. The passband width must be wide enough to select all the information contained in the channel. Typical bit-rates of existing WDM system are either 2.5 Gbits/s or 10 Gbits/s. At a minimum the pass-band must be this wide: 2.5

GHz or 10 GHz, depending on the system. However, due to system drift considerations, both of the laser sources and filters, designers prefer passbands that are wider than the minimum required width. Even so, a wider passband cannot be achieved at the expense of channel isolation. Typically, the passband width is a percentage of the channel spacing with most devices having bandwidth of anywhere from 25% to 40% of the channel spacing. Flat passbands with no ripples are ideal but ripples of 1-2 dB may be acceptable. In transmission, the dropped channel must be suppressed in excess of 25 dB so that the on-going remnant of the drop-signal not interfere with signals added later in the network at the dropped channel wavelength. The polarization state of the light on an optical fiber is not predictable and subject to constant change. Consequently an add/drop filter should ideally be polarization independent, that is, the spectral response be the same for TE and TM input. A polarization dependent loss of 0.5 dB is tolerable. The add/drop filters performance and wavelength stability must be insensitive to environmental changes. This is mostly a packaging issue. Commercial devices must also meet the Bellcore reliability standards. In addition, for multi-channel devices the response from channel to channel must be uniform.

The three predominant technologies [7] currenly available for add/drop filters are: dielectric thin-film filters (DTFs), fiber-bragg gratings (FBGs) [8], and arrayed waveguide gratings (AWGs) [10]. Arrayed waveguide gratings are fabricated on a planar integrated substrate whereas the other two technologies use discrete components. Dielectric filters are the predominant filters for 200 GHz channel-spacing WDM systems. Although available for 100 GHz spaced channel applications, it is difficult to make 50 GHz spacing dielectric filters. FBGs on the other hand are available for 200 GHz, 100 GHz and 50 GHz applications. Since they are a reflection based devices, an add/drop filter using FBGs requires two optical circulators to separate the input and output signals. Optical circulators are expensive and, as a result, FBGs are costly. Moreover, it is difficult to achieve large passband widths using FBGs and thus this technology may not be well adapted to 40 Gbits/s bit-rate systems. Both FBGs and DTF filters serially drop wavelengths if used as Mux/DeMux filter and are mostly suitable for low channel counts of 8-16. Higher channel counts lead to unacceptable insertions losses. Typically, the devices are packaged to be environmentally stable which may include temperature compensation techniques. However, it is difficult to actively tune or reconfigure DTFs and FBGs, other than by using temperature. This mechanism is
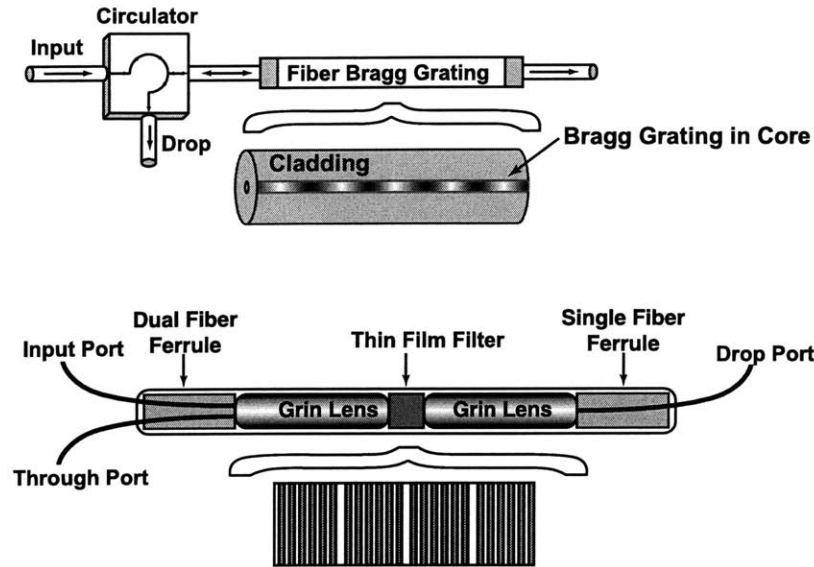
**Figure 1-3:** Fiber Bragg Gratings and Dielectric Thin Film filters are some of the commonly used components in Add/Drop Filters

slow and may be a limiting factor for future systems that will require rapidly tunable or reconfigurable add/drop filters.

AWGs, unlike the other two devices, are integrated filters typically fabricated in a silica-based material system [11]. They simultaneously resolve all the WDM channels and are more suitable as full spectral resolvers rather than add/drops. Add/Drop application requires two back-to-back AWGs; an inelegant approach with large insertion loss. AWGs because of their parallel approach naturally support high channel counts from 16 to 64. They are available for 200, 100, and 50 GHz channel spacings [12]. They do, however, have higher insertion losses. Moreover, packaging these devices is difficult and costly. Consequently AWGs are quite expensive. Since AWGs are integrated on planar substrates it is possible to integrate them with other components such as switches and lasers to form more complex devices. However, since silica is an optically passive material, integration with active devices such as lasers and switches requires heterogenous integration of different material systems. This is very challenging and expensive. AWGs can also be made tunable by the use of heaters that alter the refractive index of the waveguides. This mechanism is slow and, as before, faster tuning strategies are prefered.
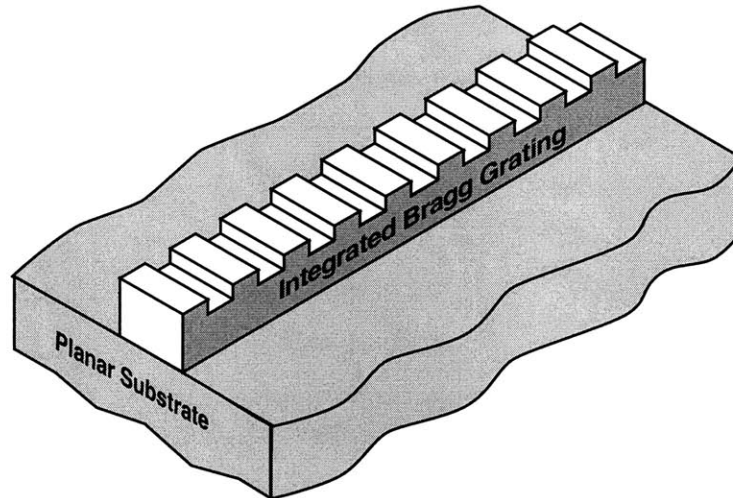
**Figure 1-4:** A schematic of an integrated Bragg grating showing the physical corrugation etched on the waveguide; the device may include a top cladding layer that is not shown.

## 1.3    Integrated Bragg Gratings

As networks evolve towards sophisticated architectures, with more intelligence in the network nodes, there is a push towards integrated optical devices that offer greater functionality. Integration offers the potential for producing tunable, low-cost, compact and manufacturable devices.

Integrated Bragg gratings are frequency selective devices that can be used as the basic building block in add/drop filters. Like AWGs, integrated Bragg gratings are fabricated on a planar substrate with the two main choices of materials systems being Silicon-based and InP-based. Unlike FBGs, where the gratings are produced by a UV-induced photorefractive index change of the core of the fiber, integrated gratings are formed by etching a physical corrugation on a waveguide, Fig. (1-4). Integrated gratings are specified in terms of waveguide geometries and grating etch depths. These geometries are defined by fabrication processes that are controllable and allow greater freedom in designing the properties of integrated Bragg grating structures. The integrated gratings structures are much smaller than fiber-optic based devices, thus packing more functionality into less space. Unlike FBGs the separation of the input and output signals can be performed by integrated techniques which by-pass the need for expensive discrete components such as circulators and isolators.

Gratings fabricated in InP-based material systems can be readily integrated with active devices such as lasers and detectors to form complex sub-systems. Moreover, gratings in InP

can be made tunable by using active techniques such as current injection [13] and reverse-biasing [14]. These control mechanisms are much faster than temperature tuning [15] and are thus promising for next generation rapidly re-configurable add/drop filters. Furthermore the integrated devices offer the potential for mass-production with many devices being made on each planar substrate thereby reducing cost of the devices.

## 1.4 Outline of Thesis

This thesis provides an in-depth study of optical filters made using integrated Bragg grating structures. Various topologies for making add/drop filters using integrated gratings are outlined. Each class of devices is studied in detail and the theoretical tools needed for designing the add/drop filters are developed. The relative advantages and disadvantages of the various possiblities are outlined. Preliminary integrated Bragg grating devices in InP were designed, fabricated and measured as part of the thesis work.

Chapter 2 introduces basic waveguide mode concepts and waveguide couplers. This chapter is intended to introduce the notation which is used in subsequent chapters and is not meant to be an exhaustive study of waveguides.

Chapter 3 derives the Coupled Mode Theory in space equations needed to analyse integrated Bragg structures. A generalized transfer matrix method for solving these equations is developed. Apodized gratings, chirped gratings, Bragg resonators and their spectra are analysed. These are the basic building blocks of all the devices that follow. The alternate Coupled Mode Theory in time representation of resonators is introduced and related to equivalent circuits. The chapter concludes with a discussion of Mach-Zehnder based add/drop filters using these structures along with design considerations.

Chapter 4 introduces the second class of optical filters that are possible using Bragg resonators. These devices are formed by side-coupling Bragg resonators to optical waveguides. A first-order add/drop filter made using this topology is discussed in detail. The design parameter choices and constraints are outlined. Higher-order filters are motivated and a topology to use Bragg resonators to form higher-order filters is derived. Equivalent circuit techniques are used to enable higher-order filter optical parameter selection by refering to standard LC-ladder circuit tables. Limitations of this topology motivate the following chapter.

Chapter 5 discusses an alternate topology which uses coupled Bragg resonators side-

coupled to *two* waveguides to form add/drop filters. This topology allows "traveling-wave" device behavior to be reproduced by using degenerately coupled standing wave resonators. A scheme to design higher-order add/drops capable of complete power transfer is derived; optical parameter selection is again reduced to looking up standard LC-ladder circuit tables.

Chapter 6 presents the measurement process and results on a preliminary set of fabricated devices. The measurement data is used to extract optical parameters of the devices and compared with designe values. Comparison between Coupled Mode Theory and the data is also presented.

The thesis ends with a conclusions and future-work section.

# Chapter 2

# Waveguides and Couplers

The most basic device used in integrated optics is a dielectric waveguide. Its function is analogous to that of wires in integrated electronic circuits guiding optical energy to the various locations on the photonic chip. Dielectric waveguides have been studied extensively and are the subject of many books [17, 18, 19]. No attempt is made here to reproduce that work; instead this chapter focusses on introducing some basic waveguide theory concepts and notation which is used in later chapters.

## 2.1  Waveguide Modes [18]

A dielectric waveguide in most general terms is an axial system which is defined by a dielectric cross-sectional distribution, $\epsilon(x, y)$ or equivalently an index distribution $n(x, y)$. For a purposes of analytical considerations a waveguide is assumed to be uniform in the axial direction, defined to be the $z$-axis. A waveguide generally consists of a region of high index surrounded by regions of lower index. Many possible configurations exist but cross-sections of two of the most common waveguide geometries are shown in Fig. (2-1). These are the channel and rib waveguide geometries. A channel waveguide has a central core region surrounded by bottom and top cladding regions. Typically the cladding regions have the same index. A rib waveguide has a cross-sectional profile as shown in Fig. (2-1). The region of high index is either $n_2$ or $n_3$ and often the top-most cladding layer is air.
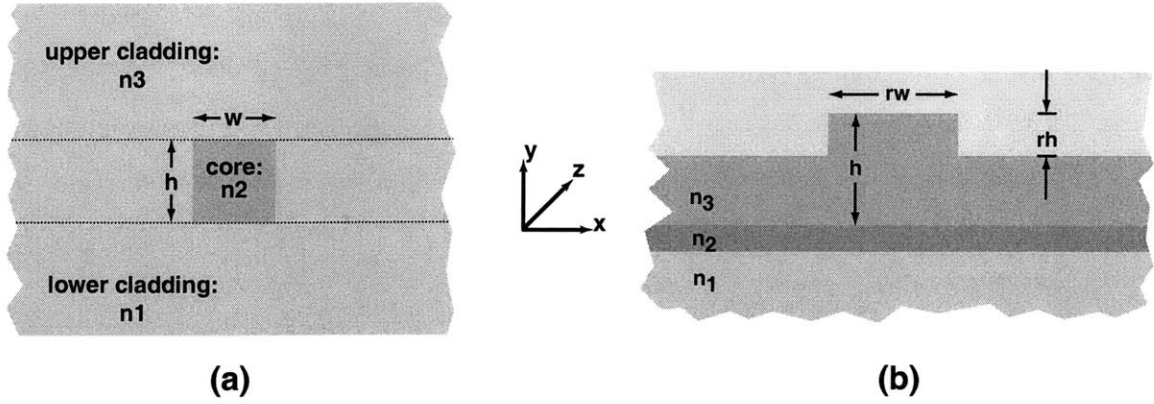
**Figure 2-1:** Two commonly used waveguide geometries: (a) buried channel waveguide, (b) rib
waveguide.

### 2.1.1   Normal Modes

The electric field, **E**, and the magnetic field, **H**, solutions in the guide which stay bounded
for infinite $x$ and $y$ in the absence of a source and have an $e^{-j\beta z}$ dependence are called the
normal modes or eigen-modes of the waveguide. They satisfy Maxwell equations:

$$\beta\,\mathbf{E}_T - j\nabla_T E_z = -\omega\mu\mathbf{i}_z \times \mathbf{H}_T \tag{2.1}$$

$$\beta\,\mathbf{H}_T - j\nabla_T H_z = \omega\mu\mathbf{i}_z \times \mathbf{E}_T \tag{2.2}$$

$$\nabla_T \cdot (\mathbf{i}_z \times \mathbf{E}_T) = j\omega\mu H_z \tag{2.3}$$

$$\nabla_T \cdot (\mathbf{i}_z \times \mathbf{H}_T) = -j\omega\mu E_z \tag{2.4}$$

where the subscripts $T$ and $z$ represent the transverse and longitudinal components respec-
tively. $\mathbf{i}_z$ is a z-directed unit vector. The coordinate system is defined in Fig. (2-1) and $\beta$
is the eigen-value or propagation constant of the mode. Since the guides are assumed to
be uniform in the $z$ direction, the field profile remains constant to within a phase factor
along the axis of the waveguide. The entire $z$ dependence for a axially uniform waveguide
is encapsulated in the phase factor $e^{-j\beta z}$. Forward traveling modes have $\Re e\{\beta\} > 0$ and
backward traveling waves have $\Re e\{\beta\} < 0$.

All waveguides support an infinite number of independent normal modes. Typically
these modes are labelled according to some property of the modal solution which is waveg-
uide dependent. For instance in a slab waveguide the mode labels may correspond to the
number of electric field zero crossings in the core of the guide. In general we can label the

normal modes using an abstract index $n$ which spans a set $\mathcal{N}$ with infinite members. Due to a $z$-mirror symmetry assumed for an ideal waveguide a forward travelling mode $(n)$ can be transformed to a backward traveling modes $(-n)$ and the relationship between them is as follows:

$$\text{mode } (+n): \quad \left\{ \mathcal{E}_{Tn}(x,y), +\mathcal{E}_{zn}(x,y), \mathcal{H}_{Tn}(x,y), +\mathcal{H}_{zn}(x,y) \right\} e^{-j\beta_n z} \qquad (2.5)$$

$$\text{mode } (-n): \quad \left\{ \mathcal{E}_{Tn}(x,y), -\mathcal{E}_{zn}(x,y), -\mathcal{H}_{Tn}(x,y), +\mathcal{H}_{zn}(x,y) \right\} e^{j\beta_n z} \qquad (2.6)$$

Normal modes of dielectric waveguides fall into two sets: one set has a finite number of elements, which could be zero, with discrete values of the propagation constant $\beta_n$; its members are called discrete or guided modes. Guided modes carry finite power and are confined in space such that the fields decay to zero as $x$ and $y$ tend to infinity. They do not carry time-averaged power out of the waveguide radially. Guided modes have a physical meaning individually and are the modes of the dielectric waveguide that are most useful in transporting power from one point to another with minimal loss of power. The other set of normal modes have infinite elements with propagation constants $\beta_n$ which span a continuous range rather than a discrete set of points; its members are called continuous or radiating modes. Radiation modes have a finite value at $(x,y) \to \infty$ and do carry infinite power individually. They also carry power radially out of the waveguide and contribute to loss. Individually radiating modes do not correspond to physical excitation but integrals over the continuous range of radiation modes can produce physical fields. This is obvious in the case of plane waves, $e^{-j\mathbf{k} \cdot \mathbf{r}}$ which are the normal modes of a homogeneous dielectric medium "waveguide". The values of the propagation vector, $\mathbf{k} = (k_x \mathbf{i}_x, k_y \mathbf{i}_y, k_z \mathbf{i}_z)$ span a continuous range with $|\mathbf{k}|^2$ varying from $-\infty$ to $+\infty$. Even though individually these modes do not carry finite power they can be summed up to create field distributions with finite power.

The number of discrete or guided modes depends on frequency. Typically a discrete mode vanishes below a special frequency called the cut-off frequency which is characteristic to the mode. On the other hand radiation modes exist at all frequencies as they span a continuous $\beta$ range.The most general solution to Maxwells equations in any part of the waveguides limited by two cross-sectional planes is a linear combination of all the forward traveling and backward traveling normal modes and is given by [18].

$$\left\{ \begin{array}{c} \mathbf{E}(x,y,z) \\ \mathbf{H}(x,y,z) \end{array} \right\} = \sum_{n \in \mathcal{N}} \left[ A_n \left\{ \begin{array}{c} \mathcal{E}_n(x,y) \\ \mathcal{H}_n(x,y) \end{array} \right\} e^{-j\beta_n z} + B_n \left\{ \begin{array}{c} \mathcal{E}_{-n}(x,y) \\ \mathcal{H}_{-n}(x,y) \end{array} \right\} e^{+j\beta_n z} \right] \qquad (2.7)$$

where $\mathcal{E}(x,y)$ and $\mathcal{H}(x,y)$ are the z-independent part of the field and can have $x, y$ or $z$ components, i.e $\mathcal{E}(x,y) = \{\mathcal{E}_x(x,y), \mathcal{E}_y(x,y), \mathcal{E}_z(x,y)\}$ . $A_n$ and $B_n$ are the coefficients of the forward traveling and backward traveling waves and can be uniquely determined by matching boundary conditions at the two cross-sectional planes. The relation between the $(+n)$ modes and the $(-n)$ modes is defined by eqs. (2.5) and (2.6).

### 2.1.2   TE, TM and hybrid modes

Normal modes with $E_z = 0$ are called TE or transverse electric modes. Likewise modes with $H_z = 0$ are called TM or transverse magnetic modes. Slab waveguides for example can have strict TE and TM modes such that the field $\mathcal{E}$ or $\mathcal{H}$ is polarized exclusively in the $y$ direction. Generally dielectric waveguides do have non-zero $E_z$ and $H_z$ and support hybrid modes. However, often it occurs that at least one of the components dominates and the modes can be considered quasi TE or TM.

### 2.1.3   Completeness of normal modes

The principle of completeness of normal modes states that any two component distribution, $\mathbf{V}_T(x,y)$ can be expanded or represented as a linear combination of the transverse electric (or magnetic) field of the normal modes of the waveguide system, i.e

$$\mathbf{V}_T(x,y) = \sum_{n \in \mathcal{N}} a_n \, \mathcal{E}_{Tn}(x,y) \tag{2.8}$$

or:

$$\mathbf{V}_T(x,y) = \sum_{n \in \mathcal{N}} b_n \, \mathcal{H}_{Tn}(x,y) \tag{2.9}$$

In a sense this is generalized "Fourier" representation of an arbitrary distribution $\mathbf{V}_T(x,y)$ in terms of a complete basis set of functions; in this case the basis set is the set of eigenmodes of the waveguide system. It should be pointed out that $\mathbf{V}_T(x,y)$ has no a priori relationship to the waveguide.

Completeness of the normal modes of a waveguide is a very important property that allows us to use perturbation techiques to analyze non-ideal waveguides which are not uniform in the axial direction. The fields in the non-ideal waveguide are expanded in terms of the modes of the ideal waveguide system as in eq. (2.7). The unknown coefficients $A_n(z)$ and $B_n(z)$ are now assumed to have a z dependence which is caused by the perturbation. By relating the coefficient to the perturbation, differential equations can be written down

in terms of the coefficients and the perturbation. In fact we will utilize this technique in the following chapter to derive the Coupled Mode Theory that models the behavior of Bragg gratings.

### 2.1.4   Orthogonality relations

Another interesting property of normal modes is that they obey an orthogonality relationship. In its most general form this relation is:

$$\iint \mathcal{E}_m(x,y) \times \mathcal{H}_n(x,y) \cdot \mathbf{i}_z \, dx \, dy = N_m \, \delta_{mn} \tag{2.10}$$

where $N_m$ is an arbitrary function of $m$ and determines the normalization of the modes. $\delta_{mn}$ is the generalized Dirac delta function. The above orthogonality relationship is always valid whether the guides are lossy, have gain or are lossless. However, in the case of lossless guides the normalization can be written as

$$\iint \mathcal{E}_m(x,y) \times \mathcal{H}_n^*(x,y) \cdot \mathbf{i}_z \, dx \, dy = 2P_m \, \delta_{mn} \tag{2.11}$$

For the case of a truly guided mode ($m$) with a real propagation constant $\beta_m$, $P_m$ is the power carried by the mode. Moreover for the special case of the fields being TE modes, i.e $\mathcal{E}_z = 0$ the orthogonality conditions simplifies to

$$\frac{\beta_n}{2\omega\mu} \iint \mathcal{E}_{Tm}(x,y) \cdot \mathcal{E}_{Tn}^*(x,y) \, dx \, dy = 2P_m \delta_{mn} \tag{2.12}$$

A corresponding expression exists for TM modes in terms of the transverse $\mathcal{H}_T(x,y)$ field. Note that the normalization factor is arbitrary and we may choose the following convenient normalization for the orthonormal TE normal modes:

$$\iint \mathcal{E}_{Tm}(x,y) \cdot \mathcal{E}_{Tn}^*(x,y) \, dx \, dy = \delta_{mn} \tag{2.13}$$

Using the above orthogonality relationship we can find the generalized Fourier coefficients, $a_n$, of the expansion in eq. (2.8). They are

$$a_m = \iint \mathbf{V}_T(x,y) \cdot \mathcal{E}_{Tm}^*(x,y) \, dx \, dy \tag{2.14}$$

## 2.2   Coupling between Waveguides

When two waveguides are fabricated next to each other as shown in Fig. (2-2) the fields in one guide extend via the evanescent tails to the other and can excite a mode in the adjacent
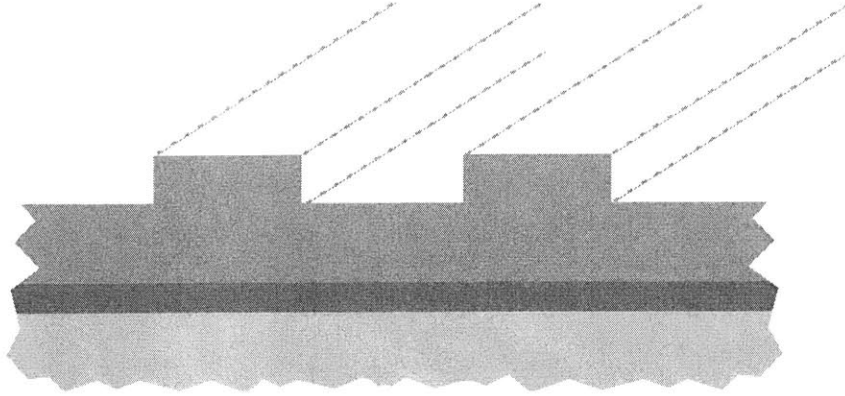
**Figure 2-2:** Two coupled waveguides; coupling occurs via evanescent tails of the waveguide modes.

guide. Figure (2-3) shows an overlay of the first guided modes (the guides are assumed single-moded at the wavelength of operation) on the waveguide structure. We see that the evanescent tails of the mode of guide 1 extend into guide 2 and vice-versa. These fields in guide 1 are associated with a polarization current density which can excite a mode in guide 2. If power is launched in guide 1 it eventually transfers completely to the guide 2 provided the propagation constants of two guides are identical. If the propagation constants are mismatched the power transfer is incomplete [20, 21].

Electric fields in any medium defined by a dielectric distribution, $\epsilon(x, y)$ obey the following wave equation in the absence of a source.

$$\left(\nabla_T^2 + \frac{\partial^2}{\partial z^2} + \omega^2 \mu \epsilon(x, y)\right) \mathbf{E}(x, y, z) = 0 \tag{2.15}$$

The fields in the the coupled waveguide structure must obey the wave equation which simply follows from Maxwell's equations in the absence of a source. The waveguide coupling problem can be solved using the technique alluded to above which involves coupling the normal modes of the unpertubed waveguide structures [21]. Consider the case of the two planar waveguides coupled to each other. Figure (2-3) shows the dielectric profiles of the individual waveguides in the absence of the coupling. The are denoted by $\epsilon_1(x)$ and $\epsilon_2(x)$ for waveguides 1 and 2 respectively. The electric fields in the unperturbed structures are denoted by $\mathbf{E}_1(\mathbf{r})$ and $\mathbf{E}_2(\mathbf{r})$ respectively and are given by:

$$\mathbf{E}_1(\mathbf{r}) = A_1' \mathcal{E}_1(x, y) e^{-j\beta_1 z} \tag{2.16}$$

$$\mathbf{E}_2(\mathbf{r}) = A_2' \mathcal{E}_2(x, y) e^{-j\beta_2 z} \tag{2.17}$$

In the absence of the perturbation provided by the presence of the adjacent guides, the
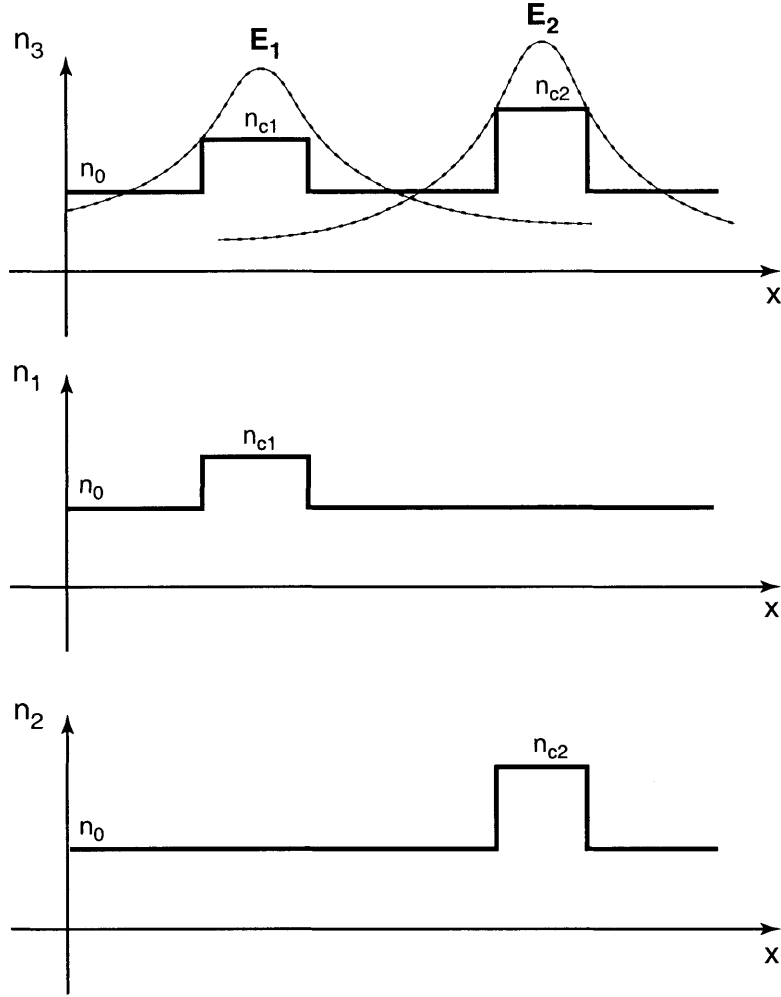
**Figure 2-3:** Dielectric distribution of the unperturbed waveguides and coupled-waveguide structure.

fields obey the wave equation

$$\nabla_T^2 \, \mathcal{E}_1(x, y) + (\omega^2 \mu \epsilon_1(x, y) - \beta_1^2)\mathcal{E}_1(x, y) \;=\; 0 \tag{2.18}$$

$$\nabla_T^2 \, \mathcal{E}_2(x, y) + (\omega^2 \mu \epsilon_2(x, y) - \beta_2^2)\mathcal{E}_2(x, y) \;=\; 0 \tag{2.19}$$

where the amplitudes $A_1'$ and $A_2'$ are constants. The unperturbed waveguides modes propagate undisturbed along the $z$-direction.

The field in the composite coupled structure must obey eq. (2.15) with $\epsilon(x, y) = \epsilon_3(x, y)$. We assume the total field solution, $\mathbf{E}(x, y, z)$ is a combination of the modes of the unperturbed structure.

$$\mathbf{E}(x, y, z) = A_1'(z) \, \mathcal{E}_1(x, y)e^{-j\beta_1 z} + A_2'(z) \, \mathcal{E}_2(x, y)e^{-j\beta_2 z} \tag{2.20}$$

where the amplitude coefficients $A_1'(z)$ and $A_2'(z)$ are a function of $z$. This is necessary to allow for the fact that the perturbation enables transfer of power from one waveguide to the other. Substituting the above in eq. (2.15) with $\epsilon(x, y) = \epsilon_3(x, y)$ we find that:

$$\left\{ \nabla_T^2 \mathcal{E}_1(x, y) + (\omega^2 \mu \epsilon_1(x, y) - \beta_1^2) \mathcal{E}_1(x, y) \right\} A_1'(z) e^{-j\beta_1 z} +$$

$$\left\{ \nabla_T^2 \mathcal{E}_2(x, y) + (\omega^2 \mu \epsilon_2(x, y) - \beta_2^2) \mathcal{E}_2(x, y) \right\} A_2'(z) e^{-j\beta_2 z} +$$

$$\left\{ \omega^2 \mu \Big( \epsilon_3(x, y) - \epsilon_1(x, y) \Big) A_1'(z) - 2j\omega\beta_1 \frac{dA_1'}{dz} \right\} \mathcal{E}_1(x, y) e^{-j\beta_1 z} +$$

$$\left\{ \omega^2 \mu \Big( \epsilon_3(x, y) - \epsilon_2(x, y) \Big) A_2'(z) - 2j\omega\beta_2 \frac{dA_2'}{dz} \right\} \mathcal{E}_2(x, y) e^{-j\beta_2 z} \quad = \quad 0 \quad (2.21)$$

where we have assumed that

$$\left| \frac{d^2 A_i'}{dz^2} \right| \ll \left| \beta_i \frac{dA_i'}{dz} \right| \tag{2.22}$$

This assumption merely states that the perturbation caused by the presence of the adjacent guide is relatively small so that the changes in field amplitudes occur over distances much larger than the propagation wavelength. The first two terms in eq. (2.21) are zero as the unperturbed fields obey their respective wave eqs. (2.18) and (2.18). We multiply eq. (2.21) by $\mathcal{E}_1^*(x, y)$ and integrate over the cross-section. Using the normalization condition we obtain the following equation:

$$\left[ \frac{dA_1'}{dz} + j\mathbf{M}_1 A_1' \right] e^{-j\beta_1 z} + j\mu_{12} A_2' e^{-j\beta_2 z} = 0 \tag{2.23}$$

A similar equation follows if we multiply eq. (2.21) by $\mathcal{E}_2^*(x, y)$ and integrate over the cross-section.

$$\left[ \frac{dA_2'}{dz} + j\mathbf{M}_2 A_2' \right] e^{-j\beta_2 z} + j\mu_{21} A_1' e^{-j\beta_1 z} = 0 \tag{2.24}$$

where

$$\mathbf{M}_{(1,2)} = \frac{\omega}{4} \int_{D_{(2,1)}} [\epsilon_3(x) - \epsilon_{(1,2)}(x)] |\mathcal{E}_{(1,2)}(x)|^2 \, dx \tag{2.25}$$

$$\mu_{12} = \frac{\omega}{4} \int_{D_2} [\epsilon_3(x) - \epsilon_1(x)] \mathcal{E}_2(x) \mathcal{E}_1^*(x) \, dx \tag{2.26}$$

$$\mu_{21} = \frac{\omega}{4} \int_{D_1} [\epsilon_3(x) - \epsilon_{(2)}(x)] \mathcal{E}_1(x) \mathcal{E}_2^*(x) \, dx \tag{2.27}$$

and where $D_i$ indicates an integral over the cross-section of guide $i$. This follows from the fact that $(\epsilon_3 - \epsilon_i)$ is only non-zero across the core region of guide $j \neq i$. Note that when the two guides 1 and 2 are identical then $\mu_{12} = \mu_{21}^*$. In fact it can be shown that even if the guides are dissimilar the above relation holds true [20]. We can see how this may be

true by considering the integrals for $\mu_{12}$ and $\mu_{21}$. Notice that these integrals are taken over different cross-sections. If the guides are not identical then the products of the field values, $\mathcal{E}_1\mathcal{E}_2^*$, and $\mathcal{E}_2\mathcal{E}_1^*$ at the cross-sections of the two guides are different such that $\mu_{12} = \mu_{21}^*$ still holds true. In fact power conservation requires this relationship between $\mu_{12}$ and $\mu_{21}$. By defining new quantities $A_1(z)$ and $A_2(z)$ to represent the total $z$-dependence,

$$A_1(z) = A_1'(z)e^{-j\beta_1 z} \tag{2.28}$$

$$A_2(z) = A_2'(z)e^{-j\beta_2 z} \tag{2.29}$$

the coupled mode equations can be rewritten as

$$\frac{dA_1}{dz} + j\beta_1 A_1 + j\mathbf{M}_1 A_1 + j\mu_{12}A_2 = 0 \tag{2.30}$$

$$\frac{dA_2}{dz} + j\beta_2 A_2 + j\mathbf{M}_2 A_2 + j\mu_{21}A_1 = 0 \tag{2.31}$$

Furthermore $M_{(1,2)}$ is a second-order term and significantly smaller than $\mu_{ij}$. To first-order it can be ignored and the equations modelling the behavior of two coupled waveguides can be rewritten as:

$$\frac{dA_1}{dz} = -j\beta_1 A_1 - j\mu A_2 \tag{2.32}$$

$$\frac{dA_2}{dz} = -j\beta_2 A_2 - j\mu A_1 \tag{2.33}$$

where we have used the fact that $\mu_{12}$ and $\mu_{21}$ are real. If modes are launced in each of the guides at $z = 0$ with amplitudes $A_1(0)$ and $A_2(0)$ then the solution of the above equations is given by [20]:

$$A_1(z) = \left[A_1(0)\left(\cos\beta_0 z + j\frac{\beta_2 - \beta_1}{2\beta_0}\sin\beta_0 z\right) - j\frac{\mu}{\beta_0}A_2(0)\sin\beta_o z\right] \cdot e^{-j[(\beta_1+\beta_2)/2]z} \tag{2.34}$$

$$A_2(z) = \left[-j\frac{\mu}{\beta_0}A_1(0)\sin\beta_o z + A_2(0)\left(\cos\beta_0 z + j\frac{\beta_2 - \beta_1}{2\beta_0}\sin\beta_0 z\right)\right] \cdot e^{-j[(\beta_1+\beta_2)/2]z} \tag{2.35}$$

where

$$\beta_0 = \sqrt{\left(\frac{\beta_2 - \beta_1}{2}\right)^2 + |\mu|^2} \tag{2.36}$$

This discussion above is intended to motivate a derivation of the Coupled Mode equations describing waveguide couplers. For an exhaustive and rigorous treatment of the subject the readers are referred to [22, 23, 24]

# Chapter 3

# Bragg Gratings

In the previous chapter we saw that a dielectric waveguide can support TE and TM guided modes. These modes are orthogonal to each other and if excited in an ideal waveguide without imperfections, propagate along the guide undisturbed with their characteristic group velocities and propagation constants, $\beta_m$, without interacting with one another. However, practical waveguides are not without imperfections. The imperfections can be in the form of index inhomogeneities, rough surfaces, non-uniform widths of the guide, etc. These imperfections can result in the guided modes of a waveguide interacting and exchanging power with each other [17]. Thus, it is possible for energy from one mode of the guide to couple to another mode propagating in the same guide. In many cases this is not desirable. For example, if guided modes couple power to the continuum radiation modes, it results in waveguide losses. However, coupling between modes is not always an undesired effect. In fact, in some structures perturbations are intentionally introduced so as to couple modes. One class of such devices are the distributed feedback (DFB) structures or Bragg gratings.

Bragg gratings are produced by periodic perturbations in the refractive index [25] along the length of the guiding structure. In integrated optical devices this periodic variation is typically produced by etching a corrugation on a dielectric waveguide as shown in Fig. (3-1). Other techniques to make gratings include using photo-sensitive uv effects to produce periodic variations in the material index. These techniques are more common in optical fibers and produce weaker gratings [8]. Gratings couple the forward and backward travelling waves of the same mode, when appropriately designed. This is due to coherent reflections from adjacent dielectric interfaces. Mathematically gratings are most conveniently described by Coupled-Mode Theory (CMT) which uses perturbation theory. The equations describing
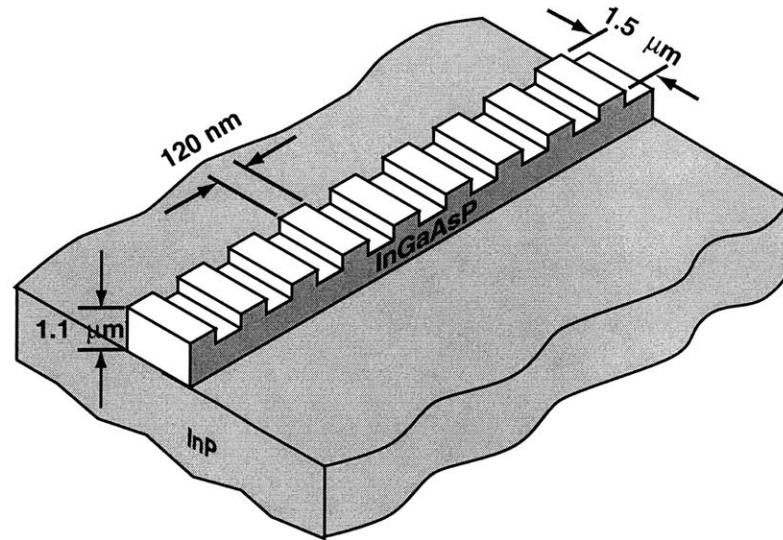
**Figure 3-1:** An integrated Bragg grating in InP and its dimensions. Top cladding InP layer not
shown.

the behavior of the optical modes in the DFB grating will be derived using perturbation
theory. Gratings are the basic building block of all the devices to follow in the dissertation
and their behavior will be discussed in detail. Spectral response of uniform, apodized,
chirped and phase-shifted gratings will be calculated.


## 3.1    Coupled Mode Equations

Figure (3-1) shows a schematic of an integrated Bragg grating. All the Bragg grating
devices were fabricated in an InP material system by etching a periodic corrugation on the
top surface of the InGaAsP core. The waveguide was then overgrown (not shown in the
fig.) with an InP cladding layer to form a channel waveguide. Bragg gratings made by
physically etching a corrugation in a guide, as opposed to using photo-refractive effects,
have stronger reflection characteristics than a UV-induced grating of an equivalent length.
Before we derive the Coupled-Mode equations describing a Bragg grating, let us gain some
insight by considering what happens to the optical wave in the region of the corrugations.
Across the cross-section of the corrugations the optical waveguide mode is presented with
a region of alternating refractive index. Consequently, we expect part of the mode to be
reflected at each interface between a tooth and a trench. The amount reflected is related
to the difference between the index of the core and the cladding regions. In the limit when

a grating consists of regions of alternating dielectric slabs the reflection at a given interface at normal incidence is given by the familiar expression:

$$\Gamma = \frac{n_2 - n_1}{n_2 + n_1} \tag{3.1}$$

where $\Gamma$ is the reflection coefficient. At the immediately adjacent interface, the reflection coefficient is $-\Gamma$ as the indices are reversed. If the distance between the two interfaces is exactly a quarter of the optical wavelength, such that the round-trip traversal phase is $\pi$, the reflections from adjacent interfaces add in phase. At this wavelength, called the Bragg wavelength, $\lambda_B$, we expect a strong reflection from the grating. This simplistic reasoning suggests that the Bragg grating is a frequency sensitive reflector which couples the forward-propagating and backward-propagating waveguide modes. To quantify this coupling and to exactly determine how the response of the grating varies with frequency we will resort to an approach which treats the corrugations as a perturbative effect and derives a simple set of equation characterizing the Bragg grating [21].

The electric field in the integrated Bragg grating obeys the wave equation

$$\nabla^2 \mathbf{E} = \mu_o \epsilon_o \frac{\partial^2 \mathbf{E}}{\partial t^2} + \mu_o \frac{\partial^2 \mathbf{P}_{\text{tot}}}{\partial t^2} \tag{3.2}$$

It is convenient to separate the total polarization density, $\mathbf{P}_{\text{tot}}$, into two parts, namely the polarization of the unperturbed waveguide, $\mathbf{P}_o$, and the polarization produced due to the perturbation, $\mathbf{P}_{\text{pert}}$. Thus,

$$\mathbf{P}_{\text{tot}} = \mathbf{P}_o + \mathbf{P}_{\text{pert}} \tag{3.3}$$

where

$$\mathbf{P}_o = \epsilon_o \chi_e \mathbf{E}(\mathbf{r}, t) = [\epsilon(r) - \epsilon_o] \mathbf{E}(\mathbf{r}, t) \tag{3.4}$$

and $\epsilon(r)$ is the dielectric constant of the unperturbed waveguide.

As mentioned in the previous chapter, the modes of the unperturbed waveguide form a complete orthonormal set. Any field distribution in an arbitrary waveguide structure can be expanded as a superposition of the modes of the unperturbed waveguide. The orthonormal set consists of all the guided modes, TE and TM and the continuum of radiation modes. To be specific, we treat the case of a TE distribution. Extension to an arbitrary guided distribution is straightforward but unnecessarily complicates the notation and thus will not be attempted. The electric field $E_y$ in the perturbed structure, i.e grating, is written as a superposition of the modes of the unperturbed guide [24]. For notational simplicity we

will assume that the radiation modes are discrete and included in the summation of eq. (3.5). Even though this assumption is not strictly valid, we will see shortly that it does not affect the result of the derivation. Consequently, the electric field, $E_y$, in the Bragg grating structure can be written as

$$E_y(r, t) = \frac{1}{2}\sum_m A'_m(z)\mathcal{E}_y^m(x, y)e^{j(\omega t - \beta_m z)} + B'_m(z)\mathcal{E}_y^m(x, y)e^{j(\omega t + \beta_m z)} + c.c. \qquad (3.5)$$

The first term in the summation represents the forward-propagating $m^{th}$ mode of the unperturbed waveguide; the second term represents same mode travelling in the opposite direction. The weighting coefficients $A'_m$ and $B'_m$ are functions of $z$ to account for the fact that the perturbation itself has a $z$-dependance.

Recall that $\mathcal{E}_y^m(x, y)e^{j(\omega t \pm \beta_m z)}$ are solutions of the unperturbed waveguide and hence obey the following equation:

$$\nabla_{\mathbf{T}}^2 \mathcal{E}_y^m(x, y) - \beta_m^2 \mathcal{E}_y^m(x, y) = -\omega^2 \mu_o \epsilon(r) \mathcal{E}_y^m(x, y) \qquad (3.6)$$

where

$$\nabla^2 \equiv \nabla_{\mathbf{T}}^2 + \frac{\partial^2}{\partial z^2}$$

$$\nabla_{\mathbf{T}}^2 \equiv \frac{\partial^2}{\partial x^2} + \frac{\partial^2}{\partial y^2}$$

Using (3.3) and (3.4), we can rewrite (3.2) as

$$\nabla_{\mathbf{T}}^2 \mathbf{E} + \frac{\partial^2 \mathbf{E}}{\partial z^2} - \mu_o \epsilon(r)\frac{\partial^2 \mathbf{E}}{\partial t^2} = \mu_o \frac{\partial^2 \mathbf{P}_{\text{pert}}}{\partial t^2}$$

Substituting the expression for the electric field distribution, (3.5), in the above equation, we find

$$e^{j\omega t}\{ \quad \sum_m \frac{A'_m}{2}(\nabla_{\mathbf{T}}^2 - \beta_m^2 + \omega^2 \mu_o \epsilon(r))\mathcal{E}_y^m(x, y)e^{-j\beta_m z}$$

$$+ \quad \sum_m \frac{B'_m}{2}(\nabla_{\mathbf{T}}^2 - \beta_m^2 + \omega^2 \mu_o \epsilon(r))\mathcal{E}_y^m(x, y)e^{j\beta_m z}$$

$$+ \quad \sum_m \frac{1}{2}(\frac{\partial^2 A'_m}{\partial z^2} - 2j\beta_m \frac{\partial A'_m}{\partial z})\mathcal{E}_y^m(x, y)e^{-j\beta_m z}$$

$$+ \quad \sum_m \frac{1}{2}(\frac{\partial^2 B'_m}{\partial z^2} + 2j\beta_m \frac{\partial B'_m}{\partial z})\mathcal{E}_y^m(x, y)e^{j\beta_m z}\}$$

$$= \mu_o^2 \frac{\partial^2}{\partial t^2}[\mathbf{P}_{\text{pert}}]_y \qquad (3.7)$$

The above equation can be simplified considerably by realizing that the first two summations are zero according to (3.6). Thus far no approximations have been made. The

above equations are exact provided we assume that the modes of the unperturbed guide form a complete set. We now make our first approximation. Since the perturbation is small, we assume that $A'_m$ and $B'_m$ are slowly varying functions of $z$. This is a reasonable assumption since in the limit that the perturbation tends to zero we expect $A'_m$ and $B'_m$ to become constants; i.e the fields in the summation are eigenmodes of the unperturbed structure and propagate indefinitely along the waveguide without any change. Using this "slow" varying approximation, we conclude that [21]

$$\left| \frac{\partial^2 A'_m}{\partial z^2} \right| \ll \left| \beta_m \frac{\partial A'_m}{\partial z} \right|$$

and

$$\left| \frac{\partial^2 B'_m}{\partial z^2} \right| \ll \left| \beta_m \frac{\partial B'_m}{\partial z} \right|$$

These inequalities simply state that $A'_m(z)$ and $B'_m(z)$ change very slowly over distances on the order of a single optical-mode wavelength. This assumption is consistent with treating the corrugation as a perturbation, which means that it can not have large effects on the optical field over short distances. Taking this into account, we can rewrite (3.7) as

$$e^{j\omega t} \sum_m -j\beta_m \left[ \frac{\partial A'_m}{\partial z} e^{-j\beta_m z} - \frac{\partial B'_m}{\partial z} e^{j\beta_m z} \right] \mathcal{E}_y^{\ m}(x,y) + \text{c.c} = \mu_o \frac{\partial^2}{\partial t^2} [\mathbf{P}_{\text{pert}}]_y \qquad (3.8)$$

We use the orthonormality of waveguide modes to isolate a single mode from the summation. In this chapter we use a slightly different normalization condition for the fields. Instead of normalizing the power in the mode to unity we choose the integral of the square of the **E** field to be unity. This choice yields a particularly simple form for the coupling coefficient, as we will see later.

$$\iint_\infty^\infty \mathcal{E}_y^m(x,y) \mathcal{E}_y^l(x,y) dx dy = \delta_{lm} \qquad (3.9)$$

as found in chapter 2. ($\delta_{lm}$ is the Kronecker delta function.) Multiplying both sides of (3.8) with $\mathcal{E}_y^s(x,y)$ and integrating over $x$, we obtain

$$\frac{dA'_s}{dz} e^{j(\omega t - \beta_s z)} - \frac{dB'_s}{dz} e^{j(\omega t - \beta_s z)} + \text{c.c} = j\frac{\mu_o}{\beta_s} \frac{\partial^2}{\partial t^2} \iint_\infty^\infty [\mathbf{P}_{\text{pert}}]_y \mathcal{E}_y^s(x,y) dx dy \qquad (3.10)$$

The above equation relates the forward and backward propagating $s^{th}$ mode to the perturbation polarization current density. We have not yet discussed how $\mathbf{P}_{\text{pert}}$ is related to the

perturbation. The corrugations along the guide can be described by a dielectric perturbation $\Delta\epsilon(r)$ such that the total dielectric constant $\epsilon_{\text{tot}}$ is given by

$$\epsilon_{\text{tot}} = \epsilon(r) + \Delta\epsilon(r) \tag{3.11}$$

In general $\Delta\epsilon$ may be purely real, imaginary or complex. For our purposes $\Delta\epsilon$ may be considered purely real. Note that since $\Delta\epsilon$ is a scalar, we see that these type of structures can only couple TE to TE and TM and TM modes [21]. It is not possible to couple TE to TM with a Bragg gratings. We know that

$$\epsilon_{\text{tot}}\mathbf{E} = \epsilon_o\mathbf{E} + \mathbf{P}_{\text{tot}}$$

where $\mathbf{P}_{\text{tot}}$ is the total polarization defined in (3.3). Using (3.3), (3.4) and (3.11) in the above expression, we find that

$$\mathbf{P}_{\text{pert}} = \Delta\epsilon(\mathbf{r})\mathbf{E}$$

Use of eq. (3.5) and the above expression yields

$$\frac{dA'_s}{dz}e^{j(\omega t - \beta_s z)} - \frac{dB'_s}{dz}e^{j(\omega t + \beta_s z)} + \text{c.c} =$$
$$-j\frac{\omega^2\mu_o}{2\beta_s}e^{j\omega t}\iint_{-\infty}^{\infty}\Delta\epsilon(\mathbf{r})\mathcal{E}_y^s(x,y)\mathcal{E}_y^m(x,y)\left[\sum_m A'_m(z)e^{-j\beta_m z} + B'_m(z)e^{j\beta_m z}\right]dxdy \tag{3.12}$$

$\Delta\epsilon(\mathbf{r})$ is a periodic function of $z$ which can expanded in a Fourier series as:

$$\Delta\epsilon(\mathbf{r}) = \Delta\epsilon(x,y)\sum_n a_n e^{j\frac{2\pi n}{\Lambda}}$$

where

$$\Delta\epsilon(x,y) = \begin{cases} \frac{(\epsilon_1 - \epsilon_2)}{2} & \text{if } |x| \le d_g \\ 0 & |x| > d_g \end{cases}$$

and $\Lambda$ is the wavelength of the perturbation. Use of the above expression in (3.12) results in

$$\frac{dA'_s}{dz}e^{-j\beta_s z} - \frac{dB'_s}{dz}e^{j\beta_s z} = -\frac{jk_o^2}{2\beta_s}\iint_{-\infty}^{\infty}\frac{\Delta\epsilon(x,y)}{\epsilon_o}\mathcal{E}_y^s(x,y)\mathcal{E}_y^m(x,y) \times$$
$$\left[\sum_n a_n \sum_m A'_m(z)e^{-j(\beta_m - \frac{2\pi n}{\Lambda})z} + B'_m(z)e^{j(\beta_m + \frac{2\pi n}{\Lambda})z}\right]dxdy$$

where we have divided out the common time dependence, $e^{j\omega t}$. The term on the right hand side acts as a driving term for the propagating modes $A'_s$ and $B'_s$. Only the term which is phase matched to those on the left side will effectively couple to them. Thus, if there is a

term on the right hand side of the form $e^{-j\beta z}$ where $\beta \approx \beta_s$, it will strongly couple to the forward travelling mode, $A'_s(z)$ and we can ignore the contribution due to those terms for which $\beta$ is not approximately equal to $\beta_s$. [21] To be specific, let us assume that

$$\beta_o \equiv \beta_s(\omega_o) \approx \frac{\pi}{\Lambda}$$

so that

$$\beta_s(\omega_o) - \frac{2\pi}{\Lambda} \approx -\beta_s(\omega_o)$$

For this case the term on the right hand side which effectively couples power to the forward propagating mode is $m = s$ and $n = -1$. Similarly the term which effectively drives the backward propagating mode is $m = s$ and $n = 1$. Writing out the equation for the modes separately, we obtain:

$$\frac{dA'_s}{dz} = \left[ -\frac{jk_o^2}{2\beta_s} \iint a_{-1} \frac{\Delta\epsilon(x,y)}{\epsilon_o} [\mathcal{E}_y{}^s(x,y)]^2 dxdy \right] B'_s e^{2j(\beta_s - \frac{\pi}{\Lambda})z} \tag{3.13}$$

$$\frac{dB'_s}{dz} = \left[ \frac{jk_o^2}{2\beta_s} \iint a_1 \frac{\Delta\epsilon(x,y)}{\epsilon_o} [\mathcal{E}_y{}^s(x,y)]^2 dxdy \right] A'_s e^{-2j(\beta_s - \frac{\pi}{\Lambda})z} \tag{3.14}$$

We define the following coupling coefficients

$$\kappa_{AB} = -\frac{jk_o^2}{2\beta_s} \iint a_{-1} \frac{\Delta\epsilon(x,y)}{\epsilon_o} [\mathcal{E}_y^s(x,y)]^2 dxdy \tag{3.15}$$

$$\kappa_{BA} = \frac{jk_o^2}{2\beta_s} \iint a_1 \frac{\Delta\epsilon(x,y)}{\epsilon_o} [\mathcal{E}_y^s(x,y)]^2 dxdy \tag{3.16}$$

Using these definitions of coupling coefficients (3.13) and (3.14) can be rewritten as

$$\frac{dA'_s}{dz} = \kappa_{AB} B'_s e^{2j(\beta_s - \frac{\pi}{\Lambda})z} \tag{3.17}$$

$$\frac{dB'_s}{dz} = \kappa_{BA} A'_s e^{-2j(\beta_s - \frac{\pi}{\Lambda})z} \tag{3.18}$$

Implicit in the above derivation is that $A'_s$ and $B'_s$ correspond to guided modes. The above discussions suggest that the only coupling is that between the forward and backward propagating guided mode $s$. This is the most dominant coupling. In general, however, $s$ could be radiation modes phase-matched by the grating to a guided mode. In ignoring other terms in the summation we have not taken into account this kind of coupling which contributes to radiation loss from gratings. To express the above equations in the conventional coupled-mode form, we define two new quantities $A(z)$ and $B(z)$ which are related to $A'_s(z)$ and $B'_s(z)$ as follows

$$a(z) \equiv A(z)e^{-j\beta_o z} = A'_s(z)e^{-j\beta_s z} \tag{3.19}$$

$$b(z) \equiv B(z)e^{j\beta_o z} = B'_s(z)e^{j\beta_s z} \tag{3.20}$$
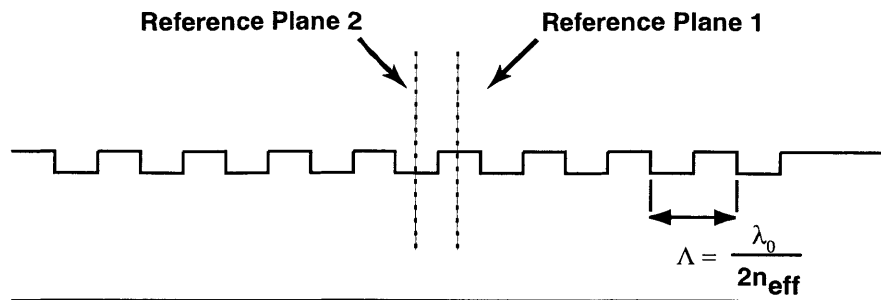
**Figure 3-2:** Reference planes for defining the grating strength parameter, $\kappa$

The total $z$-dependence of the modes is expressed by either side of the above equations and denoted by the lower case variables, $a(z)$ and $b(z)$. Substituting for $A'_s$ and $B'_s$ into (3.17) and (3.18) we get

$$
\begin{aligned}
\frac{dA(z)}{dz} &= -j\delta A(z) + \kappa_{AB}B(z) \\
\frac{dB(z)}{dz} &= j\delta B(z) + \kappa_{BA}A(z)
\end{aligned}
$$

where

$$
\delta \equiv \beta_s - \beta_o = \beta_s - \frac{\pi}{\Lambda} \tag{3.21}
$$

Expanding $\beta_s(\omega)$ around $\omega_o$ we find that

$$
\begin{aligned}
\beta_s(\omega_o) &= \beta_s(\omega_o) + \left.\frac{d\beta_s}{d\omega}\right|_{\omega=\omega_o} (\omega - \omega_o) \\
&= \beta_o + \frac{(\omega - \omega_o)}{v_g}
\end{aligned}
$$

where we have used the fact that the group velocity, $v_g = \frac{d\omega}{d\beta_s}$. The above expansion assumes that dispersion effects in the guide are negligible and can be ignored, that is $\left|\frac{d^2\beta}{d\omega^2}\right| \ll \left|\frac{d\beta}{d\omega}\right|$. Consequently,

$$
\delta = \frac{\omega - \omega_o}{v_g}
$$

and is the "frequency" parameter of the system. Note that the definitions of $\kappa_{AB}$ and $\kappa_{BA}$ have Fourier coefficients, $a_{\pm 1}$. These coefficients depend on where we define the reference plane for the series expansion. Consequently the phase of $\kappa_{AB}$ and $\kappa_{BA}$ depends on our choice of the reference plane. Two obvious choice of planes are marked in the Fig. (3-2). For the choice of plane 1, from the symmetry of the waveform we know that

$$
a_1 = -a_{-1} \quad \text{and} \quad \Re\{a_{\pm 1}\} = 0
$$

For this case, then $\kappa_{AB}$ and $\kappa_{BA}$ from eq. (3.15) are purely real and equal to each other.

$$\kappa_{AB} = \kappa_{BA} \equiv \kappa$$

and the coupled mode equations become

$$\frac{dA}{dz} = -j\delta A + \kappa B \tag{3.22}$$

$$\frac{dB}{dz} = j\delta B + \kappa A \tag{3.23}$$

Likewise if plane 2 is chosen, from the symmetry of the waveform we have

$$a_1 = a_{-1} \quad \text{and} \quad \Im\{a_{\pm 1}\} = 0$$

In this case $\kappa_{AB}$ and $\kappa_{BA}$ are imaginary and are of opposite signs; i.e they are complex conjugates of each other.

$$\kappa_{AB} = \kappa_{BA}^* \equiv j\kappa$$

$\kappa_{AB}$ and $\kappa_{BA}$ are complex conjugates of each other. For an arbitrary reference plane, power conservation requirements can be used to show that $\kappa_{AB}$ and $\kappa_{BA}$ are always complex conjugates of each other, i.e

$$\kappa_{AB} = \kappa_{BA}^*$$

and in the most general form the coupled mode equations are given by

$$\frac{dA}{dz} = -j\delta A + \kappa B \tag{3.24}$$

$$\frac{dB}{dz} = j\delta B + \kappa^* A \tag{3.25}$$

For the choice of reference plane 1, substituting the above result in eq. (3.15) we find that

$$\kappa = \frac{1}{\lambda\, n_{eff}} \iint \Delta n^2(x, y) \left[ \mathcal{E}_y^{\,s}(x, y) \right]^2 dx\, dy \tag{3.26}$$

where

$$\Delta n^2(x, y) \equiv \frac{2\Delta\epsilon(x, y)}{\epsilon_o}$$

i.e

$$\Delta n^2(x, y) = \begin{cases} (n_1^2 - n_2^2) & |x| \leq d_g \\ 0 & |x| > d_g \end{cases}$$

The integral is limited to the cross-section of the grating. For a first-order square wave oscillation of the index, the coupling coefficient $\kappa$ is given by

$$\kappa = \frac{1}{\lambda\, n_{eff}} \Delta n^2\, \Gamma \tag{3.27}$$

where $\Gamma$ is the overlap integral of the power in the field over the cross section of the grating. Having derived the coupled mode equations for the distributed feedback structures, we turn to solving them and studying the response of a passive Bragg grating.

### 3.1.1 $\overline{\overline{\text{T}}}$-matrix Formalism

The coupled mode equations describing the Bragg grating are set of two first-order coupled differential equations with constant coefficients. These equations are very simple to solve analytically. However, we will cast the equation in matrix form as an eigen-value problem. The reason for this approach is that it is very general and is suitable for structures discussed later in the thesis which are described by more complicated $2N \times 2N$ equations. The coupled mode equation cast in matrix form are :

$$\frac{d}{dz}\begin{bmatrix} A(z) \\ B(z) \end{bmatrix} = \begin{pmatrix} -j\delta & \kappa \\ \kappa^* & j\delta \end{pmatrix}\begin{bmatrix} A(z) \\ B(z) \end{bmatrix} \equiv \overline{\overline{\text{M}}}\begin{bmatrix} A(z) \\ B(z) \end{bmatrix} \tag{3.28}$$

which is the eigenvalue problem

$$\overline{\overline{\text{M}}}\vec{A} = \gamma\vec{A}. \tag{3.29}$$

where $\gamma$ are the eigenvalues and the vector $\vec{A}$ represents the field-amplitudes and is given by

$$\vec{A}(z) = \begin{bmatrix} A(z) \\ B(z) \end{bmatrix}$$

The most general solution of eigenvalue problems is given by [26]:

$$\vec{A}(z) = \overline{\overline{\text{S}}}\,\overline{\overline{\Lambda}}(z)\,\vec{c} \tag{3.30}$$

where $\overline{\overline{\text{S}}}$ is a matrix with the eigenvectors of $\overline{\overline{\text{M}}}$ as its columns. $\overline{\overline{\Lambda}}$ is a diagonal matrix with the exponentiated eigenvalues of $\overline{\overline{\text{M}}}$, $e^{\gamma_i z}$, along its diagonal. $\gamma_i$ is the $i^{th}$ eigenvalue and $\vec{c}$ is the vector of weighting coefficients which indicates how much of each eigenvector is excited. $\vec{c}$ is determined from the boundary conditions. Thus if $\vec{A}(z)$ is known at $z = z_o$, using eq. (3.30), the weighting coefficient vector $\vec{c}$ is given by:

$$\vec{c} = [\overline{\overline{\Lambda}}(z_o)]^{-1}[\overline{\overline{\text{S}}}]^{-1}\vec{A}(z_o) \tag{3.31}$$

Combining the above equation with eq. (3.30) we find that $\vec{A}(z)$ is given by

$$\vec{A}(z) = \overline{\overline{\text{S}}}\,\overline{\overline{\Lambda}}(z)\,[\overline{\overline{\Lambda}}(z_o)]^{-1}[\overline{\overline{\text{S}}}]^{-1}\vec{A}(z_o) \tag{3.32}$$

$$\vec{A}(z) \equiv \overline{\overline{\text{T}}}(z, z_o)\vec{A}(z_o) \tag{3.33}$$

Thus if we know the forward and backward propagating field amplitudes, $\vec{A}(z)$, at location $z = z_o$ the transfer-matrix $\overline{\overline{\mathbf{T}}}(z, z_o)$ allows us to calculate the field amplitudes $\vec{A}(z)$ at any other location.

## $N$ Coupled Structures

In general an arbitrarily coupled system of $N$ waveguide structures is described by a $2N \times 2N$ matrix, $\overline{\overline{\mathbf{M}}}$ describing the interaction between each of the $N$ forward and backward propagating waves. The transfer-matrix, $\overline{\overline{\mathbf{T}}}(z, z_o)$ in this case is given by

$$\overline{\overline{\mathbf{T}}}(z, z_o) = \overline{\overline{\mathbf{S}}} \, \overline{\overline{\mathbf{\Lambda}}}(z) \, [\overline{\overline{\mathbf{\Lambda}}}(z_o)]^{-1} [\overline{\overline{\mathbf{S}}}]^{-1} \tag{3.34}$$

with

$$\overline{\overline{\mathbf{S}}} = \begin{pmatrix} \uparrow & \uparrow & & \uparrow \\ \vec{v}_1 & \vec{v}_2 & \cdots & \vec{v}_{2N} \\ \downarrow & \downarrow & & \downarrow \end{pmatrix} \tag{3.35}$$

$$\overline{\overline{\mathbf{\Lambda}}}(z) = \begin{pmatrix} e^{\gamma_1 z} & & \\ & \ddots & \\ & & e^{\gamma_{2N} z} \end{pmatrix} \tag{3.36}$$

where $\overline{\overline{\mathbf{S}}}$ has the $2N$ eigenvectors of $\overline{\overline{\mathbf{M}}}$ as its columns and $\overline{\overline{\mathbf{\Lambda}}}$ is a matrix with the $2N$ exponentiated eigenvalues of $\overline{\overline{\mathbf{M}}}$ along its diagonal. If the mode amplitude values of the $N$ forward and backward propagating fields are known at any $z$-plane, for eg. at $z = z_o$, i.e

$$\vec{A}(z_o) = \begin{bmatrix} A_1(z_o) \\ \vdots \\ A_N(z_o) \\ B_1(z_o) \\ \vdots \\ B_N(z_o) \end{bmatrix}$$

the transfer matrix $\overline{\overline{\mathbf{T}}}(z_1, z_o)$ can be used to determine the field amplitudes at $z = z_1$ simply by

$$\vec{A}(z_1) = \overline{\overline{\mathbf{T}}}(z_1, z_o)\vec{A}(z_o) \tag{3.37}$$

If a system is made of $n$ piece-wise constant sections the transfer matrices can be cascaded such that

$$\vec{A}(z_n) = \overline{\overline{\mathbf{T}}}_n(z_n, z_{n-1}) \cdots \overline{\overline{\mathbf{T}}}_2(z_2, z_1)\overline{\overline{\mathbf{T}}}_1(z_1, z_o)\, \vec{A}(z_o) \tag{3.38}$$

$$\equiv \overline{\overline{\mathbf{T}}}(z_n, z_o)\, \vec{A}(z_o) \tag{3.39}$$

and the combined transfer matrix is the product of the transfer matrices of the $n$ regions. Figure (3-3(a)) shows this transformation schematically. This simply follows from the continuity of the field amplitudes at the interfaces between adjacent regions.

Typically, all the $2N$ field amplitudes are not known at a single $z$-plane. Rather the boundary conditions are specified as inputs to the system, i.e $A_i(z_n)$ and $B_i(z_o)$ are known as shown schematically in Fig. (3-3(b)). All the same, the transfer matrix approach can be used to solve the problem. To solve this problem we must convert the tranfer-matrix, $\overline{\overline{\mathbf{T}}}(z_n, z_o)$ to a scattering matrix, $\overline{\overline{\mathbf{S}}}_{\mathbf{T}}(z_n, z_o)$. This is a relatively straightforward. As mentioned before the transfer matrix relates the field amplitudes at $z = z_o$ to those at $z = z_n$, i.e

$$\begin{bmatrix} \vec{A}(z_n) \\ \vec{B}(z_n) \end{bmatrix} = \begin{pmatrix} \overline{\overline{\mathbf{T}}}_1 & \overline{\overline{\mathbf{T}}}_2 \\ \overline{\overline{\mathbf{T}}}_3 & \overline{\overline{\mathbf{T}}}_4 \end{pmatrix} \begin{bmatrix} \vec{A}(z_o) \\ \vec{B}(z_o) \end{bmatrix} \tag{3.40}$$

The bold-faced quantities are the inputs to the system that are known. We can convert the matrix so that the unknowns are expressed in terms of the known quantities. This is a straightforward operation and the result is:

$$\begin{bmatrix} \vec{A}(z_o) \\ \vec{B}(z_n) \end{bmatrix} = \begin{pmatrix} \overline{\overline{\mathbf{T}}}_1^{-1} & \overline{\overline{\mathbf{T}}}_2 \\ \overline{\overline{\mathbf{T}}}_3\overline{\overline{\mathbf{T}}}_1^{-1} & \overline{\overline{\mathbf{T}}}_4 - \overline{\overline{\mathbf{T}}}_3\overline{\overline{\mathbf{T}}}_1^{-1}\overline{\overline{\mathbf{T}}}_2 \end{pmatrix} \begin{bmatrix} \vec{A}(z_n) \\ \vec{B}(z_o) \end{bmatrix} \tag{3.41}$$

with

$$\overline{\overline{\mathbf{S}}}_{\mathbf{T}}(z_n, z_o) \equiv \begin{pmatrix} \overline{\overline{\mathbf{T}}}_1^{-1} & \overline{\overline{\mathbf{T}}}_2 \\ \overline{\overline{\mathbf{T}}}_3\overline{\overline{\mathbf{T}}}_1^{-1} & \overline{\overline{\mathbf{T}}}_4 - \overline{\overline{\mathbf{T}}}_3\overline{\overline{\mathbf{T}}}_1^{-1}\overline{\overline{\mathbf{T}}}_2 \end{pmatrix} \tag{3.42}$$

For a $N$ coupled structure system $\overline{\overline{\mathbf{T}}}_1, \overline{\overline{\mathbf{T}}}_2, \overline{\overline{\mathbf{T}}}_3, \overline{\overline{\mathbf{T}}}_4$ are $N \times N$ block matrices contained within $2N \times 2N$ tranfer matrix, $\overline{\overline{\mathbf{T}}}(z_n, z_o)$. For a simple Bragg grating device $\overline{\overline{\mathbf{T}}}_i$ are just numbers.

The general formalism discussed above can be used to solve an arbitrary system of $N$ coupled structures provided we can write down the matrix $\overline{\overline{\mathbf{M}}}$ describing the system and the inputs to the system are know. This approach will be used repeatedly in the following chapters.
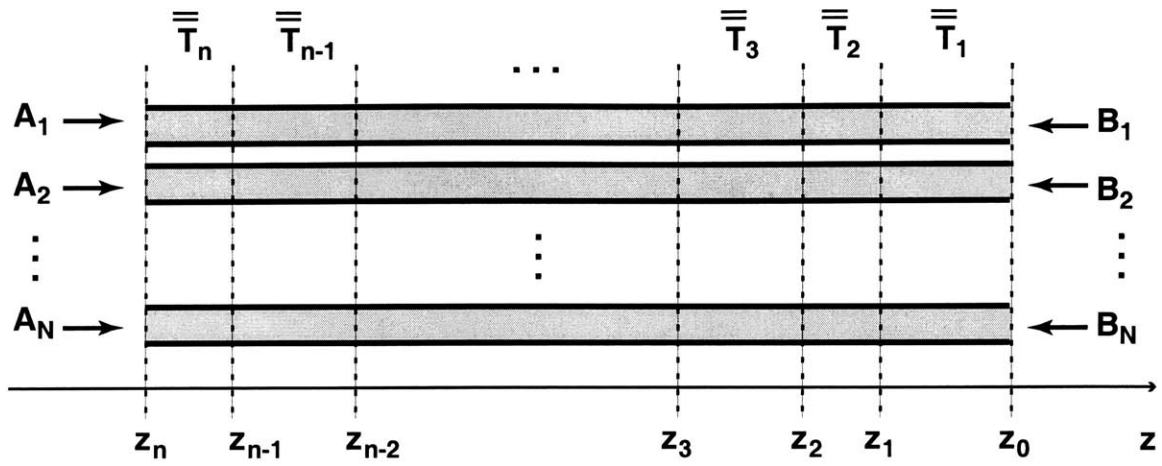
(a)
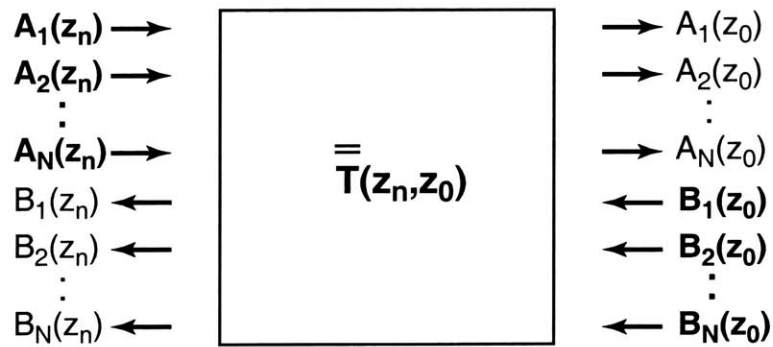


(b)

**Figure 3-3:** Schematic transformation across a $n$-section structure composed of $N$ coupled waveguides.

### 3.1.2 Bragg Grating Response

We now apply this formalism to the case of a Bragg grating that is excited from one side. The matrix, $\overline{\overline{\mathbf{M}}}$ has been derived earlier and is given by:

$$\overline{\overline{\mathbf{M}}} = \begin{pmatrix} -j\delta & \kappa \\ \kappa^* & j\delta \end{pmatrix} \tag{3.43}$$

The eigenvalues of this matrix can be found easily and are:

$$\gamma_1 = -\gamma_2 \equiv \gamma = \sqrt{|\kappa|^2 - \delta^2} \tag{3.44}$$

Similarly the eigenvectors of $\overline{\overline{\mathbf{M}}}$ are found easily and are given by:

$$\vec{v}_1 = \begin{bmatrix} 1 \\ \frac{j\delta + \gamma_1}{\kappa} \end{bmatrix}, \quad \vec{v}_2 = \begin{bmatrix} 1 \\ \frac{j\delta + \gamma_2}{\kappa} \end{bmatrix} \tag{3.45}$$

Thus, using eqs. (3.35) and (3.36) we find that

$$\overline{\overline{\mathbf{S}}} = \begin{pmatrix} 1 & 1 \\ \frac{j\delta + \gamma}{\kappa} & \frac{j\delta - \gamma}{\kappa} \end{pmatrix}$$

$$\overline{\overline{\mathbf{\Lambda}}}(z) = \begin{pmatrix} e^{\gamma z} & 0 \\ 0 & e^{-\gamma z} \end{pmatrix}.$$

Use of eq. (3.34) yields the transfer matrix, $\overline{\overline{\mathbf{T}}}$:

$$\overline{\overline{\mathbf{T}}}(z, z_o) = \begin{bmatrix} \cosh[\gamma(z - z_o)] - \frac{j\delta}{\gamma}\sinh[\gamma(z - z_o)] & \frac{\kappa}{\gamma}\sinh[\gamma(z - z_o)] \\ \frac{\kappa^*}{\gamma}\sinh[\gamma(z - z_o)] & \cosh[\gamma(z - z_o)] + \frac{j\delta}{\gamma}\sinh[\gamma(z - z_o)] \end{bmatrix} \tag{3.46}$$

For an input from the left side only i.e $A(z_n) = A_o$, we can easily find the field amplitudes at any other location in the grating by converting the transfer matrix, $\overline{\overline{\mathbf{T}}}(z, z_o)$ to a corresponding scattering matrix, $\overline{\overline{\mathbf{S}}}_{\mathbf{T}}(z, z_o)$ using eq. (3.42). In this case we find that

$$\Gamma(z_n) \equiv \frac{B(z_n)}{A(z_n)} = \frac{\frac{\kappa^*}{\gamma}\sinh(\gamma L)}{\cosh(\gamma L) + \frac{j\delta}{\gamma}\sinh(\gamma L)} \tag{3.47}$$

$$T(z_o) \equiv \frac{A(z_o)}{A(z_n)} = \frac{1}{\cosh(\gamma L) + \frac{j\delta}{\gamma}\sinh(\gamma L)} \tag{3.48}$$

where $L = z_n - z_o$ is the length of the grating. The response is shown in Fig. (3-4(a)). As expected based on the previous discussion a Bragg grating reflects light strongly over
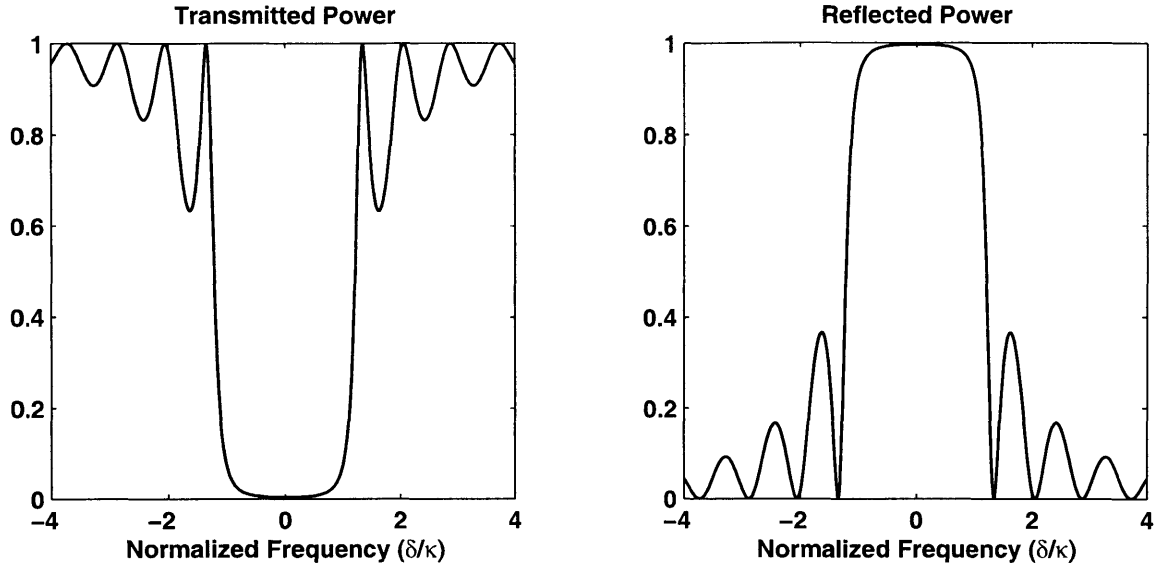
**Figure 3-4:** Frequency spectrum of a uniform Bragg grating.

a certain frequency range. The reflection peaks at the Bragg wavelength, i.e $\lambda = \lambda_B$ or alternately $\delta = 0$. This is exactly the wavelength for which the the tooth and trench of a grating are spaced by $\lambda/4$ and the reflections from adjacent interfaces are precisely in phase. At the Bragg wavelength the reflection and transmission are given by

$$\Gamma(z_n) = \frac{\kappa^*}{|\kappa|} \tanh(|\kappa|L) \tag{3.49}$$

$$T(z_n) = \frac{1}{\cosh(|\kappa|L)} \tag{3.50}$$

We note that the strength of the reflected power depends on the $\kappa L$ product. This makes good sense; $\kappa$ is a measure of the strength of the reflection from a single interface between the teeth and trenches of the grating. The total reflection is the cumulative reflection from all the interfaces and thus depends on the length $L$ of the grating. The stopband of the grating is defined as the frequency range over which $\gamma$ is real, i.e

$$\delta_{SB} = \pm\kappa.$$

In terms of frequency the width of the stopband is given by

$$\Delta\omega_{SB} = 2\kappa v_g \tag{3.51}$$

In the frequency range within the stopband of the grating the eigen-values $\gamma_{(1,2)}$ are real and the field amplitudes $A(z)$ and $B(z)$ decay or grow exponentially along the length of the
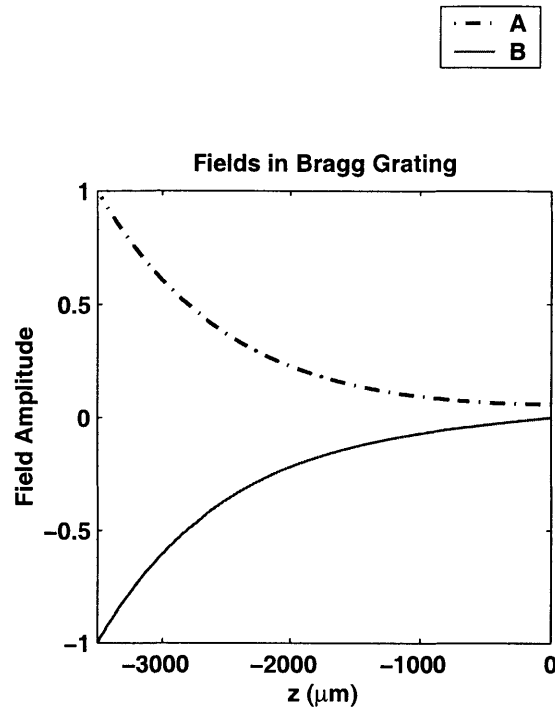
**Figure 3-5:** Field amplitude variation along a grating at $\delta = 0$.

grating. Figure (3-5) shows the field amplitude as a function of distance along the grating at the Bragg wavelength for a semi-infinite grating extending beyond $z \geq 0$. From eq. (3.24) it is obvious that at $\delta = 0$ the field amplitudes are given by [20]:

$$A(z) = A_o e^{-|\kappa|z} \tag{3.52}$$

$$B(z) = -\frac{|\kappa|}{\kappa} A_o e^{-|\kappa|z} \tag{3.53}$$

The other positive eigenvalue, $\gamma = +\kappa$ is not needed for a semi-infinite grating. Its inclusion would lead to a solution that blows up at infinity. However, for a semi-infinite grating in the region $z \leq 0$, the solution is given by:

$$A(z) = A_o e^{|\kappa|z} \tag{3.54}$$

$$B(z) = \frac{|\kappa|}{\kappa} A_o e^{|\kappa|z} \tag{3.55}$$

Outside the stopband the eigenvalues are purely imaginary and the fields can propagate in the grating region and the reflection drops considerably. Thus as expected the grating is a frequency sensitive mirror which couples the forward propagating and backward propagating waves. Figure (3-4) shows the transmission response of the grating. From power
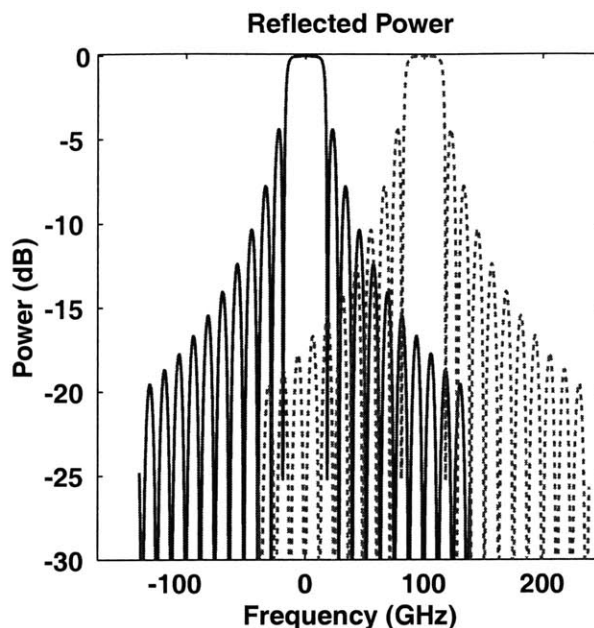
**Figure 3-6:** Uniform Bragg grating response plotted on a logarithmic scale reveals high side-lobe levels. The side-lobes decay slowly and results in high crosstalk levels from the adjacent channel shown in the dotted line.

conservation the transmitted power and the reflected power are related by the following equation:

$$|T|^2 = 1 - |\Gamma|^2.$$

Outside the stopband we see that the transmission is almost completely restored.

**Side-lobes in Grating Response**

On a linear scale the Bragg grating response shows that it acts as a good reflector filter. However, it is useful to view it on a logarithmic scale. This is shown in Fig. (3-6). We can see that outside the stopbands the reflection sidelobes come back up quite high and that the roll-off of these sidelobes is fairly slow with "frequency", $\delta$. These sidelobes are a problem if the Bragg grating is to be used as a reflection filter since the high side-lobes means that the rejection outside the stopband is not adequate. To understand the source of these sidebands, consider the eq. (3.25)

$$\frac{dB}{dz} = j\delta B(z) + \kappa^* A(z)$$

The solution of this equation can be found by completing the form and is given by

$$B(z) = e^{j\delta z} \left\{ \int_{-\infty}^{+\infty} A(z')\kappa(z')e^{-j\delta z'}dz' \right\} \qquad (3.56)$$

This is an exact solution of eq. (3.25). However, $A(z)$ is also unknown and we have to solve coupled mode equations simultaneously. In the limit when we can assume that $A(z)$ does not deplete significantly and is to first order constant $A_o$, the above equation can be rewritten as

$$B(z) = e^{j\delta z}A_o \left\{ \int_{-\infty}^{+\infty} \kappa(z')e^{-j\delta z'}dz' \right\}$$

This non-depletion approximation is valid when the grating strength is "weak" and the grating is "short" so that the incoming wave $A(z)$ does not suffer significant change. In this limit the quantity within the parenthesis looks like a Fourier transform and we note that the reflected wave $B(z)$ spectrally is the Fourier transform of the grating strength function $\kappa(z)$. Thus for a uniform grating with a small $\kappa L$ product, the reflected wave must look like a

$$B(-L) = \kappa_o L \frac{\sin(\delta L/2)}{\delta L/2}$$

where $L$ is the length of the grating. This is confirmed by solving the coupled mode equations eqs. (3.24) and (3.25) exactly using the tranfer matrix approach. The results are shown in Fig. (3-7) for gratings with increasing $\kappa$. As the $\kappa L$ product increases the spectral shape of the reflected wave deviates from the sinc function as the non-depletion approximation does not hold. For the sinc function, the first sidelobe occurs when $\delta L \approx \pm 9$ and the height of the sidelobe is $\approx 0.22\kappa L$. Thus as $\kappa L$ increases we expect the sidelobe level to rise. This is evident by looking at Fig. (3-7). For small $\kappa L$ products the ratio of the main lobe to the first sidelobe is $\approx 0.22$. However, the maximum height that the main lobe can attain is 1.0 and thus as $\kappa L$ increases the height of the sidelobes increases relative to the main lobe.

## 3.2 Apodized Gratings

As we have seen in the preceding section a Bragg grating is a frequency sensitive mirror which can strongly reflect wavelengths within its stopband. In principle, it appears that a uniform Bragg grating can be used in WDM systems for filtering out a desired channel. WDM systems typically require that the dropped channel is suppressed at least 20 dB to 25 dB relative to the on-going channels. At the Bragg wavelength, $\lambda_B$ or equivalently at
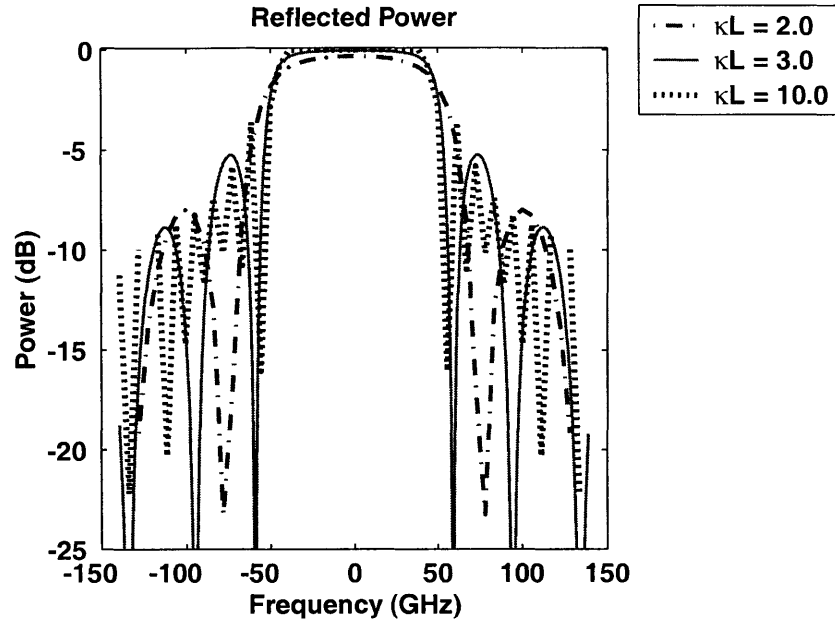
**Figure 3-7:** Uniform Bragg grating response for increasing $\kappa L$ reveals effect on sidelobes and peak reflected power.

$\delta = 0$, the transmitted power is given by eq. (3.48). A peak suppression of 25 dB requires that

$$\kappa L > 3.5.$$

Typical WDM systems have data channels spaced by 100 GHz. For filtering purposes its is required that the 1 dB bandwidth of the add/drop filter cover 20% to 40% of the channel spacing. For a uniform Bragg grating of $\kappa L = 3.5$ product, the 1 dB bandwidth is given by

$$\frac{\delta_{1dB}}{\kappa} = \pm 1.12$$

Using eq. (3.21) we can rewrite the above expression in terms of frequency

$$\Delta f_{1dB} = \frac{1.12\kappa c}{\pi n_g} \tag{3.57}$$

where $n_g$ is the group index of the guided mode. Using typical $n_g$ values for a Bragg grating made in an InGaAsP/InP material, assuming $\Delta f_{1dB} = 30$ GHz, we find that the grating strength needed is $\kappa \sim 10$. The reflection spectrum for a uniform grating with $\kappa L = 3.5$ is shown in Fig. (3-6). We can see from the figure that the reflection spectrum has very high sidelobe levels that decay slowly so that at the suppression of the next adjacent channel is less than 20 dB. Suppression ratios of less than 20 dB are unacceptable for WDM channels.

Typically the crosstalk from adjacent channels must be less than 25 dB. Thus the two requirements of (a) suppressing the selected channel by more than 20 dB (b) keeping the crosstalk from adjacent channels lower than 25 dB are difficult to meet with a uniform Bragg grating. The $\kappa L$ product resulting from condition (a) results in high sidelobes which make it impossible to meet condition (b) without reducing the $\Delta f_{1dB}$.

We saw in the previous section that in the weak $\kappa L$ regime, the grating response is given by the Fourier transform of the $\kappa(z)$ function. For a uniform grating with $\kappa(z) = \kappa_o$ over the length $L$ of the grating, the response is a sinc function with certain height sidelobes. If $\kappa(z)$ had a triangular profile i.e

$$\Delta \kappa(z) = \begin{cases} \kappa_o(1 + \frac{2z}{L}) & \text{if } -\frac{L}{2} \le z \le 0 \\ \kappa_o(1 - \frac{2z}{L}) & \text{if } 0 \le z \le \frac{L}{2} \end{cases}$$

from Fourier transform relationship we recognize that the reflection spectrum would be a $(\text{sinc})^2$ and hence lower sidelobes. Thus, if $\kappa(z)$ has a profile or windowing function it reduces sidelobes in the grating spectral response [27, 28]. This is reminiscent of windowing functions used in signal processing for reducing sidelobes of digital filters [29, 30, 31]. By having a non-uniform grating with a varying $\kappa(z)$ the grating sidelobes can be suppressed. Gratings with a varying $\kappa(z)$ are called apodized gratings. From signal processing theory, we are aware of several apodization or windowing functions like the "Hanning", "Hamming" windows to reduce sidelobes (see Fig. (3-8)). To solve a grating with a varying $\kappa(z)$ we do a piece-wise analysis where we break the grating into $n$ pieces and assume that the grating strength is constant over each piece. This technique is a valid way of analysing apodized gratings provided we use a large enough number of pieces, $n$. Typically this approximation models the physical strucure very well since the fabricated structure is a concatenation of piece-wise constant segments. In the previous section we saw that the transfer matrix, $\overline{\overline{T}}$ is a function of $\kappa$, eq. (3.46). Moreover for a grating made of $n$ sections the complete transfer matrix is the product of the transfer matrices of the individual sections, i.e

$$\overline{\overline{T}}(z_n, z_o) = \overline{\overline{T}}_n(\kappa_n, z_n, z_{n-1}) \cdots \overline{\overline{T}}_3(\kappa_3, z_3, z_2)\overline{\overline{T}}_2(\kappa_2, z_2, z_1)\overline{\overline{T}}_1(\kappa_1, z_1, z_o) \qquad (3.58)$$

The transfer matrix method discussed above was used to calculate the apodized grating responses shown in Fig. (3-9). The length of gratings used were such that

$$\int_0^L \kappa(z')dz' = 3.5$$
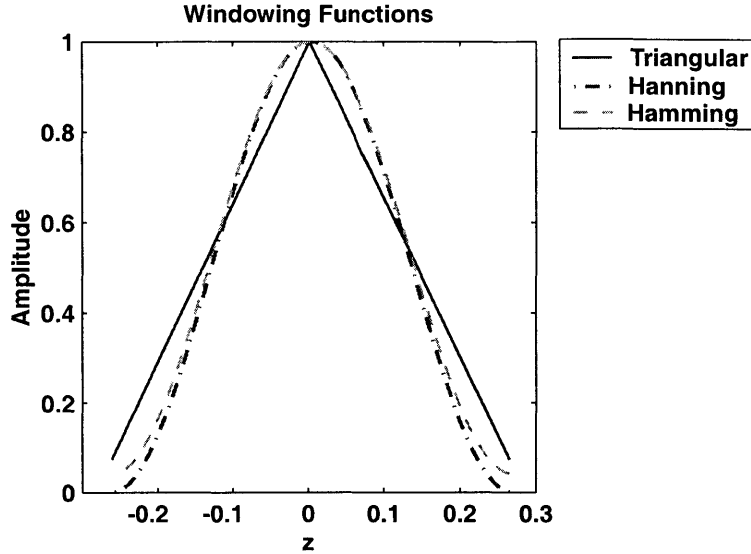
**Figure 3-8:** Apodized Bragg grating windowing functions to taper the grating strength, $\kappa$.

Comparison with uniform grating response, we see that the sidelobes have dropped considerably. The different windowing functions have different sidelobe properties which are discussed in detail in various signal processing books, [29]. We see that if gratings are to be used as reflection filters in WDM systems to drop channels it is necessary to apodize the gratings.

## 3.3 Chirped Gratings

In the above section we saw how it may be useful to change the grating strength along the length of Bragg grating. Sometimes it is useful to chirp the period of the gratings along their length. Chirped gratings are used for dispersion compensation [8, 32, 9]. Chirping may also be used as a way to expand the width of the stopband of a grating while keeping $\kappa$ constant. Once again, the approach used to solve a chirped grating will be to divide the grating into $n$ piece-wise regions of constant period, $\Lambda_i$. In each of these regions, the coupled mode equations describing the wave interaction are

$$\frac{dA}{dz} = -j\delta_i A + \kappa B \tag{3.59}$$

$$\frac{dB}{dz} = j\delta_i B + \kappa^* A \tag{3.60}$$

where from eq. (3.21)

$$\delta_i \equiv \beta_s - (\beta_o)_i = \beta_s - \frac{\pi}{\Lambda_i} \tag{3.61}$$

**Apodized Grating Response**
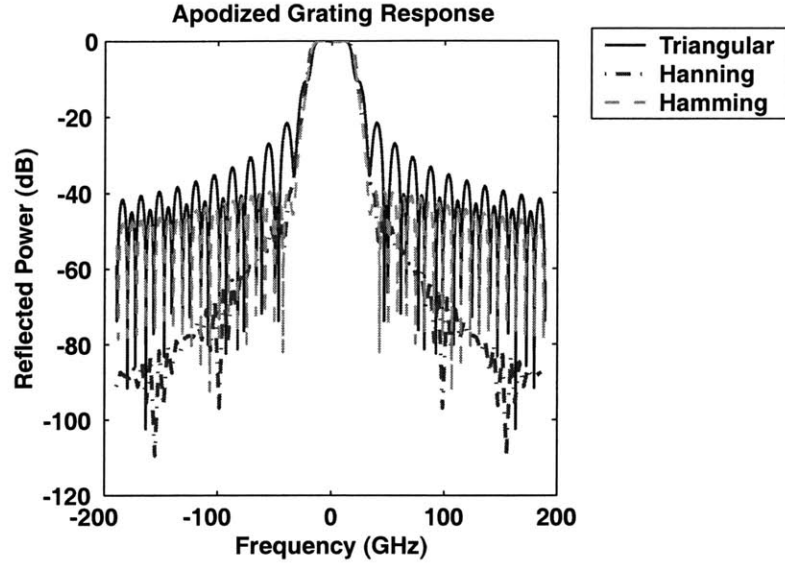


**Figure 3-9:** Apodized Bragg grating responses for various windowing functions applied to the grating strength, $\kappa$.

The transfer matrix for each of these segments is again given by eq. (3.46) where the appropriate value of $\delta_i$ is used. Thus the transfer matrix, $\overline{\overline{\mathbf{T}}}_i(\Lambda_i, z_i, z_{i-1})$, of the $i^{th}$ region is implicitly a function of the grating period $\Lambda_i$ via $\delta_i$. In the previous section we have seen that the total transfer matrix is the product of the transfer matrices of the individual regions. This follows from the continuity of the field amplitudes across the boundary between the piece-wise constant regions. The quantities that must be continuous across the boundaries are total z-dependence of the fields [eqs. (3.19), (3.20)], $a(z)$, $b(z)$ and not $A(z)$, $B(z)$. i.e

$$
\begin{aligned}
a_i(z) &\equiv A_i(z)e^{-j(\beta_o)_i z} \\
b_i(z) &\equiv B_i(z)e^{j(\beta_o)_i z}
\end{aligned}
\tag{3.62}
$$

For gratings with constant periods but varying magnitude of $\kappa(z)$, continuity of $A(z)$ and $B(z)$ assures the continuity of $a(z)$ and $b(z)$. This is not the case when either the grating period changes or equivalently the phase of $\kappa$ varies with $z$. Continuity of the total field amplitudes at the interface, $z_i$ between region $i$ and $i-1$ yields

$$
a_i(z_i) = A_i(z_i)e^{-j\frac{\pi}{\Lambda_i}z_i} = a_{i-1}(z_i) = A_{i-1}(z_i)e^{-j\frac{\pi}{\Lambda_{i-1}}z_i}
\tag{3.63}
$$

$$
b_i(z_i) = B_i(z_i)e^{j\frac{\pi}{\Lambda_i}z_i} = B_{i-1}(z_i) = B_{i-1}(z_i)e^{j\frac{\pi}{\Lambda_{i-1}}z_i}
\tag{3.64}
$$

Rewriting the continuity condition in terms of $\vec{A}_i$ and $\vec{A}_{i-1}$ we get

$$\begin{bmatrix} A_i(z_i) \\ B_i(z_i) \end{bmatrix} = \begin{pmatrix} e^{-j\pi(\frac{1}{\Lambda_i} - \frac{1}{\Lambda_{i-1}})z_i} & 0 \\ 0 & e^{j\pi(\frac{1}{\Lambda_i} - \frac{1}{\Lambda_{i-1}})z_i} \end{pmatrix} \begin{bmatrix} A_{i-1}(z_i) \\ B_{i-1}(z_i) \end{bmatrix} \tag{3.65}$$

$$\vec{A}_i(z_i) \equiv \overline{\overline{\mathbf{P}}}_{i-1}(z_i)\vec{A}_{i-1}(z_i) \tag{3.66}$$

From the previous section we already know how to relate $\vec{A}_{i-1}(z_i)$ to $\vec{A}_{i-1}(z_{i-1})$ using the transfer matrix, $\overline{\overline{\mathbf{T}}}_{i-1}(\Lambda_{i-1}, z_i, z_{i-1})$ given by eq. (3.46), i.e

$$\vec{A}_{i-1}(z_i) = \overline{\overline{\mathbf{T}}}_{i-1}(\Lambda_{i-1}, z_i, z_{i-1})\vec{A}_{i-1}(z_{i-1}) \tag{3.67}$$

Subsitituting this in eq. (3.66) we get

$$\vec{A}_i(z_i) = \overline{\overline{\mathbf{P}}}_{i-1}\overline{\overline{\mathbf{T}}}_{i-1}(\Lambda_{i-1}, z_i, z_{i-1})\vec{A}_{i-1}(z_{i-1}) \tag{3.68}$$

Generalizing this to the $n$ regions of different period, $\Lambda_i$ we get.

$$\vec{A}_i(z_i) = \left\{ \overline{\overline{\mathbf{T}}}_n(\Lambda_n)\overline{\overline{\mathbf{P}}}_{n-1}\overline{\overline{\mathbf{T}}}_{n-1}(\Lambda_{n-1}) \cdots \overline{\overline{\mathbf{P}}}_2\overline{\overline{\mathbf{T}}}_2(\Lambda_2)\overline{\overline{\mathbf{P}}}_1\overline{\overline{\mathbf{T}}}_1(\Lambda_1) \right\} \vec{A}_1(z_o) \tag{3.69}$$

Thus the total transfer matrix for a chirped grating with $n$ piece-wise constant regions is given by

$$\overline{\overline{\mathbf{T}}}(z_n, z_o) = \overline{\overline{\mathbf{T}}}_n(\Lambda_n, z_n, z_{n-1})\overline{\overline{\mathbf{P}}}_{n-1}(z_{n-1})\overline{\overline{\mathbf{T}}}_{n-1}(\Lambda_{n-1}, z_{n-1}, z_{n-2}) \cdots \overline{\overline{\mathbf{P}}}_1(z_1)\overline{\overline{\mathbf{T}}}_1(\Lambda_1, z_1, z_o) \tag{3.70}$$

where

$$\overline{\overline{\mathbf{P}}}_i(z_i) = \begin{pmatrix} e^{-j\pi(\frac{1}{\Lambda_i} - \frac{1}{\Lambda_{i-1}})z_i} & 0 \\ 0 & e^{j\pi(\frac{1}{\Lambda_i} - \frac{1}{\Lambda_{i-1}})z_i} \end{pmatrix} \tag{3.71}$$

and $\overline{\overline{\mathbf{T}}}_i(\Lambda_i, z_i, z_{i-1})$ is given by eq. (3.46) with the appropriate value of $\delta_i$ substituted in the equation. The previous two sections show how the tranfer-matrix formalism can be applied to nonuniform Bragg gratings. For additional information on modeling of non-uniform gratings the reader are refered to [33]

## 3.4 Bragg Resonators

Bragg gratings reflect light strongly within their stopband. The electric fields decay exponentially along the length of the grating as propagation is "forbidden" within the stopband. Any transmission within the stopband is due to "tunneling" of the light through the grating. Outside the stopband light can propagate through the grating and the transmission
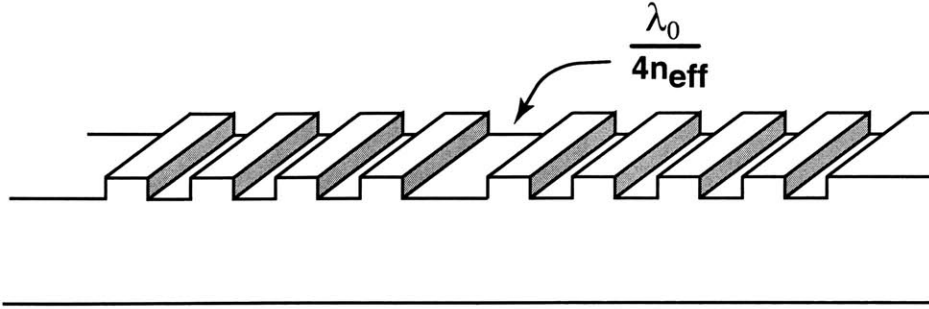
**Figure 3-10:** Quarter-wave shifted Bragg grating stores forms an optical resonator.

rapidly returns to near unity. It is, however, possible to modify the grating structure so as to introduce a resonant transmission state exactly in the center of the stopband, i.e is at the Bragg wavelength, $\delta = 0$. This is done by introducing a precise $\lambda/4$-wave shift in the grating. The resulting structure acts as an optical resonator locally "trapping" the electromagnetic energy in the vicinity of $\lambda/4$-wave shift. In the following sections we will examine this structure and the applications to which it can be applied.

### 3.4.1   Single quarter-wave shift in Bragg grating - Bragg resonator

Figure (3-10) shows a Bragg grating with a precise phase-shift of a quarter of the optical wavelength introduced in its center. A quarter-wave shift means that the reflections from the interfaces immediately to the right of the phase-shift are exactly out of phase with those to its the left. This reversal of phase destroys the coherence of the reflection from the grating interfaces and modifies the field distribution such that there is complete transmission at the Bragg wavelength. One way to understand this is by considering two semi-infinite gratings extending in the opposite direction. The reflection coefficent, $\Gamma$, of the grating in the region, $0 \leq z \leq \infty$ is given by eqs. (3.52) and (3.53)

$$\Gamma(z = 0_+) \equiv \frac{B(z)}{A(z)} = -\frac{|\kappa|}{\kappa} \quad z = 0_+ \tag{3.72}$$

Likewise for the other semi-infinite grating in the region $-\infty \leq z \leq 0$, $\Gamma$ is given by eqs. (3.54) and (3.55):

$$\Gamma(z = 0_-) \equiv \frac{B(z)}{A(z)} = \frac{|\kappa|}{\kappa} \quad z = 0_- \tag{3.73}$$

An introduction of a quarter-wave shift between $z = 0_+$ and $z = 0_-$ matches $\Gamma(z = 0_+)$ to $\Gamma(z = 0_-)$ as $\Gamma$ changes to $-\Gamma$ across a $\lambda/4$-wave shift section [20]. This $\pi$ phase shift is

evident when we take into account the complete z-dependence of the fields with their $e^{\pm j \frac{\pi}{\Lambda} z}$ factors, eqs. (3.63) and (3.64).

To calculate the spectral response of a $\lambda/4$-wave shifted grating we again use the transfer matrix method. The $\lambda/4$-wave shifted grating naturally divides into two piece-wise constant regions on either side of the phase-shift. Across the $\lambda/4$-wave shift the phase of the grating strength $\kappa$ changes by $\pi$ to account for the phase-shift. Thus if

$$\kappa(z \geq 0) = +\kappa$$

then

$$\kappa(z < 0) = -\kappa$$

The total transfer matrix is given by eq. (3.38)

$$\overline{\overline{T}} = \overline{\overline{T}}_2(-\kappa, -L_2, 0)\,\overline{\overline{T}}_1(\kappa, 0, L_1) \tag{3.74}$$

where $L_1$ and $L_2$ are the lengths of the gratings on either side of the $\lambda/4$-wave shift. With the transfer matrix, $\overline{\overline{T}}$, known the spectral response can be found as before by converting to a scattering matrix, $\overline{\overline{S}}_T$. The spectral response for different length $\lambda/4$-wave shifted gratings is shown in Fig. (3-11). The spectrum was calculated assuming equal lengths on either side of the $\lambda/4$-wave shift. The total length, $L = L_1 + L_2$. As expected we see a distinct resonant transmission state exactly in the center of the stopband at $\delta = 0$. The transmission sharply peaks to unity and is then suppressed within the stopband. It recovers as for a uniform grating outside the stopband. The corresponding reflection response is shown in the same figure. Note that the bandwidth of the transmission state depends on the total length of the grating. We can understand this by considering the field distribution in the $\lambda/4$-wave shifted grating at $\delta = 0$. Using eqs. (3.44) we know that the general solution to the CMT equations on either side of the phase-shift is given by [20]

$$A(z) = A_+ e^{-|\kappa|z} + A_- e^{|\kappa|z} \tag{3.75}$$

$$B(z) = -\frac{|\kappa|}{\kappa}\left\{A_+ e^{-|\kappa|z} - A_- e^{|\kappa|z}\right\} \tag{3.76}$$

Since the grating is only excited from $z = -L_2$, $B(z = L_1) = 0$ and hence

$$A_- = A_+ e^{-2|\kappa|L_1}$$

The forward propagating wave at $z = L_1$ is given by

$$A(z = L_1) = 2A_+ e^{-|\kappa|L_1} \tag{3.77}$$
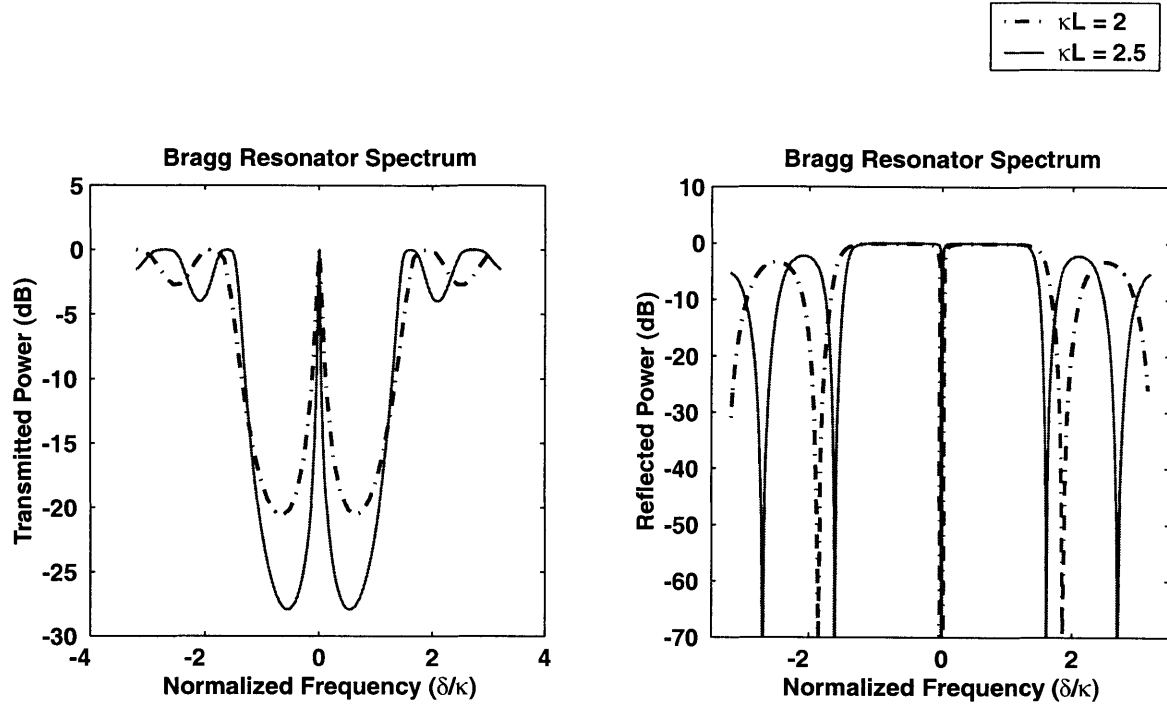
**Figure 3-11:** Spectral response of a $\lambda/4$-wave shifted Bragg grating or Bragg resonator.

The power escaping through this port is simply given by the square of the field amplitude, $A(z = L_1)$. This follows from the normalization condition, eq. (3.9). Thus

$$P(z = L_1) = 4|A_+|^2 e^{-2|\kappa|L_1} \qquad (3.78)$$

The total energy, $W$, stored in the $\lambda/4$-wave shifted Bragg grating is given by integrating the energy per unit length, $<w>$, across the grating. $<w>$ is given by[20]:

$$<w> = \frac{1}{v_g} \left\{ |A|^2 + |B|^2 \right\} \qquad (3.79)$$

Hence the energy stored is

$$W = \int_{-L_2}^{L_1} <w> dz \simeq \int_{-\infty}^{\infty} \frac{1}{v_g}(|A(z)|^2 + |B(z)|^2)\, dz = \frac{2|A_+|^2}{v_g|\kappa|} \qquad (3.80)$$

where the energy in the actual structure is approximated by an infinite length grating structure. The approximation is valid as the fields decay rapidly on either side of phase-shift and very little energy is stored in the wings of the structure.

The actual field distribution at $\delta = 0$ in the $\lambda/4$-wave shifted Bragg grating is shown in Fig. (3-12). The fields were calculated numerically using the transfer matrix method. However, for this simple structure they can be analytically calculated by matching boundary

**Fields in Bragg Resonator**
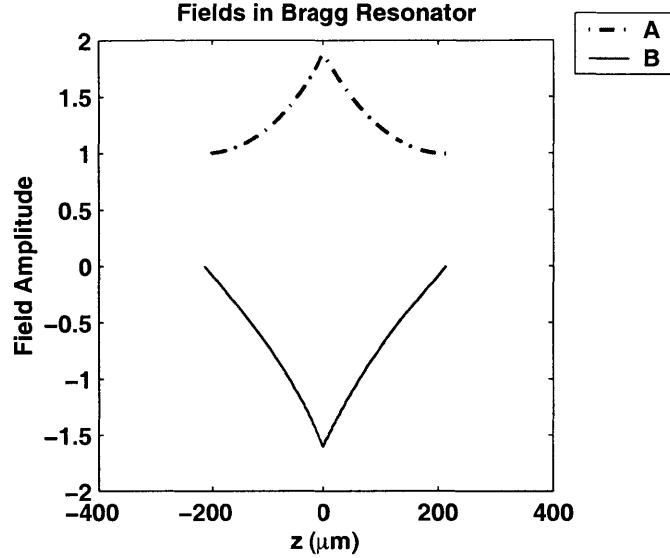


**Figure 3-12:** Field distribution at Bragg wavelength, or $\delta = 0$, in a Bragg grating resonator.

conditions and requiring continuity of fields at the $\lambda/4$-wave shift. Note, that fields are peaked about the $\lambda/4$-wave shift and decay on either side. The fields are localized and and the phase-shifted Bragg grating acts as an optical resonator storing electromagnetic energy. This resonator communicates to the "outside" world through either port. It leaks energy through either side via its exponential tails. If the Bragg resonator is made infinitely long and excited, the field are completely trapped inside there is no loss of power. Spectrally this means that the resonance has a zero linewidth or an infinite quality factor, $Q$. Conversely if the grating has a finite length there is loss of power and the resonance acquires a finite width. The shorter the grating the more loss there is from the resonator and the broader is the resonance linewidth. It is easy to relate the linewidth of the resonance to the lengths on either side of the $\lambda/4$-wave shift, $L_1$ and $L_2$. From resonator theory [34, 35, 20], we know that the quality factor, $Q$, of any resonant structure is defined as the energy stored in the resonator divided by the power lost per unit cycle:

$$Q \equiv \frac{W}{(P/\omega_o)} = \frac{\omega_o}{\Delta\omega} \tag{3.81}$$

where $W$ is the energy stored. $P$ is the lost power and $\omega_o$ is the resonance frequency. $\Delta\omega$ is the linewidth of the resonance. Using eqs. (3.78) and (3.80) we know that

$$P = P(z = L_1) + P(z = -L_2) = 4|A_+|^2 e^{-2|\kappa|L_1} + 4|A_+|^2 e^{-2|\kappa|L_2} \tag{3.82}$$

$$W = \frac{2|A_+|^2}{v_g|\kappa|} \tag{3.83}$$
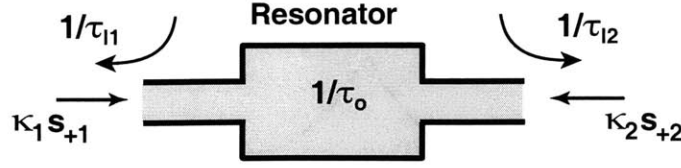
**Figure 3-13:** Schematic of a general resonator system described by CMT-time formalism.

Hence

$$\frac{\Delta\omega}{\omega_o} = \frac{2|\kappa|v_g}{\omega_o}(e^{-2|\kappa|L_1} + e^{-2|\kappa|L_2}) \tag{3.84}$$

As expected from the physical arguments, the linewidth of the resonance does in fact depend on the length of the grating sections.

## 3.4.2 Coupled Mode Theory in Time description of Bragg resonator [20]

Thus far we have used CMT-space to solve the problem of the Bragg resonator. There is an alternate approach, Coupled Mode Theory in time (CMT-time), that is general and is applicable to any kind of resonator system. CMT-time describes the resonant mode behavior in terms of the resonant frequency, $\omega_o$; decay terms $\frac{1}{\tau}$ which model loss from the resonator system; this loss may either be internal loss or loss from the resonator system to the outside world; and input coupling terms $\underline{\kappa}_i$ which model how effectively power can be coupled into the resonator, [20, 36]. A general resonator system, shown in Fig. (3-13) can be described by the following equation.

$$\frac{da}{dt} = \left(j\omega_o - \frac{1}{\tau_{l1}} - \frac{1}{\tau_{l2}} - \frac{1}{\tau_o}\right)a + \underline{\kappa}_1 s_{+1} + \underline{\kappa}_2 s_{+2} \tag{3.85}$$

$a$ is the resonant mode amplitude and is normalized such that $|a|^2$ is the total energy stored in the resonator. $\omega_o$ is the resonance frequency. $\frac{1}{\tau_{li}}$ represents the escape of power from the either side resonator to the outside world. $\frac{1}{\tau_o}$ represents the internal loss of the resonator. In the absence of any internal loss mechanism the only way the resonator loses power is by coupling from either side to the "outside" world. With inputs $s_i = 0$, the above equation can be used to show that

$$\frac{d|a|^2}{dt} = -2\left(\frac{1}{\tau_{l1}} + \frac{1}{\tau_{l2}}\right)|a|^2 \equiv -\frac{2}{\tau_l}|a|^2. \tag{3.86}$$

The energy, $|a|^2$, in the resonator decays as $e^{-2\frac{t}{\tau_l}}$ as expected. $1/\tau_l$ is simply the sum of the escape mechanisms. If there were internal resonator loss, $1/\tau_l$ would be given by

$$\frac{1}{\tau_l} = \frac{1}{\tau_{l1}} + \frac{1}{\tau_{l2}} + \frac{1}{\tau_o} \tag{3.87}$$

where $1/\tau_o$ is the internal resonator loss term. As stated above $\underline{\kappa}_i$ are the input coupling terms. Physically we expect the coupling to be related to how strongly the resonator interacts with the external world which is described by $1/\tau_l$. Power conservation and time-reversibility can be used to relate the two quantities and we find [20] that

$$\underline{\kappa}_i = \sqrt{\frac{2}{\tau_{li}}} \tag{3.88}$$

This expression is proved in Appendix 1. Likewise it is rather straightforward to relate the incoming waves $s_{+i}$ to the corresponding outgoing waves, $s_{-i}$. As shown in [20], power conservation yields

$$s_{-i} = -s_{+i} + \sqrt{\frac{2}{\tau_{li}}}\, a \quad i = \{1, 2\} \tag{3.89}$$

We are now in a position to calculate the response of the resonator near resonance. As before we consider the case when the resonator is excited from the left side only at a frequency $\omega$ i.e

$$s_{+1} = e^{j\omega t}$$

$$s_{+2} = 0$$

In this case it can be shown easily that

$$\frac{s_{-1}}{s_{+1}} = \frac{-j(\omega - \omega_o) + \frac{1}{\tau_{l1}} - \frac{1}{\tau_{l2}}}{j(\omega - \omega_o) + \frac{1}{\tau_{l1}} + \frac{1}{\tau_{l2}}} \tag{3.90}$$

$$\frac{s_{-2}}{s_{+1}} = \frac{\frac{2}{\sqrt{\tau_{l1}\tau_{l2}}}}{j(\omega - \omega_o) + \frac{1}{\tau_{l1}} + \frac{1}{\tau_{l2}}} \tag{3.91}$$

The above expression give the transmission and reflection from a general resonator when it is excited from one side. To be able to apply these expressions to the specific case of a Bragg resonator case we need to relate $1/\tau_{li}$ to the Bragg resonator parameters, $\kappa$, $L_i$. This follows immediately from the definition of the $Q$ of resonators. From eq. (3.81)

$$Q \equiv \frac{W}{(P/\omega_o)} = \frac{\omega_o}{\Delta\omega}$$

Using eq. (3.86) it follows that that the power escaping the resonator is given by

$$P = \frac{d|a|^2}{dt} = -2\left(\frac{1}{\tau_{l1}} + \frac{1}{\tau_{l2}}\right)|a|^2 \equiv -\frac{2}{\tau_l}|a|^2. \tag{3.92}$$

Using this in above equation we find that

$$Q \equiv \frac{W}{(P/\omega_o)} = \frac{|a|^2}{P/\omega_o} = \frac{\omega_o\tau_l}{2} = \frac{\omega_o}{\Delta\omega} \tag{3.93}$$
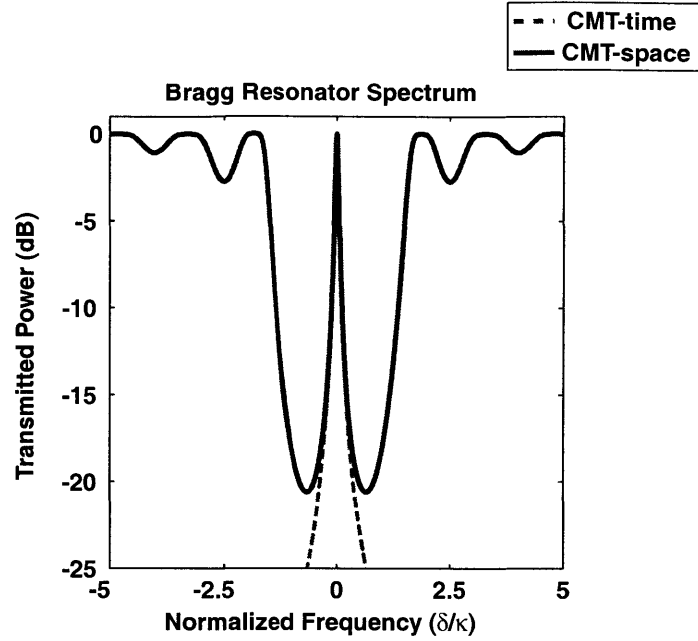
**Figure 3-14:** Bragg resonator spectrum calculated using CMT-space and CMT-time. The overlay shows that CMT-time predicts the response of the resonator well only near resonance. Far from resonance the responses deviate significantly and only CMT-space is reliable.

Comparison with eq. (3.84) yields:

$$\frac{1}{\tau_{li}} = |\kappa| v_g e^{-2|\kappa|L_i} \tag{3.94}$$

The above expression allows the use of eqs. (3.91) and (3.90) to compare the spectral response of a Bragg grating resonator of arm lengths $L_1$ and $L_2$ calculated from CMT-time with that calculated from CMT-space. Figure (3-14) shows the overlay of the two responses. It is obvious from the figure that the CMT-time faithfully reproduces the response of the Bragg grating resonator in the vicinity of the resonance, i.e near $\delta = 0$. Moreover, eq. (3.91) shows that near resonance the transmitted spectrum is a Lorentzian with the characteristic

$$\frac{s_{-2}}{s_{+1}} = \frac{1}{1 + \frac{j(\omega - \omega_o)\tau_{lo}}{2}}.$$

The above expression is for a resonator with equal arm lengths. We see that the bandwidth of the transmission spectrum is related to the total power escape term $2/\tau_{lo}$. The Lorentzian response has the characteristic roundtop and a roll-off of 20 dB/decade. Further away, from resonance the two responses, calculated from CMT-time and CMT-space, increasingly deviate. This is most obvious near and outside the stopband where Bragg resonator response

with CMT-space is completely different from CMT-time. In this frequency range CMT-space is accurate. This should be expected as the CMT-time is a phenomelogical description of resonators and only describes behavior near resonance. This allows the simple eq. (3.85) to be written down which is analytically tractable. This equation is an absolutely general description of any resonator and does not account for Bragg grating behavior far from the resonance state. CMT-space equations (3.24) and (3.25), on the other hand, were derived specifically to model the detailed behavior of Bragg gratings and are thus an accurate description over a wide frequency range.

The CMT-time approach offers over CMT-space is its simplicity in solving the response near resonance. It provides an analytic handle on the problem which otherwise needs to be calculated numerically using the transfer-matrix method. Whereas, this advantage may not be so obvious in the case if a simple Bragg grating resonator, we will see that it is extremely useful for analysing more complicated structures. Moreover, as we will see in the following section CMT-time allows us to derive an equivalent circuit for the Bragg grating resonator using $L$'s, $C$'s and $R$'s. We will see in later chapters that equivalent circuits are an indispensable tool in designing add/drop filters using Bragg gratings.

### 3.4.3 Equivalent Circuit of a Bragg Grating Resonator

The previous section showed how CMT-time can be used to describe a general resonator system and then applied it to the case of a Bragg resonator. Another resonator system that we are very familiar with is an $L$, $C$, $R$ circuit connected to transmission lines. The $L$-$C$-$R$ system is also described by eqs. (3.85). A rigorous derivation of this is given in [20]. Consider the $L$-$C$ circuit attached to a transmission line as shown in Fig. (3-15). On resonance, we know that the impedance of the parallel $L$-$C$ branch is infinite or in other words it is an open circuit. Thus any power incident from the left passes through completely. This behavior is similar to that of a Bragg grating resonator that allows complete transmission on resonance. To draw an equivalence between a Bragg grating resonator described by CMT-time eqs. (3.91) and (3.90) and the $L$-$C$ circuit of Fig. (3-15) we calculate its response. From standard transmission line theory, we know that

$$\Gamma = \frac{1 - Y_n}{1 + Y_n} \tag{3.95}$$

$$T = 1 + \Gamma \tag{3.96}$$
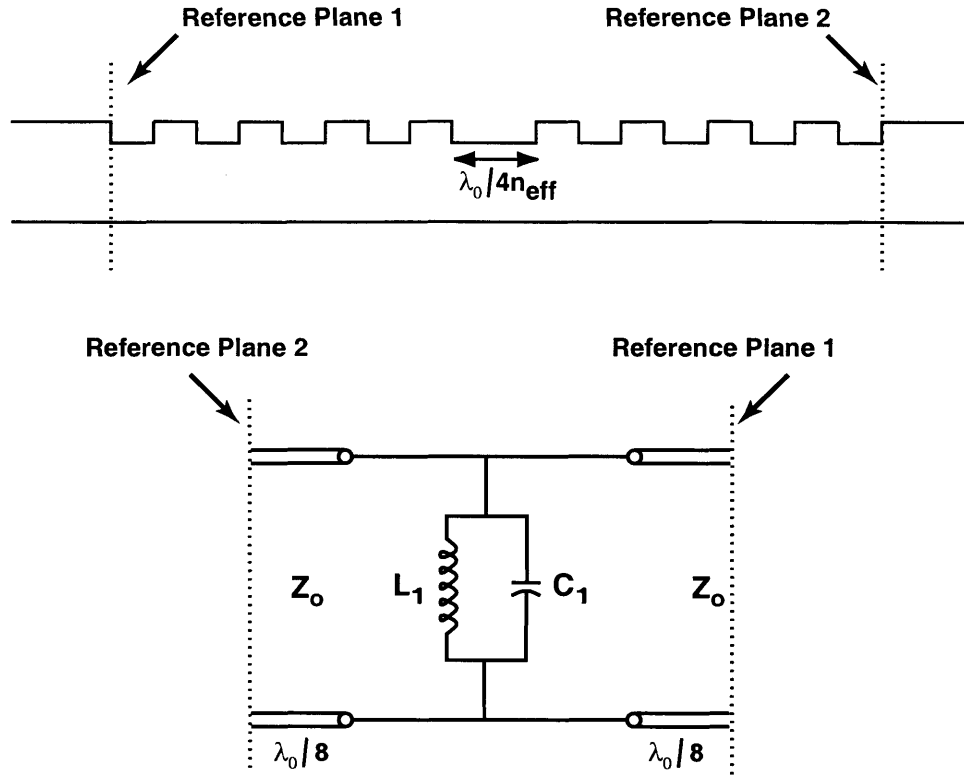
**Figure 3-15:** Bragg grating resonator and its equivalent circuit.

where $Y_n$ is the total admittance looking from the left of the $L\text{-}C$ branch and is given by

$$Y_n = \frac{Y}{Y_o} = 1 + \frac{1}{Y_o}\left(j\omega C + \frac{1}{j\omega L}\right) \simeq 1 + 2j(\omega - \omega_o)\frac{C}{Y_o}; \qquad (3.97)$$

the approximation holds true near resonance. Substituting into eqs. (3.95) and (3.96) we find that

$$\Gamma = \frac{-2j(\omega - \omega_o)\frac{C}{Y_o}}{1 + 2j(\omega - \omega_o)\frac{C}{Y_o}} \qquad (3.98)$$

$$T = \frac{1}{1 + 2j(\omega - \omega_o)\frac{C}{Y_o}} \qquad (3.99)$$

The CMT-time response of a Bragg grating resonator with equal lengths $L_1 = L_2 \equiv L_o$ so that $\tau_{l1} = \tau_{l2} \equiv \tau_{lo}$ is given by

$$\frac{s_{-1}}{s_{+1}} = \frac{-j(\omega - \omega_o)\tau_l}{1 + j(\omega - \omega_o)\tau_l} \qquad (3.100)$$

$$\frac{s_{-2}}{s_{+1}} = \frac{1}{1 + j(\omega - \omega_o)\tau_l} \qquad (3.101)$$

where

$$\frac{1}{\tau_l} = \frac{1}{\tau_{l1}} + \frac{1}{\tau_{l2}} = \frac{2}{\tau_{lo}} = 4|\kappa|v_g e^{-2|\kappa|L_o}$$
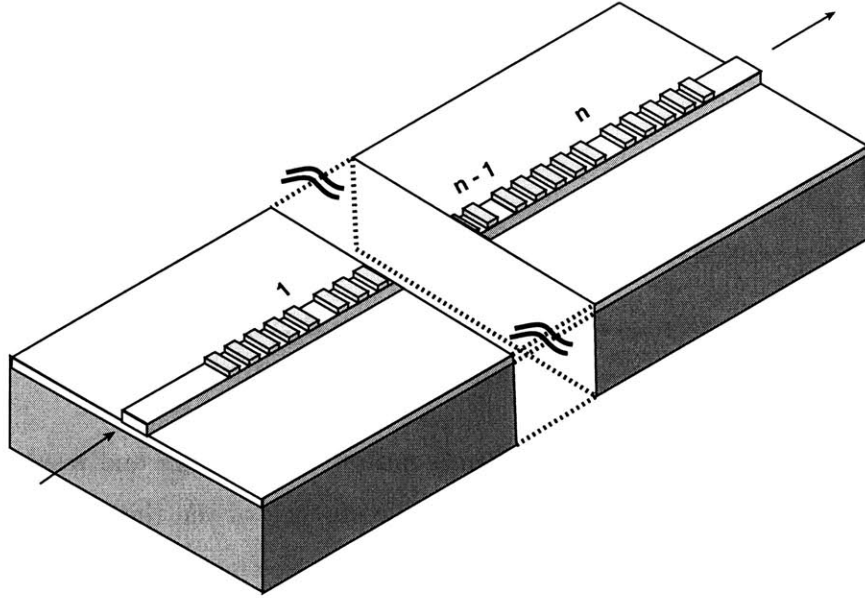
**Figure 3-16:** $n$ Coupled Bragg Grating Resonators

Comparison between the above sets of equations we find there is a one-to-one correspondence provided we draw the following equivalence

$$\frac{Y_o}{C} = \frac{1}{\tau_{lo}} = 2|\kappa|v_g e^{-2|\kappa|L_o} \tag{3.102}$$

This expression allows us to relate the Bragg resonator parameters, $\kappa$ and $L_o$ to the circuit parameters. With this equivalence, writing down the transmission and reflection response of a Bragg grating resonator becomes trivial. In the simple case of a single Bragg grating resonator the value of the equivalent circuit is not so obvious. However, equivalent circuits are a recurring theme in this thesis and we will see that they are invaluable in optical filter design. Figure (3-15) shows a Bragg grating resonator and its equivalent circuit. The reference planes defining the beginning and end of the Bragg grating resonator are marked in the figure.

### 3.4.4 Multiple Quarter-wave Shifts in Gratings - Coupled Bragg resonators, [36]

Consider the structure shown in Fig. (3-16) which shows a integrated Bragg grating with multiple quarter-wave shifts. We can use the intuition developed in the preceding section to understand how this device will behave. Conceptually we can divide the device with three $\lambda/4$-wave shifts into three Bragg resonators. This is marked in the figure by the
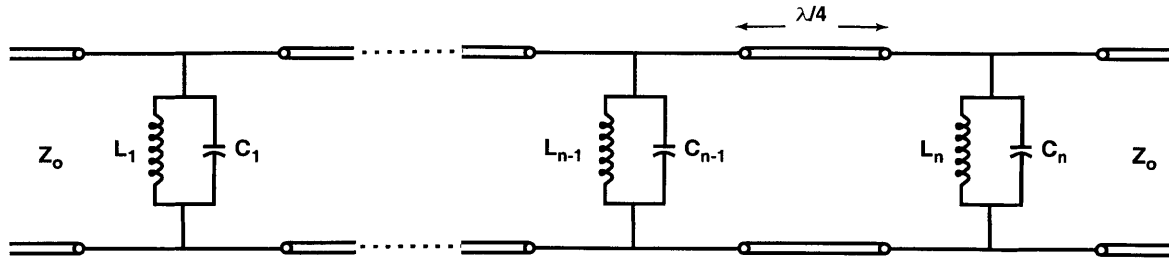
**Figure 3-17:** Equivalent Circuits of Inline Coupled Bragg Grating Resonators that can be used to make inline Higher-order Filters.

reference planes. Notice the reference planes end on a tooth edge and result in a gap of half a grating period or a $\lambda/4$-wave section between each of the three Bragg resonators. From the equivalent circuit derivation of the previous section we can immediately draw the equivalent circuit for this device. It is shown in Fig. (3-17) and consists of three $L$-$C$ circuits connected by $\lambda/4$-wave segment transmission lines. The $\lambda/4$-wave segments follow from the definition of the reference planes of a single Bragg resonator. The equivalent circuit picture shows the three coupled resonators. Each resonator couples it to its adjacent neighbor via its ends. The equivalent circuit picture reduces this coupling to familiar $L$-$C$ circuits and transmission line segments. Using impedance transformation across $\lambda/4$-wave segments, we can redraw the equivalent circuit to yield a standard LC-ladder circuit The LC ladder-circuit is a very well-studied circuit for which filter design tables exist. That is, there are look-up tables available which give values of $L_i$ and $C_i$ needed to get desired spectral responses like Butterworth, Gaussian, Elliptical, etc. filters. From the previous equivalent circuit derivation we know that

$$\frac{Y_o}{C_i} = 2|\kappa|v_g e^{-2|\kappa||L_i}$$

(3.103)

where $L_i$ are the lengths of the individual Bragg resonators. Immediately we notice the benefit of using equivalent circuits. It reduces a relatively complicated structure into a well-known circuit and allows uses of standard filter design tables to engineer desired spectral responses. For instance to design a three Bragg grating resonator system such that the transmission spectrum is a maximally flat Butterworth filter response, the normalized values of $L_i$ and $C_i$ needed are:

$$C_1 = C_3 = 1$$

(3.104)

$$C_2 = 2$$

(3.105)
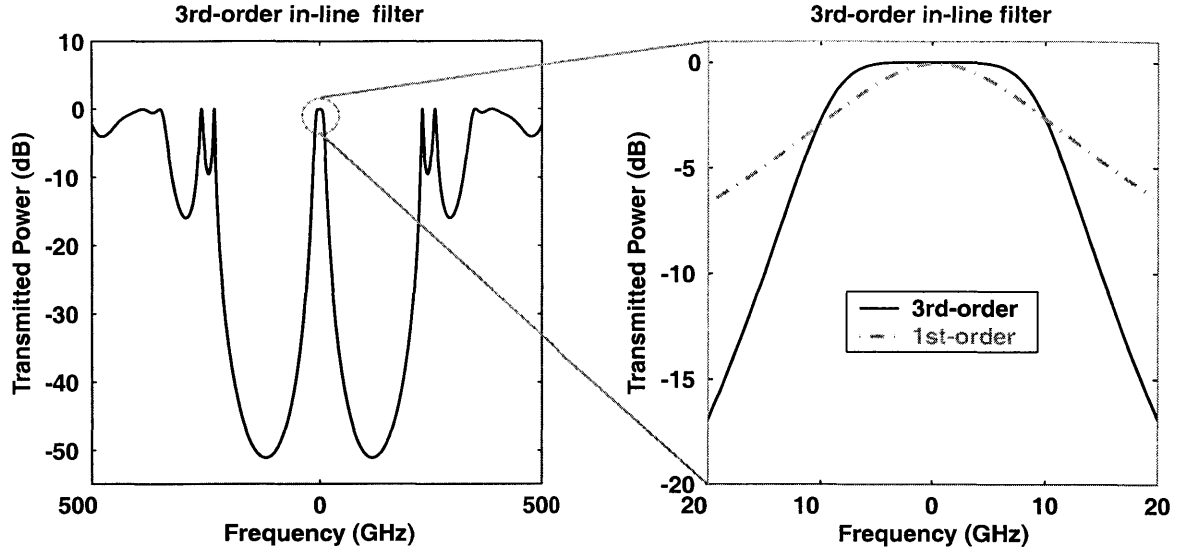
**Figure 3-18:** Third-order Butterworth filter response using inline coupled Bragg grating resonators.

We can use eq. (3.103) to translate these values into the lengths, $L_i$ for the individual Bragg resonators for a given $\kappa$ value. Figure (3-18) shows the response of third-order Butterworth filter of Fig. (3-16) calculated using CMT-space. We can see that the response is indeed maximally flat and rolls-off $N$ times faster, where $N$ is the number of Bragg grating resonators, than a single $\lambda/4$-wave response which is shown by the dashed-dotted line. This is characteristic of higher-order filters made using coupled resonators. We see here that the equivalent circuit approach provides a simple way to design a complex coupled resonator system such that it has the desired spectral response near resonance. CMT-space can be used to verify the filter response. The transfer-matrix, $\overline{\overline{T}}$ in the CMT-space formalism follows by dividing the device into 4 regions between the $\lambda/4$-wave shifts. $\overline{\overline{T}}$ is given by:

$$\overline{\overline{T}} = \overline{\overline{T}}_4(\kappa, z_4, z_3)\,\overline{\overline{T}}_3(-\kappa, z_3, z_2)\,\overline{\overline{T}}_2(\kappa, z_2, z_1)\,\overline{\overline{T}}_4(-\kappa, z_1, 0) \tag{3.106}$$

Across each $\lambda/4$-wave shift the $\kappa$ undergoes a $\pi$ phase-shift.

## 3.5 Mach-Zehnder Bragg Grating Filter

The above sections show that both the Bragg grating and a Bragg resonator act as a frequency selective device allowing a frequency range to be selected from a wider band signal. The Bragg grating does this by reflecting light within the stopband. The Bragg resonator, on the other hand, is a transmission filter which allows light near resonance
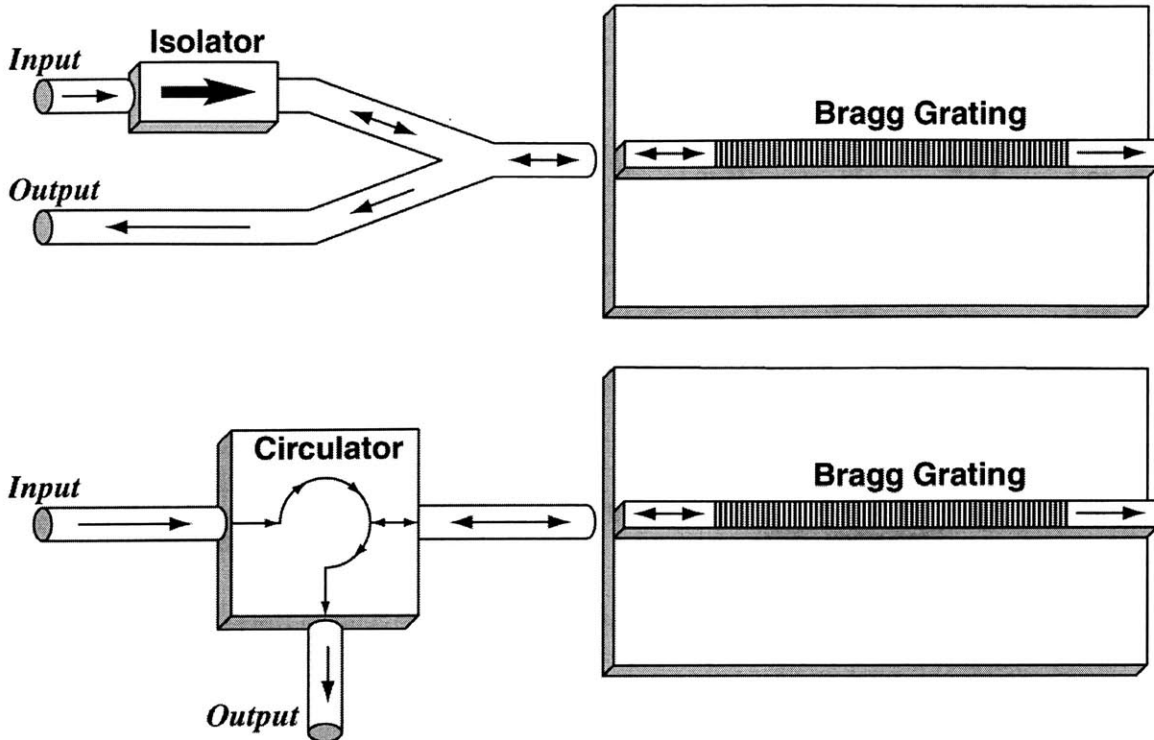
**Figure 3-19:** Strategies for separating the input and output using Bragg grating filters

at the center of the stopband to be transmitted whilst reflecting everywhere else in the stopband. To be used as add/drop filters, there is a need to physically separate the input signal from the dropped channel output and the throughput channels. Figure (3-19) shows two possible schemes for separating input and output. The techniques require either an isolator or a circulator. These are discrete optical components which must be added on to the integrated grating-based device and are quite expensive. A totally integrated approach is preferred both for cost reasons and also because it is a more elegant approach.

One possible integrated techique of making add/drop filters using Bragg gratings is shown in Fig. (3-21). The Bragg grating structure is integrated into the two arms of a balanced Mach-Zehnder with 3 dB couplers. At the first coupling section the multi-wavelength signal is split equally into the two arms. The dropped channel wavelength is reflected by the gratings and as it returns through the first coupler it recombines at the dropped port. The throughput channels on the other hand continue through and as they pass through the second coupler they are recombined at the throughput port. The dropped/throughput channel specturm is the reflection/transmission response of the grating. To get better side-lobe levels the Bragg gratings in the Mach-Zehnder may be apodized.
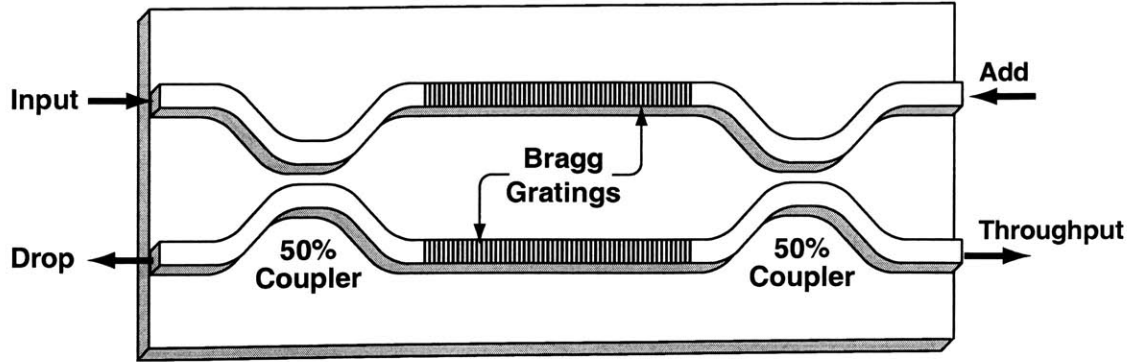
**Figure 3-20:** Integrated Mach-Zehnder add/drop filter made using Bragg gratings in the two balanced arms of the interferometer.

In the case that the Bragg gratings in the arms of the Mach-Zehnder are replaced by Bragg resonators, either a single resonator or multiple coupled inline resonators, the position of the dropped and throughput channels is reversed. In this case the dropped/throughput channel spectrum is the transmission/reflection response of the Bragg resonator system. If multiple Bragg resonators are used the transmission response can be shaped as seen in section (3.4.4) to yield a Butterworth, Chebychev etc. response. Use of Bragg resonators instead of gratings in the balanced arms of a Mach-Zehnder offers the advantage of obtaining the desired spectral response by just choosing the spacings between the $\lambda/4$-wave shifts appropriately. The gratings do not need to be apodized if Bragg resonators are used as the channels within the stopband are reflected strongly. The integrated Mach-Zehnder add/drop filter allows the input signal to be physically separated from both the dropped signal and the throughput signal.

The spectral response of the Mach-Zehnder can be calculated quite readily using CMT-space and transfer matrices. The device naturally breaks into three regions: From the previous discussion of waveguide couplers and Bragg gratings, we can easily write down the coupled mode equations for the coupler and grating sections. The forward and backward waves in the top and bottom arms are denoted $A_1$, $B_1$ and $A_2$, $B_2$. $\overline{\overline{\mathbf{M}}}_{c1}$ and $\overline{\overline{\mathbf{M}}}_{c2}$ denote the interaction matrices of the coupling regions. $\overline{\overline{\mathbf{M}}}_g$ is the interaction matrix describing
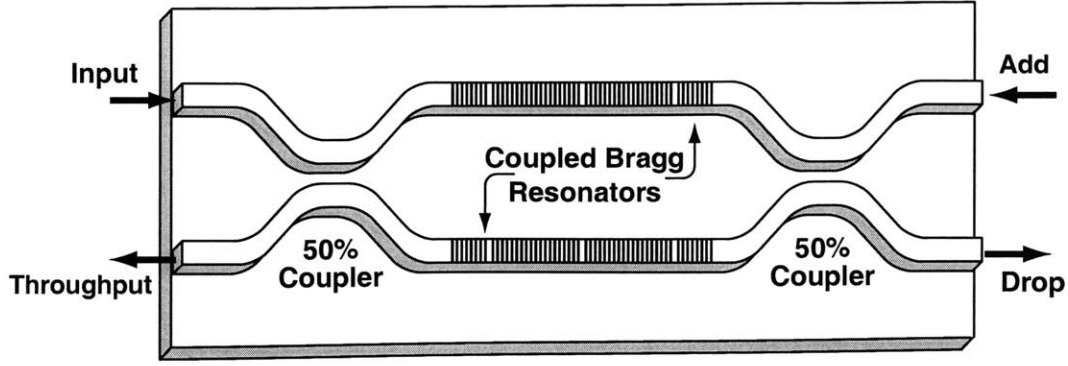
**Figure 3-21:** Integrated Mach-Zehnder add/drop filter made using inline coupled Bragg resonators in the two balanced arms of the interferometer. The position of the throughput and drop ports are interchanged relative to a Mach-Zehnder add/drop filter using Bragg gratings.

the grating region.

$$\frac{d}{dz}\begin{bmatrix} A_1 \\ A_2 \\ B_1 \\ B_2 \end{bmatrix} = \begin{pmatrix} -j\delta_1 - \alpha_1 & -j\mu_{12} & 0 & 0 \\ -j\mu_{12} & -j\delta_2 - \alpha_2 & 0 & 0 \\ 0 & 0 & j\delta_1 + \alpha_1 & j\mu_{12} \\ 0 & 0 & j\mu_{12} & j\delta_2 + \alpha_2 \end{pmatrix} \begin{bmatrix} A_1 \\ A_2 \\ B_1 \\ B_2 \end{bmatrix} \tag{3.107}$$

$$= \overline{\overline{\mathbf{M}}}_{c1}\, \vec{A} \tag{3.108}$$

where $\delta_i$'s are the "propagation" constants of the two guides and as before are given by

$$\delta_i = \beta_i - \frac{2\pi}{\Lambda_g}; \tag{3.109}$$

$\Lambda_g$ is the grating period. $\alpha_i$ is the loss in the guides and $\mu_{12}$ represents the coupling between the two guides. A similar interaction matrix, $\overline{\overline{\mathbf{M}}}_{c2}$ can be written from the second coupler region.

Likewise, the equations describing the interaction between the forward and backwards waves in the grating section are given by

$$\frac{d}{dz}\begin{bmatrix} A_1 \\ A_2 \\ B_1 \\ B_2 \end{bmatrix} = \begin{pmatrix} -j\delta_1 - \alpha_1 & 0 & \kappa_1 & 0 \\ 0 & -j\delta_2 - \alpha_2 & 0 & \kappa_2 \\ \kappa_1^* & 0 & j\delta_1 + \alpha_1 & 0 \\ 0 & \kappa_2^* & 0 & j\delta_2 + \alpha_2 \end{pmatrix} \begin{bmatrix} A_1 \\ A_2 \\ B_1 \\ B_2 \end{bmatrix} \tag{3.110}$$

$$= \overline{\overline{\mathbf{M}}}_g\, \vec{A} \tag{3.111}$$

Having written down the interaction matrices in each of the three regions, the transfer matrices can be written down readily. The transfer matrices for the coupling regions, $\overline{\overline{\mathbf{T}}}_{c1}$ and $\overline{\overline{\mathbf{T}}}_{c2}$ are given by:

$$\overline{\overline{\mathbf{T}}}_{\{c1,c2\}}(z, z_o) = \overline{\overline{\mathbf{S}}}_{\{c1/c2\}} \overline{\overline{\mathbf{\Lambda}}}_{\{c1,c2\}}(z) \left[\overline{\overline{\mathbf{\Lambda}}}_{\{c1,c2\}}(z_o)\right]^{-1} \left[\overline{\overline{\mathbf{S}}}_{\{c1,c2\}}\right]^{-1} \tag{3.112}$$

where we have used eq. (3.34) derived earlier. Likewise, the grating section described the transfer matrix $\overline{\overline{\mathbf{T}}}_g$ is given by

$$\overline{\overline{\mathbf{T}}}_g(z, z_o) = \overline{\overline{\mathbf{S}}}_g \overline{\overline{\mathbf{\Lambda}}}_g(z) \left[\overline{\overline{\mathbf{\Lambda}}}_g(z_o)\right]^{-1} \left[\overline{\overline{\mathbf{S}}}_g\right]^{-1} \tag{3.113}$$

where $\overline{\overline{\mathbf{S}}}_j$ contains the eigenvector of the interaction matrix $\overline{\overline{\mathbf{M}}}_j$ as its column vectors and $\overline{\overline{\mathbf{\Lambda}}}_j$ is a matrix with the exponentiated eigenvalues of $\overline{\overline{\mathbf{M}}}_j$ along its diagonal. $\overline{\overline{\mathbf{M}}}_j$ is one of the three interaction matrices $\overline{\overline{\mathbf{M}}}_{c1}$, $\overline{\overline{\mathbf{M}}}_{c2}$ or $\overline{\overline{\mathbf{M}}}_g$. In this case the complete transfer matrix representing the Mach-Zehnder is given by

$$\overline{\overline{\mathbf{T}}} = \overline{\overline{\mathbf{T}}}_{c1} \overline{\overline{\mathbf{T}}}_g \overline{\overline{\mathbf{T}}}_{c2}. \tag{3.114}$$

As before by converting to a scattering matrix and using the inputs to the device we can calculate the spectral response of Mach-Zehnder device.

### 3.5.1 Design Considerations

The key component in the design of a Mach-Zehnder is the Bragg grating. The Bragg grating must be engineered such that its spectrum meets the specifications for add-drop filters needed for WDM networks. Currently deployed WDM systems currently use channel spacings, $\Delta f_{sp}$, of 50, 100 and 200 GHz. WDM experiments with channel spacings of 25 GHz are being reported [37, 38]. The 1-dB pass bandwidth, $\Delta f_{1dB}$, of add-drop filters is generally specified in terms of a percentage of the channel spacing with

$$\Delta f_{1dB} \approx \left(25\% - 50\%\right)\Delta f_s$$

being typical values for currently available devices. In addition to this another requirement on add-drop filters is that the cross-talk or channel isolation of the adjacent channels must be in excess of 25 dB. Furthermore, the dropped channel suppression must also be around 25 dB. These specifications on the spectrum of the device translates to grating parameter constraints. As discussed in section 3.2 the 1-dB bandwidth of a straight grating is given by

$$\Delta f_{1dB} = \frac{1.12\kappa c}{\pi n_g} \tag{3.115}$$

**Apodized Bragg grating based MachZehnder Filter**   **Apodized Bragg grating based MachZehnder Filter**
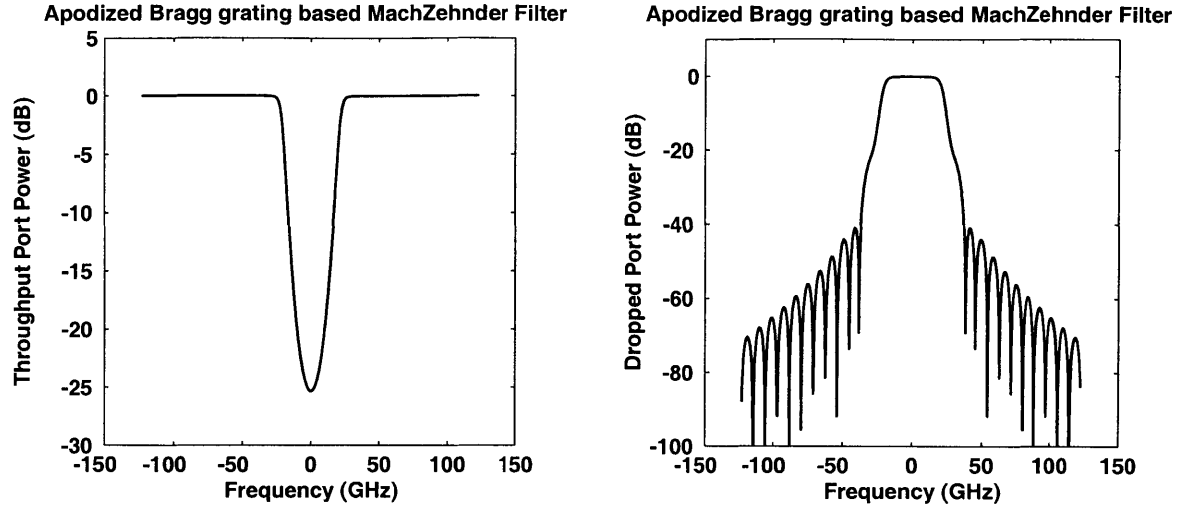
**Figure 3-22:** Spectrum of a Mach-Zehnder add/drop filter with Apodized Bragg grating in the two balanced arms.

Using the above expression to design a 1-dB bandwidth which is 40% of the channel spacing we find that

$$\kappa = 6.5\,\mathrm{cm}^{-1} \qquad \Delta f_{sp} = 50\mathrm{GHz} \tag{3.116}$$

$$\kappa = 12.9\,\mathrm{cm}^{-1} \qquad \Delta f_{sp} = 100\mathrm{GHz} \tag{3.117}$$

$$\kappa = 25.8\,\mathrm{cm}^{-1} \qquad \Delta f_{sp} = 200\mathrm{GHz} \tag{3.118}$$

We used group index, $n_g$, values corresponding to the InP material system which the choice material system for all the devices we fabricated. The requirement that the dropped channel suppression be around 20-25 dB requires that $\kappa L \approx 3.5$. Using this we find that the lengths of the gratings for the various channel spacings are:

$$L = 5.4\,\mathrm{mm} \qquad \Delta f_{sp} = 50\mathrm{GHz} \tag{3.119}$$

$$L = 2.7\,\mathrm{mm} \qquad \Delta f_{sp} = 100\mathrm{GHz} \tag{3.120}$$

$$L = 1.3\,\mathrm{mm} \qquad \Delta f_{sp} = 200\mathrm{GHz} \tag{3.121}$$

Fabricating long coherent Bragg gratings is challenging. Gratings in excess of 3 mm are quite difficult to make. Thus we see that integrated add-drop filters using Bragg gratings in the armos of a Mach-Zehnder is unrealistic for WDM channel spacings of 50 GHz or less. Given the fabrication constraints, the Mach-Zehnder configuration may be best suited for wider channel spacing WDM sytems of 200 GHz. In section 3.2 we also saw that the side-lobes of Bragg gratings directly impact the cross-talk or channel isolation requirements.

It was pointed out that straight Bragg gratings may be unable to meet the cross-talk specification. As a result apodized Bragg gratings are needed. Since, the apodized gratings have a lower average grating strength, $\bar{\kappa}$, even longer grating lengths are needed. However, it is still possible to design add-drops for 100 GHz channel spacing. Using the techniques developed in earlier section, an apodized Mach-Zehnder device suitable for a 100 GHz WDM channel spacing was designed. The spectral response is shown in Fig. (3-22). The filter has a 30 GHz 1 dB passband width, drop suppression in excess of 20 dB and channel isolation in excess of 60 dB.

The Mach-Zehnder add-drop filter performance is critically dependent on the alignment of the gratings in the two arms. If the start of the two gratings is misaligned by half an optical wavelength, $\lambda$, the effect is identical to the introduction of a phase difference in one arm. It results in the destructive interference at the drop port and all dropped channel power being returned at the input port. This requirement of precise alignment presents a fabrication challenge. Techniques have been developed to ensure alignment of the Bragg gratings in the two arms [39].

Finally the 50%-coupler region also impacts the overall Mach-Zehnder performace. Any deviation of the power splitting ratio from 50% results in an effective insertion loss increase of the device. Also any wavelength dependence of the coupler produces wavelength sensitive performance. Wavelength insensitive couplers have been proposed to account for this [40, 41].

The Mach-Zehnder with Bragg grating in its arms has been studied extensively elsewhere [42]. Section (3.5) is not meant to be an exhaustive study of this device. Rather it presents a basic overview of the device, the basic tools needed to calculate its spectrum and some of the design considerations involved in making a Mach-Zehnder based add-drop filter.

# Chapter 4

# Side-coupled Bragg Resonators

In the previous chapter, we discussed at length how to model Bragg gratings and Bragg resonators. A Mach-Zehnder interferometer with integrated Bragg grating structures in the two arms is one possible configuration that can be used as an Add/Drop filter. For typical WDM channel spacing, Mach-Zehnder interferometers with Bragg gratings require low grating strength, $\kappa$ structures. Moreover, the dropped channel suppression requirements result in rather long structures as the gratings can be several millimeters. Alternate possible topologies exist that use Bragg resonators coupled to waveguides to form Add/Drop filters. These devices, as we will see rely, on resonant transfer of power from a multi-channel "bus" waveguides to coupled Bragg resonator structures. Devices of this class need not be of low grating strength, $\kappa$. This leads to smaller, more compact devices which is desireable.

## 4.1  Resonant Optical Reflector (ROR) [43]

Figure (4-1) shows a Bragg grating resonator side-coupled to waveguide. The arms of the Bragg resonator on either side of the $\lambda/4$-wave shift are assumed to be very long. As we saw in the previous chapter the fields in a Bragg resonator decay exponentially. Thus, for the Bragg resonator of Fig. (4-1) we can assume that no power can leak out from either end; in addition we assume that the resonator has no internal loss mechanism. In chapter 2 we saw that two adjacent waveguides can couple to each other via the modes' exponential tails. Here too the mode in the resonator guide can couple to the mode in the waveguide. As a result the Bragg resonator can lose power to the outside world via coupling to the adjacent waveguide. Mathematically we can represent this system of two coupled
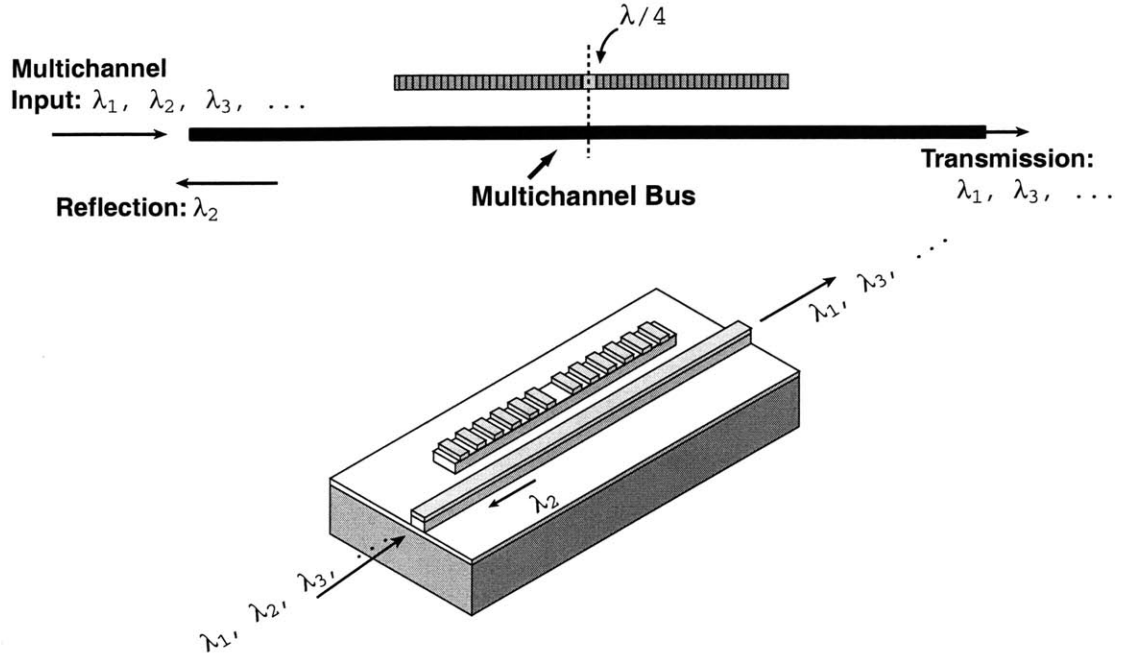
**Figure 4-1:** Bragg grating resonator side-coupled to a waveguide.

structures by CMT-space equations:

$$\frac{dA_1}{dz} = -j\delta_1 A_1 - j\mu A_2 \tag{4.1}$$

$$\frac{dA_2}{dz} = -j\mu A_1 - j\delta_2 A_2 + \kappa B_2 \tag{4.2}$$

$$\frac{dB_1}{dz} = j\delta_1 B_1 + j\mu B_2 \tag{4.3}$$

$$\frac{dB_2}{dz} = \kappa A_2 + j\mu B_1 + j\delta_2 B_2 \tag{4.4}$$

where $A_1$, $A_2$ and $B_1$, $B_2$ are the forward and backward travelling waves, respectively, in the waveguide and the Bragg resonator. $\delta_i$ is defined as before by eq. (3.109) and is the normalized frequency parameter.

$$\delta_i = \beta_i - \beta_o = \frac{\Delta\omega_i}{v_g^i} \tag{4.5}$$

Alternately, it can be thought of as the "propagation constant" of the respective waveguide or Bragg resonator guide. $\mu$ as in chapter 2 is the coupling coefficient and represents power transfer between the two guides. The transfer matrix method can be employed to solve the above equations. The coupled structure naturally breaks into two regions on either side of the $\lambda/4$-wave shift. The total transfer matrix, $\overline{\overline{T}}$ is given by:

$$\overline{\overline{T}} = \overline{\overline{T}}_2(-\kappa, \mu, z_1, z_2)\, \overline{\overline{T}}_1(\kappa, \mu, z_2, z_3) \tag{4.6}$$
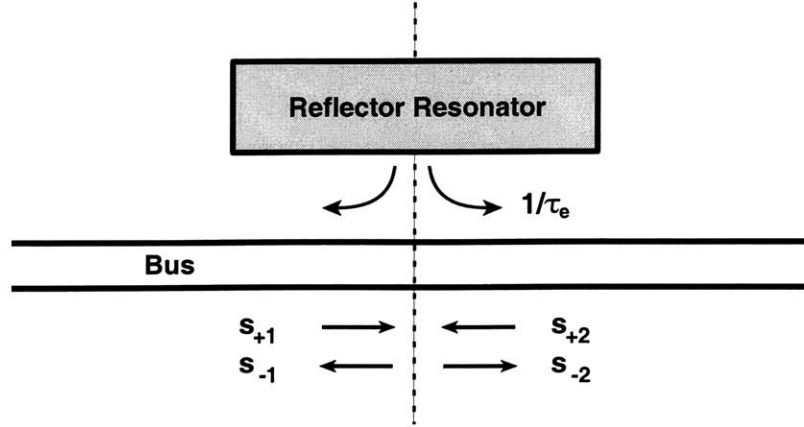
**Figure 4-2:** Schematic of the coupled Bragg resonator-waveguide system.

where across the $\lambda/4$-wave shift $\kappa$ reverses sign. The transfer matrix method can be used to solve for the spectrum of this device. Alternatively, it can be used to calculate field values along the length of the device at a given frequency of $\delta_i$.

CMT-space equations describe the coupled system in terms of the counter-propagating waves. They are somewhat numerically involved. The alternate, CMT-time, approach is analytically more tractable and represents the system of Fig. (4-1) as a resonator coupled to the outside world (see Fig. (4-2)). The system is described by the following equation:

$$\frac{da_o}{dt} = j(\omega_o - \frac{1}{\tau_e})a_o + \underline{\kappa}(s_{+1} + s_{+2}) \tag{4.7}$$

As before $a_o$ is the resonator mode amplitude and normalized such that it $|a_o|^2$ is the energy in the resonator. $\omega_o$ is the resonant frequency. The resonator coupling to the adjacent waveguide can result in power being transferred into the adjacent waveguide. This power loss from the resonator the guide is represented by $1/\tau_e$. Thus we can expect $1/\tau_e$ to be related to the CMT-space coupling parameter $\mu$. $s_{+1}$ and $s_{+2}$ are the incoming waves that can excite the resonator and are normalized such that $|s_{+i}|^2$ is the power carried by them. $s_{+1}$ and $s_{+2}$ are related to $A_1$ and $B_1$. $s_{-i}$ are the corresponding outgoing waves. Finally $\underline{\kappa}$, not to be confused with the CMT-space grating strength parameter, $\kappa$, is the input coupling coefficient; it expresses the degree of coupling between the resonator and the input waves $s_{+i}$. By symmetry this coefficient is the same for both input waves. Time reversibility and power conservation arguments can be used to give the following expression [20].

$$\underline{\kappa} = \sqrt{\frac{1}{\tau_e}} \tag{4.8}$$

It should not be surprising that $\underline{\kappa}$ is related to the power loss term $1/\tau_e$; how strongly the

fields can couple into the resonator must depend on how strongly the resonator interacts with the outside world. The outgoing waves are related to the incoming waves by

$$s_{-1} = s_{+2} - \sqrt{\frac{1}{\tau_e}} a_o \tag{4.9}$$

$$s_{-2} = s_{+1} - \sqrt{\frac{1}{\tau_e}} a_o \tag{4.10}$$

These expressions follow from power conservation. If the resonator is not excited, eqs. (4.9) and (4.10) simply state that the input waves pass through undisturbed. Using the above equations, we can readily calculate the response of the coupled structure when excited only from one side, i.e when

$$s_{+1} = e^{j\omega t} \tag{4.11}$$

$$s_{+2} = 0; \tag{4.12}$$

We find that

$$\frac{s_{-1}}{s_{+1}} = \frac{-1/\tau_e}{j(\omega - \omega_o) + \frac{1}{\tau_e}} \tag{4.13}$$

$$\frac{s_{-2}}{s_{+1}} = \frac{j(\omega - \omega_o)}{j(\omega - \omega_o) + \frac{1}{\tau_e}} \tag{4.14}$$

We see that that on resonance, all the incoming power is reflected and transmission drops to zero. Beyond resonance, the transmission recovers to near unity. The reflection spectrum has a characteristic lorentzian response indicative of a single-pole or single resonator system. Figure. (4-3) shows the overlay of the spectral response calculated from CMT-time with that calculated using transfer-matrices and CMT-space. As expected CMT-time is only accurate near resonance where eq. (4.7) is valid. Far from resonance we have to rely on CMT-space to yield accurate results.

We can understand the behavior of the coupled Bragg resonator-waveguide system from physical reasoning. The incoming wave on the waveguide couples via the transverse mode's exponential tail to the Bragg resonator. Near resonance the resonator supports a mode. The light from the waveguide excites this mode. From the previous chapter, we know that near resonance the fields in the Bragg resonator are localized near the $\lambda/4$-wave shift and decay exponentially on either side. Since the arms of the Bragg resonator are very long no power leaks through its ends. However, the fields in the Bragg resonator can couple back to the waveguide. The resonant mode consists of both forward and backward travelling waves
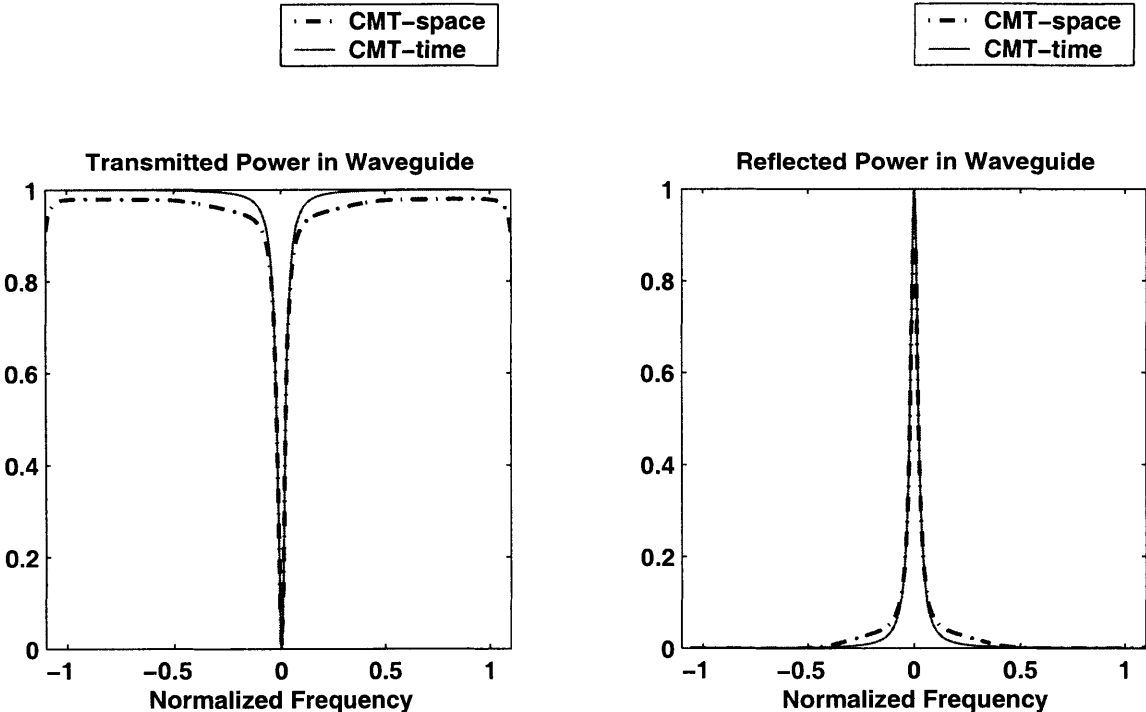
**Figure 4-3:** Spectral response of the resonant optical reflector calculated from CMT-time and CMT-space.
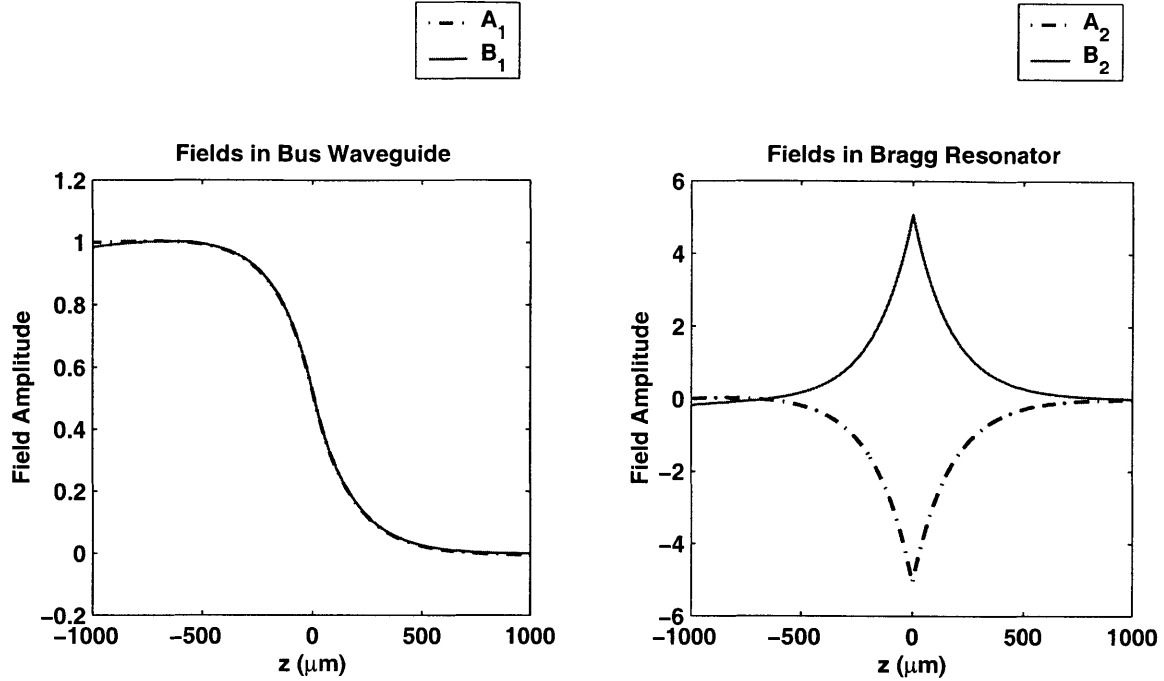
**Figure 4-4:** Field in the resonant optical reflector calculated from CMT-time and CMT-space on resonance, $\delta = 0$.

and couples in both directions onto the waveguide. The coupling from the waveguide to the resonator and back to the waveguide results in a 180° phase shift of the fields such that the fields add out-of-phase in transmission. Consequently at resonance all the light is reflected. The sharp reflection response of this device gives it the name resonant optical reflector. Off resonance but within the stopband of the grating the Bragg resonator does not support a propagating mode and thus no light can couple from the waveguide to the resonator. Outside the stopband the grating effect is neglible and standard broadband waveguide-to-waveguide coupling occurs beween the input waveguide and the resonator guide. The fields inside the resonator and waveguide on resonance are shown in Fig. (4-4). They were computed using CMT-space and transfer matrices assuming that $\delta_1 = \delta_2 = 0$. Note that beyond the $\lambda/4$-wave shift the fields in the waveguide decay to zero. This is due to the out-of-phase addition of the coupled fields from the resonator.

CMT-time allowed us to analytically calculate the response of the resonant optical reflector (ROR) near resonance (eqs. (4.13) and (4.14)) in terms of the resonant frequency and decay term, $1/\tau_e$. However, we have not related this term to the optical parameters, $\mu$, and $\kappa$. We alluded earlier that $\tau_e$ must be related to $\mu$. To relate $\tau_e$ to the optical parame-

ters we follow an approach identical to that in sections (3.4.1) and (3.4.2) and calculate the $Q$ of the resonator where

$$Q \equiv \frac{W}{(P/\omega_o)} = \frac{\omega_o \tau_e}{2}.$$

As before $W$ is the energy stored in the resonator and $P$ is the power lost by the resonator due to coupling to the adjacent waveguide. To calculate $Q$ we need analytical expressions for the fields in the ROR at resonance. We numerically calculated these fields on resonance using CMT-space and $\overline{\overline{T}}$-matrices. This method does not lend itself readily to an analytical approach. However, there is an alternate approach which estimates the fields by using a source-free, time reversed, steady-state construction (SFTRSS). This approach is well described in [43] and we will only quote the final results here. The fields in the resonator and the waveguide on resonance when the the ROR is excited from the left side on the bus waveguide are:

$$A_1 = B_1 = (1 - \frac{1}{2}e^{\kappa z}) \qquad z < 0; \tag{4.15}$$

$$A_1 = B_1 = \frac{1}{2}e^{-\kappa z} \qquad z > 0; \tag{4.16}$$

$$A_2 = -B_2 = -j\frac{\kappa}{\mu}e^{\kappa z} \qquad z < 0; \tag{4.17}$$

$$A_2 = -B_2 = -j\frac{\kappa}{\mu}e^{-\kappa z} \qquad z > 0; \tag{4.18}$$

These field values can be compared with the exact field solution calculated from CMT-space. This is shown in Fig. (4-4). The power coupled into the adjacent waveguide and the energy stored in the resonator can be used to give the $Q$ of the resonator and hence $\tau_e$, [43]

$$\frac{1}{Q} = \frac{2}{\omega_o \tau_e} = 4 \left(\frac{\mu}{\kappa}\right)^2 \frac{\kappa v_g}{\omega_o} \tag{4.19}$$

$$\frac{1}{\tau_e} = 2 \kappa v_g \left(\frac{\mu}{\kappa}\right)^2. \tag{4.20}$$

Having related $\tau_e$ to the optical parameters $\mu$ and $\kappa$ allows to write down simple analytical expressions for the ROR spectrum using CMT-time in terms of the physical parameters of the system.

## 4.1.1 Equivalent Circuit of the ROR

Consider the circuit shown in Fig. (4-5) consisting of a series $L$-$C$ branch across a transmission line of characteristic impedance $Y_o$. On resonance, the series $L$-$C$ branch shorts out the transmission line so that all the incoming power is reflected. This behavior is similar to the
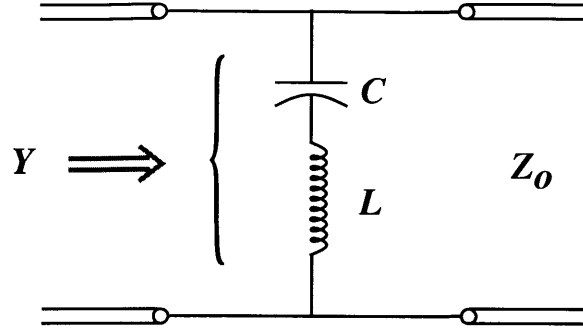
**Figure 4-5:** Equivalent circuit of a Resonant Optical Reflector

ROR which reflects completely on resonance. However, to prove an equivalence between the circuit response and the ROR spectral response the reflection and transmission coefficients of the circuit must be compared with the CMT-time expressions, eqs. (4.13) and (4.14). From transmission line theory the reflection coefficient $\Gamma$ and the transmission coefficient are given by

$$\Gamma = \frac{1 - Y_n}{1 + Y_n} \tag{4.21}$$

$$T = 1 + \Gamma = \frac{2}{1 + Y_n} \tag{4.22}$$

where $Y_n$ is the normalized impedance looking from the left of the series $L$-$C$ branch and is given by

$$Y_n = \frac{Y}{Y_o} = 1 + \frac{1}{2j\Delta\omega L Y_o} \tag{4.23}$$

Using the above equations we find that

$$\Gamma = \frac{-1/4LY_o}{j\Delta\omega + \frac{1}{4LY_o}} \tag{4.24}$$

$$T = \frac{j\Delta\omega}{j\Delta\omega + \frac{1}{4LY_o}} \tag{4.25}$$

We see that the above equations are identical to the CMT-time expression, eqs. (4.13) and (4.14) provided we make the following correspondance:

$$\tau_e \longleftrightarrow 4LY_o \tag{4.26}$$

Use of eq. (4.20) allows us to relate the circuit parameters to the optical parameters, i.e

$$LY_o = \frac{1}{8\,\kappa\,v_g} \left(\frac{\kappa}{\mu}\right)^2. \tag{4.27}$$

We will see shortly that equivalent circuits are very valuable tools in filter design.
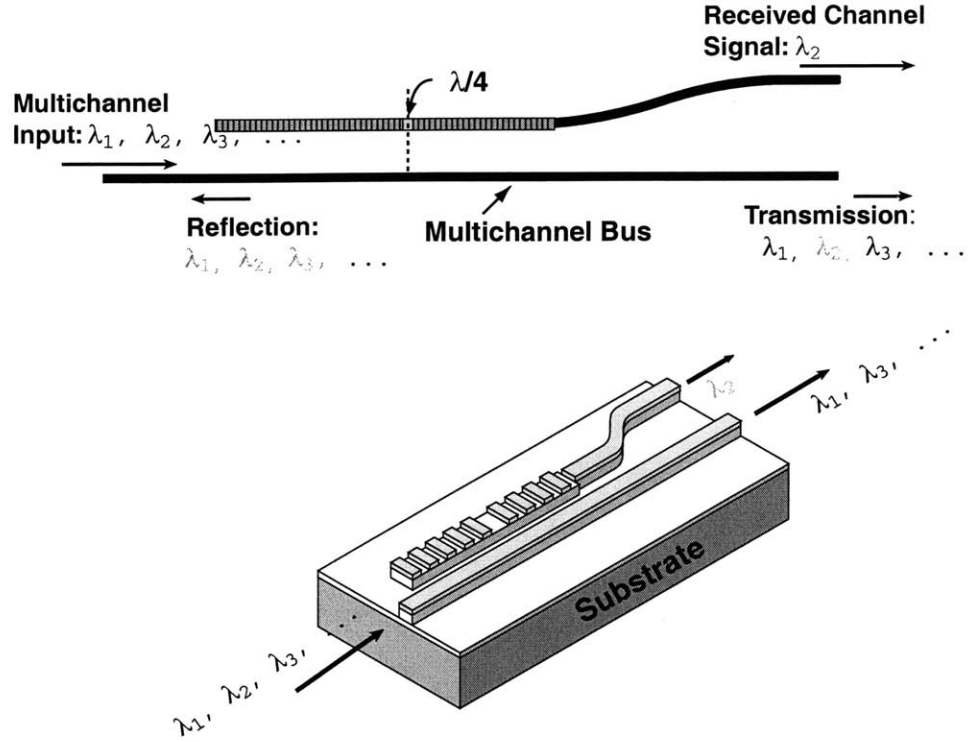
**Figure 4-6:** A single side-coupled receiver resonator coupled to a waveguide to form an SCR.

## 4.2 Side-coupled Receiver (SCR)

A slight variation of the resonant optical reflector is the device shown in Fig. (4-6). As before a Bragg resonator is side-coupled to a bus waveguide, except that one arm of the resonator is short such that power can leak out of this port. The CMT-space equations and $\overline{\overline{T}}$-matrices describing this system are identical to those for a ROR and given in the previous section. The CMT-time equation, however, must now include a decay term which models loss of power from the resonator due to it leaking out of the shorter arm. The CMT-time equation describing this system is:

$$\frac{da_o}{dt} = j(\omega_o - \frac{1}{\tau_e} - \frac{1}{\tau_l})a_o + \underline{\kappa}(s_{+1} + s_{+2}) \qquad (4.28)$$

where $1/\tau_l$ is the decay term that models power leakage from the short arm of the Bragg resonator. All other quantities in the equation are as decribed in the previous section. A schematic of the single side-coupled Bragg resonator is shown in Fig. (4-7) Loss from the ends of a Bragg resonator was previously calculated in section (3.4.2). $\tau_l$ is given by eq. (3.94)

$$\frac{1}{\tau_l} = |\kappa| v_g e^{-2|\kappa| L_g} \qquad (4.29)$$
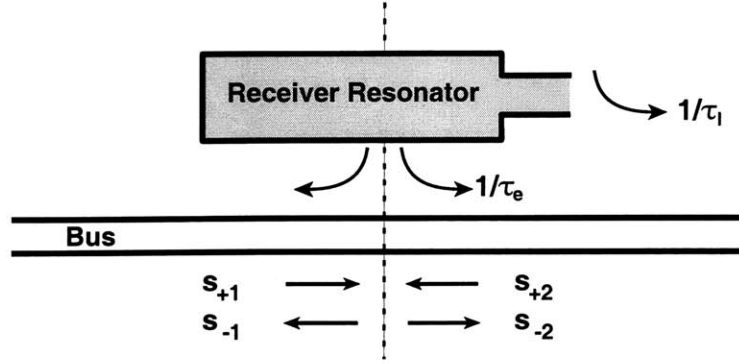
**Figure 4-7:** A CMT-time schematic of a single Bragg resonator side-coupled to a waveguide to form an SCR.

where $L_g$ is the length of the shorter arm. $v_g$ as before is the group velocity in the Bragg resonator guide. As before the backward travelling waves, $s_{-1}$ and $s_{-2}$, on the waveguide are given by eqs. (4.10) and (4.9)

$$s_{-1} = s_{+2} - \sqrt{\frac{1}{\tau_e}} a_o \qquad (4.30)$$

$$s_{-2} = s_{+1} - \sqrt{\frac{1}{\tau_e}} a_o \qquad (4.31)$$

Note that the outward propagating waves on the waveguide only depend on $\tau_e$ - the coupling mechanism of the resonator to the outside world. Based on the intuition developed from the preceding section we can guess what will be the response of this system when excited from a signal from the bus. The wave on the bus will excite the resonator mode which will: (a) couple back to the waveguide as in the case of a ROR cancelling some of on-going transmission on the bus waveguide; (b) leak out of the shorter arm of the resonator. We, therefore, expect incomplete reflection on the bus waveguide and some power leakage via the "open" arm of the resonator. These two power decay mechanisms will compete with each other. Figure (4-8) shows the spectrum of this device calculated using CMT-space. The length $L$, the coupling $\mu$ and the grating strength $\kappa$ were taken to be typical values. As expected we see that some of the power is reflected on the bus waveguide and some is transmitted while the remaining power leaks through the shortened arm of the resonator. As the length of resonator arm is varied so that $1/\tau_l$ changes the amount of power received in the resonator changes. There is a trade-off between the power reflected and transmitted in the waveguide and that transfered to the resonator. We can solve the CMT-time equations to determine the exact response. Solving the equations we find that [36]

### Transmitted Power in Waveguide

### Reflected Power in Waveguide

### Power transfered to Resonator
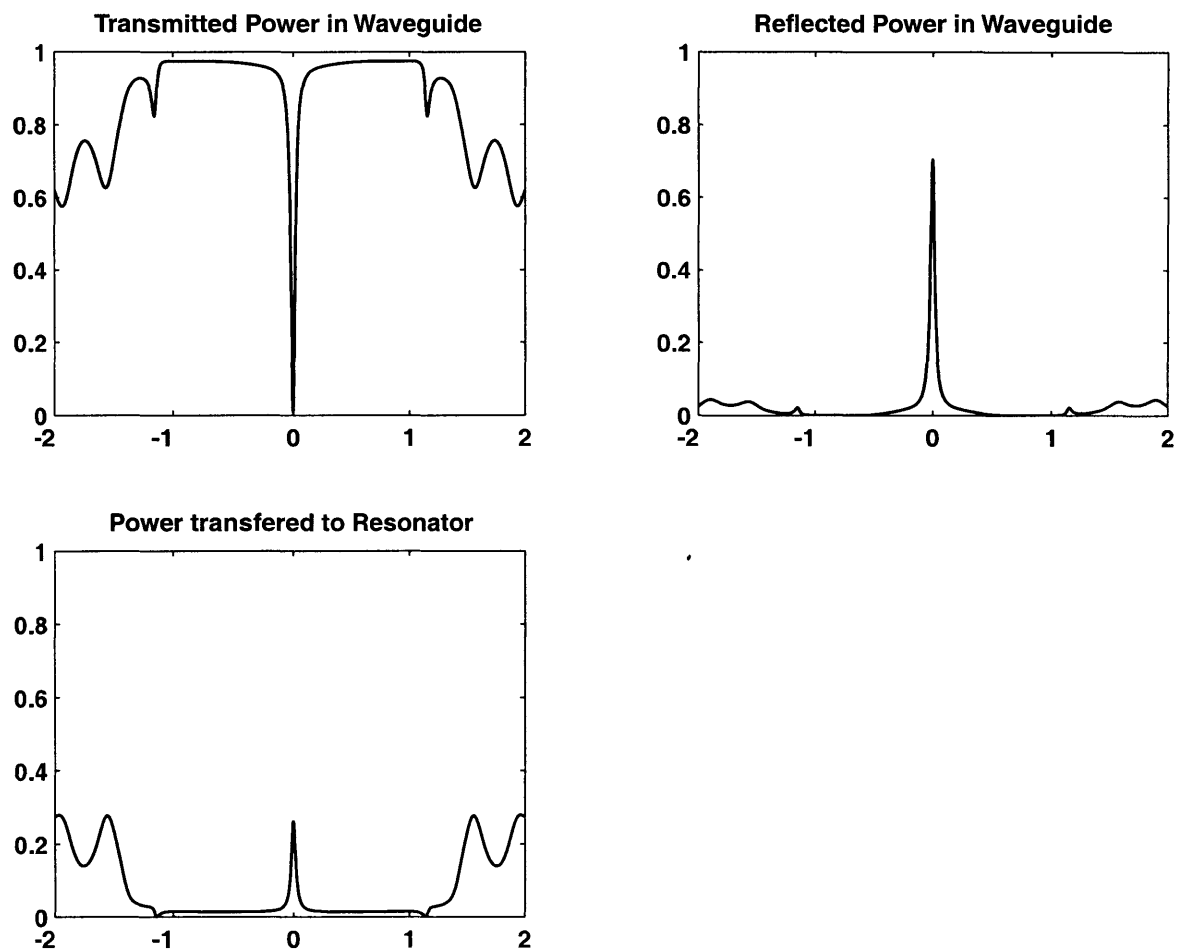
**Figure 4-8:** Spectral response of a side-coupled receiver (SCR).

**Transmitted Power in Waveguide**

**Reflected Power in Waveguide**

**Power transfered to Resonator**
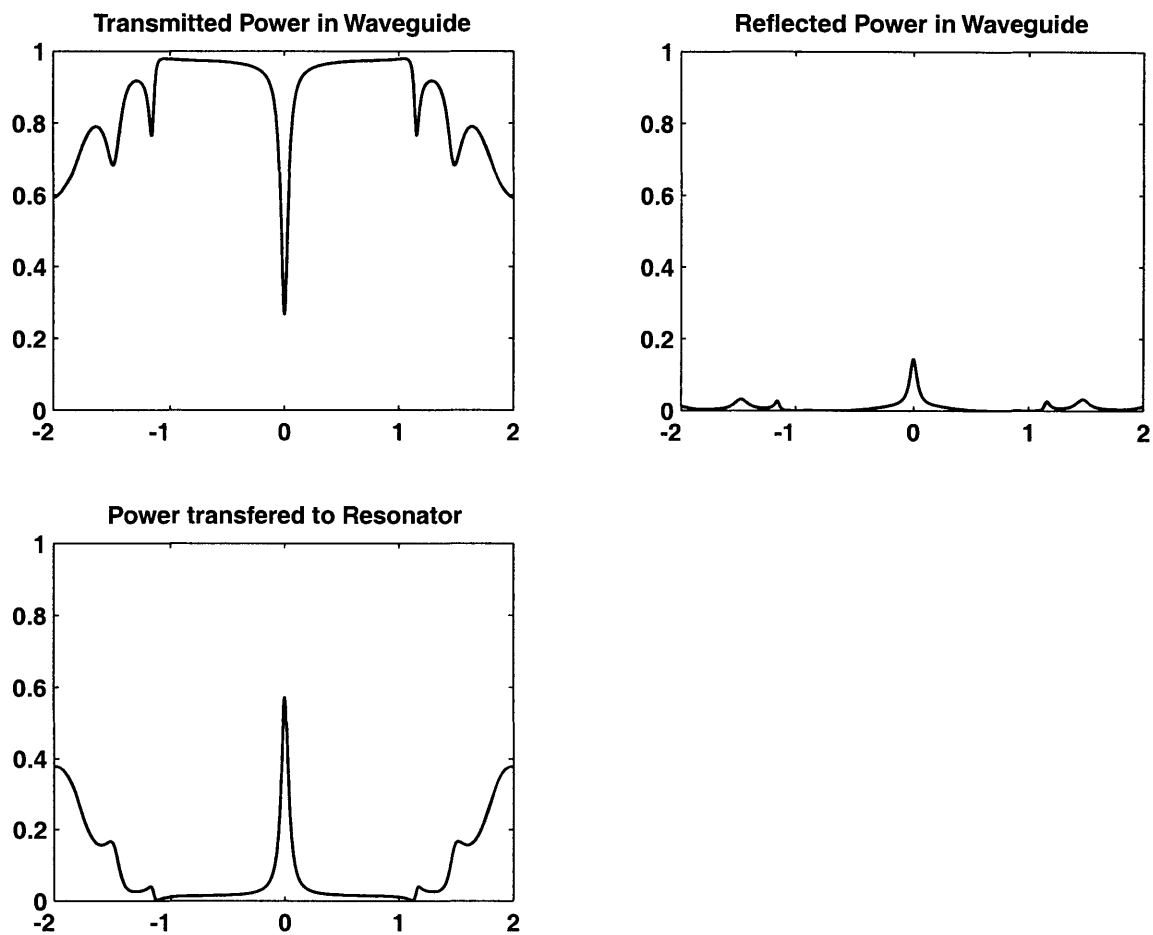
**Figure 4-9:** Spectral response of a side-coupled receiver (SCR) optimized for maximum power transfer.

$$\frac{s_{-1}}{s_{+1}} = \frac{-1/\tau_e}{j(\omega - \omega_o) + \frac{1}{\tau_e} + \frac{1}{\tau_l}} \tag{4.32}$$

$$\frac{s_{-2}}{s_{+1}} = \frac{j(\omega - \omega_o) + \frac{1}{\tau_l}}{j(\omega - \omega_o) + \frac{1}{\tau_e} + \frac{1}{\tau_l}} \tag{4.33}$$

To calculate the power transfered to the resonator we used power conservation. The incoming power must be equal to the sum of the power reflected and transmitted in the bus waveguide and that transfered to the resonator. Thus,

$$P_r = |s_{+1}|^2 - |s_{-1}|^2 - |s_{-2}|^2; \tag{4.34}$$

on resonance, i.e $\omega = \omega_o$ using the above expressions we find

$$P_r = \left\{ 1 - \left| \frac{\frac{1}{\tau_e}}{\frac{1}{\tau_e} + \frac{1}{\tau_l}} \right|^2 - \left| \frac{\frac{1}{\tau_l}}{\frac{1}{\tau_e} + \frac{1}{\tau_l}} \right|^2 \right\} |s_{+1}|^2 \tag{4.35}$$

where we have used the power normalization of the waves $s_{\pm i}$. By maximizing $P_r$ with respect to $\tau_l$ we find that

$$\tau_l = \tau_e \tag{4.36}$$

The above expressions allows the length, $L$, of the shorter arm of the receiver resonator to be related to the grating strength, $\kappa$ and the coupling parameter, $\mu$.

$$L = -\frac{1}{\kappa} \ln(\frac{\kappa}{\sqrt{2}\mu}) \tag{4.37}$$

In this case 1/4 of the power is reflected on the bus waveguide, 1/4 is transmitted on the bus waveguide and 1/2 of the incident power is transferred to the resonator on resonance. Figure (4-9) shows the spectrum of the side-coupled receiver. As expected half the power is transferred to the resonator at resonance. The power coupled into the resonator has a lorentzian response and this device acts like a filter transferring power in a certain frequency range into the receiver port while letting other frequencies through. However, this device has the shortcoming that not all the power is transferred to the receiver resonator and that some of the incident power is reflected on the bus guide.

### 4.2.1 Equivalent Circuit of the SCR

The equivalent circuit of the ROR gives us an excellent clue as to what is the equivalent circuit of the SSCR. The SSCR is similar to the ROR except that it has a source of loss via its shortened arm. This loss of power from the resonator can be modelled by adding a
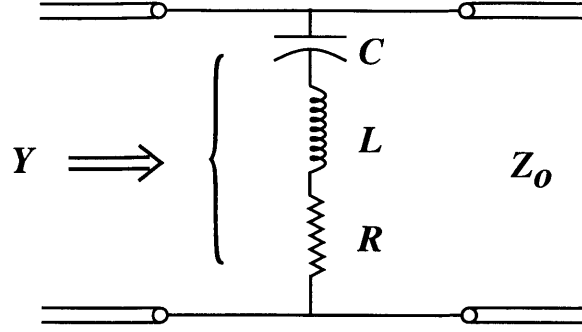
**Figure 4-10:** Equivalent circuit of a single resonator side-coupled to waveguide to form a Side-coupled Receiver.

resistor, $R$ in the series $L$-$C$ branch of Fig. (4-5). Thus the equivalent circuit of the SSCR is as shown in Fig. (4-10) $Y$ is the admittance looking from left of the series branch is

$$Y_n = \frac{Y}{Y_o} = \frac{1}{Y_o}\left(\frac{1}{R + 2j\Delta\omega L} + Y_o\right) \tag{4.38}$$

Using eqs. (4.21) and (4.22) we can calculate the response of the SSCR equivalent circuit:

$$\Gamma = \frac{\frac{-1}{4LY_o}}{j\Delta\omega + \frac{1}{4LY_o} + \frac{R}{2L}} \tag{4.39}$$

$$T = \frac{j\Delta\omega + \frac{R}{2L}}{j\Delta\omega + \frac{1}{4LY_o} + \frac{R}{2L}} \tag{4.40}$$

Comparison of the above equations with the CMT-time expressions given by eqs. (4.32) and (4.33) show that the two are equivalent if we draw the following correspondence:

$$\tau_e \longleftrightarrow 4LY_o \tag{4.41}$$

$$\tau_l \longleftrightarrow \frac{2L}{R} \tag{4.42}$$

The first correspondence is the same as that for a ROR. The second correspondence relates the resistance, $R$ to the loss from the resonator. We saw that maximum power transfer to the resonator occured when $\tau_e = \tau_l$. Using the above equations this translates to

$$R = 2Z_o$$

which is what we would expect by simply considering the equivalent circuit of the SSCR and maximizing power into $R$.
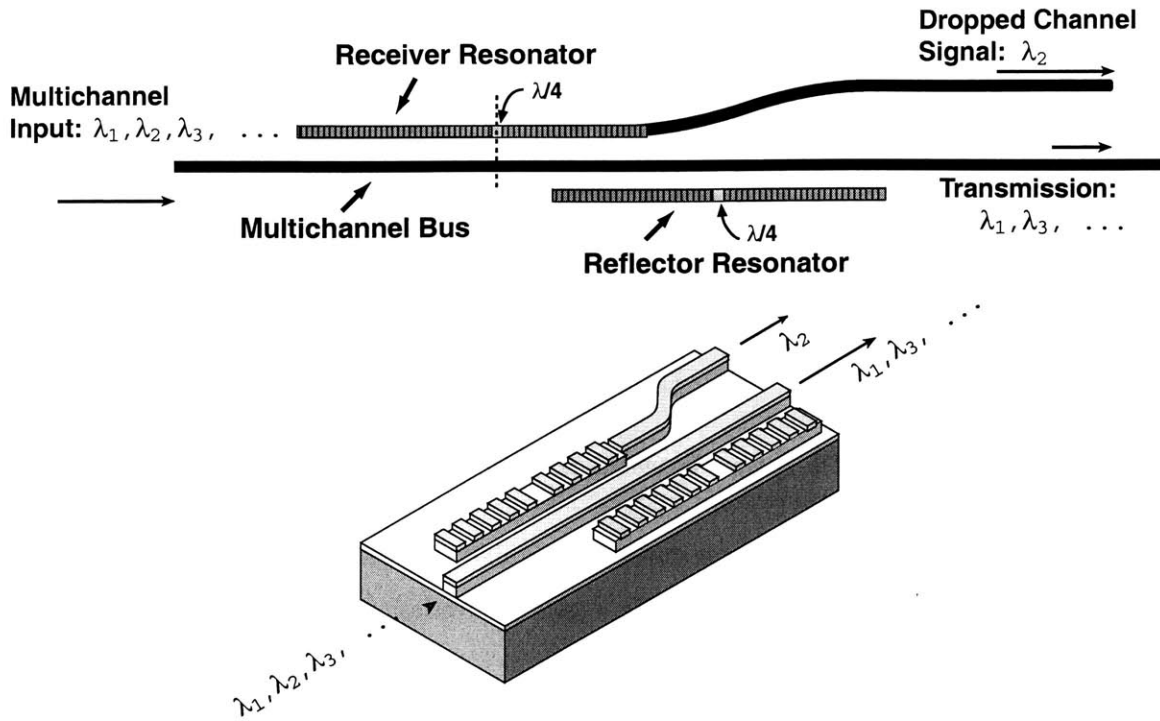
**Figure 4-11:** An add/drop filter capable of complete power transfer to the receiver port.

## 4.3 First-order Add/Drop Filter

In the previous section we saw that a single Bragg resonator side-coupled to a bus waveguide acts as a receiver filter. At and around resonance it transfers power from the waveguide to the receiver resonator. The most that can be transferred is half the incident power. A quarter of the incident power is reflected and a quarter is transmitted on the bus waveguide. If we had a way to cancel out the reflected power on the bus and to re-direct the on-going transmitted power back into the receiver resonator, we would create an Add/Drop filter capable of complete power transfer. One way to do this is to couple the on-going light to a resonant reflector - i.e a side-coupled Bragg resonator with long arms [44]. If this Bragg reflector is out-of-phase with the receiver resonator then the light it reflects will cancel the light reflected from the receiver resonator. Moreover the on-going power from the receiver resonator would get redirected back towards it. Consider the system of Fig. (4-11) which shows a bus waveguide side-coupled two Bragg resonators; one is a receiver resonator (with one short arm) and the other is Bragg reflector resonator. The two resonators are quarter-wave shifted with respect to each other, thereby introducing the appropriate phase-shift needed for complete power transfer. For fabrication purposes the quarter-wave shift
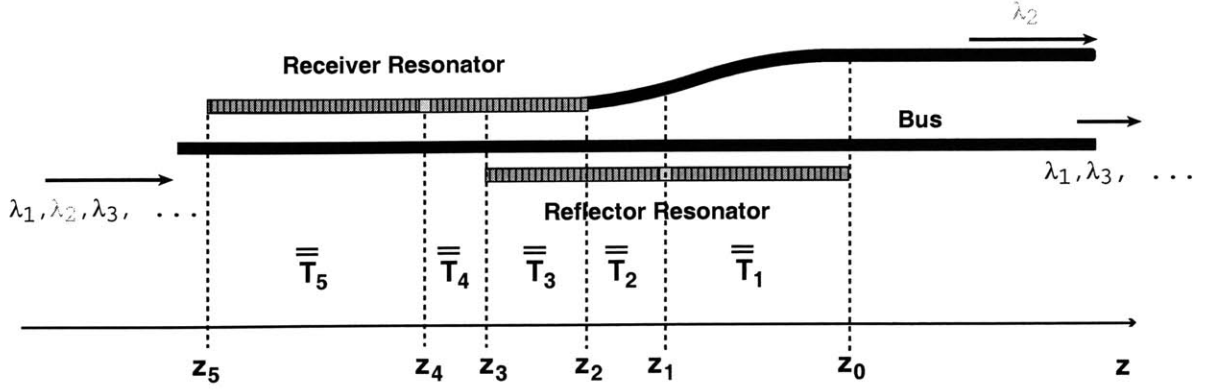
**Figure 4-12:** A transfer-matrix analysis of an Add/Drop Filter.

between the two resonators can be ensured by aligning the teeth on the receiver resonator with those on the reflector resonator in the region of overlap. The system of Fig. (4-11) is described by the following CMT-space equations:

$$\frac{dA_1}{dz} = -j\delta_1 A_1 - j\mu_{12}A_2 \tag{4.43}$$

$$\frac{dA_2}{dz} = -j\mu_{12}A_1 - j\delta_2 A_2 + \kappa_2 B_2 \tag{4.44}$$

$$\frac{dA_3}{dz} = -j\mu_{13}A_1 - j\delta_3 A_3 + \kappa_3 B_3 \tag{4.45}$$

$$\frac{dB_1}{dz} = j\delta_1 B_1 + j\mu_{12}B_2 \tag{4.46}$$

$$\frac{dB_2}{dz} = \kappa_2 A_2 + j\mu_{12}B_1 + j\delta_2 B_2 \tag{4.47}$$

$$\frac{dB_3}{dz} = \kappa_3 A_3 + j\mu_{13}B_1 + j\delta_3 B_3 \tag{4.48}$$

where $A_1$, $A_2$ and $A_3$ are the forward traveling wave in the bus waveguide, the receiver resonator and the reflector resonator respectively. $B_i$ are the corresponding backward travelling waves in the three guides respectively. $\mu_{12}$ and $\mu_{13}$ are the coupling constant for the bus-receiver resonator and the bus-reflector resonator sub-systems. As before, $\delta_i$ is the normalized frequency parameter or the propagation constant and is given by:

$$\delta_i = \beta_i - \beta_o$$

Transfer matrices can be employed once again to solve the spectrum of this device. The device breaks up into 5 regions indicated in Fig. (4-12); each region is represented by a transfer matrix $\overline{\overline{\mathbf{T}}}_i(\mu_{12}, \mu_{13}, \kappa_2, \kappa_3, z_i, z_{i-1})$ with the appropriate input parameters. The total transfer matrix $\overline{\overline{\mathbf{T}}}$ is given by
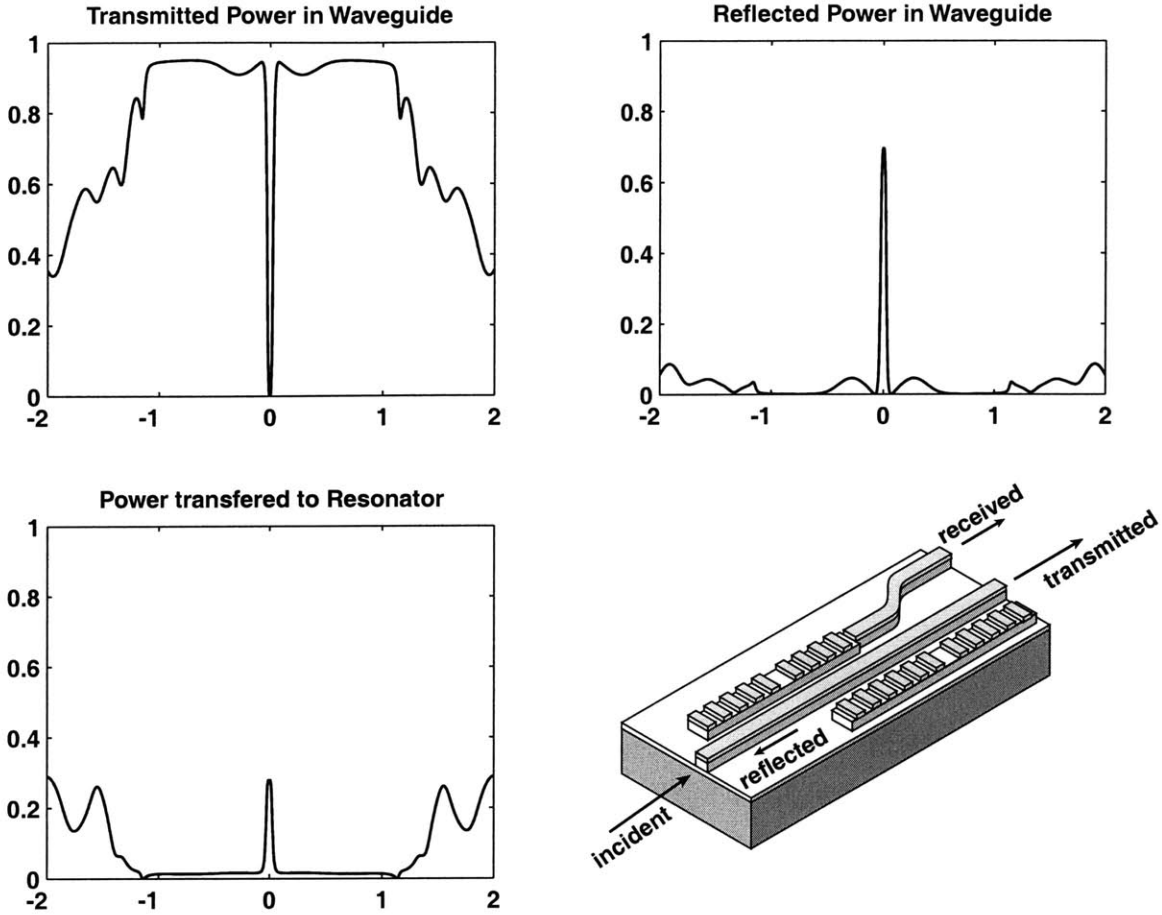
**Figure 4-13:** Spectrum of the Add/Drop filter with un-optimized optical parameters.

$$\overline{\overline{\mathbf{T}}} = \overline{\overline{\mathbf{T}}}_5(\mu_{12}, 0, +\kappa_2, 0, z_5, z_4) \cdot \overline{\overline{\mathbf{T}}}_4(\mu_{12}, 0, -\kappa_2, 0, z_4, z_3) \cdot \overline{\overline{\mathbf{T}}}_3(\mu_{12}, \mu_{13}, -\kappa_2, -\kappa_3, z_3, z_2) \cdots$$

$$\overline{\overline{\mathbf{T}}}_2(0, \mu_{13}, 0, -\kappa_3, z_2, z_1) \cdot \overline{\overline{\mathbf{T}}}_1(0, \mu_{13}, 0, +\kappa_3, z_1, z_0) \tag{4.49}$$

The transfer matrix, $\overline{\overline{\mathbf{T}}}$ can be used to calculate the spectrum of the device or the field values along the length of the Add/Drop filter for any frequency. Figure (4-13) shows the spectral response of the Add/Drop filter for typical optical parameter values in InP material systems. $\kappa_i$ were assumed to be equal. The coupling parameters $\mu_{12}$ and $\mu_{23}$ were chosen to be typical values; however their values were not chosen to be equal. The coupling coefficients, $\mu_{ab}$, are determined by lateral spacing between guides which can be lithographically controlled. We notice an enhancement of the light transferred to the receiver resonator output port. We see that the transmitted power on the bus drops to zero. The input power is either reflected on the bus or transferred to receiver resonator.
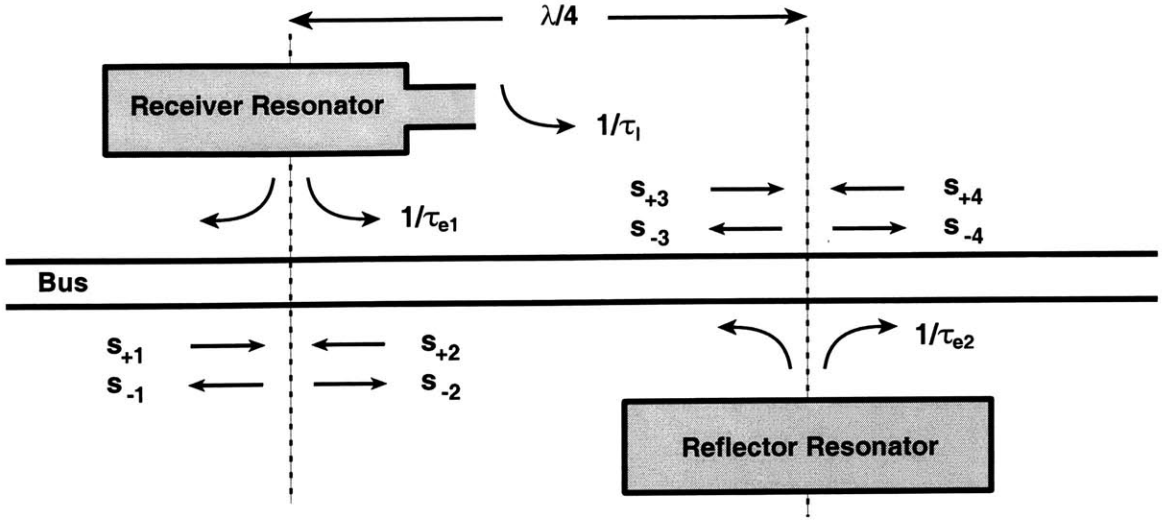
**Figure 4-14:** Schematic representation of the Add/Drop Filter.

## 4.3.1   CMT-Time Analysis of the Add/Drop Filter

To determine the optimal optical parameters for the Add/Drop filter we rely on CMT-time which provides an analytically tractable formalism for calculating the spectral response. Using the CMT-time description of the ROR and SSCR we can write down the equations for the Add/Drop filter:

$$\frac{da_1}{dt} = j(\omega_o - \frac{1}{\tau_{e1}} - \frac{1}{\tau_l})\,a_1 + \underline{\kappa_1}\,(s_{+1} + s_{+2}) \tag{4.50}$$

$$\frac{da_2}{dt} = j(\omega_o - \frac{1}{\tau_{e2}})\,a_2 + \underline{\kappa_2}\,(s_{+3} + s_{+4}) \tag{4.51}$$

where $a_1$ and $a_2$ are the amplitude modes in the receiver and reflector resonators respectively. $1/\tau_{e1}$ and $1/\tau_{e2}$ represent the loss of power from the receiver and reflector resonators via coupling to the adjacent bus waveguide. As before

$$\underline{\kappa_1} = \sqrt{\frac{1}{\tau_{e1}}}$$

$$\underline{\kappa_2} = \sqrt{\frac{1}{\tau_{e2}}}$$

$s_{+\{1,2\}}$ are the input waves on the bus that can excite the receiver resonator; $s_{+\{3,4\}}$ are the input waves on the bus waveguide for the reflector resonator. $s_{-i}$ are the corresponding ouput waves as indicated Fig. (4-14) The light from the receiver resonator is coupled via the bus waveguide to the reflector resonator. $s_{-2}$, the output wave for the receiver resonator system serves as the input, $s_{+3}$ to the reflector resonator. Similarly $s_{-3}$ is related to $s_{+2}$.

These relationships are as follows:

$$s_{+3} = -js_{-2} \tag{4.52}$$

$$s_{+2} = -js_{-3} \tag{4.53}$$

These $j$ factors are simply the $e^{j\beta\frac{\lambda}{4}}$ factors needed to account for the quarter-wave shift between the two resonator systems. As before $s_{-i}$ are related to $s_{+j}$ according to the following equations.

$$s_{-1} = s_{+2} - \sqrt{\frac{1}{\tau_{e1}}} a_1 \tag{4.54}$$

$$s_{-2} = s_{+1} - \sqrt{\frac{1}{\tau_{e1}}} a_1 \tag{4.55}$$

$$s_{-3} = s_{+4} - \sqrt{\frac{1}{\tau_{e2}}} a_2 \tag{4.56}$$

$$s_{-4} = s_{+3} - \sqrt{\frac{1}{\tau_{e2}}} a_2 \tag{4.57}$$

Using the above expressions we can calculate the mode amplitudes in both the resonators when the system is excited from the left side, i.e $s_{+1} = e^{j\omega t}$ and $s_{+4} = 0$. We find that

$$a_1 = \frac{D_2 \kappa_1 + \kappa_2 \left(\frac{1}{\sqrt{\tau_{e1}\tau_{e2}}}\right)}{D_1 D_2 + \frac{1}{\tau_{e1}\tau_{e2}}} s_{+1} \tag{4.58}$$

$$a_2 = -j \frac{D_1 \kappa_2 + \kappa_1 \left(\frac{1}{\sqrt{\tau_{e1}\tau_{e2}}}\right)}{D_1 D_2 + \frac{1}{\tau_{e1}\tau_{e2}}} s_{+1} \tag{4.59}$$

where $D_1$ and $D_2$ are shorthand notations for

$$D_1 = j(\omega - \omega_o) + \frac{1}{\tau_l} + \frac{1}{\tau_{e1}} \tag{4.60}$$

$$D_2 = j(\omega - \omega_o) + \frac{1}{\tau_{e2}} \tag{4.61}$$

These can be used along with the other equations above to calculate the power transmitted and reflected on the bus as a function of frequency

$$\frac{s_{-4}}{s_{+1}} = -j \left[1 - \frac{D_1 \kappa_2^2 + D_2 \kappa_1^2}{D_1 D_2 + \left(\frac{1}{\tau_{e1}\tau_{e2}}\right)}\right] \tag{4.62}$$

$$\frac{s_{-1}}{s_{+1}} = \frac{D_1 \kappa_2^2 - D_2 \kappa_1^2 - \frac{2}{\tau_{e1}\tau_{e2}}}{D_1 D_2 + \left(\frac{1}{\tau_{e1}\tau_{e2}}\right)} \tag{4.63}$$

Exactly at resonance the expression simplifies to

$$\frac{s_{-4}}{s_{+1}} = 0 \tag{4.64}$$

$$\frac{s_{-1}}{s_{+1}} = \frac{\left(\frac{1}{\tau_l} - \frac{2}{\tau_{e1}}\right)\frac{1}{\tau_{e2}}}{D_1 D_2 + \frac{1}{\tau_{e1}\tau_{e2}}} \tag{4.65}$$
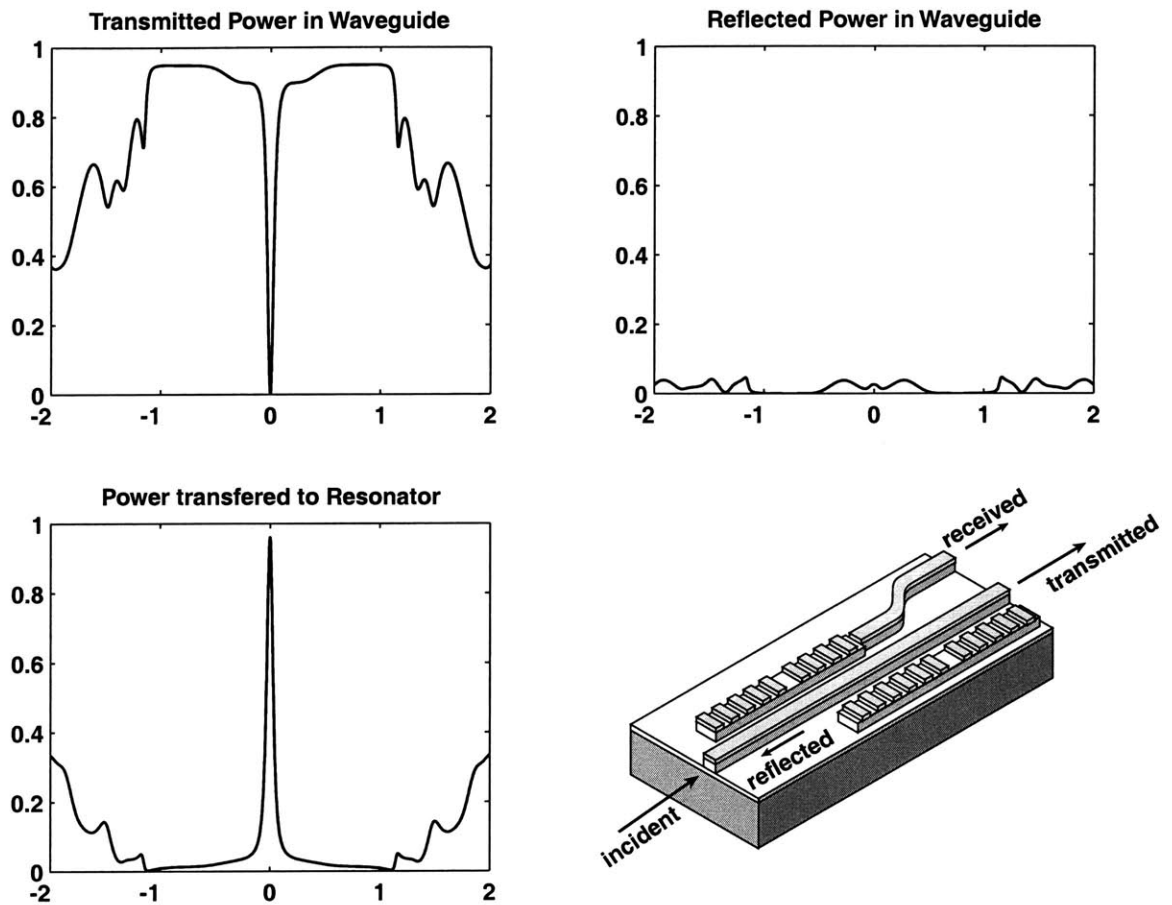
**Figure 4-15:** Spectrum of the first-order Add/Drop Filter optimized for complete power transfer; overlay of CMT-space and CMT-time response is shown.

It is obvious from the above expression that the requirement of no power being reflected on the bus translates to the condition that

$$\tau_l = \frac{\tau_{e1}}{2} \tag{4.66}$$

Since on resonance the transmitted power on the bus is always zero, the above condition guarantees complete power transfer to receiver resonator. Compare this condition with that required for maximal power transfer in the case of SSCR, eq. (4.36). SSCR. The power transferred to the receiver resonator is given by

$$P_R = \frac{2}{\tau_l}|a_1|^2 \tag{4.67}$$

that is the rate of decay of the modal energy in the receiver resonator via the shortened arm. Substituting for $a_1$ using eq. (4.58) and using the condition of eq. (4.66) for maximum power transfer to the receiver resonator, we find that

$$P_R = \frac{4}{\tau_{e1}^2} \left| \frac{j\Delta\omega + \frac{2}{\tau_{e2}}}{(j\Delta\omega)^2 + j\Delta\omega(\frac{1}{\tau_{e2}} + \frac{3}{\tau_{e1}}) + \frac{4}{\tau_{e1}\tau_{e2}}} \right|^2 \tag{4.68}$$

where $\Delta\omega = \omega - \omega_o$. At $\Delta\omega = 0$ as expected $P_R = 1$. The above expressions simplifies considerably for the special case when $\tau_{e1} = \tau_{e2}$ to

$$P_R = \left| \frac{1}{1 + j\frac{\Delta\omega\tau_{e1}}{2}} \right|^2 \tag{4.69}$$

Figure (4-15) shows the spectral response of the first-order Add/Drop filter optimized for complete power transfer with $\tau_{e1} = \tau_{e2}$. The deviation of the received power, $P_R$, from unity is due to the small power loss via the longer arm of the receiver resonator. $P_R$ can be brought arbitrarily close to unity by lengthening this arm to reduce power leakage. Note that for this case the response of the Add/Drop filter is a lorentzian, given by eq. (4.69). Far from resonance the spectrum has a characteristic roll-off of $(1/\Delta\omega)^2$ with frequency . Even in the general case described by eq. (4.68) the power received in receiver resonator rolls of with the same dependency far from resonance. This is characteristic of first-order filters.

## 4.3.2  Equivalent Circuit of First-order Add/Drop Filter

The equivalent circuit of this Add/Drop filter, shown in Fig. (4-16), follows immediately by concatenating the equivalent circuit of the SSCR with that of the ROR; the quarter-wave transmission line segment is needed to take into account the phase-shift between the
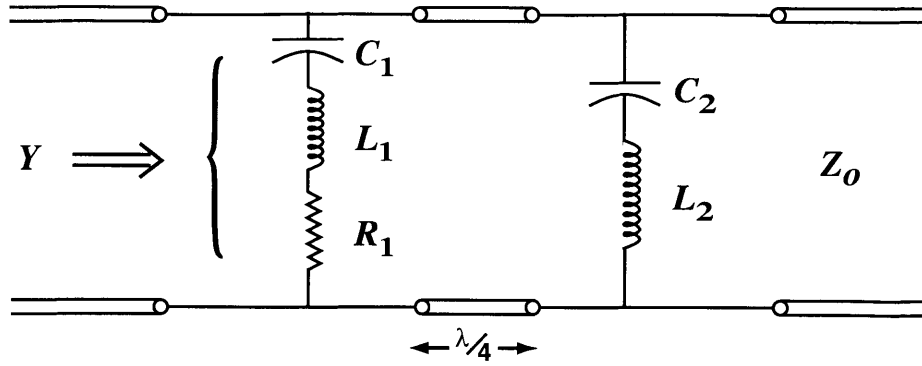
**Figure 4-16:** Equivalent Circuit of the first-order Add/Drop Filter.

two Bragg resonators [44]. At resonance the series L-C branches short out. Transforming the short corresponding to the ROR across the quarter-wave shift results in the output transmission line being open circuited. On resonance, the circuit simplifies to a resistor, $R$ hanging at the end of a transmission line. To maximize power into the resistor it is obvious that is must be matched to the characteristic impedance, $Z_o$, of the transmission line, i.e

$$R = Z_o \tag{4.70}$$

From correspondence between the equivalent circuit and CMT-time parameters given by eqs. (4.41) and (4.42) it follows that

$$R = Z_o \implies \tau_l = \frac{\tau_{e1}}{2} \tag{4.71}$$

This is the same result as that derived from the CMT-time analysis. We see that the equivalent circuit yields this result with almost no algebraic manipulation. Moreover, it is obvious from the equivalent circuit that there is no transmission on the bus waveguide on resonance. Not only is the equivalent circuit an excellent tool for selecting the optimal parameters for the Add/Drop filter but it also helps to obtain a better physical understanding as to how the device works. It takes a distributed device and provides a lumped element model for which our intuition is better.

### 4.3.3 A closer look at the Add/Drop filter spectrum

We have used CMT-time to optimize the Add/Drop filter response at and near resonance. However far from resonance we must rely on CMT-space to calculate the response of the Add/Drop filter. CMT-time equations are an approximate set that are only valid near resonance; moreover, they are completely general and are applicable to any resonator system;
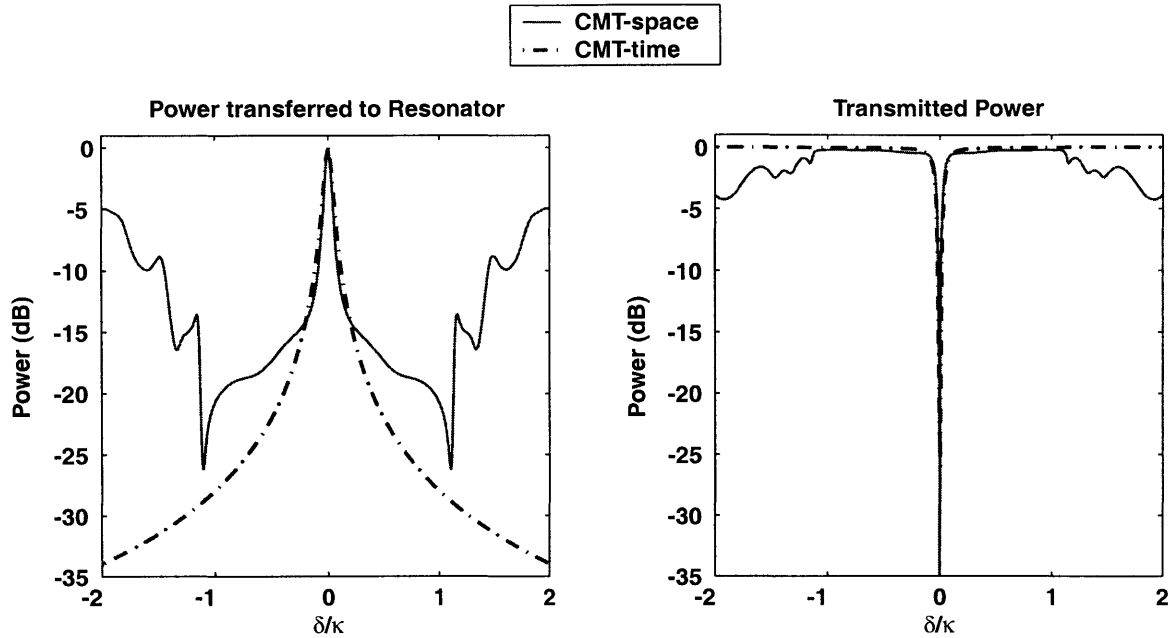
**Figure 4-17:** Overlay of CMT-space and CMT-time response for a first-order add/drop filter tha tis optimized for power transfer to the receiver resonator.

CMT-space equations, on the other hand are specific to Bragg gratings and resonators. They accurately model the behavior of Bragg resonators over a wide frequency range.

Figure (4-17) shows a spectral plot, plotted on dB scale of the transmitted port and the dropped channel or receiver port calculated with CMT-space. Overlayed is the CMT-time response. Expectedly, we see that the two responses deviate further from the resonance. Whereas CMT-time predicts a continous roll-off with frequency, of the power transferred to the receiver resonator of the CDF, the CMT-space response flattens within the stopband of the grating. To understand this floor we recognize that there are two competing mechanisms which either enable or inhibit power transfer from the bus waveguide to the receiver resonator. The transfer of power from the bus to the resonator occurs due to the regular waveguide-to-waveguide coupling accounted for by the coefficient, $\mu_{12}$. The degree of coupling is related to the $\mu_{12}L_c$ product where $L_c$ is the total length of the receiver resonator. This coupling mechanism is fairly frequency independent. However, off resonance but within the stopband the Bragg grating resonator does not support a propagating mode. Since, a propagating resonator mode does not exist off resonance power transfer from the bus to the resonator is inhibited in this frequency range. The degree of suppression of this transfer is related to the $\kappa L_c$. For an infinite length grating, the power from the bus would
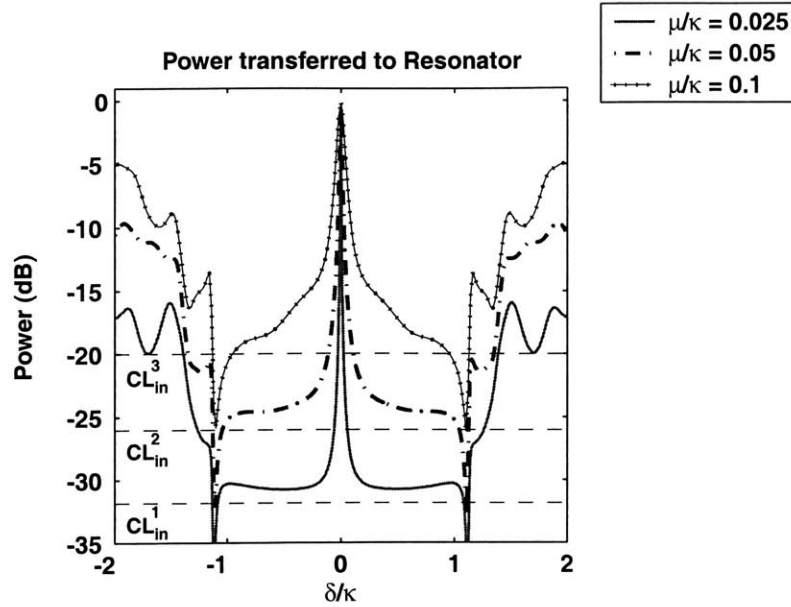
**Figure 4-18:** $CL_{\text{in}}$ is shown for increasing $\mu_{12}/\kappa$ ratios.

only couple to the Bragg resonator exactly and only on resonance within the stopband. However for a finite length grating some power does couple off resonance and within the stopband. Not surprisingly, the amount that couples into the resonator off of resonance but with the stopband is given by [43, 45]

$$\text{CL}_{\text{in}} \approx \left(\frac{\mu_{12}}{\kappa}\right)^2 \tag{4.72}$$

where $\text{CL}_{\text{in}}$ is the coupling level within the stopband off resonance. Fig. (4-18) shows the $\text{CL}_{\text{in}}$ for different $\mu_{12}/\kappa$ ratios.

The deviation between CMT-space and CMT-time is even more apparent beyond the stopband. The CMT-space calculated received signal level restores considerably, whereas the CMT-time signal continues its roll-off. The level of the received signal recovers because in the frequency range outside of the stopband the grating ceases to be effective as a reflector and supports propagating modes. In this frequency range the Bragg grating resonator appears just like an ordinary waveguide. The result is that the normal waveguide-to-waveguide mechanism dominates and the power coupled from the bus to the receiver port approaches the level, $\text{CL}_{\text{out}}$ given by

$$\text{CL}_{\text{out}} = \sin^2(\mu_{12}L_c) \tag{4.73}$$

Similarly, for the transmitted signal we see that the CMT-time predicts the response generally accurately within the stopband but that beyond the stopband the transmitted

level drops. This drop is due to the same reason which results in $\mathrm{CL_{out}}$ level; waveguide-to-waveguide coupling dominates outside the stopband resulting in power transfer from the bus to the receiver resonator and a corresponding drop in the transmitted power.

### 4.3.4 Design Considerations

The $\mathrm{CL_{in}}$ and $\mathrm{CL_{out}}$ levels both place restrictions on the bandwidths of the first-order add-drop filters that can be designed using Bragg resonators in the configuration of Fig. (4-11). From eq. (4.69) we know that the 3 dB bandwidth, $\Delta\omega_{3dB}$ in the case that $\mu_{12} = \mu_{23} \equiv \mu$ is given by

$$\Delta\omega_{3dB} = \frac{4}{\tau_{e1}} = 8\kappa v_g \left(\frac{\mu}{\kappa}\right)^2 \tag{4.74}$$

Defining a quantity, $N_r$, which is the stopband of the grating expressed in terms of a multiple of 3-dB filter bandwidth

$$N_r \equiv \frac{2\kappa v_g}{\Delta\omega_{3dB}} \tag{4.75}$$

we find that

$$\left(\frac{\mu}{\kappa}\right)^2 = \frac{1}{4N_r} \tag{4.76}$$

As mentioned earlier adjacent channel cross-talk or isolation must be better than 25 dB to meet WDM system requirements. This imposes the condition that

$$10\log(\mathrm{CL_{in}}) \leq -25 \text{ dB} \tag{4.77}$$

Using the definition of $\mathrm{CL_{in}}$ given by eq. (4.72) we find that the above condition requires that

$$N_r \geq 80. \tag{4.78}$$

In other words the stopband must be at least 80 3-dB filter bandwidths wide if the crosstalk from the adjacent channels is to be less than 25 dB. For a given grating strength, $\kappa$, the above constraint places an upper bound on the maximum allowable 3-dB bandwidth for the first-order add/drop filter. The length, $L$, of the shorter arm of the receiver resonator in the add/drop filter is determined by the relationship

$$\frac{1}{\tau_l} = \frac{2}{\tau_{e1}} \quad \Longrightarrow \tag{4.79}$$

$$e^{-\kappa L} = \frac{1}{\sqrt{N_r}} \tag{4.80}$$

where we made use of eqs.(4.20) and (4.29). The above expression can be used to give

$$\mu L = \frac{1}{2\sqrt{N_r}} \ln(\sqrt{N_r}) \tag{4.81}$$

For $N_r \geq 80$ we find that $\mu L \leq 0.122$. Using the eq. (4.80) and insisting that the power leaking out the longer arm of the receiver resonator is at least 30 dB down we find in this case that the total length, $L_c \approx 4L$. Using this we determine the condition on the coupling level outside the stopband, $CL_{out}$:

$$CL_{out}^{(dB)} = 10 \log \left( \sin^2 4\mu L \right) \leq -6.5 \text{ dB} \tag{4.82}$$

The coupling level outside the stopband is at least -6.5 dB in the case that adjacent channel crosstalk within the stopband $CL_{in}$ at least -25 dB. Since, $CL_{out}$ limits the adjacent channel isolation, an immediate constraint imposed on first-order add/drop of this kind us that the adjacent WDM channels must all lie within the stopband of the grating.

### 4.3.5   $\kappa$ Considerations

As we saw above, for the channel isolation to be at least 25 dB or alternatively $|CL_{in}| \geq$ 25 dB, $N_r \geq 80$. Thus, to have a first-order filter with a reasonable size bandwidth the stopband must be large. This translates into a large grating strength $\kappa$. Ideally we prefer $\kappa$ to be large. However, there are two considerations. One is related to inherent difficulties in fabricating high $\kappa$ gratings. Gratings are made by etching a periodic structure on top a waveguide. High grating strength structures require deep etches. These etches are further complicated by the fact that the gratings are on top of tall waveguide structures. In addition to the difficulty of etching, another fabrication challenge which is equally daunting is overgrowing the top cladding material. Even the case of air-clad rib guides has its issues of polarization sensitivity and difficulty of making high $\kappa$ structures due to reduced mode overlap with the grating regions. Overgrowing over structures with a lot of relief is difficult and a poor growth can lead to high loss structures.

Even if fabrication challenges can be overcome, another limitation exists for high $\kappa$ structures. It is well known that finite length Bragg gratings couple to radiation modes. This coupling to radiation modes exists even for perfectly fabricated gratings and contributes to loss. Furthermore, this loss increases with $\kappa$. Thus high $\kappa$ gratings inherently have more radiation loss that can be limiting. Consequently, we must work with gratings that have moderate $\kappa$. The grating strength of all fabricated devices discussed in this dissertation was

chosen to be on the low side for ease of fabrication and was $\approx 60$ cm$^{-1}$. We follow up the topic of loss in gratings via radiation in chapter 6.4.1.

Consider the case of a first-order filter designed to have a 10 GHz 3-dB bandwidth and an chanel isolation of 25 dB. Using the minimum needed $N_r = 80$ and typical values for group velocity in InGaAsP/InP based material system eq. (4.75) yields that $\kappa = 270$ cm$^{-1}$. It is very difficult to fabricate a Bragg grating with this value for $\kappa$ without having excessive loss. Consequently we see that it is difficult to fabricate a first-order filter with a 10 GHz bandwidth and a channel isolation of 25 dB. A more realistic value of $\kappa$ that is achievable and has reasonably low loss is in the range of about 100-150 cm$^{-1}$.

### 4.3.6 $(\mu/\kappa)$ and $\mu$ Considerations

$(\mu/\kappa)$ effects two quantities; one is the 3-dB filter bandwidth and the other is the coupling level or channel isolation within the stopband. These relationships are expressed mathematically by eqs. (4.74) and (4.72). We see that a larger $(\mu/\kappa)$ results in a larger filter bandwidth but at the same time it worsens the channel isolation. For a given $\kappa$ there is a trade-off between the channel bandwidth and the adjacent channel isolation. If we assume a $\kappa$ of 150 cm$^{-1}$ and an adjacent channel isolation of 20 dB we find that the maximum 3-dB bandwidth of the filter is $\sim 18$ GHz.

Once the $(\mu/\kappa)$ ratio is chosen based on bandwidth and channel isolation considerations and $\kappa$ is known, the coupling coefficient, $\mu$ is determined. There is an upper bound on how large a value $\mu$ can realistically take; the limitation is fabrication related. $\mu$ depends exponentially on the separation between the two guides. The closer the guides the higher the $\mu$. This is evident by looking at the expression for $\mu$ given by eqs. (2.27) where the field overlap has an exponential dependence on separation between the guides. There is, however, a physical constraint that limits how close two waveguides can be fabricated without fusing them. This sets an upper bound on the $\mu$.

Another issue to consider is that when $\mu$ increases the simple coupling of mode equations described by eq. 2.31 and 2.31 are no longer valid. The first-order corrections represented by $\mathbf{M}_{1,2}$ as given by eq. (2.26) must be included. Inclusion of these terms in the modelling of Bragg gratings-based filters shows a deterioration of device performance. Finally, if $\mu$ gets too large the coupled mode equation formalism is not accurate as it is impossible to treat the presence of one guide as a perturbation to the dielectric distribution of the other

guide, [22].

### 4.3.7 $\Delta\beta$ Considerations

A first-order filter consists of a bus waveguide and two Bragg resonator guides. Associated with each guide is a propagation constant $\beta_i$ which is accounted for in CMT-space formalism via the parameter, $\delta_i = \beta_i - \beta_o$. In the calculation of spectra of all the devices considered thus far, it was assumed that the propagation constants in all the guides were equal. That is $\delta_i = \delta$ or alternately $\Delta\beta_{ij} \equiv \beta_i - \beta_j = 0$. The performance of these devices critically depends on $\Delta\beta_{ij}$. Fig. (4-19) shows a plot of the dropped channel spectrum in a first-order filter for increasing values of $\Delta\beta_{12} = \Delta\beta_{23} \equiv \Delta\beta$. We note that spectrum of the dropped channel is distorted as $\Delta\beta$ increases. Not only does the spectrum get asymmetrized but the peak power picked up at the dropped port decreases. This is because the coupling from the bus waveguide to the receiver resonators is reduced due to a propagation constant mismatch. Corresponding to the decrease in the dropped port power output is an increase in transmitted power (not shown in the figure). If however, the difference in the propagation constants between the bus and resonators is small relative to the grating strength, i.e $\Delta\beta/\kappa \leq 0.1$, the add/drop response is acceptable. Designing two identical waveguides to have the same propagation constant is a relatively straightforward task. The challenge in keeping $\Delta\beta$ small, however, lies in designing two dissimilar waveguides (the resonator and bus waveguides) to have similar propagation constants. The technique to achieve low $\Delta\beta$ in dissimilar waveguideas has been discussed at length in [45]. The technique, however, relies on knowing the refractive index of the core to a high degree of precision. What complicates the issue further is the fact that the core index is highly sensitive to the growth process. Moreover, there may even be variations in the core index across the wafer. Designing low $\Delta\beta$ devices in the absence of precise knowledge of the core index can limit the ability to make add/drop filter using side-coupled Bragg resonators. It may be necessary to have an active control mechanism which can "tune" the propagation constants into a synchronous regime. This could potentially be achieved by modifying the index of refraction of the waveguide core to get synchornous coupling between the bus and resonator waveguides. This tuning of the refractive index can be achieved by a variety of methods including current-induced index change [13, 46], field-induced refractive index change [47, 48] or by temperature-induced changes [49]. While this requirement makes the fabrication of these
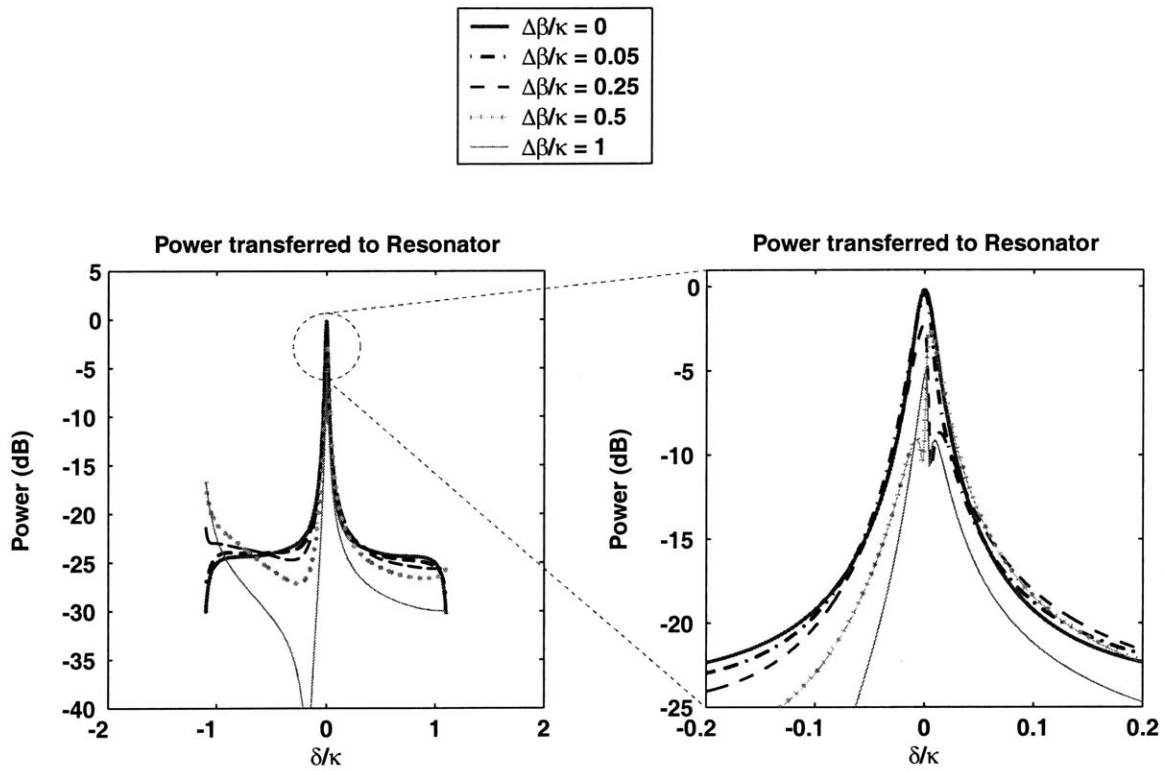
**Figure 4-19:** Effect of $\Delta\beta$ on the dropped power in a first-order add/drop filter for increasing $\Delta\beta/\kappa$ ratios. The spectrum is asymmetrized and the dropped power level drops.
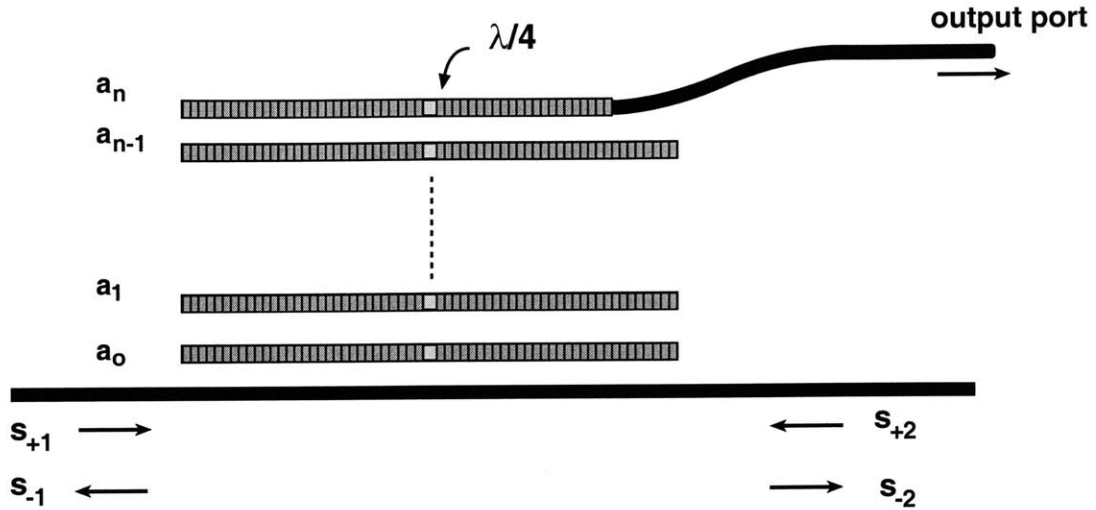
**Figure 4-20:** Side-coupled Bragg grating resonators in a "stack" configuration driven from an adjacent bus waveguide.

devices challenging, having a control mechanism to vary $\Delta\beta$ may provide an interesting way to switch the add/drop filters on or off by tuning the guides in and out of sync.

## 4.4   Higher-Order Side-Coupled Filters

In the previous section we saw how side-coupled Bragg resonators can be used to construct an Add/Drop filter capable of completely transferring power in a specific frequency range to the receiver resonator output port. We calculated the spectrum of the dropped channel port of this first-order system and saw that near resonance it had a lorentzian response. Lorentzians are characterized by rounded-tops and a $|1/\Delta\omega|^2$ power roll-off with frequency far from resonance. Yet further away from the resonance but within the stopband we saw that CMT-time no longer accurately models the spectrum of the add/drop filter. We rely on CMT-space which shows that the residual coupling within the stopband creates a floor, $CL_{in}$ which limits the channel isolation. Ideally we would like a filter response which has a flat pass-band and a fast roll-off with frequency such that adjacent channels are suppressed to the desired level. Moreover, we would like to design filters where the floor within the stopband drops does not limit channel isolation and has a functional dependence that it is a stronger function of $(\mu/\kappa)$. Likewise, a design which reduces $CL_{out}$ is also desireable.

Pass-band shape and widths considerations along with adjacent channel suppression requirements for the typical WDM channel spacings necessitate filters with roll-offs greater

than $|1/\Delta\omega|^2$. This cannot be achieved with first-order filters and we turn to higher-order multipole devices. In addition to faster roll-offs, higher-order filters offer the advantage of allowing spectral shaping in the passband to obtain Butterworth, Gaussian, Chebychev like responses. Furthermore, we will see that they also result in improved $CL_{in}$ and $CL_{out}$ levels.

From circuit theory we know that higher-order filters can be made by coupling together multiple energy storage elements. A Bragg resonator is such an energy storage element. Based on this intuition we speculate that higher-order filters must involve coupling together several resonators. In fact, we saw this earlier in section (3.4.4) where higher-order transmission filters were made by in-line "series" coupling of several resonators.

One way to make an $n^{th}$ order Add/Drop is to have $n$ adjacent DFB resonators which are evanescently coupled to one another with the last resonator side-coupled to a bus as shown in Fig. (4-20). The side-coupled configuration of resonators will be referred to as a "stack". Another approach is to cascade $n$ quarter-wave shifted resonators which are then side-coupled to the bus. The advantage which the "stack" configuration offers over the cascade is that it results in relatively compact devices. This is desirable, not only because it saves "real-estate" on the chip, but also because it leads to better out-of-band performance.

## 4.5   CMT-time description of Coupled Resonators

It is easy to generalize the CMT-time description of a single Bragg resonator to the case of the resonator stack system shown in Fig. 4-20. The only thing that needs to be accounted for in this case is the lossless coupling between adjacent resonators. Each of the $n+1$ resonators couples to it's immediate neighbors and this coupling is given by CMT-time parameter $\underline{\mu}_i$. $\underline{\mu}_i$ is closely related to the CMT-space coupling parameter $\mu_i$ and the relationship between them is derived in Appendix B. The arms of the first $n$ resonators are assumed long enough so that negligible power escapes from their ends. The last resonator, of course, has one shortened arm which acts as the output port of the device through which power can be
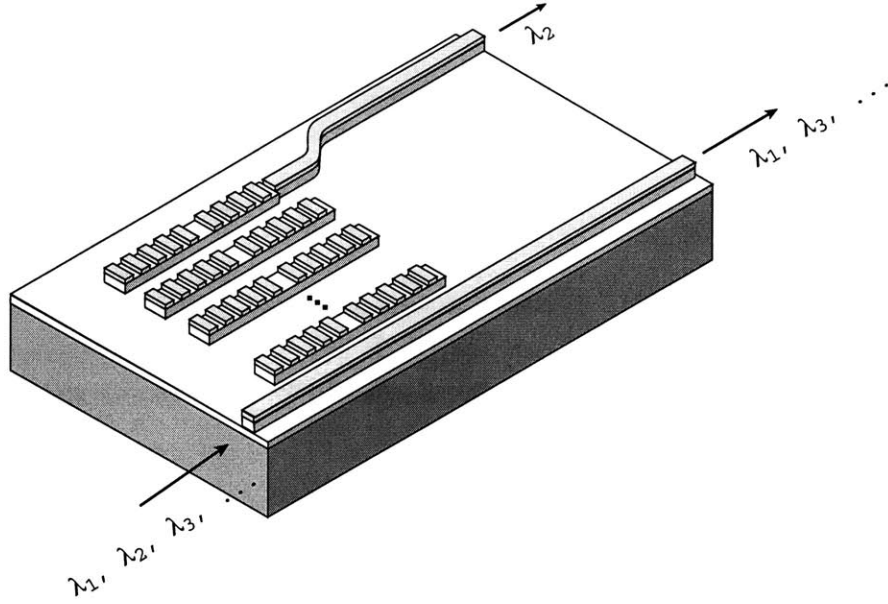
**Figure 4-21:** Side-coupled Bragg grating resonators in a "stack" configuration driven from an adjacent bus waveguide.

tapped-out. The coupled mode equations describing this system are:

$$
\begin{aligned}
\frac{da_n}{dt} &= j(\omega_n - \frac{1}{\tau_n})a_n + j\underline{\mu}_n a_{n-1} \\
\frac{da_{n-1}}{dt} &= j\omega_{n-1}a_{n-1} + j\underline{\mu}_n a_n + j\underline{\mu}_{n-1} a_{n-2} \\
&\vdots \\
\frac{da_1}{dt} &= j\omega_1 a_1 + j\underline{\mu}_2 a_2 + j\underline{\mu}_1 a_o \\
\frac{da_o}{dt} &= j(\omega_o - \frac{1}{\tau_e})a_o + j\underline{\mu}_1 a_1 + \underline{\kappa}(s_{+1} + s_{+2})
\end{aligned}
\tag{4.83}
$$

where $a_i$ is the mode amplitude of the $(i+1)^{st}$ resonator and is normalized such that $|a_i|^2$ is the energy in that mode. Notice that the decay terms are only associated with the first and last resonators. The first resonator can lose power to the input bus waveguide via coupling to the outgoing waves $s_{-1}$ and $s_{-2}$ with an associated $\frac{1}{\tau_e}$ decay rate; likewise the last resonator loses power via the shortened arm as expressed by the decay rate, $\frac{1}{\tau_n}$. All the other resonators are lossless. The source terms $\underline{\kappa}s_{+1}$ and $\underline{\kappa}s_{+2}$ describe the coupling of the first resonator to the bus, where $s_{+1}$ and $s_{+2}$ represent counter-propagating input waves on the bus. $s_{\pm i}$ is normalized such that $|s_{\pm i}|^2$ represents the power in the respective input or output waves. As we saw before

$$
\underline{\kappa} = \sqrt{\frac{1}{\tau_e}}
\tag{4.84}
$$

and that the reflected waves $s_{-2}$ and $s_{-1}$ are related to incoming waves by

$$s_{-1} = s_{+2} - \sqrt{\frac{1}{\tau_e}} a_o \tag{4.85}$$

$$s_{-2} = s_{+1} - \sqrt{\frac{1}{\tau_e}} a_o \tag{4.86}$$

The coupled mode equations, (4.83), can be solved quite readily for $a_o$. We find that

$$a_o = \frac{\underline{\kappa}(s_{+1} + s_{+2})}{j(\omega - \omega_o) + \frac{1}{\tau_e} + \cfrac{\mu_1^2}{j(\omega - \omega_1) + \cfrac{\mu_2^2}{j(\omega - \omega_2) + \cdots \cfrac{\mu_n^2}{j(\omega - \omega_n) + \frac{1}{\tau_n}}}}} \tag{4.87}$$

which may be rewritten in a more familiar continued fraction form as

$$a_o = \frac{\underline{\kappa}(s_{+1} + s_{+2})}{j(\omega - \omega_o) + \frac{1}{\tau_e} + \cfrac{1}{j\frac{(\omega - \omega_1)}{\mu_1^2} + \cfrac{1}{j\frac{(\omega - \omega_2)\mu_1^2}{\mu_2^2} + \cdots \cfrac{1}{\left(j(\omega - \omega_n) + \frac{1}{\tau_n}\right)\left[\frac{\mu_{n-1}^2}{\mu_n^2} \cdots \frac{\mu_4^2}{\mu_3^2} \frac{\mu_2^2}{\mu_1^2}\right]}}}} \tag{4.88}$$

for the case that $n$ is odd. When $n$ is even, we find that $a_o$ is given by

$$a_o = \frac{\underline{\kappa}(s_{+1} + s_{+2})}{j(\omega - \omega_o) + \frac{1}{\tau_e} + \cfrac{1}{j\frac{(\omega - \omega_1)}{\mu_1^2} + \cfrac{1}{j\frac{(\omega - \omega_2)\mu_1^2}{\mu_2^2} + \cdots \cfrac{1}{\left(j(\omega - \omega_n) + \frac{1}{\tau_n}\right)\left[\frac{\mu_{n-1}^2}{\mu_n^2} \cdots \frac{\mu_3^2}{\mu_4^2} \frac{\mu_1^2}{\mu_2^2}\right]}}}} \tag{4.89}$$

With the denominator denoted by $D$, $a_o$ is written concisely as

$$a_o \equiv \frac{\underline{\kappa}(s_{+1} + s_{+2})}{D} \tag{4.90}$$

From eqs. (4.85) and (4.86) one may derive the reflection and transmission coefficients, $\Gamma$ and $T$ respectively, for the case that the bus is fed only from one end, i.e $s_{+2} = 0$.

$$\Gamma \equiv \frac{s_{-1}}{s_{+1}} = -\frac{1}{D\tau_e} \tag{4.91}$$

$$T \equiv \frac{s_{-2}}{s_{+1}} = 1 - \frac{1}{D\tau_e} \tag{4.92}$$

Since the resonator stack is assumed lossless, the power tapped off the last resonator at the output port, $P_r$, is given by the difference of the input power and the reflected and transmitted powers on the bus, i.e

$$P_r = |s_{+1}|^2 - |s_{-1}|^2 - |s_{-2}|^2 = |s_{+1}|^2 \left\{ \left[ \frac{1}{D\tau_e} + \frac{1}{D^*\tau_e} \right] - \frac{2}{|D|^2\tau_e^2} \right\} \tag{4.93}$$
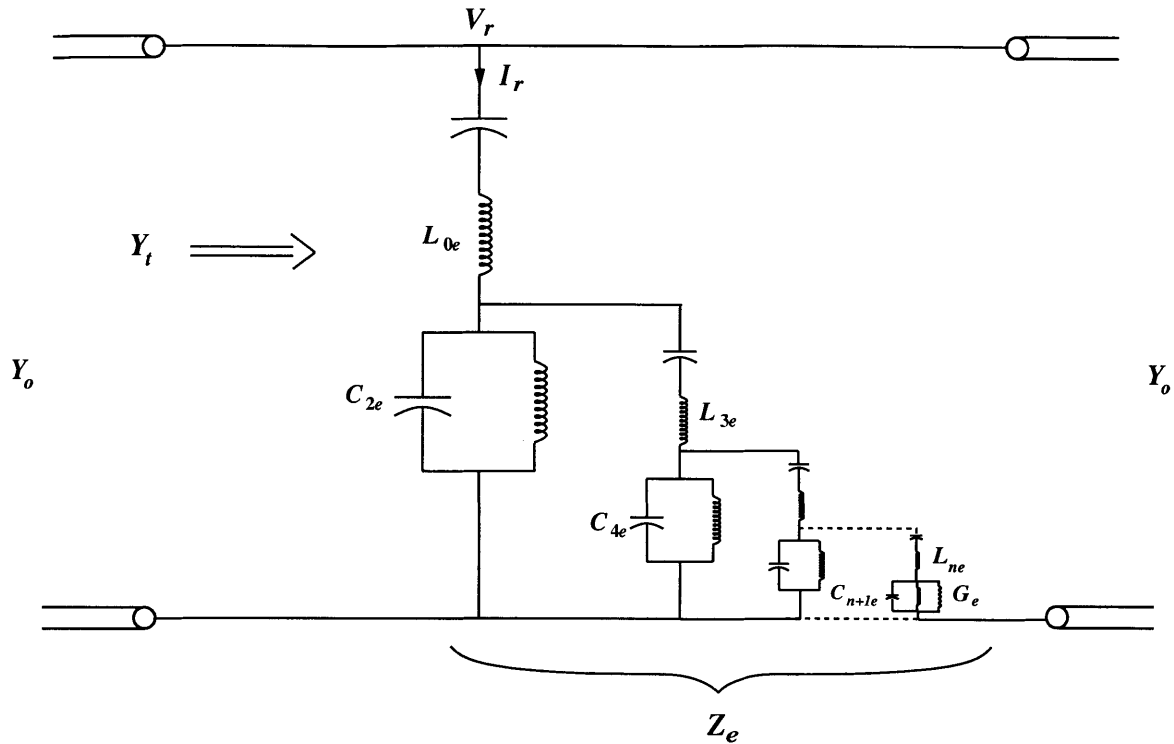
**Figure 4-22:** Equivalent circuit of the side-coupled resonators as viewed from the bus ports.

## 4.6    Equivalent Circuit of a Higher-Order Receiver Stack

Consider the circuit shown in Fig. (4-22). The impedance, $Z_e$, across the transmission line represents the net effect of the stacked resonators that is sensed across the signal waveguide. Near the resonance frequency, $\omega_o$, of the LC circuits $Z_e$ is given by

$$Z_e(\omega = \omega_o + \Delta\omega) = 2j\Delta\omega L_{0e} + \cfrac{1}{2j\Delta\omega C_{1e} + \cfrac{1}{2j\Delta\omega L_{2e} + \cdots \frac{1}{2j\Delta\omega L_{ne} + R_e}}} \qquad (4.94)$$

for the case that $n$ is even and by

$$Z_e(\omega = \omega_o + \Delta\omega) = 2j\Delta\omega L_{0e} + \cfrac{1}{2j\Delta\omega C_{1e} + \cfrac{1}{2j\Delta\omega L_{2e} + \cdots \frac{1}{2j\Delta\omega C_{ne} + G_e}}} \qquad (4.95)$$

for the case that $n$ is odd. This choice of the circuit thus leads to $Z_e$ having the form of a continued fraction. To be specific, henceforth we will write down expressions for the case that $n$ is odd, (i.e even number of resonators). The corresponding results when $n$ is even are easily derivable.

The reflection and transmission coefficients are computed by using standard transmission line theory. $Y_t$ represents the total admittance as seen looking into the transmission line

(see Fig. (4-22) and is given by

$$Y_t = Y_o + \frac{1}{Z_e}$$

The reflection coefficient, $\Gamma$, is given by

$$\Gamma = \frac{Y_o - Y_t}{Y_o + Y_t} = -\frac{1}{1 + 2Y_oZ_e} \tag{4.96}$$

$$\tag{4.97}$$

The transmission coefficient, $T$, is given by

$$T = 1 + \Gamma = 1 - \frac{1}{1 + 2Y_oZ_e} \tag{4.98}$$

$$\tag{4.99}$$

Comparing the above expressions with equations (4.91) and (4.92), we see that the equations are similar in form provided we draw the following correspondence

$$D\tau_e \longleftrightarrow 1 + 2Y_oZ_e \tag{4.100}$$

Therefore, for equivalence between these expressions, the forms of $D\tau_e$ and $1 + 2Y_oZ_e$ must be the same. Note that

$$1 + 2Y_oZ_e = 1 + 4j\Delta\omega L_{0e}Y_o + \cfrac{1}{j\Delta\omega \frac{C_{1e}}{Y_o} + \cfrac{1}{4j\Delta\omega L_{2e}Y_o + \cdots \cfrac{1}{j\Delta\omega \frac{C_{ne}}{Y_o} + \frac{G_e}{2Y_o}}}} \tag{4.101}$$

has a continued fraction form identical to $D\tau_e$ which is given by

$$D\tau_e = 1 + j(\omega - \omega_o)\tau_e + \cfrac{1}{\frac{j(\omega-\omega_1)}{\mu_1^2\tau_e} + \cfrac{1}{j(\omega-\omega_2)\frac{\mu_1^2\tau_e}{\mu_2^2} + \cdots \cfrac{1}{\left(j(\omega-\omega_n)+\frac{1}{\tau_n}\right)\left[\frac{\mu_{n-1}^2}{\mu_n^2}\cdots\frac{\mu_4^2}{\mu_3^2}\frac{\mu_2^2}{\mu_1^2}\frac{1}{\tau_e}\right]}}} \tag{4.102}$$

provided $\omega_i = \omega_o$, i.e all the Bragg resonators have the same resonance frequency. This is assured if the resonators have the same grating periodicity and phase shifts. In fact there is a term by term correspondence between these two expressions which provides the mapping

between the circuit and the optical resonator parameters.

$$4L_{0e}Y_o \quad \longleftrightarrow \quad \tau_e \tag{4.103}$$

$$\frac{C_{1e}}{Y_o} \quad \longleftrightarrow \quad \frac{1}{\underline{\mu}_1^2 \tau_e} \tag{4.104}$$

$$4L_{2e}Y_o \quad \longleftrightarrow \quad \frac{\underline{\mu}_1^2 \tau_e}{\underline{\mu}_2^2} \tag{4.105}$$

$$\frac{C_{3e}}{Y_o} \quad \longleftrightarrow \quad \frac{\underline{\mu}_2^2}{\underline{\mu}_3^2 \underline{\mu}_1^2 \tau_e} \tag{4.106}$$

$$\vdots$$

$$\frac{G_e}{2Y_o} \quad \longleftrightarrow \quad \left[ \frac{\underline{\mu}_{n-1}^2}{\underline{\mu}_n^2} \cdots \frac{\underline{\mu}_4^2}{\underline{\mu}_3^2} \frac{\underline{\mu}_2^2}{\underline{\mu}_1^2} \frac{1}{\tau_e} \right] \frac{1}{\tau_n} \tag{4.107}$$

which can be rewritten in a simple way as

$$\tau_e \quad \longleftrightarrow \quad 4L_{0e}Y_o \tag{4.108}$$

$$\underline{\mu}_1^2 \quad \longleftrightarrow \quad \frac{1}{2\sqrt{L_{0e}C_{1e}}} \tag{4.109}$$

$$\underline{\mu}_2^2 \quad \longleftrightarrow \quad \frac{1}{2\sqrt{L_{2e}C_{1e}}} \tag{4.110}$$

$$\underline{\mu}_3^2 \quad \longleftrightarrow \quad \frac{1}{2\sqrt{L_{2e}C_{3e}}} \tag{4.111}$$

$$\vdots$$

$$\tau_n \quad \longleftrightarrow \quad \frac{2C_{ne}}{G_e} \tag{4.112}$$

This proves that the circuit shown in Fig. (4-22) is indeed the equivalent circuit of the coupled resonator system as viewed from the signal bus. The power loss in the conductance $G_e$, $P_{G_e}$, represents the loss in the output port of the resonator stack or in other words the received power, $P_r$.

If the structure is excited by an incident wave from the left then part of the power is transmitted into the output transmission line of the equivalent circuit of Fig. 4-22, and part is reflected back. The maximum power that can be transferred to the load $G_e$ at resonance, when all resonators are chosen to have the same frequency, $\omega_k = \omega_o$ for $k = 1, 2, ...n$, is half the incident power. This occurs when $G_e$ is adjusted to be equal to $2Y_o$ and follows from standard transmission line theory. The same result can be obtained from eqs. (4.85) and (4.86) using eq. (4.90), and assuming that the outgoing signal bus is matched, i.e $s_{+2} = 0$. Maximation of the received power, $|s_{+1}|^2 - |s_{-1}|^2 - |s_{-2}|^2$, on resonance with respect to $\frac{1}{D\tau_e}$
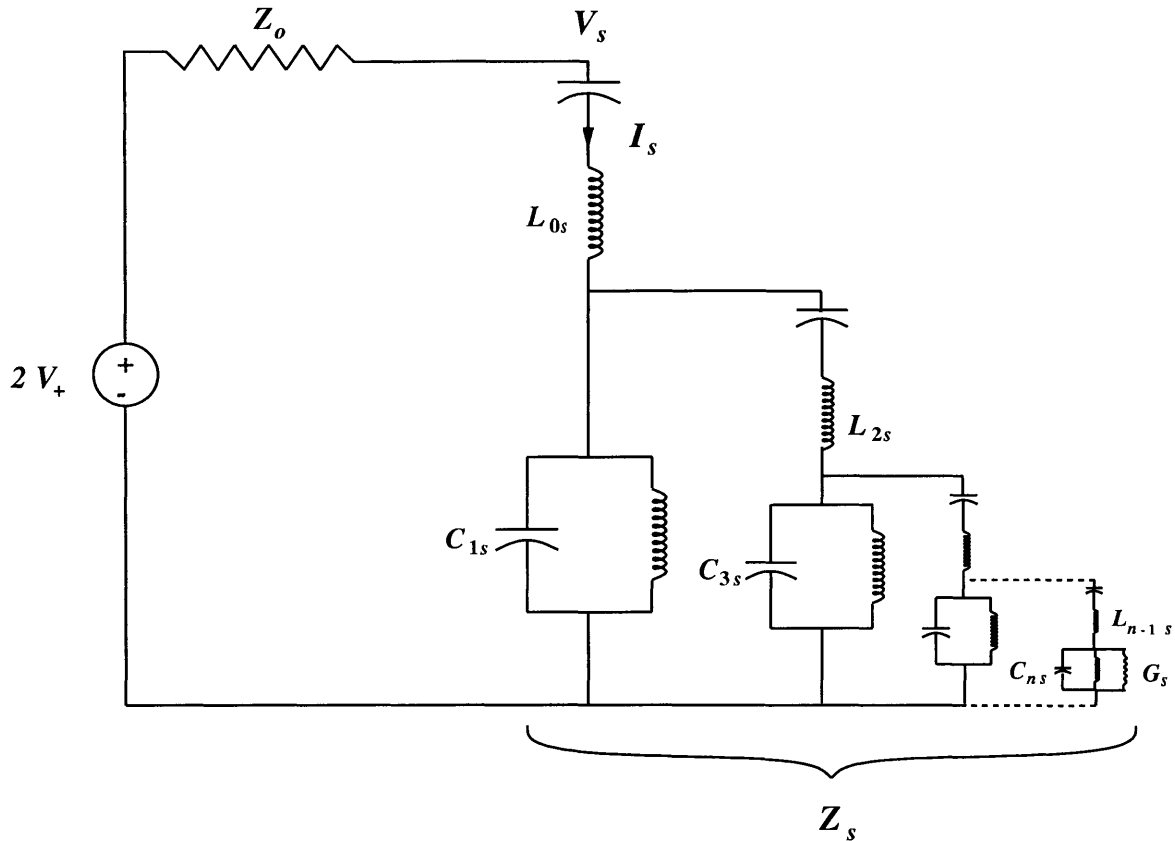
Figure 4-23: A standard LC ladder circuit.

gives $\frac{1}{D\tau_e} = \frac{1}{2}$. In this case one finds that $|s_{-1}|^2 = |s_{-2}|^2 = \frac{1}{4}$ for $\omega = \omega_o$; a quarter of the incident power is transmitted along the signal bus and a quarter is reflected on resonance.

## 4.7 Relating to a standard LC ladder circuit

The purpose of deriving the equivalent circuit of the stacked resonator system is to facilitate filter design by utilizing the extensive work already done on LC ladder circuits [50, 52, 53]. However, the circuit of Fig. 4-22 does not have a standard LC ladder configuration. Fig. 4-23 shows a "standard" LC ladder circuit for which tables are readily available that allow specific spectral responses to be designed for power dissipated in the load, $G_s$.

The approach followed is to relate the equivalent circuit of Fig. 4-22 to the standard LC ladder of Fig. 4-23. Thereby we will obtain a mapping which relates the tabulated inductance and capacitance values of the standard circuit to the impedance values of the equivalent circuit of the resonator stack. Since we will be referring repeatedly to the two

circuits we label the equivalent circuit of the coupled resonator system (Fig. 4-22) as circuit (A) and the standard ladder circuit (Fig. 4-23) as circuit (B).

Circuits (A) and (B) have different configurations and it is, therefore, not possible to draw a strict equivalence between the voltages and currents at all the ports in the two circuits. However, as we shall see, there is a correspondence between the power, $P_{G_s}$, dissipated in $G_s$, (circuit (B)) and the power, $P_{G_e}$, dissipated in $G_e$, (circuit (A)). Since we are interested in designing for a specific received power, $P_r$ or equivalently $P_{G_e}$, relating $P_{G_s}$ and $P_{G_e}$ will be sufficient for our purpose.

The power dissipated in $G_e$ is simply given by (see Fig. 4-22)

$$P_{G_e} = \frac{1}{2}\Re e\{V_r I_r^*\}$$

where

$$
\begin{aligned}
V_r &= \frac{\frac{1}{(Y_o+\frac{1}{Z_e})}}{Z_o + \frac{1}{(Y_o+\frac{1}{Z_e})}} 2V_+ \\
&= 2V_+ \frac{Z_e Y_o}{1 + 2Y_o Z_e} \\
I_r &= \frac{V_r}{Z_e}
\end{aligned}
$$

Thus,

$$P_{G_e} = \frac{1}{2}\left|2V_+ \frac{Z_e Y_o}{1 + 2Y_o Z_e}\right|^2 \frac{1}{2}\left\{\frac{1}{Z_e} + \frac{1}{Z_e^*}\right\}$$

which can be rewritten as

$$P_{G_e} = \frac{1}{2}|V_+|^2 Y_o \left\{\frac{1}{1 + 2Y_o Z_e} + \frac{1}{1 + 2Y_o Z_e^*} - \frac{2}{|1 + 2Y_o Z_e|^2}\right\} \tag{4.113}$$

Compare with eq. (4.93). Again eq. (4.100) follows.

Consider now Fig. 4-23 which shows circuit (B). $Z_s$ denotes the impedance of the LC ladder which is driven by the same source as circuit (A). Near resonance, $Z_s$ is given by

$$Z_s = 2j\Delta\omega L_{0s} + \cfrac{1}{2j\Delta\omega C_{1s} + \cfrac{1}{2j\Delta\omega L_{2s}+\cdots\frac{1}{2j\Delta\omega C_{ns}+G_s}}}$$

The power dissipated in the load conductance, $G_s$, $P_{G_s}$, is given by

$$P_{G_s} = \frac{1}{2}\Re e\{V_s I_s^*\}$$

where

$$
\begin{aligned}
V_s &= \frac{Z_s}{Z_o + Z_s} 2V_+ \\
I_s &= \frac{V_s}{Z_s}
\end{aligned}
$$
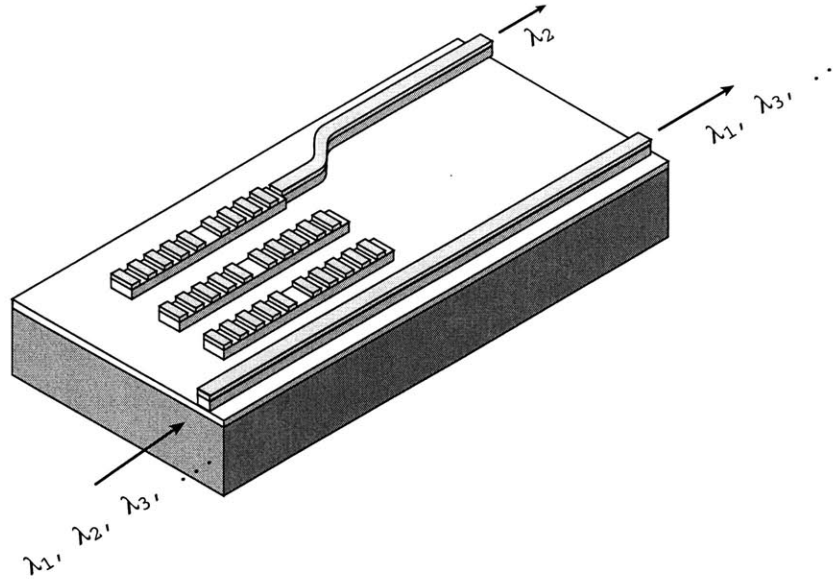
**Figure 4-24:** A third-order receiver stack.

Using the above, we find that

$$P_{G_s} = \frac{1}{2} \left| \frac{Z_s}{Z_o + Z_s} 2V_+ \right|^2 \frac{1}{2} \left\{ \frac{1}{Z_s} + \frac{1}{Z_s^*} \right\}$$

which can be rewritten as

$$P_{G_s} = |V_+|^2 Y_o \left\{ \frac{1}{1 + Y_o Z_s} + \frac{1}{1 + Y_o Z_s^*} - \frac{2}{|1 + Y_o Z_s|^2} \right\} \tag{4.114}$$

We see that $P_{G_s}$ of eq. (4.114) is equal to $P_{G_e}$ of eq. (4.113) if we make the following correspondence

$$Z_s \longleftrightarrow 2Z_e \tag{4.115}$$

In other words, the powers dissipated in the load conductances of circuits (A) and (B) are related through an impedance scaling.

## 4.8 Designing Higher Order Filters

Consider the three coupled resonator system shown in Fig. (4-24). The equivalent circuit of this system is shown in Fig. 4-25. Let us assume we wish to design the system such that the power tapped of the second resonator, $P_r$, has a Butterworth spectral response. As shown in the previous section designing for a specific $P_r$ is equivalent to choosing the appropriate L, C values to obtain the desired response for $P_{G_e}$. The equivalence between $P_{G_e}$ and the
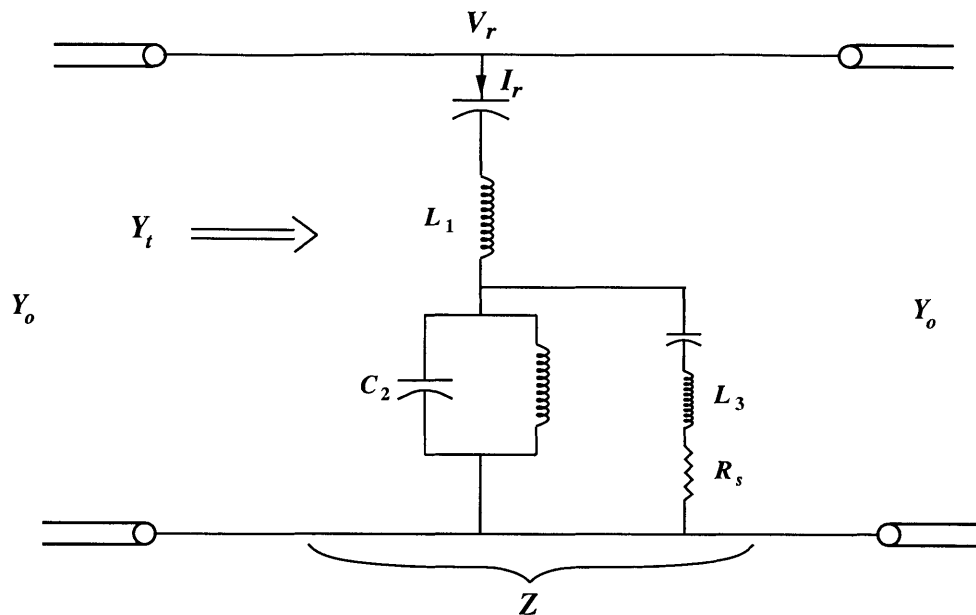
**Figure 4-25:** A third-order receiver stack.

power dissipated in the load termination of a standard LC ladder circuit (Fig. 4-23), $P_{G_s}$, allows us to use circuit (B) along with eq. (4.115) to design for $P_{G_e}$. For a Butterworth response, we know that the normalized values ($Y_o = 1$) of the inductance and capacitance of the standard circuit are

$$L_{0s} \;=\; 1 \quad \Longrightarrow \quad L_{0e} \;=\; \frac{L_{0s}}{2} \;=\; \frac{1}{2} \tag{4.116}$$

$$C_{1s} \;=\; 2 \quad \Longrightarrow \quad C_{1e} \;=\; 2C_{1s} \;=\; 4 \tag{4.117}$$

$$L_{2s} \;=\; 1 \quad \Longrightarrow \quad L_{0e} \;=\; \frac{L_{0s}}{2} \;=\; \frac{1}{2} \tag{4.118}$$

$$R_s \;=\; 1 \quad \Longrightarrow \quad R_e \;=\; \frac{R_s}{2} \;=\; \frac{1}{2} \tag{4.119}$$

where we have used the correspondence of eq. (4.115) to get the values for $L_e$ and $C_e$ from the standard ladder circuit values. Using the correspondence, $D\tau_e \longleftrightarrow 1 + 2Y_o Z_e$ (for the case when $n$ is even) we can relate the circuit parameters to the CMT-time coupling and decay parameters:

$$\tau_e \;\longleftrightarrow\; 4L_{0e}Y_o \tag{4.120}$$

$$\underline{\mu}_1^2 \;\longleftrightarrow\; \frac{1}{2\sqrt{L_{0e}C_{1e}}} \tag{4.121}$$

$$\underline{\mu}_2^2 \;\longleftrightarrow\; \frac{1}{2\sqrt{L_{2e}C_{1e}}} \tag{4.122}$$

$$\tau_2 \;\longleftrightarrow\; \frac{2L_{2e}}{R_e} \tag{4.123}$$

**Received Power in the output Bragg Resonator**

**Transmitted Power in Waveguide**

**Reflected Power in Waveguide**
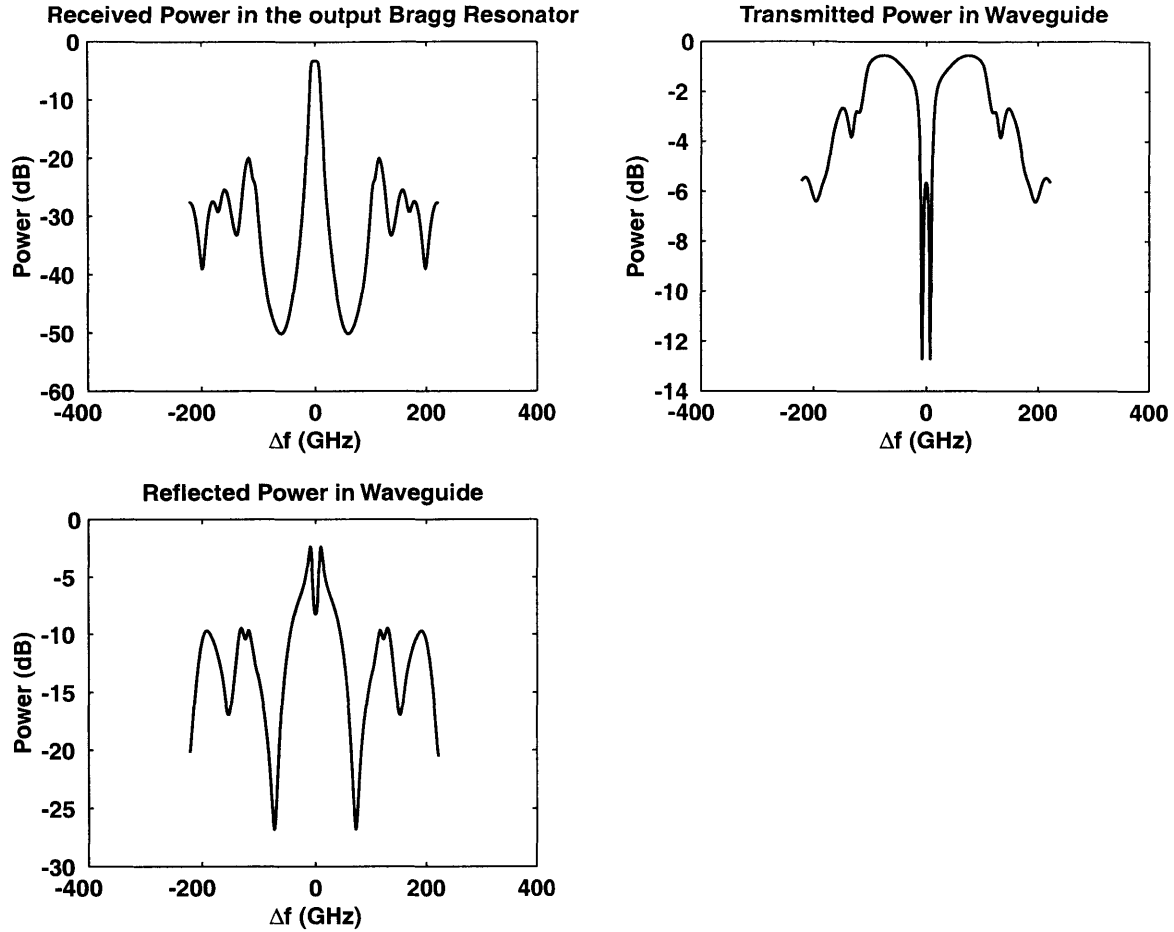
**Figure 4-26:** Spectrum of the third-order receiver stack designed to yield a Butterworth response. Only half the power is transferred on resonance; a quarter is transmitted and a quarter reflected on the bus waveguide.

In turn, $\tau_i$ and $\underline{\mu}_i$ are be related to the the CMT-space parameters. From the earlier sections we know that

$$\frac{1}{\tau_e} = 2\kappa v_g \left|\frac{\mu_{12}}{\kappa}\right|^2$$

$$\frac{1}{\tau_2} = \kappa v_g e^{-2\kappa L_{g2}}$$

Moreover,

$$\underline{\mu}_i = \mu_{\{i,i+1\}} v_g \tag{4.124}$$

It is shown in Appendix B that the CMT-time coupling parameter $\underline{\mu}_i$ is related to the CMT-space coupling parameter $\mu_{i,i+1}$ through a scale factor $v_g$, which is the group velocity of the Bragg resonator guides. CMT-space parameters are directly related to the physical

dimensions of the grating resonators and the spacing between them [44, 20]. Thus the equivalent circuit approach allows us to design for specific spectral pass-bands by looking up standard filter design tables and then translating these into physical dimensions via the correspondence above. Figure (4-26) shows the spectral response of a third-order receiver stack shown in Fig. (4-24) designed using the method detailed above. The device parameters were chosen to yield a maximally flat Butterworth response with a 3 dB bandwidth of 15 GHz. Notice that the adjacent channel cross-talk is always less that 20 dB. It is interesting to compare this to the response of a first-order filter. We saw in section 4.3.3 that a 18 GHz filter with a 20 dB channel isolation required a $\kappa = 150$ cm$^{-1}$. Morevoer, the channel isolation of 20 dB was limited to within the stopband. This higher-order filter was designed using a grating strength of $\kappa = 60$ cm$^{-1}$. Moreover the channel isolation is always better than 20 dB - both within and outside the stopband. The stopband corresponding to a $\kappa = 60$ cm$^{-1}$ is about 170 GHz. Thus we see that for a given $\kappa$ value, higher-order devices have broader and flatter passband widths, faster roll-off and better CL$_{\text{in}}$ and CL$_{\text{out}}$ levels. Higher-order filters if designed appropriately are not constrained within the stopband of the gratings. This is a tremendous advantage over first-order filters.

The filter of Fig. (4-24) would have been suitable for a WDM system with a channel spacing of 50 GHz. However, since there is incomplete power transfer to the top receiver resonator some of the dropped channel power continues down the waveguide bus. This is evident in the transmission spectrum where the dropped channel power is only suppressed by 6 dB on resonance. This, of course is unacceptable in WDM systems. The dropped channel must be suppressed in excess of 20 dB in the bus waveguide. As explained earlier we can never transfer more than half of the incident power to the output port using a a single side-coupled standing-wave resonator. A quarter of the power is reflected and a quarter is transmitted on the signal waveguide.

The difference between the equivalent circuit of the stack and the standard LC circuit suggests how we can attempt to create a system capable of complete power transfer. In the standard LC ladder we know that is possible to transfer all the incident power, on resonance, to the load $G_s$. The difference between two circuits is the section of the transmission line on the right hand side of Fig. 4-22 (compare with Fig. 4-23). On resonance, this section appears as a conductance $Y_o$ in parallel with the load conductance, $G_e$, splitting the incoming power. Some of the power is dissipated in $G_e$ and appears as the useful received
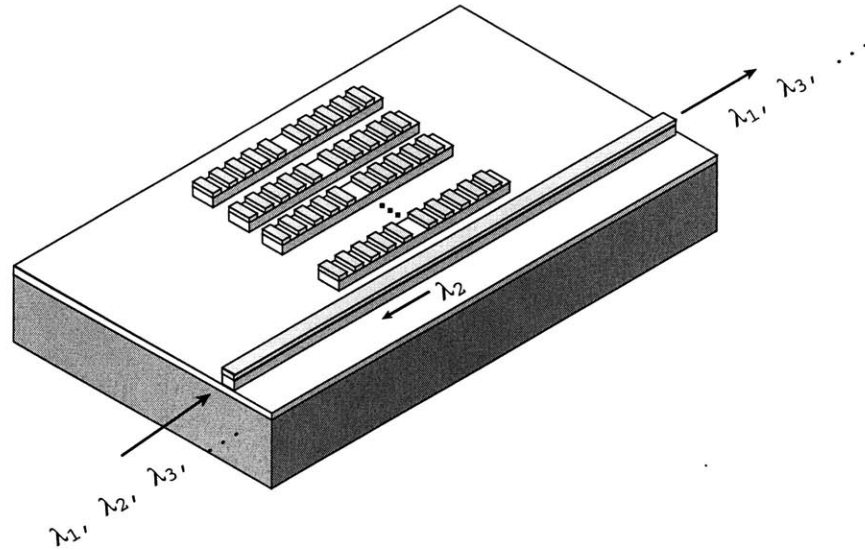
**Figure 4-27:** Higher-order reflector made by using closed Bragg resonators in a stack configuration.

power while some is "dissipated" in $Y_o$ and corresponds to the transmitted power on the bus. If we could transform the system to "eliminate" this section we would potentially achieve full power transfer. One way to achieve this is to present an open circuit at the transmission line terminals on the right. This occurs if the resonator stack is followed by a reflector. Ideally, this reflector should provide positive unity reflection over the channel bandwidth and zero outside of the band. In this case the equivalent circuit of the stacked resonators transforms into the standard LC circuit for which we know the inductance and capacitance values needed for complete power transfer. In the next section we look at how we may design Bragg reflectors appropriate for this purpose.

## 4.9   Higher-Order Bragg Reflectors

In the previous section we saw that a reflector is needed for complete power transfer to the receiver port. A single pole reflector may be realized by a closed resonator (quarter-wave shifted resonator made of long gratings) coupled to a signal guide [43]. At resonance, all of the incident wave is reflected. For higher-order filters it is obvious that we need higher order reflectors. This is because we desire that only the signal within the channel bandwidth be reflected. Generalizing to the case of a single pole reflector, for a higher order reflector we use a system of side-coupled closed resonators evanescently coupled to the signal bus. A natural choice is the stack configuration shown in Fig. (4-27). This system looks very
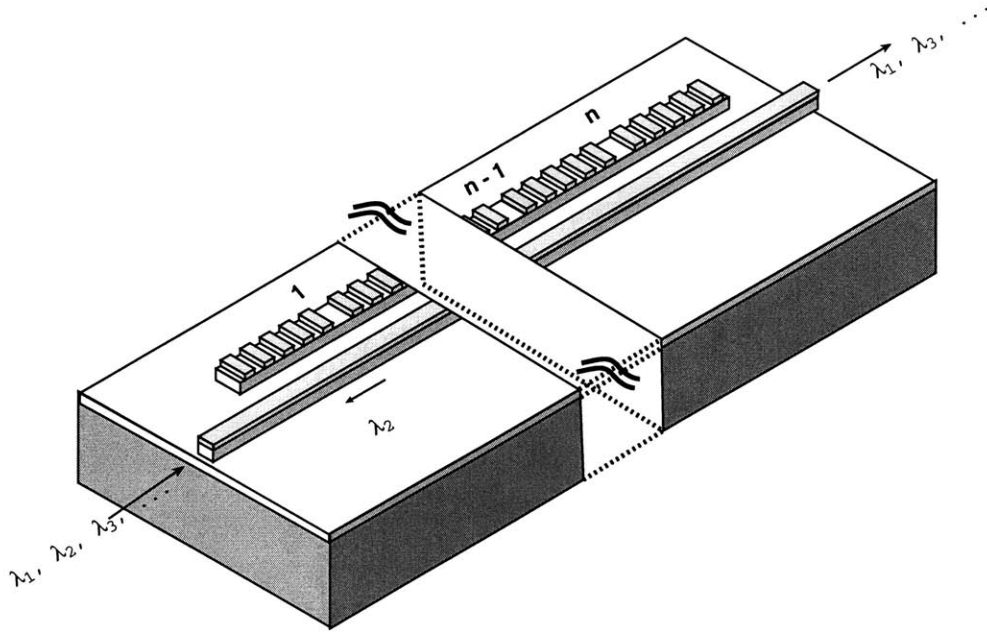
**Figure 4-28:** Higher-order reflector made by using $n$ inline closed Bragg resonators side-coupled to a bus waveguide.

much like the higher-order receiver stack shown in Fig. (4-20). However, unlike the stacked receiver, the last resonator of the reflector stack does not have a truncated Bragg resonator arm. We can use the formalism derived earlier to determine the spectral response of the stacked reflector if we utilize the fact that $\frac{1}{\tau_n} = 0$. From (4.91), using (4.87) we find that the reflection coefficient, $\Gamma$ is given by

$$\Gamma \equiv \frac{s_{-1}}{s_{+1}} = -\frac{1}{D\tau_e}$$

$$\Gamma = \frac{-1}{1 + j(\omega - \omega_o)\tau_e + \cfrac{\mu_1^2\tau_e}{j(\omega-\omega_1)+\cfrac{\mu_2^2}{j(\omega-\omega_2)+\cdots\cfrac{\mu_n^2}{j(\omega-\omega_n)}}}} \qquad (4.125)$$

Note the above expression has zeros (as well as poles). Thus, there are certain input frequencies at which there are no reflections. In fact for a system with an even number of resonators, there is a zero at the Bragg wavelength. To be specific consider the case of two resonators coupled to a bus. In this case the reflection coefficient is given by

$$\Gamma = \frac{-j(\omega - \omega_o)}{j(\omega - \omega_o)\left[1 + j(\omega - \omega_o)\tau_e\right] + \underline{\mu}_1^2\tau_e} \qquad (4.126)$$

The zero at the Bragg wavelength or $\omega = \omega_o$ is obvious. In fact it can be shown that for the stacked configuration of Fig. (4-20) with $n$ resonators, the reflected response has $n-1$ zeros
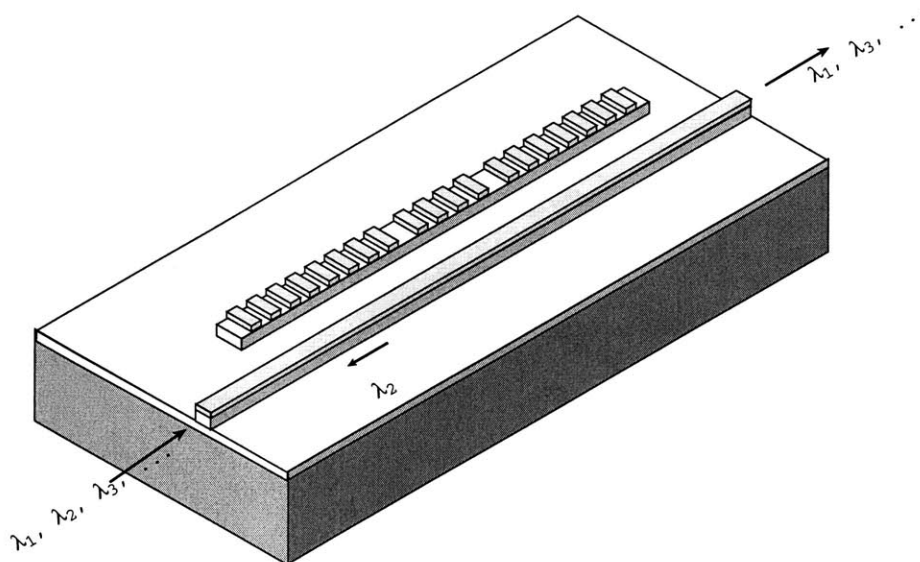
**Figure 4-29:** Higher-order reflector made by using in-line closed Bragg resonators side-coupled to a bus waveguide.

and $n$ poles. Moreover, the zeros lie within the outermost poles and thus it is not possible to obtain a constant strong reflection over any sizeable bandwidth. Furthermore, the roll off of the reflected signal with frequency is decreased due to the presence of the zeros. As a result, contrary to what might have been expected, the stack configuration of Fig. (4-27) is not an appropriate choice for a higher order reflector.

An alternative scheme to obtain a higher order reflector is shown in Fig. (4-28). It employs in-line closed higher-order resonators side-coupled to a bus waveguide. The idea is that the spectral response of the resonators can be designed by using the coupling techniques of section (3.4.4). By keeping the outermost resonator arms long, the total system is closed and can only couple power to the adjacent waveguide. As in the case of a single closed resonator coupled to a waveguide, we expect reflection at and around the resonance. This idea is applied to the case of the case of two resonators as shown in Fig. (4-29). The spectrum of the device is shown in Fig. (4-30). Note the reflected signal is constant over a reasonable bandwidth. The response is a Butterworth. A more compact device which also yields a Butterworth response for the reflected signal on the bus is shown in Fig. (4-31). It consists of two DFB resonators, separated by a quarter-wave shift and placed on opposite sides of the signal bus. Although this reflector does not have the ideal reflector response (positive unity with no phase change), the magnitude of the reflection is constant over the
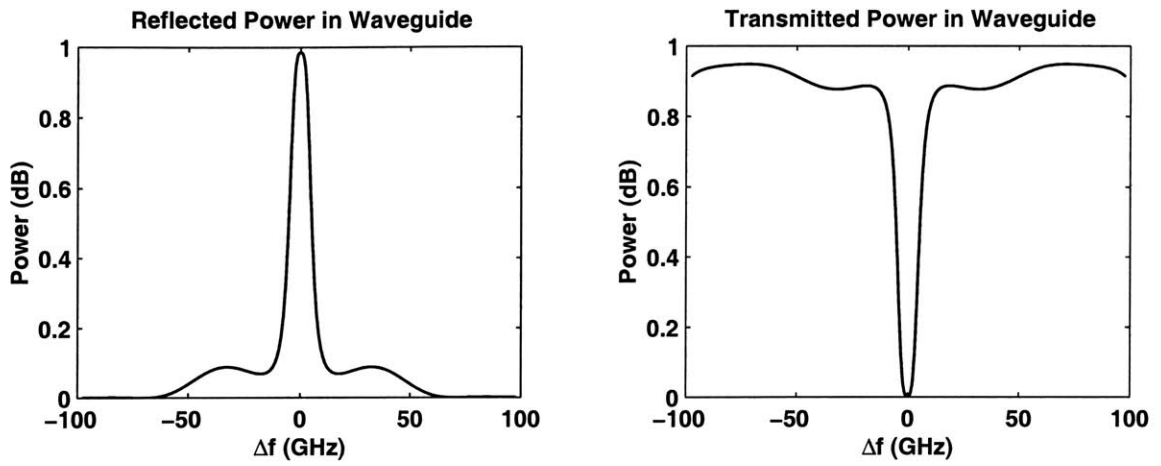
**Figure 4-30:** Spectrum of a second-order reflector of Fig. (4-29).
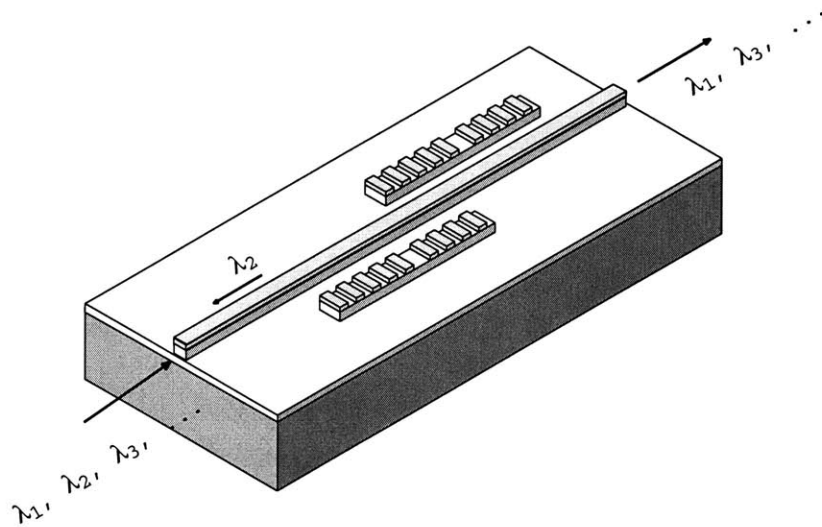


**Figure 4-31:** Second-order reflector made by side-coupling closed Bragg resonators on opposite sides of a bus waveguide.
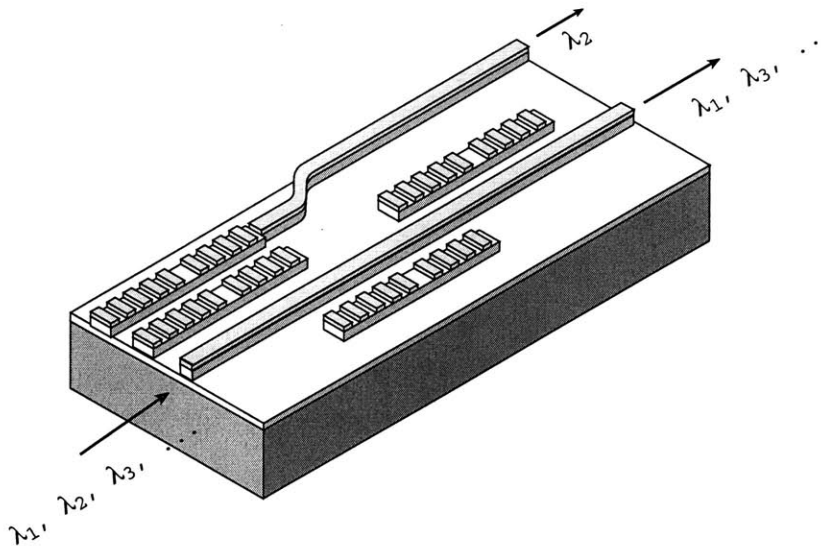
**Figure 4-32:** Higher-order reflector made by using inline closed Bragg resonators side-coupled to a bus waveguide.

channel bandwidth. It may be used as a first approximation to the ideal reflector.

Consider a stacked resonator system followed by the reflector of Fig. (4-31), as shown in Fig. (4-32). This system is designed to yield a second-order Butterworth response at the receiver port assuming that it is followed by an ideal reflector. The equivalent circuit for such an ideal system is the standard LC ladder circuit. Figure (4-33) shows the spectrum of this device when it is excited from the bus. First of all note that it is possible to transfer nearly all of the power to the receiver. This is different from the receiver stack where the best we can do is half the incident power. Thus our intuition of using a reflector following the receiver stack and changing the design parameter to yield complete power transfer is shown to be true. Moreover, the shape of the received signal is nearly maximally flat near the resonance (as in a Butterworth) is fairly constant before it falls off. The deviation of the received response from a Butterworth is due to the fact that phase of the actual reflector used varies across the channel. Even so we note that the receiver port response is very flat and falls off sharply with frequency. This filter has a 3dB bandwidth of about 6 GHz and 30 dB bandwidth of 20 GHz.

**Received Power in Receiver Resonator**

**Transmitted Power in Waveguide**

**Reflected Power in Waveguide**
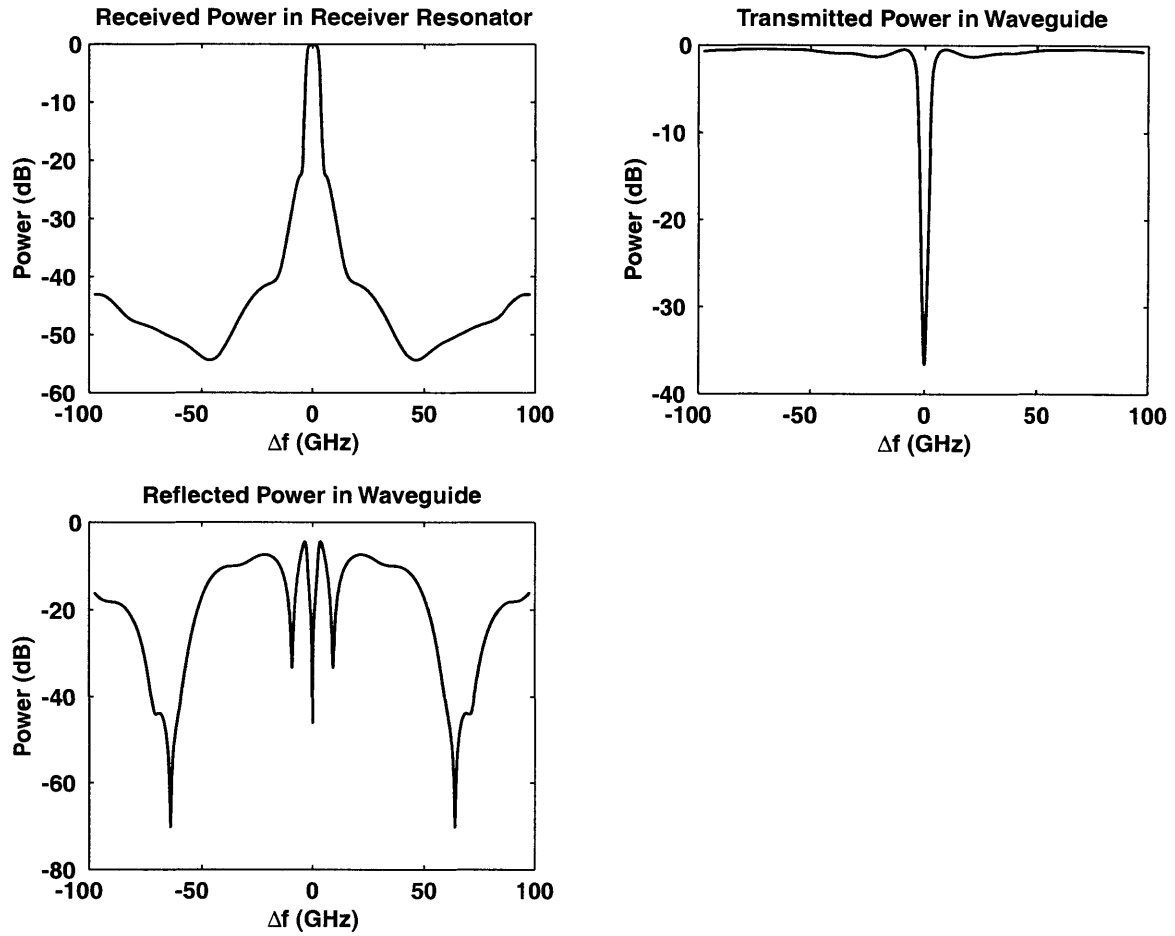
**Figure 4-33:** Spectrum of a second-order filter capable of complete power transfer.

## 4.10  Appendix

### 4.10.1  Coupling of Resonator to Bus

In the subsequent discussion we shall treat the coupling of a single resonator to an adjacent waveguide. Using perturbation theory, coupling to the other resonators can be introduced later. The resonator mode $a_o$ is excited by incident waves $s_{+1}$ and $s_{+2}$ in the bus:

$$\frac{da_o}{dt} = j\omega_o a_o - \frac{1}{\tau_e}a_o + \underline{\kappa}\,(s_{+1} + s_{+2}) \tag{4.127}$$

$|a_o|^2$ is normalized to be equal to the energy in the resonator. First we consider the case of initial excitation of the resonator which looses power via $s_{-1}$ and $s_{-2}$. Clearly the energy decay rate is $2/\tau_e$. The amplitudes of the outgoing waves can be found from energy consideration:

$$|s_{-1}|^2 + |s_{-2}|^2 = \frac{2|a_o|^2}{\tau_e} \tag{4.128}$$

where $s_{-1}$ and $s_{-2}$ have been normalized so that their absolute squares are equal to the power carried by these waves. Since the two waves have equal amplitudes by symmetry we find

$$|s_{-1}|^2 = |s_{-2}|^2 = \frac{|a_o|^2}{\tau_e} \tag{4.129}$$

Next consider the time reversed situation. The outgoing waves become the incoming waves, $s_{+1}$ and $s_{+2}$, and the amplitude $a_o$ grows at the rate of $1/\tau_e$. From eq. (4.127) we have that

$$a_o = \frac{\underline{\kappa}(s_{+1} + s_{+2})}{j(\omega - \omega_o) + \frac{1}{\tau_e}}. \tag{4.130}$$

Moreover, since

$$j(\omega - \omega_o) = \frac{1}{\tau_e} \tag{4.131}$$

we have

$$|a_o| = \left| \frac{2\kappa s_{+1}}{\frac{2}{\tau_e}} \right| \tag{4.132}$$

In the time reversed situation the incoming waves have the same magnitude as the outgoing waves in the original decay process and thus

$$|s_{+1}| = |s_{+2}| = \sqrt{\frac{1}{\tau_e}}|a_o| \tag{4.133}$$

Using eqs. (4.132) and (4.133) we find that

$$\underline{\kappa} = \sqrt{\frac{1}{\tau_e}} \tag{4.134}$$

In this way we have determined the coupling coefficient, $\underline{\kappa}$, in terms of the decay rate $1/\tau_e$.

The outgoing waves depends linearly on the incoming waves and the mode amplitude $a_o$:

$$s_{-2} = s_{+1} + ca_o \tag{4.135}$$

$$s_{-1} = s_{+2} + ca_o \tag{4.136}$$

In the absence of $a_o$ $a_o = 0$, $s_{-2} = s_{+1}$ and $s_{-1} = s_{+2}$ as must be the case. The coefficient $c$ can be found from power conservation. Clearly, the rate of increase of the energy of the mode is equal to the net power delivered to the resonator, i.e

$$\frac{d|a_o|^2}{dt} = |s_{+1}|^2 + |s_{+2}|^2 - |s_{-1}|^2 - |s_{-2}|^2 \tag{4.137}$$

Using eq. (4.127) we get

$$\frac{d|a_o|^2}{dt} = \frac{-2}{\tau_e}|a_o|^2 + \underline{\kappa}(s_{+1} + s_{+2})a_o^* + \underline{\kappa}^*(s_{+1}^* + s_{+2}^*)a_o \tag{4.138}$$

Use of eqs. (4.135), (4.136) and (4.138) in eq. (4.137) yields

$$c = -\sqrt{\frac{1}{\tau_e}}. \tag{4.139}$$

In this way we find for the mode of the first resonator:

$$\frac{da_o}{dt} = j\left(\omega_o - \frac{1}{\tau_e}\right)a_o + \sqrt{\frac{1}{\tau_e}}(s_{+1} + s_{+2}) \tag{4.140}$$

with the additional relationship between the incident and reflected waves:

$$s_{-1} = s_{+2} - \sqrt{\frac{1}{\tau_e}}a_o \tag{4.141}$$

$$s_{-2} = s_{+1} - \sqrt{\frac{1}{\tau_e}}a_o \tag{4.142}$$

If the coupling to resonator (1) is included, then (4.140) changes to

$$\frac{da_o}{dt} = j\left(\omega_o - \frac{1}{\tau_e}\right)a_o + j\underline{\mu}_1 a_1 + \sqrt{\frac{1}{\tau_e}}(s_{+1} + s_{+2}) \tag{4.143}$$

and eqs. (4.141) and (4.142) remain unchanged.

# Chapter 5

# Add-Drop Filters using Different Topology: Push-Pull Filters

In the previous chapter we saw how Bragg resonators can be side-coupled to a bus waveguide to create a variety of optical filters. We saw that at least two Bragg resonators were needed to create the lowest-order add/drop filter capable of completely dropping a selected WDM channel. We also saw that $n$ Bragg resonators side-coupled in a stack configuration could be used to create higher-order receiver filters capable of transfering half the incident power to the drop port. As in the case of a first-order filter, it can be shown that $2n$ resonators are needed to create an $n^{th}$-order filter capable of complete power transfer. The $n$ additional resonators needed serve as the higher-order reflector and follow the $n$-resonator receiver stack; they enable complete power transfer of the selected WDM channel to the drop port. Higher-order reflectors using Bragg resonators are difficult to make. In the case of a $2^{nd}$-order add/drop filter described in the previous chapter, we had to rely on some ad hoc techniques to design the $2^{nd}$-order reflector needed for complete power transfer. The techniques for making higher-order reflector could not be easily generalized for $n^{th}$-order. The optical parameters needed to design the $n$-resonator receiver stack are determined by using the equivalent circuit approach detailed in the previous chapter. However, no such convenient techniques exist for designing higher-order reflectors using the Bragg resonator topologies discussed thus far. Ideally we would like to use a coupled Bragg resonator system in some configuration where we know exactly how to determine all the requisite coupling parameters between the $2n$ resonators to design an $n^{th}$-order add/drop filter capable of complete power transfer of the selected channel to the drop port. In this chapter we discuss
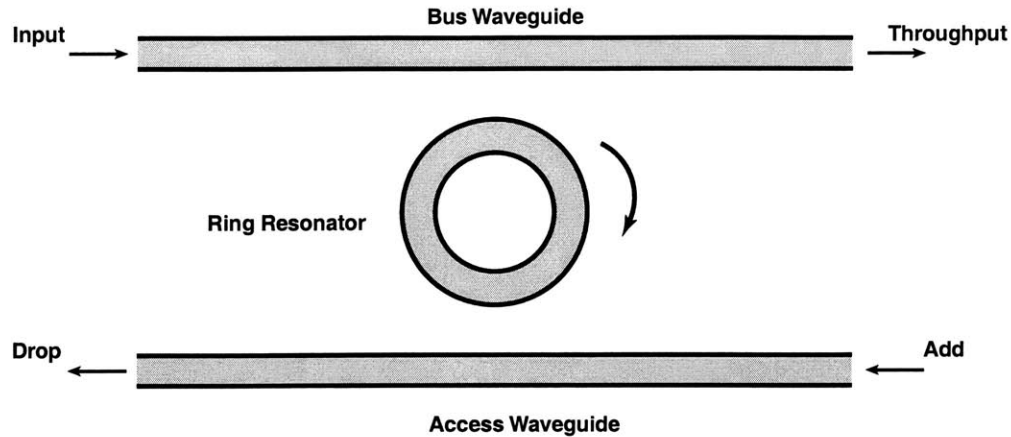
**Figure 5-1:** Add/Drop filter using ring resonator.

such a topology. The topology is inspired in part by examining a ring resonator add-drop filter. We will see that the behavior of ring resonators which are travelling-wave devices can be reproduced by using Bragg resonators even though they are standing-wave devices. Filters made using this new topology are labelled as push-pull filters because of the nature of the interaction between the coupled resonator pairs that simulate a traveling wave.

## 5.1   Add-Drop filter made single mode resonators

It has been well known that a ring resonator side-coupled to two waveguides as shown in Fig. (5-1) can be used as an add-drop filter [55, 56]. The top or bus waveguide serves as the input port and carries the multi-channel input. The bottom or access waveguide allows the signals on the bus waveguide to be accessed via the ring resonator. The principle of operation of a ring resonator add/drop is relatively straightforward. The evanescent tail of the guided mode in the bus waveguide excite the ring resonator mode in the region where the bus is close the resonator. The mode of the ring resonator circulates in the clockwise direction and couples to both the top and bottom waveguides. However, the light couples out of phase to the signal on the bus waveguide and as a result the dropped channel gets transferred to the access guide propagating in the reverse direction. The reversal of phase relative to the bus guide is due to the fact that evanescent coupling in each direction is associated with a 90° phase shift. Hence, the light coupling from the input bus to the ring resonator and back to the input bus is out of phase. Consequently all the light in the resonator ends up at the drop port. The frequency selectivity of the ring resonator add/drop
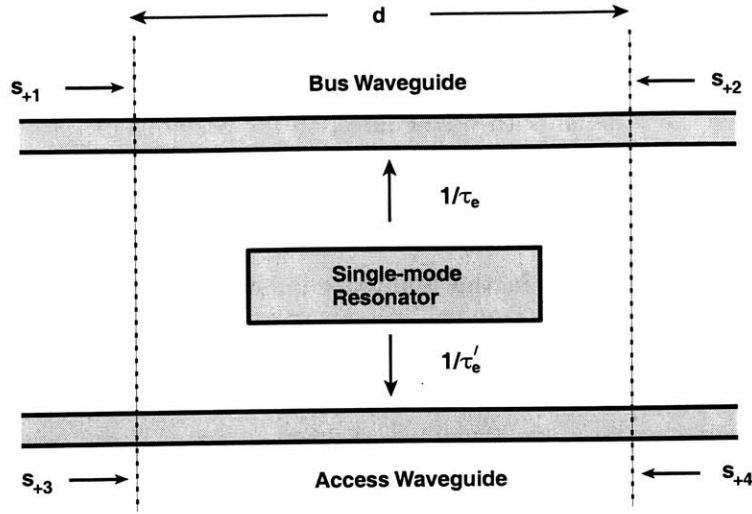
**Figure 5-2:** Single-mode resonator side-coupled to two adjacent waveguides.

filter comes from the fact that the ring resonator only supports those wavelengths that with a $2\pi m$ phase-shift complete a roundtrip of the ring.

CMT-time equations can be used to describe a general single-mode resonator coupled to two guides as shown in Fig. (5-2):

$$\frac{da}{dt} = \left( j\omega_o - \frac{1}{\tau_o} - \frac{1}{\tau_e} - \frac{1}{\tau_e'} \right) a + \underline{\kappa_1} s_{+1} + \underline{\kappa_2} s_{+2} + \underline{\kappa_3} s_{+3} + \underline{\kappa_4} s_{+4} \tag{5.1}$$

$a$ is the resonator mode amplitude and normalized such that $|a|^2$ is the energy in the mode. $\omega_o$ is the resonant frequency, $1/\tau_o$ is the decay rate due to internal resonator loss, $1/\tau_e$, $1/\tau_e'$ are the *amplitude* decay rates associated with loss from the resonator to the bus and the access waveguides, respectively. As in the previous chapter, $\underline{\kappa_1}$ and $\underline{\kappa_2}$ are the input coupling coefficients associated with the forward and backward propagating modes in the bus guide, and $\underline{\kappa_3}$ and $\underline{\kappa_4}$ are similarly defined for the access guide.

By power conservation, the outgoing waves are [57]:

$$s_{-1} = e^{-j\beta d} \left( s_{+2} - \underline{\kappa_2^*} a \right) \tag{5.2}$$

$$s_{-2} = e^{-j\beta d} \left( s_{+1} - \underline{\kappa_1^*} a \right) \tag{5.3}$$

$$s_{-3} = e^{-j\beta' d} \left( s_{+4} - \underline{\kappa_4^*} a \right) \tag{5.4}$$

$$s_{-4} = e^{-j\beta' d} \left( s_{+3} - \underline{\kappa_3^*} a \right) \tag{5.5}$$

where $\beta$ and $\beta'$ are the propagation constants in the bus and the access guides, respectively. These equations are similar to those in the previous chapter. Equations (5.2)-(5.5) show that

if the resonator is not excited then the incident waves appear at the output undisturbed, with a phase shift that is due to the finite distance $d$ between the reference planes, for simplicity taken to be the same in both waveguides. In the previous chapter it was assumed that reference planes were chosen such that this phase term was an integral number of $2\pi$'s and was thus omitted. In the most general case it should be included, as above. The coupling coefficients, $\underline{\kappa}_i$ are found in the appendix following a treatment similar to [20]. Their squared magnitudes are equal to the respective decay rates into the waveguides due to power conservation and their phases are related to the phase mismatch between the waveguide and resonator modes and the choice of reference planes. So we can write:

$$\underline{\kappa}_i = \sqrt{\frac{1}{\tau_{e_i}}}\, e^{j\theta_i} \qquad i = 1\ldots 4 \tag{5.6}$$

with $1/\tau_{e1,3}$ and $1/\tau_{e2,4}$ defined as the *power* decay rates in the forward and backward direction, respectively. They are related to the amplitude decay rates $1/\tau_e$ and $1/\tau_e'$ via power conservation:

$$\frac{1}{\tau_{e1}} + \frac{1}{\tau_{e2}} = \frac{2}{\tau_e} \tag{5.7}$$

$$\frac{1}{\tau_{e3}} + \frac{1}{\tau_{e4}} = \frac{2}{\tau_e'} \tag{5.8}$$

$\theta_i$ are the respective phases; they were assumed to be unity in the previous chapter but are included here to be most general.

Eq. (5.1) describes an arbitrary single-mode resonator coupled to bus and access waveguides. We choose port 1 as the input port and assume that the resonator is only excited from this port, i.e we set $s_{+2}$, $s_{+3}$, and $s_{+4}$ to zero. If $s_{+1}$ has a $e^{j\omega t}$ time dependence, then we find from 5.1 at steady state:

$$a = \frac{\sqrt{\frac{1}{\tau_{e1}}}\, e^{j\theta_1} s_{+1}}{j(\omega - \omega_o) + \frac{1}{\tau_o} + \frac{1}{\tau_e} + \frac{1}{\tau_e'}} \tag{5.9}$$

Substituting $a$ from (5.9) into eqs. (5.2)-(5.5), we get the filter response of the system:

$$\frac{s_{-1}}{s_{+1}} \equiv R = -e^{-j\beta d} \frac{\sqrt{\frac{1}{\tau_{e1}\tau_{e2}}} \, e^{j(\theta_1 - \theta_2)}}{j(\omega - \omega_o) + \frac{1}{\tau_o} + \frac{1}{\tau_e} + \frac{1}{\tau_e'}} \tag{5.10}$$

$$\frac{s_{-2}}{s_{+1}} \equiv T = e^{-j\beta d} \left( 1 - \frac{\frac{1}{\tau_{e1}}}{j(\omega - \omega_o) + \frac{1}{\tau_o} + \frac{1}{\tau_e} + \frac{1}{\tau_e'}} \right) \tag{5.11}$$

$$\frac{s_{-3}}{s_{+1}} \equiv D_L = -e^{-j\beta' d} \frac{\sqrt{\frac{1}{\tau_{e1}\tau_{e4}}} \, e^{j(\theta_1 - \theta_4)}}{j(\omega - \omega_o) + \frac{1}{\tau_o} + \frac{1}{\tau_e} + \frac{1}{\tau_e'}} \tag{5.12}$$

$$\frac{s_{-4}}{s_{+1}} \equiv D_R = -e^{-j\beta' d} \frac{\sqrt{\frac{1}{\tau_{e1}\tau_{e3}}} \, e^{j(\theta_1 - \theta_3)}}{j(\omega - \omega_o) + \frac{1}{\tau_o} + \frac{1}{\tau_e} + \frac{1}{\tau_e'}} \tag{5.13}$$

where $R$ is the reflection from the input port, $T$ is the transmission through the bus, and $D_L$, $D_R$ represent the transmission (channel dropping) into the left and right ports of the access guide, respectively. Equations (5.10)-(5.13) are completely general and describe the behavior of a single-mode resonator side-coupled to two guides. No assumption is made about whether the resonator is a traveling wave resonator or a standing wave resonator. We can now apply the above formalism to the case of a traveling wave resonator used in this configuration.

In the case of a a traveling wave mode, such as that supported by the ring resonator of Fig. (5-1), the power flows continuously in only one direction in the resonator. The forward traveling mode of the bus waveguide excites the clockwise propagating mode of the ring. Since this mode is uni-directional it immediately follows that the backward decay rate, $1/\tau_{e2}$ in the bus waveguide and the forward decay rate, $1/\tau_{e3}$ in the access waveguide are zero, i.e $1/\tau_{e2} = 1/\tau_{e3} = 0$ From eqs. (5.7) and (5.8) it follows that

$$1/\tau_{e1} = 2/\tau_e, \quad 1/\tau_{e4} = 2/\tau_e'$$

We find using eqs. (5.10) and (5.13) that in this case give $R = D_R = 0$, over the entire bandwidth consistent with the stated decay rates being zero. At $\omega = \omega_o$, the incident power in the bus in the forward direction is transferred to the access guide in the backward direction limited only by the loss. This confirms the argument given from physical reasoning about the behavior of a ring resonator add/drop filter. If, in addition:

$$\frac{1}{\tau_e} = \frac{1}{\tau_e'} + \frac{1}{\tau_o} \tag{5.14}$$
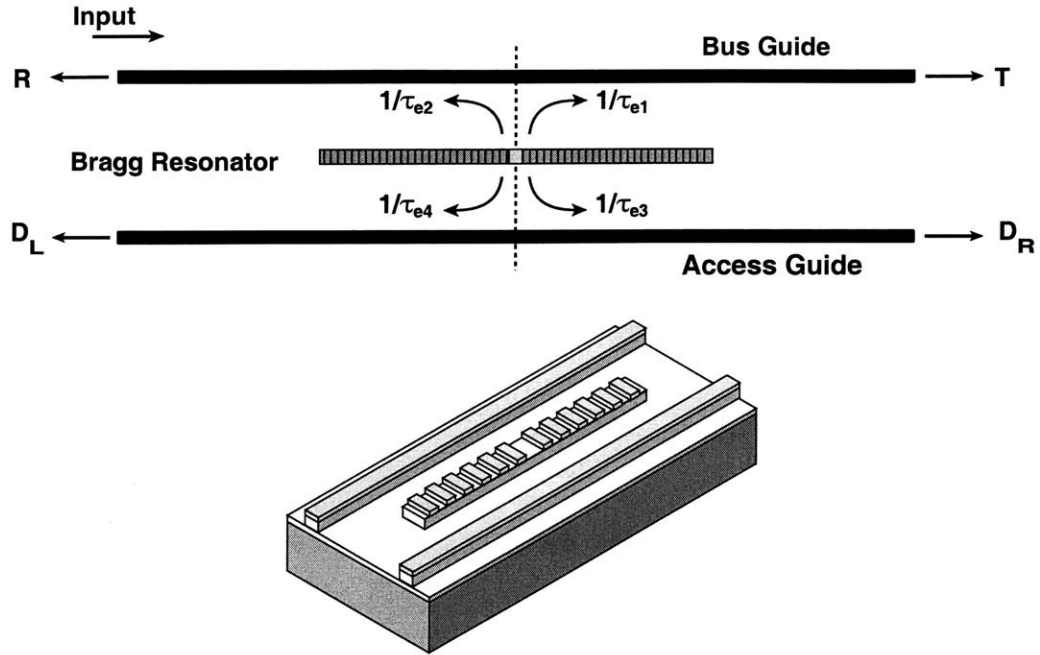
**Figure 5-3:** Bragg resonator side-coupled to two adjacent waveguides.

then, at resonance, (5.11) and (5.12) give $T = 0$ and $|D_L|^2 = (1 - \tau_e/\tau_o)$, so the input signal power at $\omega_o$ is completely removed from the bus and is dropped into port 3 of the access guide reduced by a fraction $\tau_e/\tau_o$ due to loss. Thus, the system operates as a channel dropping filter.

### 5.1.1   Standing-wave Resonator

Consider now the case of a standing wave single-mode resonator like a Bragg resonator coupled to the bus and access guides as in Fig. (5-3). We would like to see if it is possible to use a Bragg resonator in this configuration as an add/drop filter. As mentioned earlier, the response of any single-mode resonator is governed by eqs. (5.10)-(5.13). However, unlike a traveling wave resonator, the Bragg resonator mode consists of a pure standing wave; there is no net power flowing in either direction in the resonator. As a result the resonant mode decays equally into the forward and the backward propagating waveguide modes. In other words, $1/\tau_{e1} = 1/\tau_{e2}$ and $1/\tau_{e3} = 1/\tau_{e4}$. From eqs. (5.7) and (5.8) it follows that

$$\frac{1}{\tau_{e1}} = \frac{1}{\tau_{e2}} = \frac{1}{\tau_e}$$

and

$$\frac{1}{\tau_{e3}} = \frac{1}{\tau_{e4}} = \frac{1}{\tau_e'}$$

$\kappa_1 = \kappa_2 \equiv \kappa$ etc. and eqs. () exactly reduce to the generalized form of the familiar equations of chapter 4 which describe a resonator side-coupled to a waveguide. As in the case of a traveling wave resonator, the power into the access guides is maximized if eq. (5.14) is satisfied. In this case using eqs. (5.10)-(5.13) we find that

$$|R|^2 \;=\; |T|^2 = \; 0.25 \tag{5.15}$$

$$|D_L|^2 \;=\; |D_R|^2 = \; 0.25(1 - \tau_e/\tau_o). \tag{5.16}$$

At best, for the case of zero internal resonator loss, half the input power at frequency $\omega_o$ remains in the bus and is equally distributed into ports 1 and 2. The other half, is equally distributed into access guide ports 3 and 4.

Clearly, a single-mode standing wave resonator is not adequate for channel dropping as it leaves half the incident power on the bus guide as reflections and transmission. This is very different from a single-mode traveling wave resonator side coupled to the bus and the access guide which can fully transfer a channel at the resonance frequency, from the bus to the access guide. The results of the single standing wave resonator configuration of Fig. (5-3) is reminscent of that of a SSCR of the previous chapter. In the previous chapter we noted that two resonators were needed to obtain a add/drop filter capable of complete power extraction of the dropped channel from the bus guide. In the next section we show that it is possible to achieve the response of a single-mode traveling-wave resonant add/drop filter of Fig. (5-1) by using a double-mode standing-wave resonator.

## 5.2   Symmetric standing wave channel add/drop filter

We now consider a resonant structure with two standing wave modes that is placed between the bus and access guides as shown in schematic representation in Fig. (5-4). The resonator is assumed to have a symmetry plane perpendicular to the waveguides, at $z = 0$. It supports two modes which are symmetric and antisymmetric with respect to this plane. With the reference planes defined at $z = \pm d/2$, the phases of the coupling coefficients differ by even (odd) multiples of $\pi$ in the case of the symmetric (antisymmetric) modes. Thus, the forward and backward incident waves couple into the symmetric mode in phase and into the antisymmetric mode out of phase. The symmetric mode has amplitude $a_s$ and antisymmetric mode has amplitude $a_a$. Using the analysis of the previous section simplified
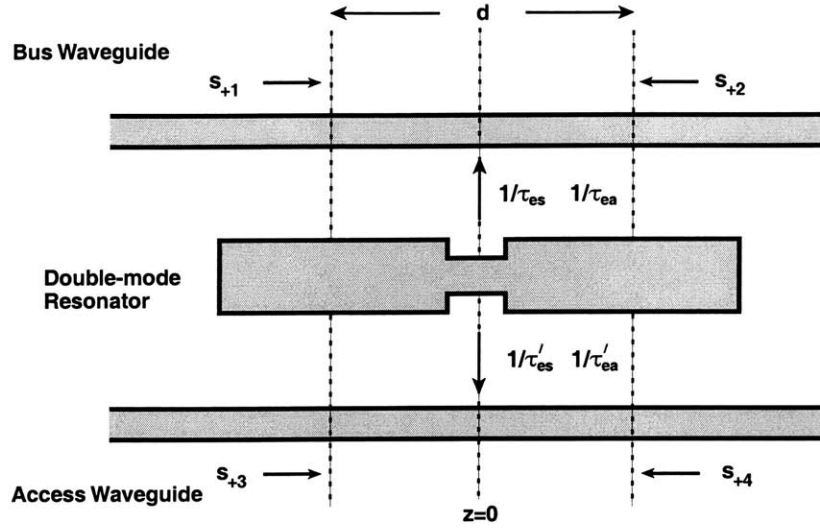
**Figure 5-4:** Schematic of a double-mode standing-wave resonator side-coupled to two adjacent waveguides.

for the case of symmetric structure, we have:

$$\frac{da_s}{dt} = \left( j\omega_s - \frac{1}{\tau_{e_s}} - \frac{1}{\tau'_{e_s}} - \frac{1}{\tau_{o_s}} \right) a_s + \underline{\kappa}_s(s_{+1} + s_{+2}) + \underline{\kappa}'_s(s_{+3} + s_{+4}) \qquad (5.17)$$

$$\frac{da_a}{dt} = \left( j\omega_a - \frac{1}{\tau_{e_a}} - \frac{1}{\tau'_{e_a}} - \frac{1}{\tau_{o_a}} \right) a_s + \underline{\kappa}_a(s_{+1} - s_{+2}) + \underline{\kappa}'_a(s_{+3} - s_{+4}) \qquad (5.18)$$

where $\omega_{s,a}$, are the resonant frequencies $1/\tau_{o_{e,a}}$ are the decay rates due to loss, $1/\tau_{e_{s,a}}$, $1/\tau'_{e_{s,a}}$ are the rates of decay into the signal bus and the access guide, respectively, and $\underline{\kappa}_{s,a}$, $\underline{\kappa}'_{s,a}$ are the input coupling coefficients associated with the bus and the access guide, respectively. The amplitudes of the outgoing waves are found by generalizing equations (5.2)-(5.5) to the case of two excited modes:

$$s_{-1} = e^{-j\beta d}\left( s_{+2} - \underline{\kappa}_s^* a_s + \underline{\kappa}_a^* a_a \right) \qquad (5.19)$$

$$s_{-2} = e^{-j\beta d}\left( s_{+1} - \underline{\kappa}_s^* a_s - \underline{\kappa}_a^* a_a \right) \qquad (5.20)$$

$$s_{-3} = e^{-j\beta' d}\left( s_{+4} - \underline{\kappa}_s'^* a_s + \underline{\kappa}_a'^* a_a \right) \qquad (5.21)$$

$$s_{-4} = e^{-j\beta' d}\left( s_{+3} - \underline{\kappa}_s'^* a_s - \underline{\kappa}_a'^* a_a \right) \qquad (5.22)$$

In analogy with (5.6), the input coupling coefficients can be written as:

$$\underline{\kappa}_{s,a} = \sqrt{\frac{1}{\tau_{e_{s,a}}}} e^{j\theta_{s,a}} \qquad \underline{\kappa}'_{s,a} = \sqrt{\frac{1}{\tau'_{e_{s,a}}}} e^{j\theta'_{s,a}} \qquad (5.23)$$

With $s_{+1}$ as the input signal at frequency $\omega$, we find the filter response at the four-ports of the system, as defined in the previous section:

$$R = e^{-j\beta d}\left(-\frac{\frac{1}{\tau_{e_s}}}{j(\omega - \omega_s) + \frac{1}{\tau_{e_s}} + \frac{1}{\tau'_{e_s}} + \frac{1}{\tau_{o_s}}} + \frac{\frac{1}{\tau_{e_a}}}{j(\omega - \omega_a) + \frac{1}{\tau_{e_a}} + \frac{1}{\tau'_{e_a}} + \frac{1}{\tau_{o_a}}}\right) \quad (5.24)$$

$$T = e^{-j\beta d}\left(1 - \frac{\frac{1}{\tau_{e_s}}}{j(\omega - \omega_s) + \frac{1}{\tau_{e_s}} + \frac{1}{\tau'_{e_s}} + \frac{1}{\tau_{o_s}}} - \frac{\frac{1}{\tau_{e_a}}}{j(\omega - \omega_a) + \frac{1}{\tau_{e_a}} + \frac{1}{\tau'_{e_a}} + \frac{1}{\tau_{o_a}}}\right)(5.25)$$

$$D_L = e^{-j\beta' d}\left(-\frac{\sqrt{\frac{1}{\tau_{e_s}\tau'_{e_s}}}\,e^{j(\theta_s - \theta'_s)}}{j(\omega - \omega_s) + \frac{1}{\tau_{e_s}} + \frac{1}{\tau'_{e_s}} + \frac{1}{\tau_{o_s}}} + \frac{\sqrt{\frac{1}{\tau_{e_a}\tau'_{e_a}}}\,e^{j(\theta_a - \theta'_a)}}{j(\omega - \omega_a) + \frac{1}{\tau_{e_a}} + \frac{1}{\tau'_{e_a}} + \frac{1}{\tau_{o_a}}}\right) \quad (5.26)$$

$$D_R = e^{-j\beta' d}\left(-\frac{\sqrt{\frac{1}{\tau_{e_s}\tau'_{e_s}}}\,e^{j(\theta_s - \theta'_s)}}{j(\omega - \omega_s) + \frac{1}{\tau_{e_s}} + \frac{1}{\tau'_{e_s}} + \frac{1}{\tau_{o_s}}} - \frac{\sqrt{\frac{1}{\tau_{e_a}\tau'_{e_a}}}\,e^{j(\theta_a - \theta'_a)}}{j(\omega - \omega_a) + \frac{1}{\tau_{e_a}} + \frac{1}{\tau'_{e_a}} + \frac{1}{\tau_{o_a}}}\right) \quad (5.27)$$

The two resonant modes are degenerate if they have equal frequencies and equal decay rates:

$$\omega_s = \omega_a = \omega_o \quad (5.28)$$

$$\tau_{o_s} = \tau_{o_a} = \tau_o \quad (5.29)$$

$$\tau_{e_s} = \tau_{e_a} = \tau_e \quad (5.30)$$

$$\tau'_{e_s} = \tau'_{e_a} = \tau'_e \quad (5.31)$$

Under these conditions, (5.24) gives $R = 0$ over the entire bandwidth of the resonator and equations (5.25)-(5.27) become:

$$T = e^{-j\beta d}\left(1 - \frac{\frac{2}{\tau_e}}{j(\omega - \omega_o) + \frac{1}{\tau_e} + \frac{1}{\tau'_e} + \frac{1}{\tau_o}}\right) \quad (5.32)$$

$$D_L = -e^{j\left(\frac{(\theta_s + \theta_a) - (\theta'_s + \theta'_a)}{2} - \beta' d\right)}\frac{\frac{2}{\sqrt{\tau_e \tau'_e}}}{j(\omega - \omega_o) + \frac{1}{\tau_e} + \frac{1}{\tau'_e} + \frac{1}{\tau_o}}\,sin\left(\frac{\Delta\theta}{2}\right) \quad (5.33)$$

$$D_R = -j\,e^{j\left(\frac{(\theta_s + \theta_a) - (\theta'_s + \theta'_a)}{2} - \beta' d\right)}\frac{\frac{2}{\sqrt{\tau_e \tau'_e}}}{j(\omega - \omega_o) + \frac{1}{\tau_e} + \frac{1}{\tau'_e} + \frac{1}{\tau_o}}\,cos\left(\frac{\Delta\theta}{2}\right) \quad (5.34)$$

where

$$\Delta\theta = (\theta_s - \theta_a) - (\theta'_s - \theta'_a) \quad (5.35)$$

At the resonance frequency $\omega_o$, from (5.32) the transmission through the bus is:

$$T = e^{-j\beta l}\frac{-\frac{1}{\tau_e} + \frac{1}{\tau'_e} + \frac{1}{\tau_o}}{\frac{1}{\tau_e} + \frac{1}{\tau'_e} + \frac{1}{\tau_o}} \quad (5.36)$$

Note that if the decay rates satisfy (5.14) we find, as in the case of a traveling wave resonator discussed in section 5.1.1, that the input signal power is completely removed from the bus and transfered to the access guide reduced by a fraction $\tau_e/\tau_o$ due to loss. Under this condition, the bandwidth of the Lorentzian response is determined entirely by the coupling to the bus waveguide and its peak is set by the ratio $\tau_e/\tau_o$. This behavior is very different from the case of a single-mode resonator where half the incident power remained on the bus guide. As we can see in (5.33) and (5.34), the distribution of the dropped signal power into the left and the right port of the access guide is determined by the phase difference $\Delta\theta$:

(a) If $\Delta\theta = 2n\pi$, where n is an integer, then $D_L = 0$ for all frequencies so the channel is dropped in the forward direction. This means that if the resonator has a horizontal symmetry plane as well, i.e. parallel to the waveguides, the symmetric and antisymmetric modes have the same symmetry (even or odd) with respect to this plane. An example for this case is a composite system made up of two identical standing wave resonators as we will see in the next section.

(b) If $\Delta\theta = (2n + 1)\pi$, then $D_R = 0$ for all frequencies so the propagation in the access guide waveguide is only in the backward direction. This means that if the resonator has a horizontal symmetry plane as well, the symmetric mode has even (odd) and the antisymmetric mode has odd (even) symmetry with respect to this plane. An example for this case is a ring resonator, if we consider its traveling wave modes as superpositions of degenerate symmetric and antisymmetric standing wave modes that are excited with a $\pi/2$-phase difference.

(c) In any other case both $D_R$ and $D_L$ are nonzero.

Thus, in agreement with ref. [60]-[62], we found that in order for a resonant system to operate as a channel dropping filter employing standing wave modes, the excitation of two degenerate modes is necessary. The superposition of these modes with the appropriate phase relation gives the behavior of a traveling wave mode.

## 5.3 Symmetric system using two identical single-mode resonators

According the previous section a symmetric resonator system with two degenerate modes coupled to bus and access waveguides can function as an add/drop filter capable of extracting the entire desired channel power from the signal bus. One way to implement a double-mode symmetric resonator system is by using two identical resonators that are coupled to each other; each resonator has as single standing-wave mode in the frequency range of interest. Bragg resonators can be used for this purpose and Fig. (5-6) shows two coupled Bragg resonators placed between the bus and the access guide waveguides so that the total system has a symmetry plane at $z = 0$. Normally, the mutual coupling of the two resonators would split the resonant frequencies, lifting the degeneracy. However, it can be shown that the coupling of the resonators to the waveguides can be designed to cancel the effect of frequency splitting due to the mutual coupling between the resonators. Consequently its possible to reestablish the degeneracy.

We can either choose to describe the system of coupled Bragg resonators in terms of the modes of symmetric and antisymmetric supermodes, $a_s$ and $a_a$ of the composite coupled-resonator system as in the previous section; conversely we can use the mode amplitudes, $a_L$ and $a_R$, of individual resonators. The two approaches are identical; in fact the normalized sum and difference of the individual resonator modes, $a_L$, $a_R$ define the symmetric and antisymmetric modes, $a_s$, $a_a$. The mode amplitudes of the resonator on the left and on the right of the symmetry plane are denoted by $a_L$ and $a_R$, respectively. The resonant frequency, decay rates and coupling constants for the left resonator are defined as in section 5.1.1 and for the right resonator are found by mirror symmetry.

The resonator on the left is excited from the left by $s_{+1}$ and $s_{+3}$ and from the right by the outputs of the right resonator. The resonator on the right is excited from the right by $s_{+2}$ and $s_{+4}$ and from the left by the outputs of the left resonator. The distance from the left (right) reference plane of the resonator on the left of the symmetry plane to the left (right) reference plane of the resonator on the right of the symmetry plane is denoted by $l$, as shown in Fig. (5-5), and for simplicity is the same in both waveguides. The equations
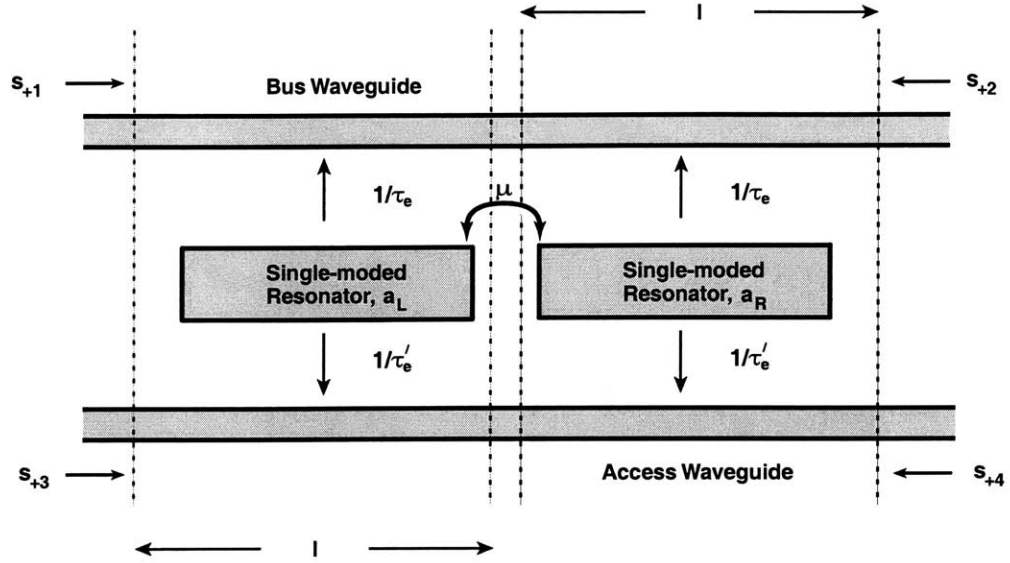
**Figure 5-5:** Two identical coupled single-mode resonators side-coupled to bus and access waveguides. This system is identical to that of Fig. (5-4).

for the mode amplitudes of the two resonators are:

$$
\frac{da_L}{dt} = \left( j\omega_o - \frac{1}{\tau_e} - \frac{1}{\tau_e'} - \frac{1}{\tau_o} \right) a_L - j\underline{\mu}a_R
$$

$$
+ \sqrt{\frac{1}{\tau_e}} e^{j\theta_1} s_{+1} + \sqrt{\frac{1}{\tau_e}} e^{j\theta_2} e^{-j\beta l} \left( s_{+2} - \sqrt{\frac{1}{\tau_e}} e^{-j\theta_1} a_R \right)
$$

$$
+ \sqrt{\frac{1}{\tau_e'}} e^{j\theta_3} s_{+3} + \sqrt{\frac{1}{\tau_e'}} e^{j\theta_4} e^{-j\beta' l} \left( s_{+4} - \sqrt{\frac{1}{\tau_e'}} e^{-j\theta_3} a_L \right) \qquad (5.37)
$$

$$
\frac{da_R}{dt} = \left( j\omega_o - \frac{1}{\tau_e} - \frac{1}{\tau_e'} - \frac{1}{\tau_o} \right) a_R - j\underline{\mu}a_L
$$

$$
+ \sqrt{\frac{1}{\tau_e}} e^{j\theta_1} s_{+2} + \sqrt{\frac{1}{\tau_e}} e^{j\theta_2} e^{-j\beta l} \left( s_{+1} - \sqrt{\frac{1}{\tau_e}} e^{-j\theta_1} a_R \right)
$$

$$
+ \sqrt{\frac{1}{\tau_e'}} e^{j\theta_3} s_{+4} + \sqrt{\frac{1}{\tau_e'}} e^{j\theta_4} e^{-j\beta' l} \left( s_{+3} - \sqrt{\frac{1}{\tau_e'}} e^{-j\theta_3} a_R \right) \qquad (5.38)
$$

where $\underline{\mu}$ is the mutual coupling coefficient between the resonators and is real by power conservation. For the decay rates we have used the fact that a standing wave mode decays equally into both directions in the waveguide as discussed in section 5.1.1. Expressions analogous to (5.2)-(5.5) have been used for the outgoing waves of the left (right) resonator

that appear as inputs to the right (left) resonator. In equations (5.37) and (5.38) we can see that, in addition to the direct coupling expressed by $\underline{\mu}$, the two resonators are also indirectly coupled through the waveguides. We define the amplitude of the symmetric and antisymmetric modes of the total system as:

$$a_s = \frac{a_L + a_R}{\sqrt{2}} \tag{5.39}$$

$$a_a = \frac{a_L - a_R}{\sqrt{2}} \tag{5.40}$$

which, due to (5.37) and (5.38), satisfy:

$$
\begin{aligned}
\frac{d}{dt} \left\{ \begin{array}{c} a_s \\ a_a \end{array} \right\} \; = \; & j \left[ \omega_o \mp \left( \underline{\mu} - \frac{1}{\tau_e} sin\phi - \frac{1}{\tau_e'} sin\phi' \right) \right] \left\{ \begin{array}{c} a_s \\ a_a \end{array} \right\} \\
& - \left[ \frac{1}{\tau_o} + \frac{1}{\tau_e} \left( 1 \pm cos\phi \right) + \frac{1}{\tau_e'} \left( 1 \pm cos\phi' \right) \right] \left\{ \begin{array}{c} a_s \\ a_a \end{array} \right\} \\
& + \sqrt{\frac{2}{\tau_e}} e^{j(\frac{\theta_1 + \theta_2 - \beta l}{2})} \left\{ \begin{array}{c} cos\frac{\phi}{2} \\ jsin\frac{\phi}{2} \end{array} \right\} (s_{+1} \pm s_{+2}) \\
& + \sqrt{\frac{2}{\tau_e'}} e^{j(\frac{\theta_3 + \theta_4 - \beta' l}{2})} \left\{ \begin{array}{c} cos\frac{\phi'}{2} \\ jsin\frac{\phi'}{2} \end{array} \right\} (s_{+3} \pm s_{+4})
\end{aligned} \tag{5.41}
$$

where

$$\phi = \beta l + \theta_1 - \theta_2 \tag{5.42}$$

$$\phi' = \beta' l + \theta_3 - \theta_4 \tag{5.43}$$

Comparing (5.41) with equations (5.17)-(5.18) we have:

$$\left\{ \begin{array}{c} \omega_s \\ \omega_a \end{array} \right\} = \omega_o \mp \left( \underline{\mu} - \frac{1}{\tau_e} sin\phi - \frac{1}{\tau_e'} sin\phi' \right) \tag{5.44}$$

$$\frac{1}{\tau_{o_s}} = \frac{1}{\tau_{o_a}} = \frac{1}{\tau_o} \tag{5.45}$$

$$\left\{ \begin{array}{c} \underline{\kappa}_s \\ \underline{\kappa}_a \end{array} \right\} = \sqrt{\frac{2}{\tau_e}} e^{j(\frac{\theta_1 + \theta_2 - \beta l}{2})} \left\{ \begin{array}{c} cos\frac{\phi}{2} \\ jsin\frac{\phi}{2} \end{array} \right\} \tag{5.46}$$

$$\left\{ \begin{array}{c} \underline{\kappa}_s' \\ \underline{\kappa}_a' \end{array} \right\} = \sqrt{\frac{2}{\tau_e'}} e^{j(\frac{\theta_3 + \theta_4 - \beta' l}{2})} \left\{ \begin{array}{c} cos\frac{\phi'}{2} \\ jsin\frac{\phi'}{2} \end{array} \right\} \tag{5.47}$$

$$\frac{1}{\tau_{e_{s,a}}} = |\underline{\kappa}_{s,a}|^2 \tag{5.48}$$

$$\frac{1}{\tau'_{e_{s,a}}} = |\underline{\kappa}'_{s,a}|^2 \tag{5.49}$$

From (5.46) and (5.47), we can see that the symmetric and the antisymmetric excitations couple into the system with a $\pi/2$ phase difference. In the special case that $\phi$ and $\phi'$ are even (odd) multiples of $\pi$, only the symmetric (antisymmetric) mode is excited, leading to the behavior of the standing wave resonant system described in section 5.1.1, with decay rates $2/\tau_e$ and $2/\tau'_e$ into the bus and the access guide, respectively, and $1/\tau_o$ due to loss.

The conclusions derived for the filter response of the symmetric system shown in section 5.2 apply to this system as well: The system can operate as a channel add/drop filter if its symmetric and antisymmetric modes satisfy the degeneracy conditions (5.28)-(5.31). The decay rates due to loss are already equal as seen in (5.45). From equation (5.44), the condition for frequency degeneracy is satisfied if:

$$\underline{\mu} - \frac{1}{\tau_e}sin\phi - \frac{1}{\tau'_e}sin\phi' = 0 \tag{5.50}$$

From equations (5.46)-(5.49), the conditions for equal decay rates are satisfied if:

$$cos\phi = 0 \tag{5.51}$$

$$cos\phi' = 0 \tag{5.52}$$

Therefore, there are two degrees of freedom in designing this system: Knowing the propagation constants $\beta$, and $\beta'$ and the phase differences $\theta_1 - \theta_2$ and $\theta_3 - \theta_4$ we must choose the distance $d$ so that the symmetric and antisymmetric modes have decay rates equal to those of the individual resonators, $1/\tau_e$, $1/\tau'_e$. Then, by varying the coupling between the waveguides and the resonators, we must make $1/\tau_e$ and $1/\tau'_e$ such that the splitting of the resonance frequencies due to direct coupling between the two resonators is cancelled.

The signal power at resonance is completely removed from the bus if the degenerate decay rates satisfy the maximum power transfer condition (5.14). In this special case the bandwidth of the Lorentzian response is then set by $\tau_e$ and the peak power at the output ports of the access guide by the ratio $\tau_e/\tau_o$.

As discussed in section 5.2, the direction of the channel dropping is determined by the phase difference $\Delta\theta = (\theta_s - \theta_a) - (\theta'_s - \theta'_a)$. Here $\theta_{s,a}$ and $\theta'_{s,a}$ are the phases of the coupling constants defined in (5.46) and (5.47), respectively. From equations (5.46) and (5.47), we can see that:

$$\theta_s - \theta_a = \begin{cases} -\frac{\pi}{2} & \text{if } sin\phi > 0 \\ \frac{\pi}{2} & \text{if } sin\phi < 0 \end{cases} \tag{5.53}$$

$$\theta'_s - \theta'_a = \begin{cases} -\frac{\pi}{2} & \text{if } sin\phi' > 0 \\ \frac{\pi}{2} & \text{if } sin\phi' < 0 \end{cases} \tag{5.54}$$

Therefore $\Delta\theta = 0$, if the degeneracy conditions are satisfied with $\phi - \phi' = 2n\pi$, where $n$ is an integer, and the channel is dropped in the forward direction, i.e in port 4. If $\phi - \phi' = (2n + 1)\pi$, then $\Delta\theta = \pm\pi$, and the channel is dropped backwards, i.e in port 3. In this particular case it is possible to satisfy (5.50) even if the resonators are not directly coupled ($\mu = 0$) provided that $1/\tau_e = 1/\tau'_e$. The design of the filter is simplified when the two resonators are individually symmetric. With the reference planes defined symmetrically on either side of each resonator as in section 5.2, the distance $l$ is equal to the distance between the individual symmetry planes. In addition, we have $\theta_1 - \theta_2 = 0\,(\pm\pi)$ and $\theta_3 - \theta_4 = 0\,(\pm\pi)$ if the mode supported by each resonator is symmetric (antisymmetric). So the conditions for degeneracy become:

$$\mu \mp \frac{1}{\tau_e}sin(\beta l) \mp \frac{1}{\tau'_e}sin(\beta'l) = 0 \tag{5.55}$$

$$cos(\beta l) = cos(\beta'l) = 0 \tag{5.56}$$

We can see that in this case, the choice of $l$ depends on the symmetry of the individual modes that make up the symmetric and antisymmetric modes of the system. For example, in the case that $\tau_e = \tau'_e$ and $\beta = \beta'$, we can see from equation (5.55), that the resonance frequencies are degenerate only if $l = (n + 1/4)\lambda_g$ for symmetric individual modes and only if $l = (n + 3/4)\lambda_g$ for antisymmetric individual modes, where $\lambda_g = 2\pi/\beta$ is the guided wavelength.

### 5.3.1 Add/Drop filter using two coupled Bragg resonators

As we saw in the above section two identical resonators can be coupled to each other to yeild a system with symmetric and antisymmetric modes. These modes are typically at different frequencies. However, by balancing the direct coupling between the resonators with the couplying via the waveguides the degeneracy can be restored. Consider a system which employs two coupled Bragg resonators. The condition for degeneracy require that the two resonators are separated by and odd multiple of quarter-wave lengths. This is
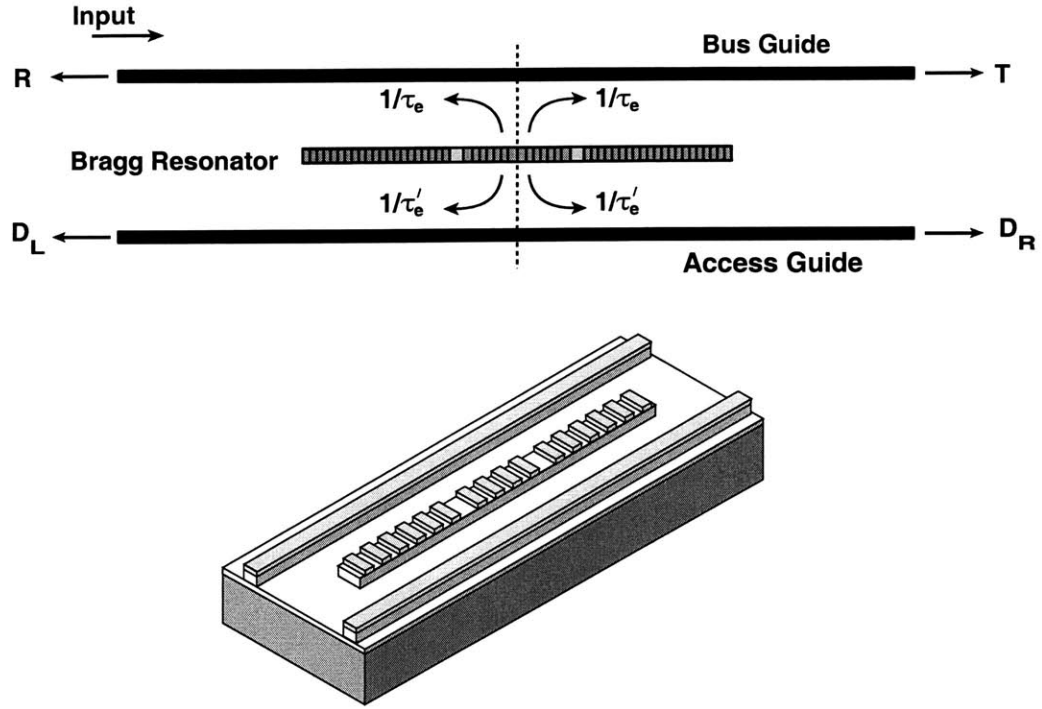
**Figure 5-6:** Two coupled Bragg resonators side-coupled to bus and access waveguides to form a push-pull add/drop filter.

automatically guaranteed for in line Bragg resonators as we saw in the previous chapter. The other condition required for degeneracy is that

$$\underline{\mu} = \frac{1}{\tau_e} + \frac{1}{\tau_e'} \tag{5.57}$$

The CMT-space equations describing the system of Fig. (5-6) is

$$\frac{d}{dz} \begin{bmatrix} A_1(z) \\ A_2(z) \\ A_3(z) \\ B_1(z) \\ B_2(z) \\ B_3(z) \end{bmatrix} = \begin{pmatrix} -j\delta_1 & -j\mu_{12} & 0 & 0 & 0 & 0 \\ -j\mu_{12} & -j\delta_2 & 0 & 0 & \kappa & -j\mu 23 \\ 0 & -j\mu_{23} & -j\delta_3 & 0 & 0 & 0 \\ 0 & 0 & 0 & j\delta_1 & j\mu_{12} & 0 \\ 0 & \kappa & 0 & j\mu_{12} & j\delta_2 & j\mu_{23} \\ 0 & 0 & 0 & 0 & j\mu_{23} & j\delta_3 \end{pmatrix} \begin{bmatrix} A_1(z) \\ A_2(z) \\ A_3(z) \\ B_1(z) \\ B_2(z) \\ B_3(z) \end{bmatrix} \tag{5.58}$$

$$\frac{d}{dz}\vec{A} \equiv \overline{\overline{\mathbf{M}}}\,\vec{A} \tag{5.59}$$

where $A_1$, $A_2$ and $A_3$ are the forward traveling waves in the bus, Bragg resonator and access waveguides respectively. $B_i$ are the corresponding backward traveling waves. $\mu_{12}$ and $\mu_{23}$ are the CMT-space coupling parameters describing the evanescent coupling between the bus-
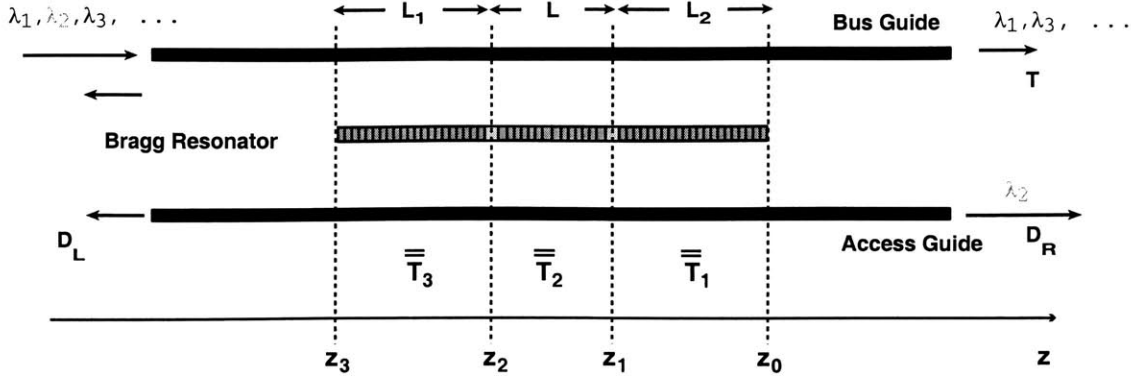
**Figure 5-7:** Schematic showing the transfer-matrix sections of two coupled Bragg resonators side-coupled to bus and access waveguides to form an add/drop filter.

resonator and resonator-access guide pairs. They are related to the CMT-time parameters, $1/\tau_e$ and $1/\tau_e'$ and are not to be confused with the CMT-time coupling parameter $\mu$ which represents the direct coupling between the two Bragg resonators. The CMT-time and CMT-space parameters are related by the following equations derived in chapter 3.

$$\mu = \kappa v_g e^{-\kappa L} \tag{5.60}$$

$$\frac{1}{\tau_e} = 2\kappa v_g \left(\frac{\mu_{12}}{\kappa}\right)^2 \tag{5.61}$$

$$\frac{1}{\tau_e'} = 2\kappa v_g \left(\frac{\mu_{23}}{\kappa}\right)^2 \tag{5.62}$$

where $L$ is the distance between the $\lambda/4$-wave shifts of the Bragg resonators. The condition of degeneracy, eq. (5.57) imposes one constraint on the, $\mu_{12}$, $\mu_{23}$ and $L$. The condition of maximum power transfer given below

$$\frac{1}{\tau_e} - \frac{1}{\tau_e'} = \frac{1}{\tau_o} \tag{5.63}$$

imposes another. For this condition we know that the response of the add/drop is given by

$$|T| = \frac{j(\omega - \omega_o)}{j(\omega - \omega_o) + |\frac{2}{\tau_e}} \tag{5.64}$$

$$|D_R| = \frac{\frac{2}{\sqrt{\tau_e \tau_e'}}}{j(\omega - \omega_o) + \frac{2}{\tau_e}} \tag{5.65}$$

$$|R| = |D_L| = 0 \tag{5.66}$$

Complete power extraction from the bus is achieved. This power ends up in the right drop port scaled down by the internal resonator loss. If this loss, associated with $1/\tau_o$ is zero
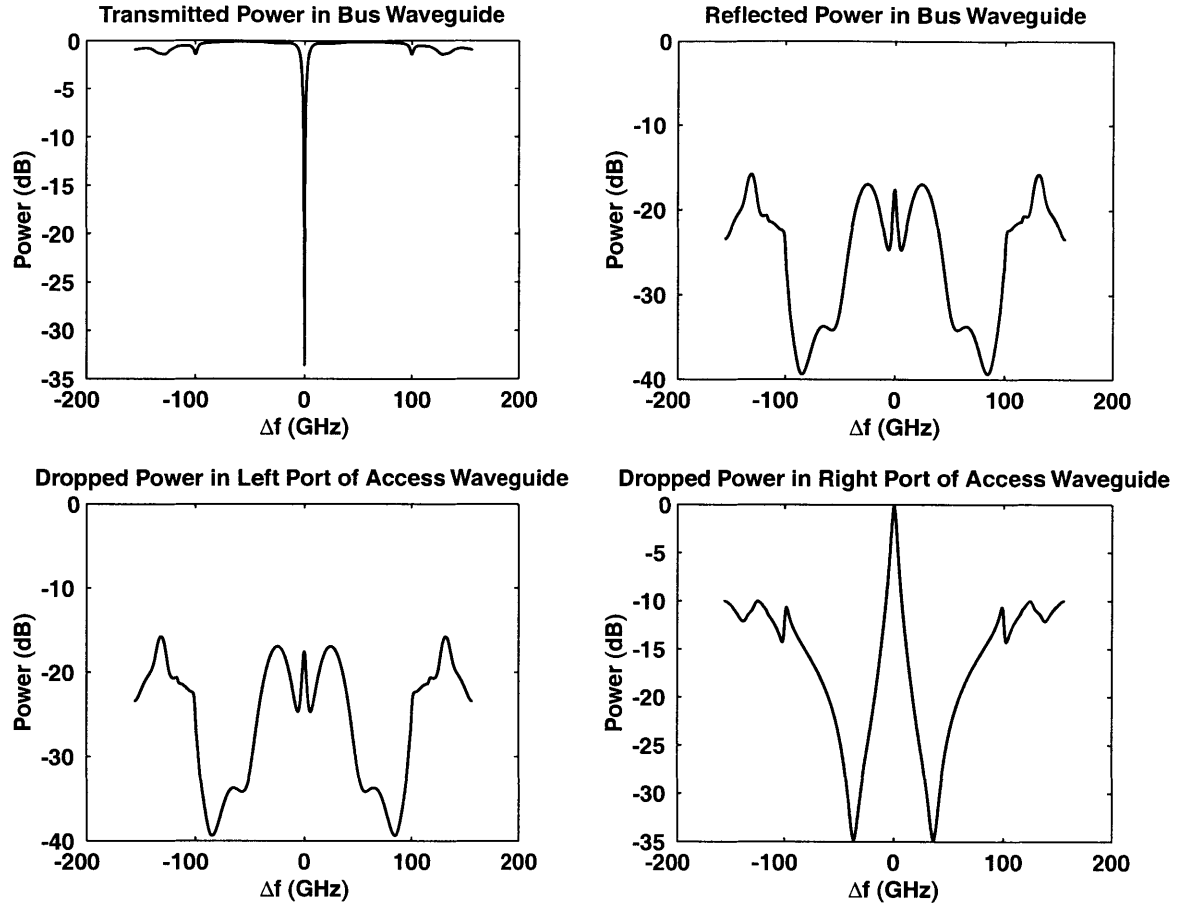
**Figure 5-8:** Spectrum of first-order push-pull add/drop made using two coupled Bragg resonators side-coupled to bus and access waveguides.

we get complete power transfer of the dropped WDM channel to the access guide. From eq. (5.66) it is clear that the bandwidth of the add/drop filter is determined by $1/\tau_e$. For a given 3 dB bandwidth of the add/drop filter response the constraints imposed by eqs. (5.57)and (5.63) allow the use of eqs. (5.60), (5.61) and (5.62) to uniquely determine the needed CMT-space parameters provided we know that grating strength $\kappa$ of the Bragg resonators.

Once the CMT-space parameters $\mu_{12}$, $\mu_{23}$, $\kappa$ and $L$ are known we can again make use of tranfer matrices, given by eq. (3.34), to solve the above structure for a given input. The total transfer matrix, as suggested by the schematic of Fig. (5-7) is given by

$$\overline{\overline{\mathbf{T}}} = \overline{\overline{\mathbf{T}}}_3(+\kappa, \mu_{12}, \mu_{23}, z_3, z_2)\, \overline{\overline{\mathbf{T}}}_2(-\kappa, , \mu_{12}, \mu_{23}, z_2, z_1)\, \overline{\overline{\mathbf{T}}}_3(+\kappa, , \mu_{12}, \mu_{23}, z_1, z_0) \qquad (5.67)$$

Figure (5-8) shows the spectrum of the device of Fig. (5-6) designed for maximum power transfer. It was assumed that the resonators were lossless. We do see some power in the ports
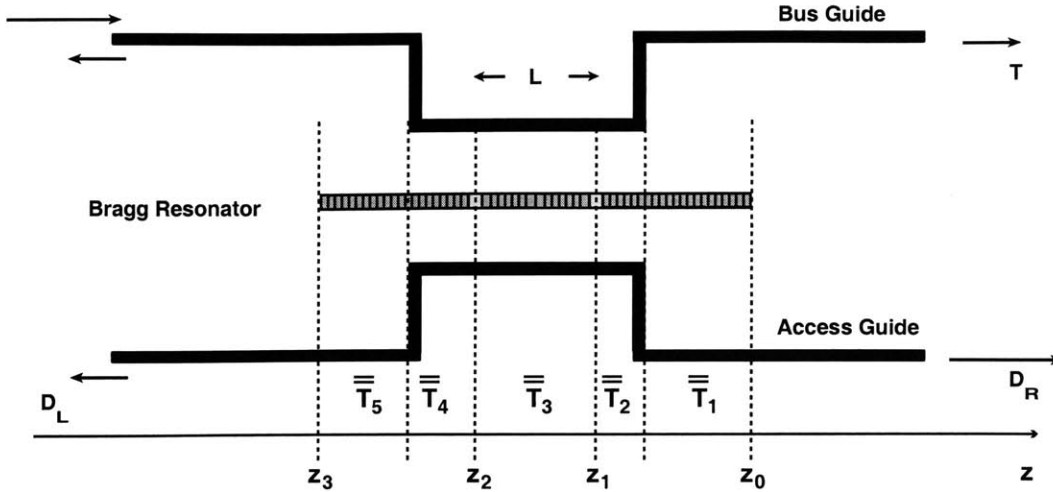
**Figure 5-9:** A scheme to reduce to reduce cross-talk levels outside the stopband due to normal waveguide-waveguide coupling by bending the bus and access guides away from the coupled resonators.

$R$ and $D_R$ but it is quite low. The power lost in these two ports is not so critical. It should be low enough that the on-going channel power, $T$, on the bus is not depleted significantly. Note that the dropped channel, $D_R$ is Lorentzian in shape and rolls-off with frequency. However beyond the stopband of the grating - for this device with a $\kappa = 58.5$ cm$^{-1}$ the stopband width is about 173 GHz - we see that the dropped channel level starts to rise. The reason for this is that outside the stopband of the Bragg gratings, propagating modes are supported and normal waveguide-waveguide evanescent coupling results in power transfer from the bus to the access guides. This power transfer outside the stopband is troublesome. It leads to noise from the adjacent channels. Typically cross-talk from adjacent channels should be lower than 25 dB. However, as we see here the cross-talk levels rise as high as 10 dB. Normal waveguide-waveguide power transfer depends on $\mu_{12}L_T$, $\mu_{23}L_T$ products where $L_T$ is the total length of the coupled Bragg resonator system and given by

$$L_T = L_1 + L + L_2$$

where the lengths are defined in Fig. (5-7). The length $L$ is determined by the degeneracy condition and cannot be changed. If the lengths $L_1$ and $L_2$ could be shortened it would reduce the waveguide-waveguide coupling due to a smaller $(\mu_{ij}L_{1,2})$ product. The only consideration is that both these grating sections must be long enough to avoid power leakages from the resonators' ends. Since power loss is exponentially dependent on the $\kappa L_i$ product.
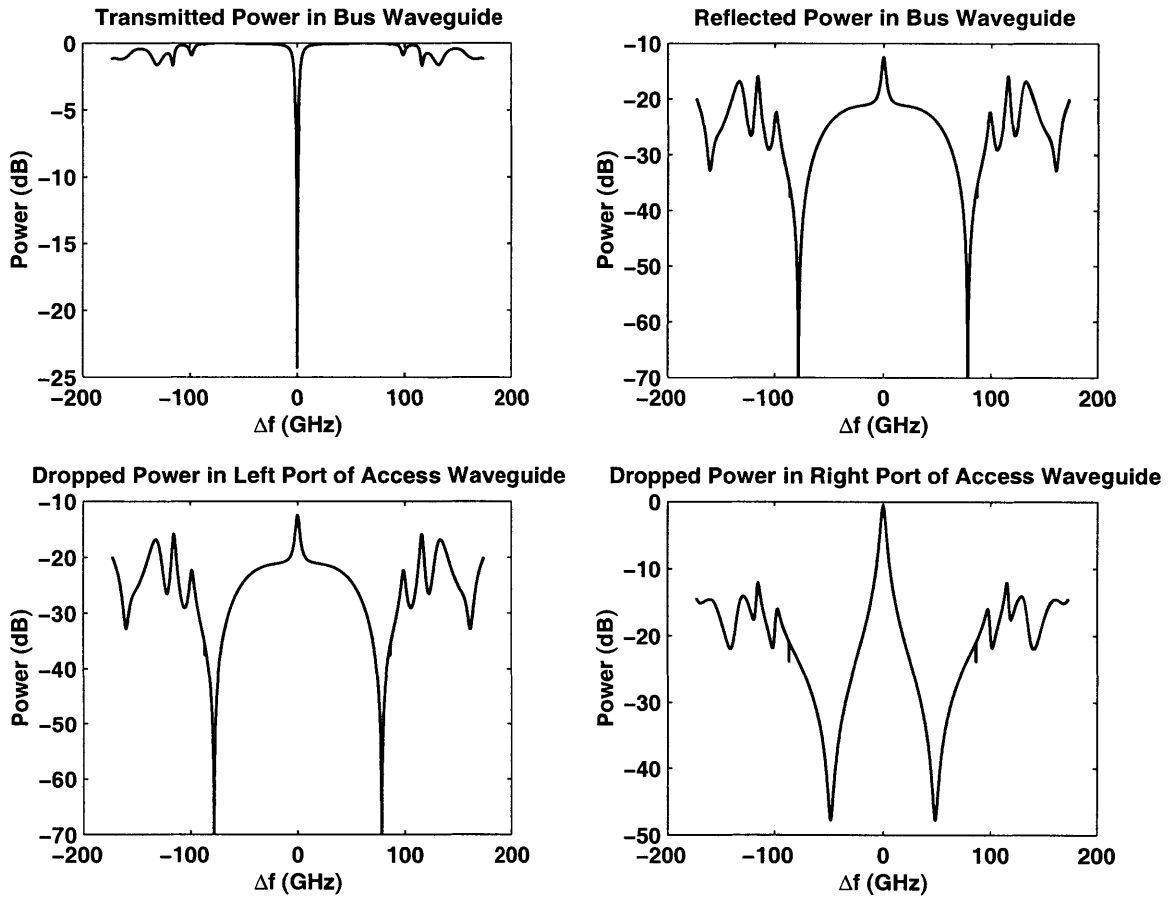
**Figure 5-10:** Spectral response at the various ports of a first-order push-pull add/drop filter.

$L_i$ must be on the order of a few inverse $\kappa$ lengths. If the $L_1$ and $L_2$ are not long enough it would translate to incomplete power extraction and transfer to the access guides. To reduce $(\mu_{ij}L_{1,2})$ product while keeping $\kappa L_{(1,2)}$ large enough we adopt the technique shown in Fig. (5-9) where the bus and access guides are bent out of the way of the resonators after a shorter distance. This way the waveguide-waveguide coupling is reduced whilst still avoiding leakage losses from the end of the resonator. An improvement in the adjacent channel cross-talk is evident by looking at spectrum of this device in Fig. (5-10)

Although the schematic implies that the waveguides are bent sharply out of the way, in practice the bends would have to be gradual enough to avoid high bend losses. For a filter of given 3 dB bandwidth there is a limit to how much we can gain using this technique. Broad bandwidth filters necessitate large coupling coefficients $\mu_{ij}$ which in turn exacerbates the out-of-band coupling problem. As a result in practice there is an upper bound to the maximum bandwidth that can be achieved using first-order add/drop filters in this configuration.

The device discussed in the this section is a first-order add/drop filter with a Lorentzian response. In order to achieve improved transfer characteristics such as low crosstalk from other channels and flattened resonance peaks, higher order filters are needed. In the next section the CMT-time is simply extended to the case of higher order filters consisting of multiple resonator pairs. The resonators are treated as lumped elements and the resulting continued fraction expressions provide a one-to-one correspondance with standard L-C filter design. An equivalent circuit is thus derived and a rough layout of the structure is based on handbook filter designs of circuit theory. A similar approach has already been used for cascaded resonators in [55] and [36]

## 5.4 $n^{th}$ Order Filter

A higher-order filter is made by generalizing the scheme described above. Instead of using one pair of resonators placed between two waveguides, $n$ pairs of resonators are evanescently coupled to each other as shown in Fig. (5-11). The resulting system behaves as an $n^{th}$ order filter that is capable of completely transfering the input power from the bus to the access guide waveguide. The $n^{th}$ order filter can be described in terms of coupled symmetric and antisymmetric modes of the pairs of resonators:
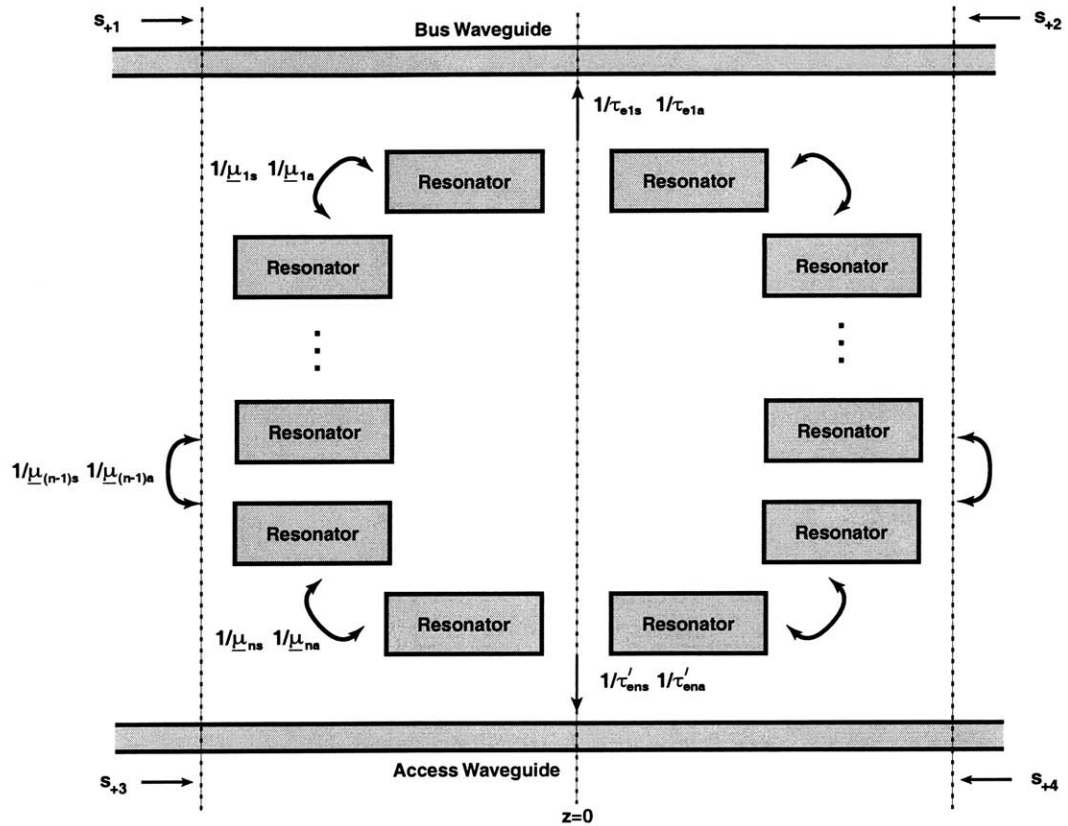
**Figure 5-11:** $n$-coupled pairs of Bragg resonators side-coupled to each other with the first and last pair side-coupled to the bus and access waveguides. The resulting system forms an $n^{th}$-order push-pull add/drop filter.

$$\frac{da_{1s}}{dt} = \left(j\omega_{1s} - \frac{1}{\tau_{es}}\right)a_{1s} + \underline{\kappa}_s(s_{+1} + s_{+2}) - j\underline{\mu}_{1s}\,a_{2s} \tag{5.68}$$

$$\frac{da_{2s}}{dt} = j\omega_{2s}a_{2s} - j\underline{\mu}_{1s}\,a_{1s} - j\underline{\mu}_{2s}\,a_{3s} \tag{5.69}$$

$$\vdots$$

$$\frac{da_{(n-1)s}}{dt} = j\omega_{(n-1)s}a_{(n-1)s} - j\underline{\mu}_{(n-2)s}\,a_{(n-2)s} - j\underline{\mu}_{(n-1)s}\,a_{ns} \tag{5.70}$$

$$\frac{da_{ns}}{dt} = \left(j\omega_{ns} - \frac{1}{\tau'_{es}}\right)a_{ns} - j\underline{\mu}_{(n-1)s}\,a_{(n-1)s} + \underline{\kappa}'_s(s_{+3} + s_{+4}) \tag{5.71}$$

$$\frac{da_{1a}}{dt} = \left(j\omega_{1a} - \frac{1}{\tau_{ea}}\right)a_{1a} + \underline{\kappa}_a(s_{+1} - s_{+2}) - j\underline{\mu}_{1a}\,a_{2a} \tag{5.72}$$

$$\frac{da_{2a}}{dt} = j\omega_{2a}a_{2a} - j\underline{\mu}_{1a}\,a_{1a} - j\underline{\mu}_{2a}\,a_{3a} \tag{5.73}$$

$$\vdots$$

$$\frac{da_{(n-1)a}}{dt} = j\omega_{(n-1)a}a_{(n-1)a} - j\underline{\mu}_{(n-2)a}\,a_{(n-2)a} - j\underline{\mu}_{(n-1)a}\,a_{na} \tag{5.74}$$

$$\frac{da_{na}}{dt} = \left(j\omega_{na} - \frac{1}{\tau'_{ea}}\right)a_{na} - j\underline{\mu}_{(n-1)a}\,a_{(n-1)a} + \underline{\kappa}'_a(s_{+3} - s_{+4}) \tag{5.75}$$

where $a_{is}$ and $a_{ia}$ represent the symmetric and antisymmetric mode amplitude of the $i^{th}$ resonator pair normalized to the energy in the mode, respectively. Likewise $\omega_{is}$ and $\omega_{ia}$ represent the resonance frequency of the $i^{th}$ resonator pair, $1/\tau_{es,a}$ $1/\tau'_{es,a}$ are the decay rates associated with the power lost by the symmetric or antisymmetric modes to the waveguides adjacent to the first and last pair of resonators, and $\underline{\mu}_{is,a}$ is the coupling between the symmetric modes and the antisymmetric modes respectively of the $i^{th}$ and $(i^{th}+1)$ resonator pair, real by power conservation. We note that the symmetric modes do not couple to the antisymmetric modes and vice versa. The coefficients $\underline{\kappa}_{s,a}$ and $\underline{\kappa}'_{s,a}$ associated with the coupling to the bus and the access guide, respectively, are found by power conservation to have the form:

$$\underline{\kappa}_{s,a} = \sqrt{\frac{1}{\tau_{es,a}}}\,e^{j\theta_{s,a}} \qquad \underline{\kappa}'_{s,a} = \sqrt{\frac{1}{\tau'_{es,a}}}\,e^{j\theta'_{s,a}} \tag{5.76}$$

The outgoing waves are described by:

$$s_{-1} = s_{+2} - \underline{\kappa}_s^*\,a_{1s} + \underline{\kappa}_a^*\,a_{1a} \tag{5.77}$$

$$s_{-2} = s_{+1} - \underline{\kappa}_s^*\,a_{1s} - \underline{\kappa}_a^*\,a_{1a} \tag{5.78}$$

$$s_{-3} = s_{+4} - \underline{\kappa}_s'^*\,a_{ns} + \underline{\kappa}_a'^*\,a_{na} \tag{5.79}$$

$$s_{-4} = s_{+3} - \underline{\kappa}_s'^*\,a_{ns} - \underline{\kappa}_a'^*\,a_{na} \tag{5.80}$$
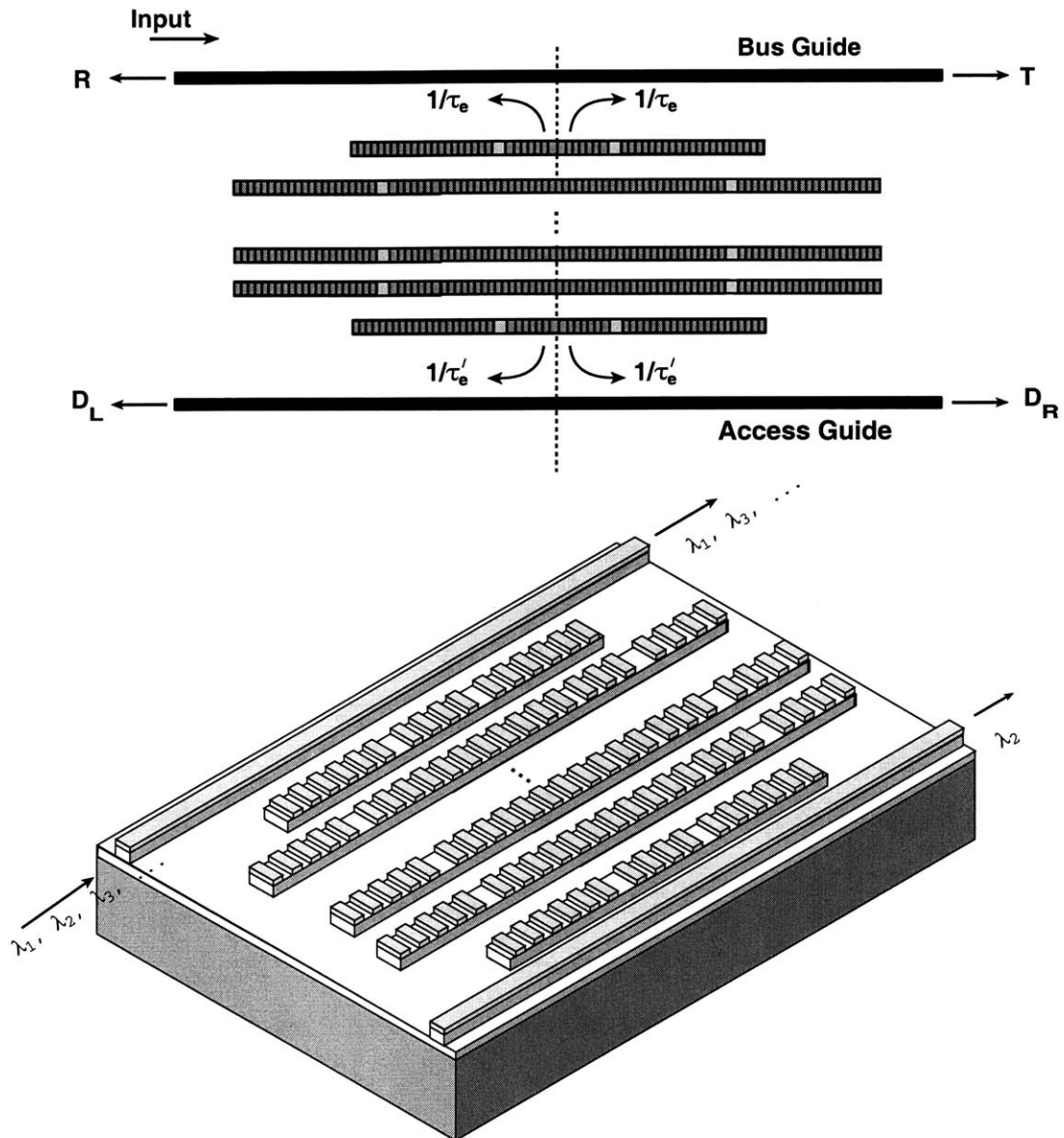
**Figure 5-12:** $n^{th}$-order push-pull add/drop filters; the first and last pair of coupled Bragg resonators are side-coupled to bus and access waveguides to balance direct coupling with coupling via waveguides to assure degeneracy of symmetric and antisymmetric modes. the intermediate $n - 2$ resonator pairs are uncoupled to ensure degeneracy.

In the following analysis we will assume for simplicity that the coupling coefficients are real. This can be accomplished by proper choice of the reference planes. A detailed analysis on how the phase of the coupling coefficients affects the filter response can be found in [57].

For the case that the system is excited only from one side of the bus, i.e: $s_{+2} = s_{+3} = s_{+4} = 0$ and $s_{+1}$ has a $e^{j\omega t}$ time dependence, we can find the mode amplitudes $a_{is,a}$ using the systems of equations (5.68)-(5.71) and (5.72)-(5.75):

$$a_{ns} = \frac{-j\underline{\mu}_{(n-1)s}\, a_{(n-1)s}}{j(\omega - \omega_{ns}) + \frac{1}{\tau'_{es}}} \equiv \frac{-j\underline{\mu}_{(n-1)s}\, a_{(n-1)s}}{D_{ns}} \tag{5.81}$$

$$a_{(n-1)s} = \frac{-j\underline{\mu}_{(n-2)s}\, a_{(n-2)s}}{j(\omega - \omega_{(n-1)s}) + \frac{\mu^2_{(n-1)s}}{j(\omega-\omega_{ns})+\frac{1}{\tau'_{es}}}} \equiv \frac{-j\underline{\mu}_{(n-2)s}\, a_{(n-2)s}}{D_{(n-1)s}} \tag{5.82}$$

$$a_{(n-2)s} = \frac{-j\underline{\mu}_{(n-3)s}\, a_{(n-3)s}}{j(\omega - \omega_{(n-2)s}) + \frac{\mu^2_{(n-2)s}}{j(\omega-\omega_{(n-1)s})+\frac{\mu^2_{(n-1)s}}{j(\omega-\omega_{ns})+\frac{1}{\tau'_{es}}}}} \equiv \frac{-j\underline{\mu}_{(n-3)s}\, a_{(n-3)s}}{D_{(n-2)s}} \tag{5.83}$$

$$\vdots$$

$$a_{1s} = \frac{\underline{\kappa}_s s_{+1}}{j(\omega - \omega_{1s}) + \frac{1}{\tau_{es}} + \frac{\mu^2_{1s}}{j(\omega-\omega_{2s})+\frac{\mu^2_{2s}}{j(\omega-\omega_{3s})+\cdots\frac{\mu^2_{(n-1)s}}{j(\omega-\omega_{ns})+\frac{1}{\tau'_{es}}}}}} \equiv \frac{\underline{\kappa}_s s_{+1}}{D_{1s}} \tag{5.84}$$

where $D_{is}$ is defined as the denominator associated with the expression for $a_{is}$. Note that the different $D_{is}$ are continued fractions of different order. Identical expressions exist for the antisymmetric mode amplitudes, $a_{ia}$, where the subscript $s$ is simply replaced by the subscript $a$, everything else remaining the same. Using (5.81)-(5.84) and (5.76) in (5.77) and (5.78) we get the reflected and transmitted waves on the bus guide:

$$\frac{s_{-2}}{s_{+1}} = 1 - \frac{1}{D_{1s}\tau_{es}} - \frac{1}{D_{1a}\tau_{ea}} \tag{5.85}$$

$$\frac{s_{-1}}{s_{+1}} = -\frac{1}{D_{1s}\tau_{es}} + \frac{1}{D_{1a}\tau_{ea}} \tag{5.86}$$

Solving for $a_{ns}$ and $a_{na}$, we find

$$a_{ns} = (\frac{-j\underline{\mu}_{(n-1)s}}{D_{ns}})(\frac{-j\underline{\mu}_{(n-2)s}}{D_{(n-1)s}})(\frac{-j\underline{\mu}_{(n-3)s}}{D_{(n-2)s}})\cdots(\frac{-j\underline{\mu}_{1s}}{D_{2s}})(\frac{\sqrt{\frac{1}{\tau_{es}}}s+1}{D_{1s}}) \qquad (5.87)$$

$$a_{na} = (\frac{-j\underline{\mu}_{(n-1)a}}{D_{na}})(\frac{-j\underline{\mu}_{(n-2)a}}{D_{(n-1)a}})(\frac{-j\underline{\mu}_{(n-3)a}}{D_{(n-2)a}})\cdots(\frac{-j\underline{\mu}_{1a}}{D_{2a}})(\frac{\sqrt{\frac{1}{\tau_{ea}}}s+1}{D_{1a}}) \qquad (5.88)$$

Use of the above yields the response at the remaining output ports:

$$\frac{s_{-3}}{s_{+1}} = -(\frac{-j\underline{\mu}_{(n-1)s}}{D_{ns}})(\frac{-j\underline{\mu}_{(n-2)s}}{D_{(n-1)s}})\cdots(\frac{-j\underline{\mu}_{1s}}{D_{2s}})(\frac{\sqrt{\frac{1}{\tau_{es}\tau'_{es}}}}{D_{1s}})$$

$$+ (\frac{-j\underline{\mu}_{(n-1)a}}{D_{na}})(\frac{-j\underline{\mu}_{(n-2)a}}{D_{(n-1)a}})\cdots(\frac{-j\underline{\mu}_{1a}}{D_{2a}})(\frac{\sqrt{\frac{1}{\tau_{ea}\tau'_{ea}}}}{D_{1a}}) \qquad (5.89)$$

and

$$\frac{s_{-4}}{s_{+1}} = -(\frac{-j\underline{\mu}_{(n-1)s}}{D_{ns}})(\frac{-j\underline{\mu}_{(n-2)s}}{D_{(n-1)s}})\cdots(\frac{-j\underline{\mu}_{1s}}{D_{2s}})(\frac{\sqrt{\frac{1}{\tau_{es}\tau'_{es}}}}{D_{1s}})$$

$$- (\frac{-j\underline{\mu}_{(n-1)a}}{D_{na}})(\frac{-j\underline{\mu}_{(n-2)a}}{D_{(n-1)a}})\cdots(\frac{-j\underline{\mu}_{1a}}{D_{2a}})(\frac{\sqrt{\frac{1}{\tau_{ea}\tau'_{ea}}}}{D_{1a}}) \qquad (5.90)$$

We consider the case where the resonators are designed such that the symmetric and anti-symmetric modes are all degenerate at frequency $\omega_o$, i.e

$$\omega_{is} = \omega_{ia} \equiv \omega_o \qquad\qquad i = 1, 2 \cdots n$$

and the decay rates of the symmetric and antisymmetric modes of the first and last pair of resonators are the same, i.e

$$\tau_{es} = \tau_{ea} \equiv \tau_e \qquad\qquad \tau'_{es} = \tau'_{ea} \equiv \tau'_e$$

The degeneracy condition for a pair of resonators adjacent to a waveguide can be satisfied by balancing the direct coupling between the resonators with the indirect coupling via the waveguide and by choosing the distance between the resonators to be an odd multiple of a quarter guided wavelength. For the resonator pairs that are not next to a waveguide, (i.e $i = 2, 3 \cdots n - 1$) the degeneracy can be achieved by placing the two resonators of each pair sufficiently far apart so that they are essentially uncoupled. The coupling between the symmetric modes and antisymmetric modes of adjacent pairs of resonators can also be made equal, i.e

$$\underline{\mu}_{is} = \underline{\mu}_{ia} \equiv \underline{\mu}_i \qquad\qquad i = 1, 2 \cdots n$$

This is possible if there is no cross coupling between resonators on either side of the symmetry plane that belong to different pairs. The above relationships imply that

$$D_{is} = D_{ia} \equiv D_i \qquad\qquad i = 1, 2 \cdots n$$

For this highly degenerate case, it is obvious, using eqs. (5.85) and (5.89), that the signal reflected on the bus and that dropped in port 3 of the access guide guide are identically zero over the entire bandwidth of the resonance, i.e

$$s_{-1} = s_{-3} = 0 \tag{5.91}$$

Also,

$$\frac{s_{-2}}{s_{+1}} = 1 - \frac{2}{D_1 \tau_e} \tag{5.92}$$

and

$$\frac{s_{-4}}{s_{+1}} = -2 \left( \frac{-j\underline{\mu}_{n-1}}{D_n} \right) \left( \frac{-j\underline{\mu}_{n-2}}{D_{n-1}} \right) \cdots \left( \frac{-j\underline{\mu}_1}{D_2} \right) \left( \frac{\sqrt{\frac{1}{\tau_e \tau_e'}}}{D_1} \right) \tag{5.93}$$

We note that the leading frequency term in the product $D_n D_{n-1} D_{n-2} \cdots D_1$ is $(-j)^n (\omega - \omega_o)^n$. Thus for high frequencies, the magnitude of $s_{-4}$ rolls off approximately as

$$\left| \frac{s_{-4}}{s_{+1}} \right| \approx \frac{\underline{\mu}_1 \underline{\mu}_2 \cdots \underline{\mu}_{n-1} \sqrt{1/\tau_e \tau_e'}}{(\omega - \omega_o)^n}$$

as expected for a $n^{th}$ order filter. It is possible to design the system to transfer the signal completely to the access guide guide on resonance. Moreover, it is possible to shape the frequency response of higher-order filters. In this case the spectral response can be engineered by choosing the appropriate coupling between adjacent resonators and the decay rates of the pairs of resonators next to the bus and access guide guides. In general, the selection of the appropriate amount of couplings between resonators for a higher-order filter, with $n > 2$, to achieve a desired spectral response is a tedious and non-trivial task and becomes increasingly harder as the order increases. If we are somehow able to map the coupled resonator system to a standard circuit used for implementing higher-order filters this task is reduced to looking up tabulated values of impedances to figure out the appropriate optical couplings and decay rates.

## 5.5   Equivalent Circuit

An equivalent circuit attempting to model the behaviour correctly at all four ports of the coupled resonator system must be a four port device. Such a circuit description would be
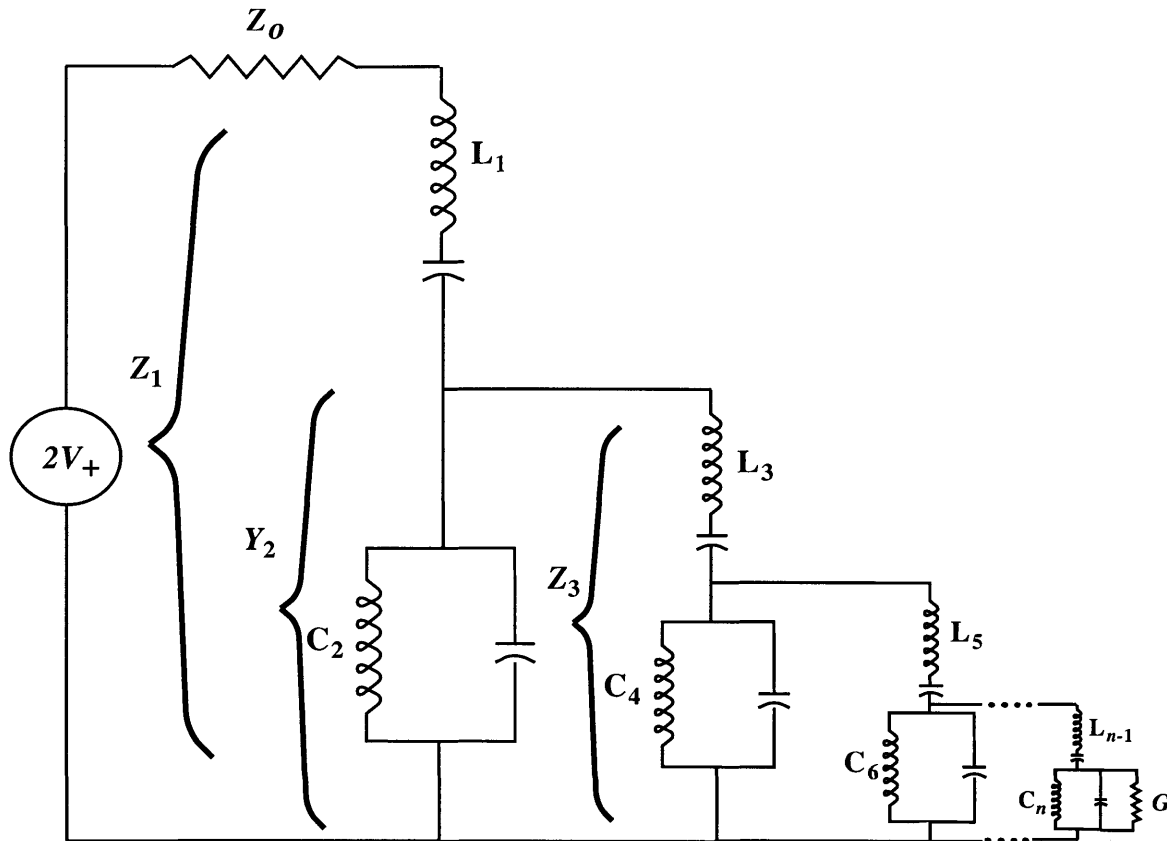
**Figure 5-13:** Proposed equivalent circuit of the $n^{th}$-order push-pull filter of Fig. (5-12)

difficult to work with. Instead, we concentrate on the port of primary interest, namely the access guide port $s_{-4}$ and derive a partial "equivalent" circuit which models the behavior of this port correctly. We are justified in following this approach as, in the degenerate case which is the case of interest, we already know the response at two ports, $s_{-1}$ and $s_{-3}$ to be identically zero over the bandwidth of interest and are really only interested in engineering the spectral response of $s_{-4}$.

The purpose of deriving the equivalent circuit of the stacked resonator system is to facilitate filter design by utilizing the extensive work already done on L-C ladder circuits [50]-[53]. Consider the ladder circuit shown in Fig. (5-13) consisting of alternating sections of series and parallel L-C circuits. This is a standard circuit used for designing higher-order filters. $Z_1$ is the impedance of the circuit looking into the ladder and $Y_2$ is the admittance of the ladder circuit beyond the first series L-C sub-circuit. Likewise $Z_3$ is the impedance looking beyond the first parallel L-C sub-circuit. In a similar fashion we define additional impedances and admittances, $Z_i$ and $Y_i$ with diminishing number of elements in them. The

choice of this notation will become clear shortly. Near resonance

$$Z_1 \approx 2j\Delta\omega L_1 + \cfrac{1}{2j\Delta\omega C_2 + \cfrac{1}{2j\Delta\omega L_3 + \cdots + \cfrac{1}{2j\Delta\omega L_{n-1} + \cfrac{1}{2j\Delta\omega C_n + G}}}} \tag{5.94}$$

$$Y_2 \approx 2j\Delta\omega C_2 + \cfrac{1}{2j\Delta\omega L_3 + \cdots + \cfrac{1}{2j\Delta\omega L_{n-1} + \cfrac{1}{2j\Delta\omega C_n + G}}} \tag{5.95}$$

$$Z_3 \approx 2j\Delta\omega L_3 + \cfrac{1}{2j\Delta\omega C_4 + \cdots + \cfrac{1}{2j\Delta\omega L_{n-1} + \cfrac{1}{2j\Delta\omega C_n + G}}} \tag{5.96}$$

$$\vdots$$

$$Y_n \approx 2j\Delta\omega C_n + G \tag{5.97}$$

For definiteness we have assumed that the order of the filter $n$ is an even number. We would follow similar procedures in the case of odd $n$. Moreover the impedances and admittances are expanded near the resonance frequencies of the L-C circuits which are assumed to be equal, i.e $L_i C_i = \omega_o^2$ for all $i$ with $\Delta\omega \equiv \omega - \omega_o$. The power, $P_d$, dissipated in the conductance $G$ of the last parallel L-C branch is given by

$$P_d = \frac{1}{2}\Re\{V_d I_d\}$$

where $V_d$ and $I_d$ are the voltage and current respectively across the conductance $G$. $V_d$ may be found using the voltage divider relationship repeatedly. We find

$$V_d = 2V_+ \left(\frac{Z_1}{Z_o + Z_1}\right)\left(\frac{\frac{1}{Y_2}}{Z_1}\right)\left(\frac{\frac{1}{Y_4}}{Z_3}\right)\cdots\left(\frac{\frac{1}{Y_n}}{Z_{n-1}}\right) \tag{5.98}$$

and

$$I_d = V_d G \tag{5.99}$$

Hence,

$$P_d = \frac{2|V_+|^2 G}{|(Z_o + Z_1)Y_2 Z_3 Y_4 \cdots Y_n|^2} \tag{5.100}$$

which can be normalized to

$$P_d = \frac{(GZ_o)}{\left|(1 + \frac{Z_1}{Z_o})(Y_2 Z_o)(\frac{Z_3}{Z_o})(Y_4 Z_o)\cdots(Y_n Z_o)\right|^2} 2|V_+|^2 Y_o \tag{5.101}$$

so that each factor in the fraction is dimensionless. The power captured by the access guide guide is given by

$$|s_{-4}|^2 = \frac{\frac{1}{\tau_e \tau_e'}\mu_1^2 \mu_2^2 \mu_3^2 \cdots \mu_{n-2}^2 \mu_{n-1}^2}{|D_1 D_2 D_3 \cdots D_{n-1} D_n|^2} |s_{+1}|^2 \tag{5.102}$$

which can be rewritten as:

$$|s_{-4}|^2 = \frac{\frac{\mu_2^2}{\mu_1^2}\frac{\mu_4^2}{\mu_3^2}\cdots\frac{\mu_{n-2}^2}{\mu_{n-1}^2}\frac{1}{\tau_e\tau_e'}}{\left|(D_1\tau_e)(D_2\frac{1}{\mu_1^2\tau_e})(D_3\frac{\mu_1^2\tau_e}{\mu_2^2})(D_4\frac{\mu_2^2}{\mu_1^2\mu_3^2\tau_e})\cdots(D_n\frac{\mu_2^2}{\mu_1^2}\frac{\mu_4^2}{\mu_3^2}\cdots\frac{\mu_{n-2}^2}{\mu_{n-1}^2}\frac{1}{\tau_e})\right|^2}|s_{+1}|^2 \qquad (5.103)$$

again so that each factor in the fraction is dimensionless. Comparing the above expressions for $P_d$ and $|s_{-4}|^2$ we see that they are similar in form provided we draw the following correspondence.

$$1 + \frac{Z_1}{Z_o} \longleftrightarrow D_1\tau_e \qquad (5.104)$$

$$Y_2 Z_o \longleftrightarrow D_2\frac{1}{\mu_1^2\tau_e} \qquad (5.105)$$

$$\frac{Z_3}{Z_o} \longleftrightarrow D_3\frac{\mu_1^2\tau_e}{\mu_2^2} \qquad (5.106)$$

$$\vdots$$

$$Y_n Z_o \longleftrightarrow D_n\frac{\mu_2^2}{\mu_1^2}\frac{\mu_4^2}{\mu_3^2}\cdots\frac{\mu_{n-2}^2}{\mu_{n-1}^2}\frac{1}{\tau_e\tau_e'} \qquad (5.107)$$

$$G Z_o \longleftrightarrow \frac{\mu_2^2}{\mu_1^2}\frac{\mu_4^2}{\mu_3^2}\cdots\frac{\mu_{n-2}^2}{\mu_{n-1}^2}\frac{1}{\tau_e\tau_e'} \qquad (5.108)$$

It appears that there are too many constraints present for a mapping between $P_d$ and $|s_{-4}|^2$ to exist but we will see that the mapping enforced by the first equation encompasses the others and the remaining equations are redundant. This is obvious if we consider the special relationship that exists between $D_i$ and $D_{i+1}$ and between $Z_i$ and $Y_{i+1}$. Specifically, we note that

$$D_1 = j(\omega - \omega_o) + \frac{1}{\tau_e} + \frac{\mu_1^2}{D_2} \qquad (5.109)$$

$$Z_1 = 2j(\omega - \omega_o)L_1 + \frac{1}{Y_2}, \qquad (5.110)$$

as is obvious from equations (5.93),(5.94) and (5.95). It follows that

$$D_1\tau_e = 1 + j(\omega - \omega_o)\tau_e + \frac{1}{D_2\frac{1}{\mu_1^2\tau_e}} \qquad (5.111)$$

$$1 + \frac{Z_1}{Z_o} = 1 + j(\omega - \omega_o)\frac{2L_1}{Z_o} + \frac{1}{Y_2 Z_o} \qquad (5.112)$$

Thus, the correspondence in equation (5.105) is satisfied.

$$Y_2 Z_o \longleftrightarrow D_2\frac{1}{\mu_1^2\tau_e}$$

Similar reasoning can be used to show that the correspondence expressed by eq. (5.106) is contained in equation (5.105). By extension it follows that all other correspondences are contained in equation (5.105). For an equivalence to exist, the form of $D_1\tau_e$ mutst be the same as that of $1 + \frac{Z_1}{Z_o}$. We note that

$$1 + \frac{Z_1}{Z_o} = 1 + j\Delta\omega\frac{2L_1}{Z_o} + \cfrac{1}{j\Delta\omega 2C_2 Z_o + \cfrac{1}{j\Delta\omega\frac{2L_3}{Z_o}+\cdots+\cfrac{1}{j\Delta\omega\frac{2L_{n-1}}{Z_o}+\frac{1}{2j\Delta\omega C_n Z_o+GZ_o}}}} \qquad (5.113)$$

has a continued fraction form identical to

$$D_1\tau_e = 1 + j(\omega-\omega_o)\tau_e + \cfrac{1}{\frac{j(\omega-\omega_o)}{\underline{\mu}_1^2\tau_e} + \cfrac{1}{j(\omega-\omega_o)\frac{\underline{\mu}_1^2\tau_e}{\underline{\mu}_2^2}+\cdots \cfrac{1}{\left(j(\omega-\omega_o)+\frac{1}{\tau_e'}\right)\left[\frac{\underline{\mu}_{n-2}^2}{\underline{\mu}_{n-1}^2}\cdots\frac{\underline{\mu}_4^2}{\underline{\mu}_3^2}\frac{\underline{\mu}_2^2}{\underline{\mu}_1^2}\frac{1}{\tau_e}\right]}}} \qquad (5.114)$$

In fact there is a term by term correspondence between the two expressions which provides a mapping between the circuit and the optical resonator parameters. This proves that the postulated circuit of Fig. (5-13 is indeed the equivalent circuit representation of the access guide port of the coupled resonator system. Consider equation (5.103); on resonance, $\omega = \omega_o$, it is obvious that

$$|s_{-4}|^2 = \frac{\underline{\mu}_2^2}{\underline{\mu}_1^2}\frac{\underline{\mu}_4^2}{\underline{\mu}_3^2}\cdots\frac{1}{\underline{\mu}_{n-1}^2}\frac{1}{\tau_e\tau_e'}|s_{+1}|^2$$

Complete power transfer is then possible on resonance if

$$\frac{\underline{\mu}_2^2}{\underline{\mu}_1^2}\frac{\underline{\mu}_4^2}{\underline{\mu}_3^2}\cdots\frac{\underline{\mu}_{n-2}^2}{\underline{\mu}_{n-1}^2}\frac{1}{\tau_e\tau_e'} = 1 \qquad (5.115)$$

or equivalently if we use the correspondence implied by eq. (5.108) when $G = Y_o$. This should be obvious if we consider the equivalent circuit. On resonance the series L-C branches are shorted and the parallel L-C branches are open. The load $G$ is directly connected to the source and perfect transfer is only possible for a matched load. For odd $n$ the condition for complete power transfer on resonance would be:

$$\frac{\underline{\mu}_2^2}{\underline{\mu}_1^2}\frac{\underline{\mu}_4^2}{\underline{\mu}_3^2}\cdots\frac{\underline{\mu}_{n-2}^2}{\underline{\mu}_{n-1}^2}\frac{\tau_e'}{\tau_e} = 1 \qquad (5.116)$$

In the following section we will design a $4^{th}$-order Butterworth filter using mappings provided by the equivalent circuit.
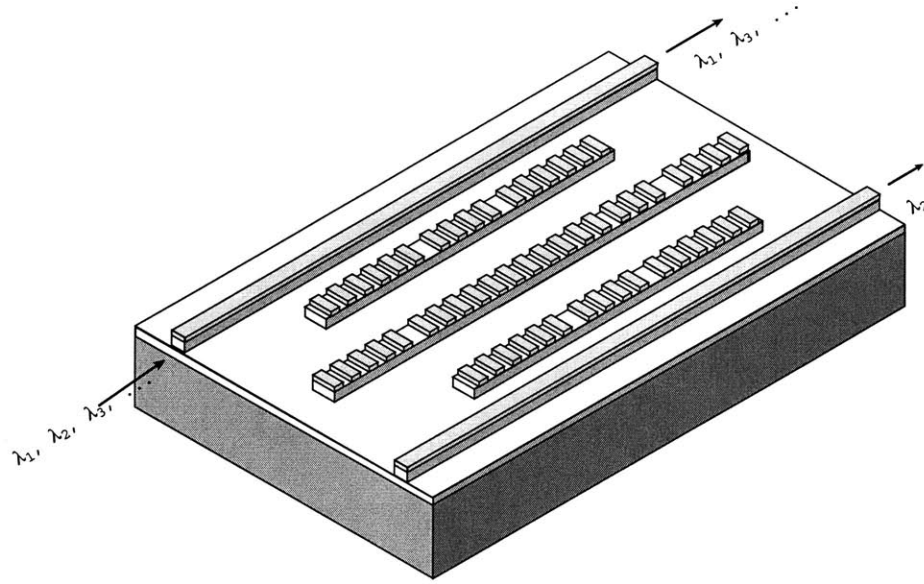
**Figure 5-14:** Third-order filter of made using three pairs of Bragg resonators with first and last pair side-coupled to bus and access guides

## 5.6   Example: $3^{rd}$-Order Filter

As an example of a higher order filter, we consider the coupled resonator system shown in Fig. (5-14) consisting of 3 pairs of resonators side-coupled to their nearest neighbors. All the pairs are designed so that their respective symmetric and antisymmetric modes are degenerate at frequency $\omega_o$ and the decay rates, $\tau_e$, and coupling coefficients, $\underline{\mu}_i$ are assumed to be the same for the symmetric and antisymmetric modes i.e.

$$\omega_{is,a} \equiv \omega_o$$

$$\tau_{es,a} \equiv \tau_e$$

$$\tau'_{es,a} \equiv \tau'_e$$

$$\underline{\mu}_{is,a} \equiv \underline{\mu}_i$$

For $n = 3$, eqs. (5.114) and (5.113) give

$$D_1\tau_e = 1 + j(\omega - \omega_o)\tau_e + \cfrac{1}{j(\omega - \omega_o)\frac{1}{\underline{\mu}_1^2\tau_e} + \cfrac{1}{j(\omega-\omega_o)\frac{\underline{\mu}_1^2\tau_e}{\underline{\mu}_2^2} + \frac{\underline{\mu}_1^2\tau_e}{\underline{\mu}_2^2\tau'_e}}} \tag{5.117}$$

$$1 + \frac{Z_1}{Z_o} = 1 + j(\omega - \omega_o)\frac{2L_1}{Z_o} + \cfrac{1}{j(\omega - \omega_o)2C_2Z_o + \cfrac{1}{j(\omega-\omega_o)\frac{2L_3}{Z_o} + \frac{R}{Z_o}}} \tag{5.118}$$

Using the correspondence given by eq. (5.105) we find the following mapping between the circuit parameters and the optical parameters.

$$\tau_e \longleftrightarrow \frac{2L_1}{Z_o} \tag{5.119}$$

$$\frac{1}{\underline{\mu}_1^2 \tau_e} \longleftrightarrow 2C_2 Z_o \tag{5.120}$$

$$\frac{\underline{\mu}_1^2 \tau_e}{\underline{\mu}_2^2} \longleftrightarrow \frac{2L_3}{Z_o} \tag{5.121}$$

$$\frac{\underline{\mu}_1^2 \tau_e}{\underline{\mu}_2^2 \tau_e'} \longleftrightarrow \frac{R}{Z_o} \tag{5.122}$$

These mappings can be rewritten as

$$\tau_e \longleftrightarrow \frac{2L_1}{Z_o} \tag{5.123}$$

$$\underline{\mu}_1 \longleftrightarrow \frac{1}{2\sqrt{L_1 C_2}} \tag{5.124}$$

$$\underline{\mu}_2 \longleftrightarrow \frac{1}{2\sqrt{C_2 L_3}} \tag{5.125}$$

$$\tau_e' \longleftrightarrow \frac{2L_3}{R} \tag{5.126}$$

For the $n^{th}$-order filter the couplings between the resonators are given by

$$\underline{\mu}_i \longleftrightarrow \frac{1}{2\sqrt{L_i C_{i+1}}} \qquad i \text{ odd} \tag{5.127}$$

$$\underline{\mu}_i \longleftrightarrow \frac{1}{2\sqrt{C_i L_{i+1}}} \qquad i \text{ even} \tag{5.128}$$

with $i = 1, 2 \cdots n$. To design a higher-order filter we look up filter design tables which give the values of inductances and capacitances needed to obtain the desired spectral response. Using the above mappings we obtain the coupling and decay parameters needed. Eqs. (5.60), (5.61) and (5.62) relate the CMT-time parameters to the CMT-space parameters. Note that the coupling coefficients can be found by inspection from the equivalent circuit once its inductances and capacitances have been chosen. This technique was used to design a $3^{rd}$-order Chebychev filter. The response at the various output ports of the coupled resonator system is shown in Fig. (5-15). The right access guide port has the characteristic Chebychev response. The device has a 3 dB bandwidth of 11 GHz. The adjacent channel crosstalk is below 25 dB. In transmission, the dropped channel is suppressed in excess of 25 dB.
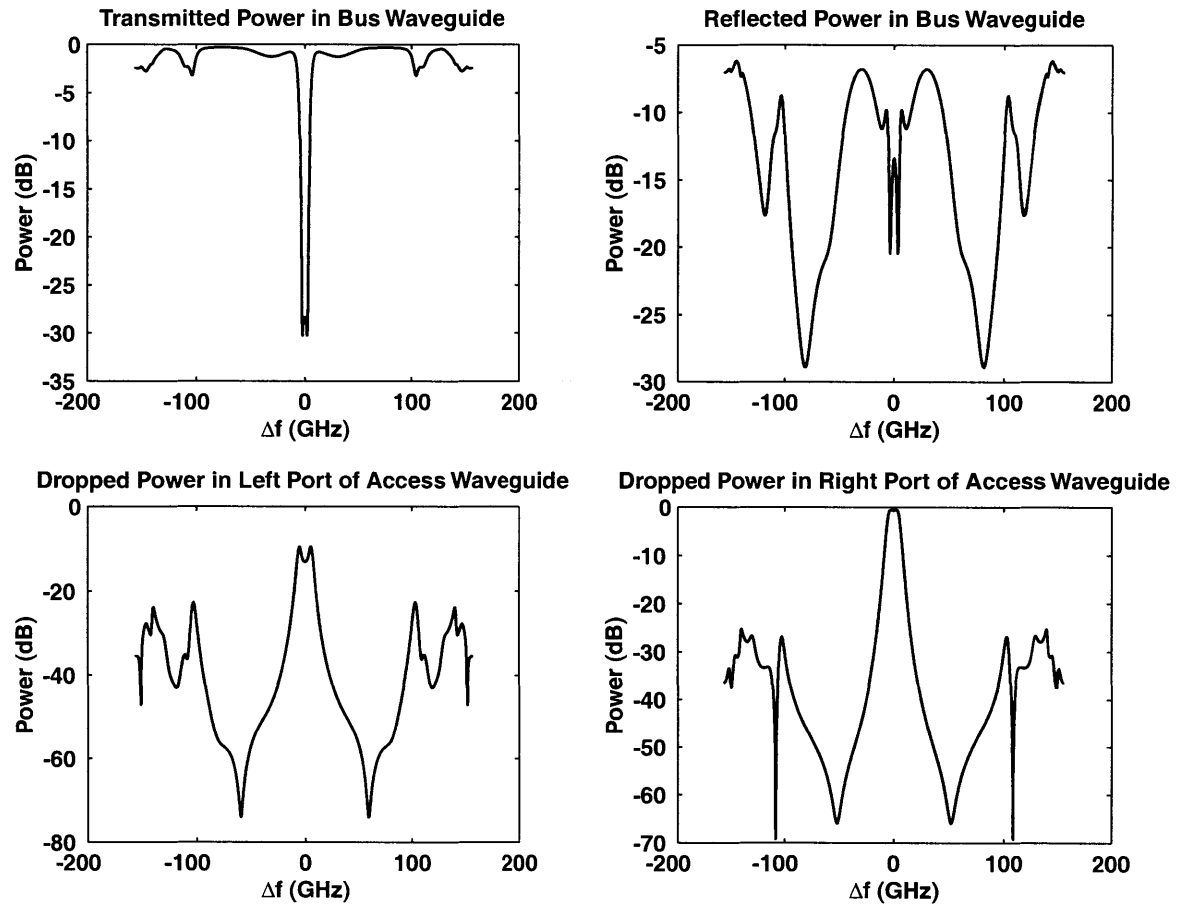
**Figure 5-15:** Spectrum of third-order push-pull filter of Fig. (5-14)

# Appendix

In order to calculate the coupling coefficients involved in the four-port system of Fig. 1 we examine the coupling to one waveguide at a time starting with the bus waveguide and following a treatment similar to [20]. This approach is valid if we assume weak coupling. Under the same assumption the spatial variation of the waveguide mode amplitudes can be described by coupled mode equations of the form:

$$\frac{d}{dz}b_\pm(z) = \mp j\beta b_\pm(z) + \underline{\kappa}_\pm(z)a \tag{5.129}$$

where $b_\pm(z)$ is the amplitude of the forward/backward waveguide mode in the bus, $\beta$ is the propagation costant and $\underline{\kappa}_\pm(z)$ describes the distributed coupling to the resonator. For reference planes located at $z = z_1$ and $z = z_2$ we have:

$$b_\pm(z_1) \quad = \quad s_{\pm 1} \tag{5.130}$$

$$b_\pm(z_2) \quad = \quad s_{\mp 2} \tag{5.131}$$

The rate of change of the waveguide mode power along $z$ is equal to the power coupled per unit length to the polarization current due to the index perturbation that the resonator mode experiences in the presence of the waveguide. The assumed electric field distribution in the waveguide is $b_+(z)\vec{e}_+(x,y) + b_-(z)\vec{e}_-(x,y)$ where $\vec{e}_\pm(x,y)$ is the unperturbed forward/backward mode profile normalized to *unit power*. In the resonator the assumed electric field distribution is $a(t)\vec{e}_r(x,y,z)$ where $\vec{e}_r(x,y,z)$ is the uncoupled resonator mode field normalized to *unit energy*. Using Poynting's theorem at steady state we have:

$$\pm\frac{d}{dz}|b_\pm|^2 = -j\frac{\omega\epsilon_o}{4}\iint dxdy(n^2 - n_r^2)\vec{e}_r \cdot \vec{e}_\pm^* ab^* + c.c. \tag{5.132}$$

where $n(x,y,z)$, $n_r(x,y,z)$ are the index distributions of the total system and the resonator, respectively. In this equation we have neglected a $z$-dependent self-coupling term

$$-j\frac{\omega\epsilon_o}{4}\iint dxdy(n^2 - n_r^2)\vec{e}_\pm \cdot \vec{e}_\pm^* ab^*$$

that modifies the propagation constant. From (5.129) we have:

$$\frac{d}{dz}|b_\pm|^2 = \underline{\kappa}_\pm ab^* + c.c. \tag{5.133}$$

Comparing (5.132) and (5.133) we have:

$$\underline{\kappa}_\pm(z) = \mp j\frac{\omega\epsilon_o}{4}\iint dxdy(n^2 - n_r^2)\vec{e}_r \cdot \vec{e}_\pm^* \tag{5.134}$$

We integrate (5.129) using the boundary conditions (5.130) and (5.131) and equation (5.134) to find the amplitudes of the outgoing waves as:

$$s_{-1} = e^{-j\beta(z_2-z_1)} \left( s_{+2} - j\frac{\omega\epsilon_o}{4} \int_{z_1}^{z_2} dz \iint dxdy(n^2 - n_r^2)\vec{e}_r \cdot \vec{e}_+^* e^{j\beta(z-z_1)}a \right) \quad (5.135)$$

$$s_{-2} = e^{-j\beta(z_2-z_1)} \left( s_{+1} - j\frac{\omega\epsilon_o}{4} \int_{z_1}^{z_2} dz \iint dxdy(n^2 - n_r^2)\vec{e}_r \cdot \vec{e}_-^* e^{-j\beta(z-z_2)}a \right) \quad (5.136)$$

The input coupling coefficients $\underline{\kappa}_{1,2}$ can be found by power conservation. Neglecting the loss, the rate of change of the energy in resonator mode must be equal to the difference between the incoming and outgoing power.

$$\frac{d|a|^2}{dt} = |s_{+1}|^2 + |s_{+2}|^2 - |s_{-1}|^2 - |s_{-2}|^2 \quad (5.137)$$

Also, from equation (5.1) with $1/\tau_e' = 0$ and $\underline{\kappa}_3 = \underline{\kappa}_4 = 0$, and have:

$$\frac{d}{dt}|a|^2 = -\frac{2}{\tau_e}|a|^2 + (\underline{\kappa}_1 s_{+1}a^* + c.c.) + (\underline{\kappa}_2 s_{+2}a^* + c.c.) \quad (5.138)$$

Substituting (5.135) and (5.136) into (5.137) and comparing with (5.138) we have:

$$\underline{\kappa}_1 = -j\frac{\omega\epsilon_o}{4} \int_{z_1}^{z_2} dz \iint dxdy(n^2 - n_r^2)\vec{e}_r^* \vec{e}_+ e^{-j\beta(z-z_1)}$$

$$\underline{\kappa}_2 = -j\frac{\omega\epsilon_o}{4} \int_{z_1}^{z_2} dz \iint dxdy(n^2 - n_r^2)\vec{e}_r^* \vec{e}_- e^{j\beta(z-z_2)}$$

and

$$|\underline{\kappa}_1|^2 + |\underline{\kappa}_2|^2 = \frac{2}{\tau_e}$$

With $z_2 - z_1 = l$ the outgoing waves can be now written as:

$$s_{-1} = e^{-j\beta l}\left(s_{+2} - \underline{\kappa}_2^* a\right)$$

$$s_{-2} = e^{-j\beta l}\left(s_{+1} - \underline{\kappa}_1^* a\right)$$

The same analysis yields analogous expressions for the input and output coupling coefficients related to the access guide waveguide.

# Chapter 6

# Measurements and

# Characterizations

Thus far, the thesis has focussed on design and modelling of integrated Bragg grating resonator devices. We have discussed in depth what kinds of devices are possible; how they are designed and what are their constraints and limitations. We now present measurements that were made on a host of preliminary devices. The purpose of this chapter is two-fold; it describes a measurement process that is suitable for high-index material based integrated optical devices and it presents the results. The results are used to extract optical parameters like the grating strength, $\kappa$, the group index, $n_g$, and the bandwidth, $\Delta\omega$, of the various devices. These are then compared to the theoretical design values to gauge the fidelity of the design and fabrication process. Discrepancies are explained.

## 6.1 Fabricated Devices

Fig. (6-1) shows the hierarchy of devices that were fabricated on the test chip. They range from simple waveguides to higher-order side-coupled integrated Bragg gratings based filters. The reason to fabricate increasing complex devices was to enable the identification of failure mode if a device did not work. All devices were comprised of three basic components: (1) waveguide (2) Bragg grating and (3) Bragg resonators. The design of the each of these components in the transverse cross-section was the same from device to device. The physical specifications and design of the waveguide, Bragg gratings and Bragg resonators is shown in Fig. (6-2).
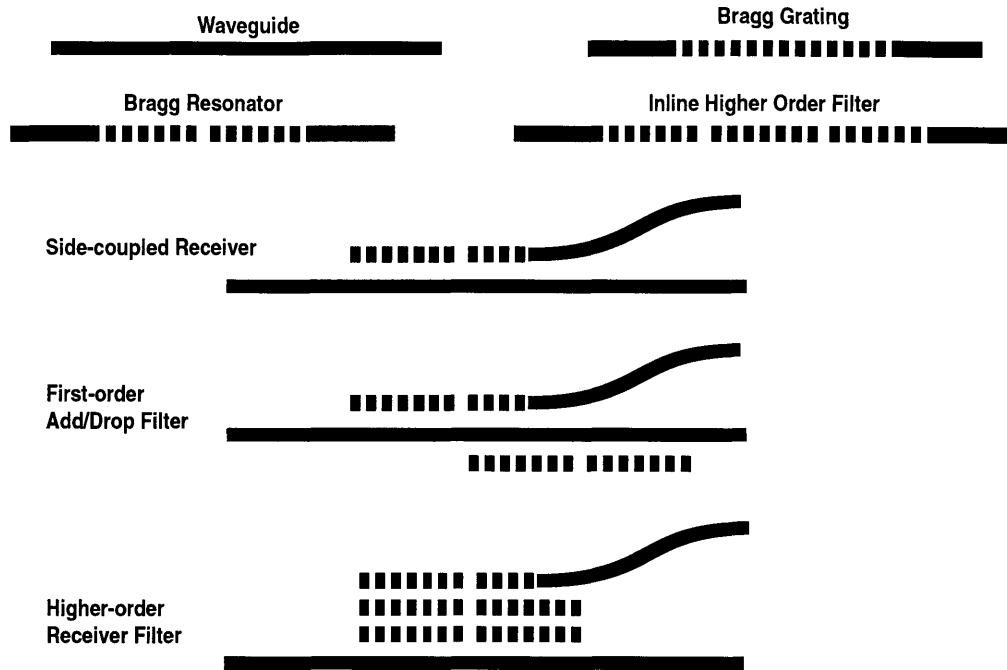
**Figure 6-1:** Hierarchy of devices that were fabricated on the optical chip.

A channel waveguide with an InGaAsP core and a InP cladding was used. InGaAsP was grown epitaxially on an InP substrate; the refractive index of the core, $n_{co}$, based on the growth was estimated to be about 3.29. A layer of InP, indicated by the semi-transparent layer on top, Fig. (6-2)) was then overgrown to form the top cladding for all the devices. The index of the cladding region was estimated to be 3.166. The dimensions of the guide were chosen to yield a single-moded structure. An important consideration of the design involved choosing the waveguide width appropriate to yield a propagation constant identical to that of the grating guides.

The physical dimensions of the Bragg gratings and resonators are as shown in Fig. (6-2). The grating period, $\lambda_g = 244$ nm, was chosen such that the center wavelength, $\lambda_o$ of the filters was 1557 nm. The relationship between the grating period and center wavelength is

$$\lambda_g = \frac{\lambda_o}{2n_{eff}}$$

where $n_{eff}$ is the effective index of the grating guides. The grating etch depth was chosen to be about 220 nm. This depth was chosen to yield a moderate grating strength, $\kappa \approx 60$ cm$^{-1}$. One reason for designing devices with a moderate $\kappa$ was to limit radiation losses from gratings; another reason was ease of fabrication. Deep vertical etches with smooth walls are non-trivial and overgrowth of a uniform top cladding layer presents even more
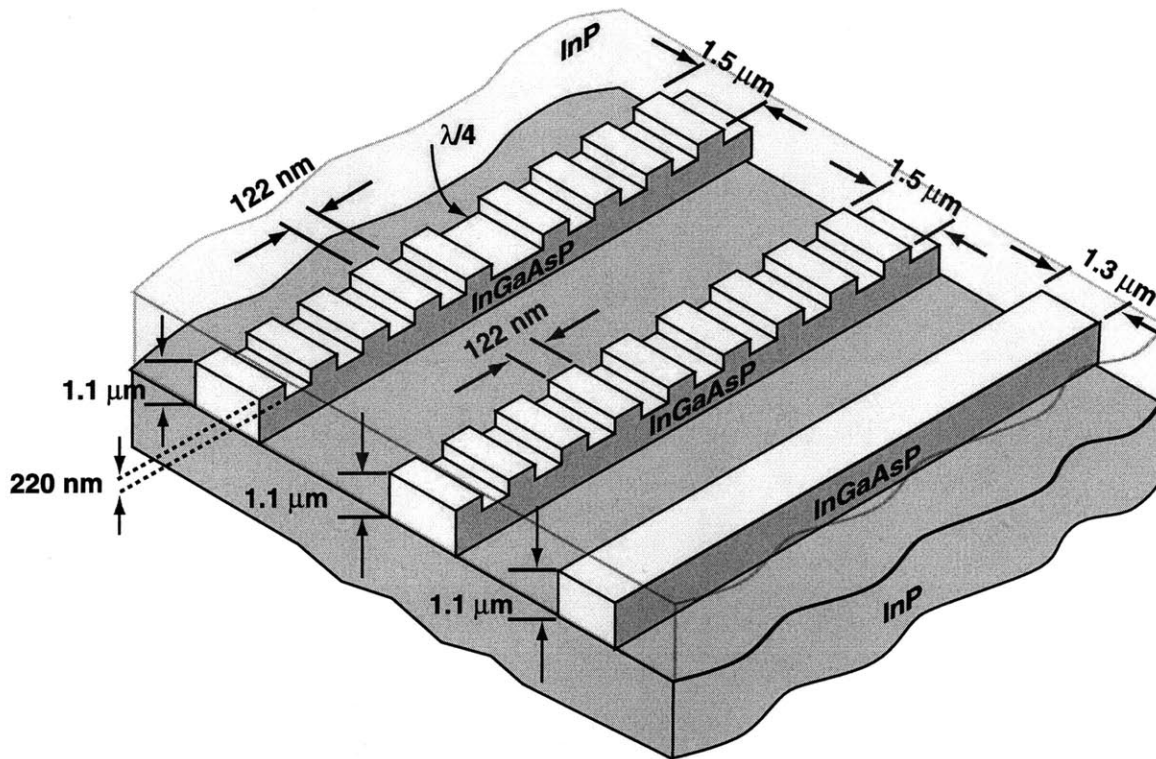
**Figure 6-2:** Waveguide, Bragg grating and Bragg resonator. These three components were used in making all the devices shown in Fig. (6-1)

challenges. If the overgrowth is not smooth or incomplete it can lead to high losses due to scattering at the interface between the core and the cladding. These considerations led to the design of moderate grating strength structures.

Notice that the width of the grating guides is larger than that of the simple waveguide. This was chosen such that the propagation constant of the grating guide and the simple waveguide were equal. Since the average effective index in the region of the grating is lowered relative to the core index, a wider guide is needed to compensate for this and result in a propagation constant equal to a guide without a grating. As mentioned in section 4.3.7 the performance of the side-coupled devices relies critically on having identical propagation constants. Designing dissimilar guides to have equal propagation constant was discussed in detail in [45]. This design is very sensitive to the starting core index, $n_{co}$, and any variation of the $n_{co}$ from its assumed value can result in designs where the propagation constants of the grating and bus guides are mismatched. This makes the design of side-coupled devices quite challenging. As can be expected the fabrication of these devices is a very involved and challenging task. The fabrication process of these devices
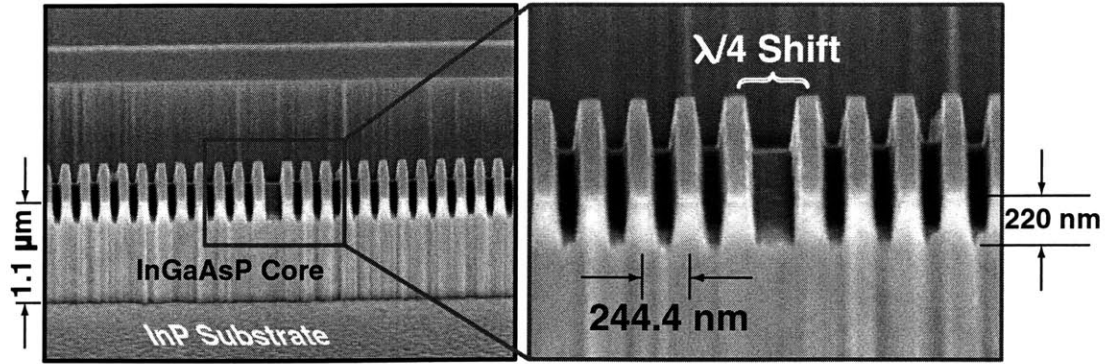
**Figure 6-3:** SEM of an Bragg resonator prior to overgrowth of the top cladding layer of InP. The precise quarter-wave shift is clearly visible. The measured dimensions are very close to the design specifications.
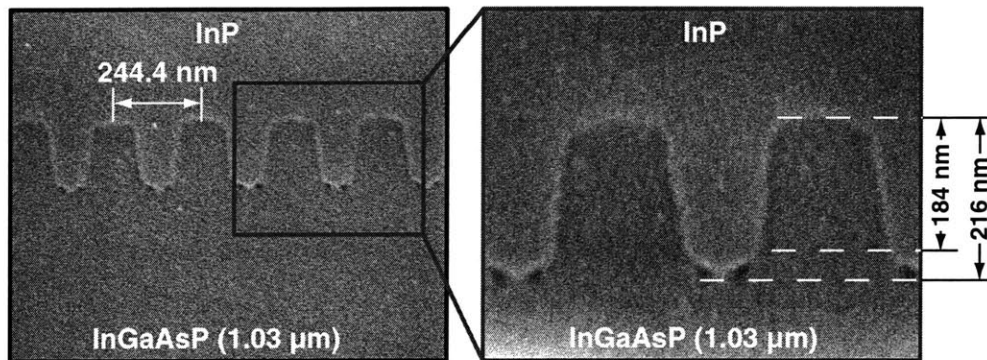


**Figure 6-4:** SEM of the overgrown InP top cladding layer. The grating teeth are preserved and clearly visible; the overgrowth is complete and without any major defects; a slight softening of the grating teeth is visible but is not expected to affect measured results by much.

uses a combination of x-ray masks and optical masks. The x-ray masks that were created using a scanning e-beam ligthography tool were used for defining the fine gratings features including the precise phase-shifts; the contact optical masks were used to define the courser waveguide features. The fabrication process [63] was the result of development over years intended to overcome significant challenges and the various aspects of it are discussed in two separate PhD dissertations [64, 65] . The readers are referred to these dissertations for a detailed review of the fabrication process. Figs. (6-3) and (6-4) shows the scanning electron micrographs of the fabricated structure. The quarter-wave shift is clearly visible in the figure. Its important to note that the shift is not a missing tooth but is rather a precise phase-shift which reverses the phase of the grating beyond the shift. The other figure shows
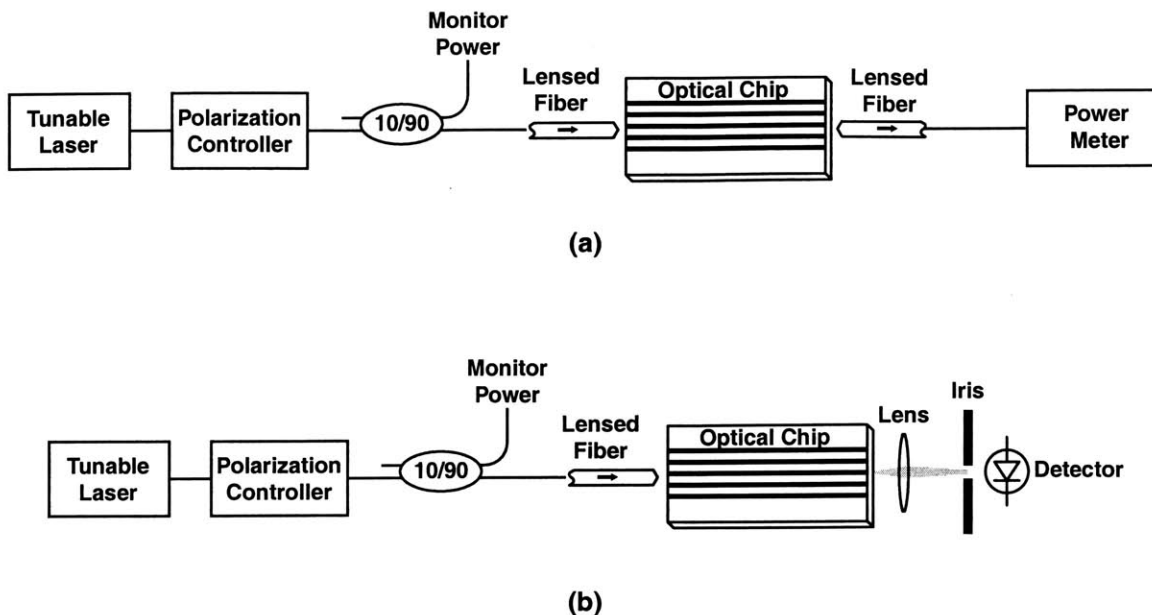
Figure 6-5: A schematic of the measurement setup used to characterize the devices.

the result of overgrowth of the top cladding above the gratings. We see that the profile of the gratings is maintained though slightly "softened". Overgrowth is a high-temperature process and it requires care to ensure that the gratings profiles are maintained and not washed away. We can see that the overgrowth is smooth and complete. The overgrowth was performed at Lucent Technologies by Dr. C. Joyner's group.

## 6.2 Measurement Setup and Process

### 6.2.1 Setup

The setup used to conduct the measurement is shown in Fig. (6-5 (a)). The input source to the devices is a tunable laser which is connected to a polarization controller. The purpose of the polarization controller is to set the input polarization state of the light feeding the devices so as to be able to individually measure the TE and TM response. The polarization controller can be bypassed to compare the unpolarized response with the polarized input response. This will allow the birefringence of the devices to be estimated. The light from the polarization controller is fed into a lensed fiber via a 10/90 power splitter. The purpose of the splitter is to serve as a power monitor enabling any power drifts of the tunable laser source to be normalized out as the wavelength is scanned . The light from the 10 % arm is

fed into channel B of the power meter. The lensed fiber has a 140° conical tip which acts like a lens squeezing the mode of a standard fiber by about 80 %. Since the waveguide modes are considerably smaller than the 10 $\mu$m mode field diameter of a standard single-mode fiber, the lens fiber is necessary to ensure good coupling between the input fiber mode and the individual on-chip devices. At the output the light is captured from the guides using another lensed fiber placed in close proximity to the output facet and is fed into channel A of the power meter.

Other options to extract the light from the chip are also available. An alternative to using the output lensed fiber is to use a lens objective to focus the light onto a large area photodetector via an iris as shown in Fig. (6-5 (b)). The purpose of the iris is to eliminate stray light travelling through the substrate. We will see in the following sections that stray light acts as a noise floor and limits the accuracy of the measurements. If the guided modes need to be visually inspected the photodetector can be replaced with an IR camera connected to a TV monitor. By comparing the alternate options it was determined that a lensed fiber at the output provided the best discrimination between guided light and noise and was thus the method of choice. The input lensed fiber, the optical chip and the output lensed fibers are all placed on separate piezo-electrically controlled stages which enable precise alignment of the optics. The whole setup is on a vibration isolated optical table as misalignments on the order of a micron can render the measurements inaccurate.

### 6.2.2   Process

Ideally we would like to control the polarization state of the input light by inserting a polarizer between the lensed fiber and the optical chip. However, since the focal length of the lensed fiber is on the order of 20 $\mu$m its impossible to insert a polarizer between the fiber and the chip. As a result, the polarization state of the input laser light to the chip is set by using an HP Polarization Controller. This is done prior to performing the measurements. The light from lensed fiber is passed through a polarizer, while the chip is not in place. The polarizer is adjusted to the state orthogonal to the desired state, (TM for TE input), and the polarization controller waveplates are adjusted to minimize the power in this polarization state. The power is measured using a large-area photodetector. Once light in this state is minimized we are assured the input laser light is primarily polarized in the desired state. Since the lensed fiber and the fiber patch-cords leading up to it, are
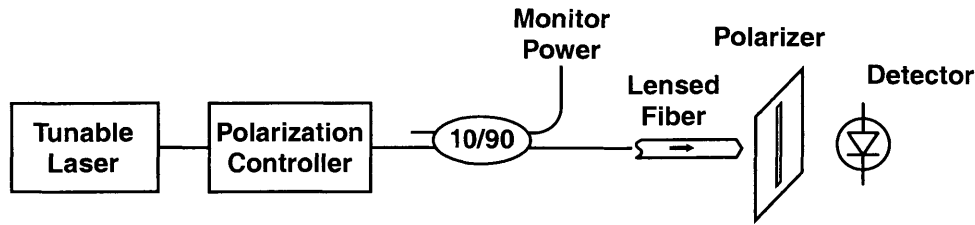
**Figure 6-6:** Setting the input polarization state.

not polarization maintaining fibers there is some concern about the stability of the this polarization state which is susceptible to changes in temperature, stress, etc. of the fiber. Stability measurements were performed over a matter of many hours to a couple days and it was found that the polarization state of the input is very well maintained provided the input fiber was not disturbed violently. Since all device measurements were done within a few hours of adjusting the polarization controller, we are fairly confident that the polarization state of the input was maintained.

With the polarization state set, the polarizer and the photodetector are replaced by the chip and the output lensed fiber. The fiber positions are carefully adjusted to excite a guided mode in the desired device. This procedure requires some level of skill and experience. The fibers are first placed visually in position with the help of a high-powered optical microscope. Final adjustments are made so as to maximize the power in channel A of the power meter. Following the alignment, wavelength scans were made on the devices using the tunable laser source. The powers in Channels A, B and the laser wavelength were recorded. Typically scans over both a narrow wavelength range with a fine step size and a wide wavelength ranges with a courser step size were made. The results for the various class of devices are presented below.

## 6.3 Waveguide

Several straight waveguides were fabricated on the device chip. The waveguides serve as monitor devices enabling the loss per unit length, $\alpha$, and the group index, $n_g$ to be estimated from measurements. Both $\alpha$ and $n_g$ are important optical parameters that need to be ascertained before a comparison between the theoretical and measured responses for the other devices can be made.

The chip input and output facets did not have an anti-reflection (AR) coating and thus a
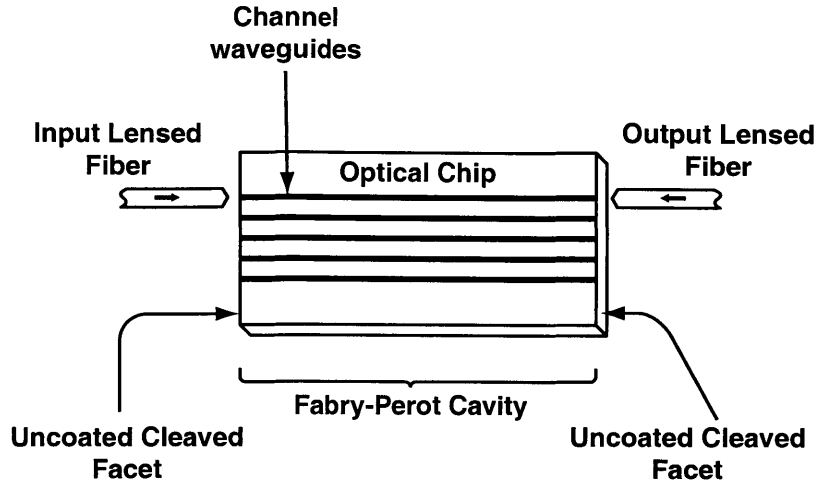
**Figure 6-7:** Characterizing waveguide loss and group index

Fabry-Perot cavity is formed between the two cleaved facets, shown in schematically in Fig. (6-7) . We expect to see power oscillations as we scan the wavelength. These oscillations correspond to the Fabry-Perot resonances. Once a guided mode had been excited in the waveguide, the wavelength of the input laser was typically scanned over a 1 nm range with a step size of 0.01 nm. The expression for the transmitted power, $P_T$ can be derived rather easily and is given by

$$P_T = \frac{C(1 - R)^2 \, e^{-2\alpha l}}{(1 - R \, e^{-2\alpha l})^2 + 4R \, e^{-2\alpha l} \sin^2(\beta l)} \tag{6.1}$$

where $l$ is the length of the chip, $\beta$ is the propagation constant and $\alpha$ is the loss per unit length of the waveguide. $C$ is the coupling efficiency from the lensed fiber into the waveguide. $R$ is the power reflectivity from the chip facets; it is difficult to calculate analytically. A rigorous treatment requires taking into account all the guided and radiation modes of the waveguides as they are scattered into plane-wave modes at the chip facet. A reasonable estimate for $R$ can be made with help of a simplified plane-wave analysis and is given by the familiar expression

$$R = (\frac{n_{eff} - n_{air}}{n_{eff} + n_{air}})^2 \tag{6.2}$$

where $n_{eff}$ is the effective index of the guided mode and related to the propagation constant, $\beta = (2\pi n_{eff})/\lambda$. The free spectral range, $\Delta f_{FSR}$, or the periodicity of the Fabry-Perot resonances is given by

$$\Delta f_{FSR} = \frac{c}{2n_g l} \tag{6.3}$$
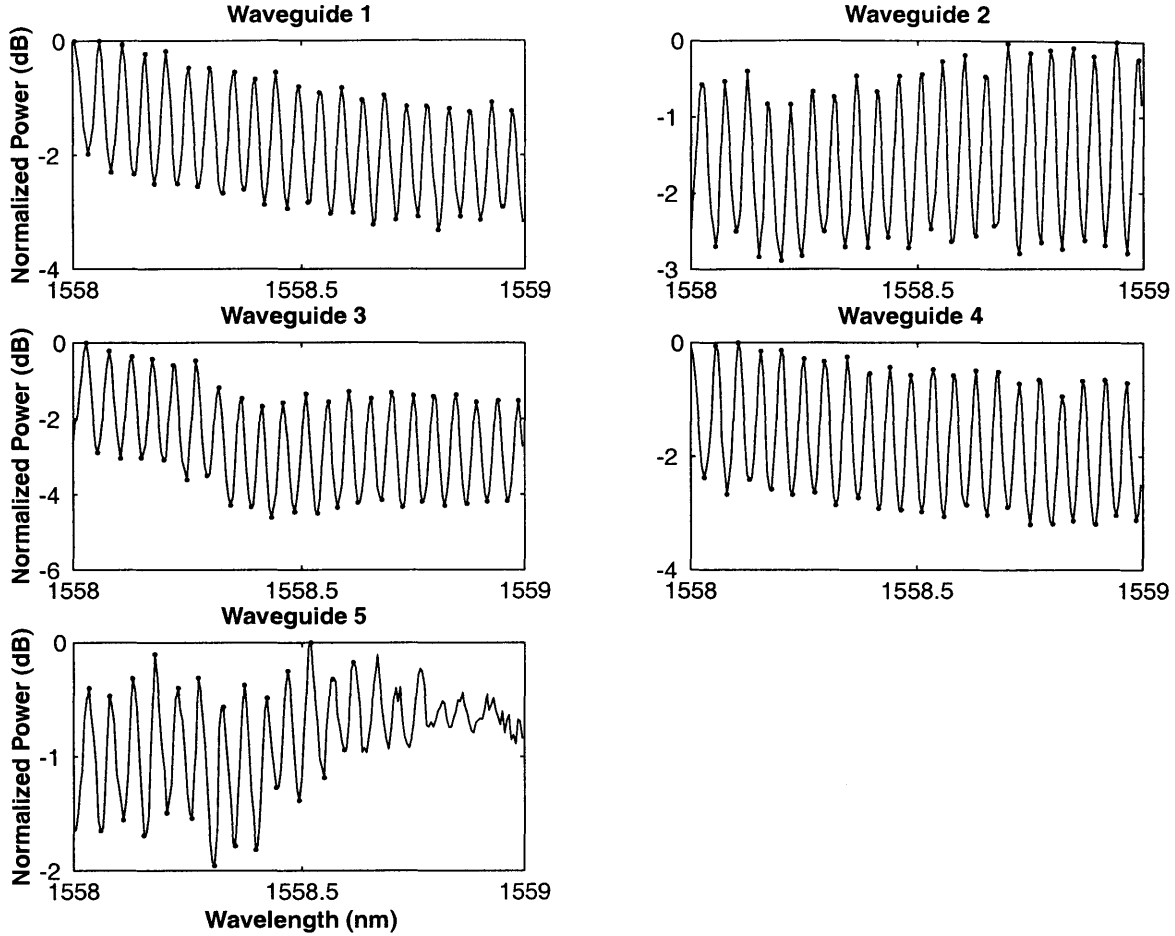
**Figure 6-8:** Wavelength scans of various waveguide devices reveal the Fabry-Perot cavity modes setup between the non-AR coated chip facets.

The above expression is in terms of frequency; it can readily be rewritten in terms of wavelength and is given by

$$\Delta\lambda_{FSR} = \frac{\lambda_o^2}{2n_g l} \tag{6.4}$$

where $\lambda_o$ is the center wavelength of the measurements. The length of the devices was measured using a microscope with a translation stage that gave the coordinate readings relative to the cross-hair marked eye-piece. By measuring the $\Delta\lambda_{FSR}$ from the data for the various waveguides the group index, $n_g$, can be extracted. Figure (6-8) shows the transmission plots for various devices. The abscissa corresponds to the normalized transmitted power (normalized relative to drifts in the absolute laser power) and the ordinate is the wavelength.

As expected we see periodic power oscillation as we scan the wavelength. The minimum

|              | Guide 1 | Guide 2 | Guide 3 | Guide 4 | Guide 5 |
|--------------|---------|---------|---------|---------|---------|
| $n_g$        | 3.448   | 3.448   | 3.484   | 3.484   | 3.442   |
| $\alpha$ (cm$^{-1}$) | 0.6238  | 0.5787  | 0.4307  | 0.5475  | 1.013   |

**Table 6.1:** Tabulated values of the group index, $n_g$ and the loss parameter, $\alpha$ for the various guides.

and maximum excursion points are marked with a dot in the plots. The $\Delta\lambda_{FSR}$ was calculated by averaging over many periods. Using eq. (6.4), $n_g$ can be readily calculated. The results for the various waveguides are shown in Table (6.1). As mentioned earlier, the chip reflectivity, $R$, is difficult to calculate analytically. Typically for laser designs, which use the same InP/InGaAsP material system, R is estimated to be between 0.28 $\sim$ 0.35. As a first approximation we can use $n_g$ in eq. (6.2) to estimate the facet reflectivity. Using the average $n_g$ from Table (6.1), we find that $R \approx 0.31$.

To calculate the loss per unit length, $\alpha$ eq. (6.1) is used. All quantities other than the coupling efficiency $C$ are known. $C$ can be estimated but the analysis is rather involved. Instead, we adopt an approach which allows $\alpha$ to be calculated without knowledge of $C$. By taking the ratio between the maximum and the minimum transmitted powers, given by the equation below, $C$ can be eliminated.

$$\frac{P_{Tmax}}{P_{Tmin}} = \frac{(1 + Re^{-2\alpha l})^2}{(1 - Re^{-2\alpha l})^2} \tag{6.5}$$

By averaging $(P_{Tmax}/P_{Tmin})$ over several periods and inverting the above formula $\alpha$ can be readily calculated. The values for the various waveguides are tabulated in Table (6.1). For the straight waveguides, the primary sources of $\alpha$ are: (1) the intrinsic material loss of the InP/InGaAsP system; (2) scattering losses from the roughness in the walls of the waveguides caused by imperfections in the fabrication process. For the bandgap of the material system used, we do expect very low material losses. We see that $\alpha$ is a rather small number which is an indication that the fabrication process produces very little sidewall roughness and is rather clean. This is also evident by looking at SEMs of the devices after etching the guides.

## 6.4 Uniform Bragg Grating

Three uniform Bragg grating reflectors or distributed Bragg reflectors (DBRs) of increasing grating length were fabricated on the chip set. Measurements were made to verify the
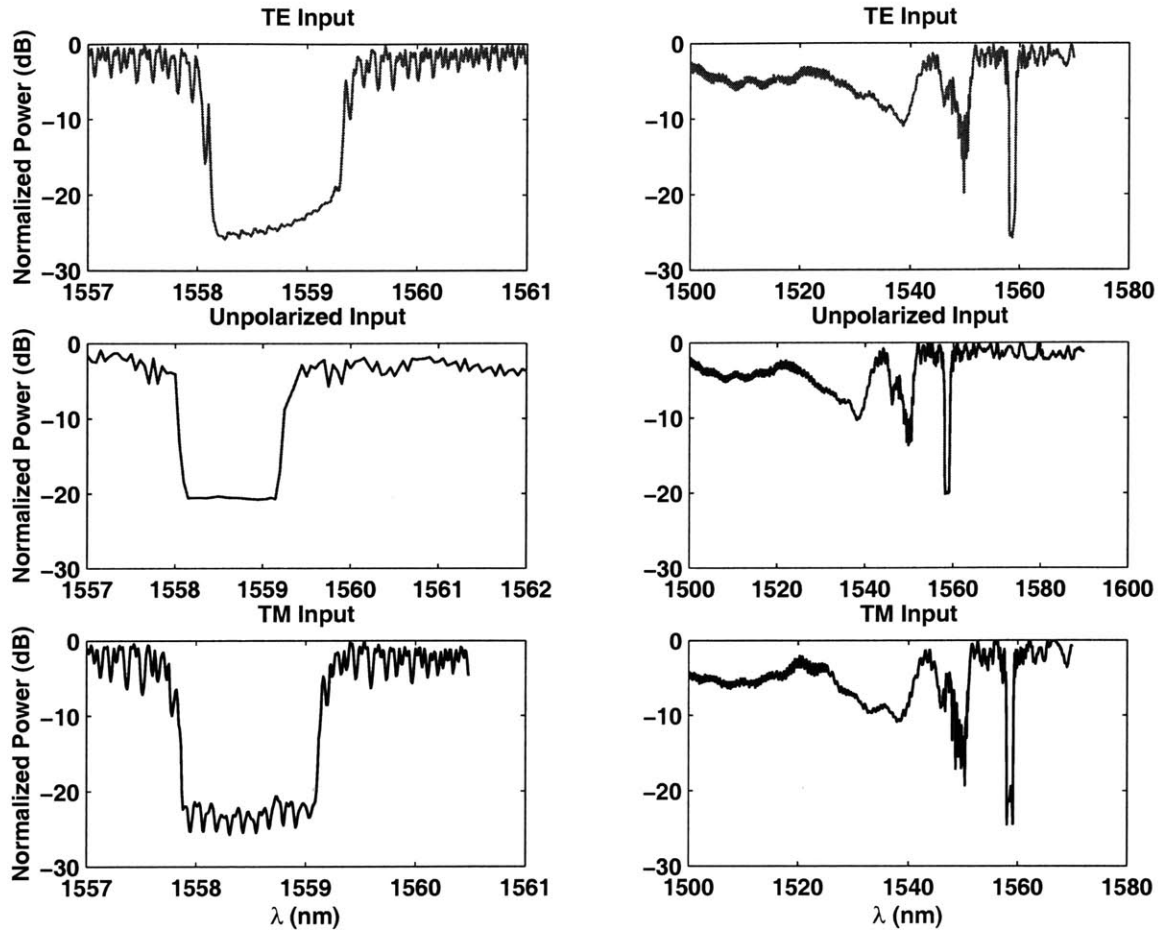
**Figure 6-9:** Transmission measurement of uniform Bragg grating; DBR device 1.

behavior of the DBRs. From theory, we expect that as the wavelength is scanned across the stopband of the gratings there will be a strong reflection from the gratings and a corresponding decrease in the transmitted power. Outside the stopband, the transmission should recover. Moreover, as seen from the chapter 6.4.1 we expect the gratings to couple the forward-propagating guided mode to backward-propagating radiation modes on the low wavelength side. Consequently, we expect decreased transmission on the low wavelength side of the stopband.

Following alignment of the input and output lensed fibers, numerous scans were performed on the DBRs. For most devices, several cases were examined: (a) Unpolarized light response. (b) TE Polarized light response. (c) TM Polarized light response. For each of these cases, scans were performed on a narrow and wide wavelength scale. The results are shown in Fig. (6-9). As can be seen from the figure we observe the expected behavior. The
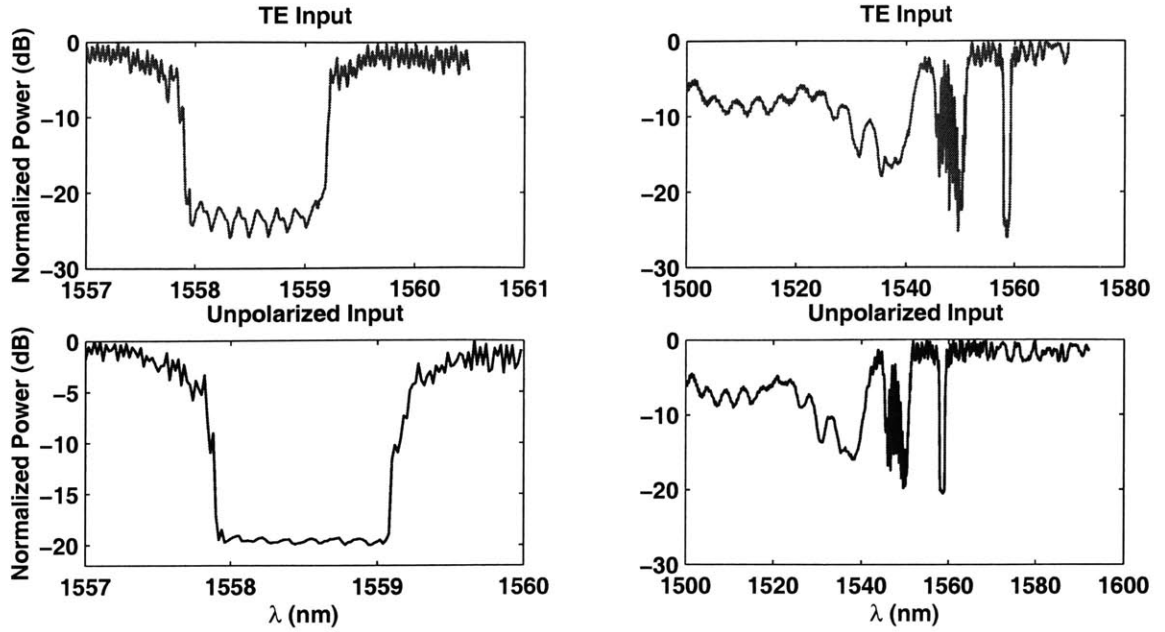
**Figure 6-10:** Transmission measurement on uniform Bragg grating; DBR device 2

| DBR | Device 1 | Device 2 | Device 3 |
|---|---|---|---|
| $\kappa_{TE}$ (cm$^{-1}$) | 49.5009 | 55.9571 | 58.8169 |
| $\kappa_{TM}$ (cm$^{-1}$) | 54.8778 | - | 58.8169 |
| $\kappa_{UP}$ (cm$^{-1}$) | 47.4412 | 48.5790 | 58.8149 |

**Table 6.2:** Grating strengths, $\kappa$, corresponding to TE, TM and unpolarized input measurements of uniform Bragg grating devices.

transmission is fairly constant but drops steeply in the stopband. It recovers rapidly on the other side of the stopband. The width of the stopband is related to the grating strength, $\kappa$ by eq. (6.6).

$$\Delta\lambda_{SB} = \frac{\kappa\lambda_o^2}{\pi n_g} \qquad (6.6)$$

The group index, $n_g$ has already been estimated from the waveguide Fabry-Perot scans. By measuring the stopband width from the data, eq. (6.6), can be inverted to yield $\kappa$. The stopband widths, $\Delta\lambda_{SB}$ and the corresponding grating strengths, $\kappa$ for the DBRs are tabulated in Table (6.2). The results found from measurements match up very well with the design value of $\kappa \approx 58.5$ cm$^{-1}$.
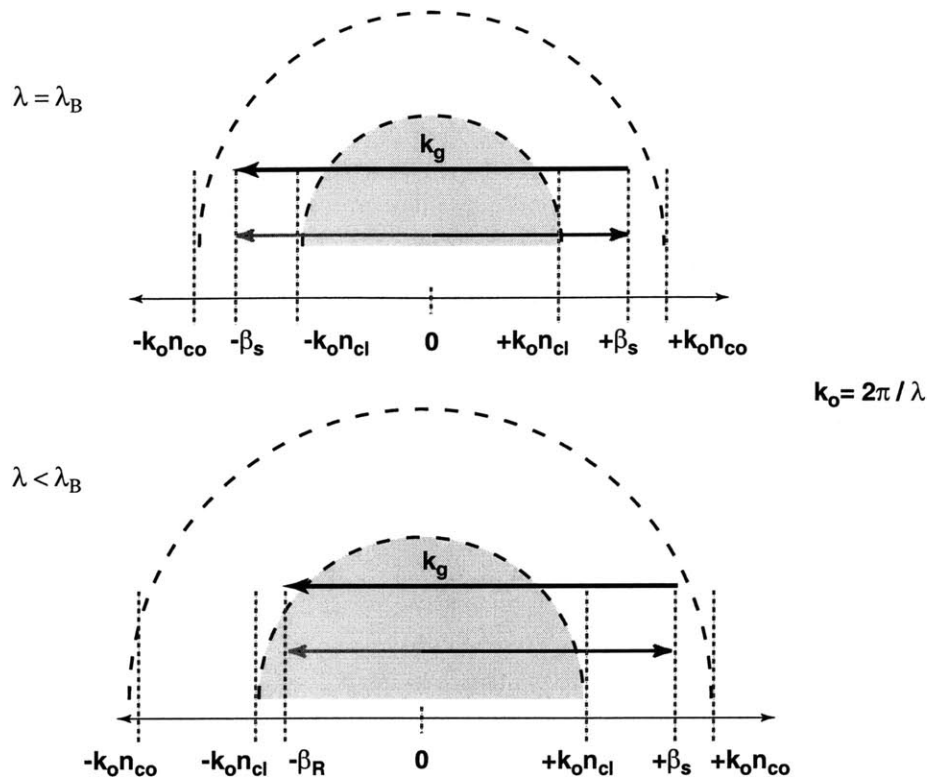
**Figure 6-11:** $k$-vector addition shows phase-matched coupling to radiation modes away from resonance.

## 6.4.1 Radiation

It is well known that integrated Bragg gratings lose power out of the waveguide. One mechanism of loss is related to fabrication surface imperfections [66]. If the surface of a Bragg grating is rough, it is possible to scatter light out of guided modes into the cladding or substrate. However, even a grating that has no imperfections but is of finite size loses power out of guided modes into cladding and substrate [70]. This coupling to unguided modes results in unwanted losses. The coupled mode theory discussed earlier in chapter 3 does not predict these loses. Radiation from Bragg gratings has been studied quite extensively and several approximate methods of varying levels of accuracy and difficulty for estimating losses exist [67]-[69]. In chapter 3 we derived the coupled mode equations (eqs. (3.24) and (3.25)) which model a Bragg grating. We saw that the effect of a Bragg grating was to couple the forward traveling guided mode to the same mode propagating in the reverse direction. In deriving the equations it was argued that the dielectric perturbation with a wavelength, $\Lambda$, and a grating $k$-vector, $k_g = 2\pi/\Lambda$ only phase-matched the forward traveling

mode $\mathcal{E}_s(x)$, with a propagation constant $\beta_s(\omega_o) = \beta_o \approx \pi/\Lambda$, to the same mode traveling in the reverse direction, i.e

$$\beta_s - k_g \approx -\beta_s \tag{6.7}$$

The $k$-vector addition in Fig. (6-11) shows this coupling between a $\beta_s$ forward-traveling mode and a $-\beta_s$ backward propagating mode at the Bragg wavelength, $\lambda_B$. The coupling to other modes $\mathcal{E}_m(x)$ with propagation constants $\beta_m$ which were not phase-matched near the Bragg wavelength, $\lambda_B$ was omitted. The result is that according to the CMT equations, all interactions in a Bragg grating are limited to the coupling between the two counter-propagating modes; all power can be accounted for in the interactions between them. However, we know that gratings do scatter light out of guided modes into unguided modes which results in radiation losses. Since this interaction was ignored in deriving the CMT equations of chapter (3), naturally they do not predict radiation losses.

The approximation that there is negligible coupling to other modes including, radiation modes, is generally good; particularly near the Bragg frequency, $\omega_o$. However, further away from resonance, especially on the low wavelength or high frequency side, it does not hold so well. In fact on the low wavelength side it can be shown that Bragg gratings phase-match the guided mode $\mathcal{E}_s(x)e^{-j\beta_s z}$ to backward-traveling radiation modes $\mathcal{E}_R(x)e^{+j\beta_R z}$

$$\beta_s(\lambda < \lambda_B) - k_g \approx \beta_R \tag{6.8}$$

This is shown pictorially in Fig. (6-11). Radiation modes have $\beta_R < 2\pi n_{cl}/\lambda$ indicated by the shaded region in Fig. (6-11) where $n_{cl}$ is the cladding index. As the wavelength becomes smaller $\beta_s = 2\pi n_{eff}/\lambda$ increases in magnitude such that beyond a certain frequency the addition of the grating $k$-vector $k_g$ to $\beta_s$ results in phase-matched coupling to backward-traveling radiation modes with propagation constant in the vicinity of $\beta_R$. Consequently, we expect decreased transmission on the low wavelength side. This is also apparent in the wide wavelength scans shown in figs. (6-9), (6-10) and (6-12) for the three DBR structures. On the basis of the coupling mechanism described in the chapter 6.4.1, we would expect the radiation losses to be fairly constant on the low wavelength side. However, the data shows increased radiation loss in the wavelength range from 1542 nm $\sim$ 1551 nm. This preferential coupling to modes cannot be explained by coupling to radiation modes alone. It indicates the presence of some mode or modes with a relatively strong overlap with the guided mode and a modal index in the 2.85 $\sim$ 3.17 range. Since coupling between guided and radiation modes is not very strong due to the strong mismatch between their modal shapes, the larger
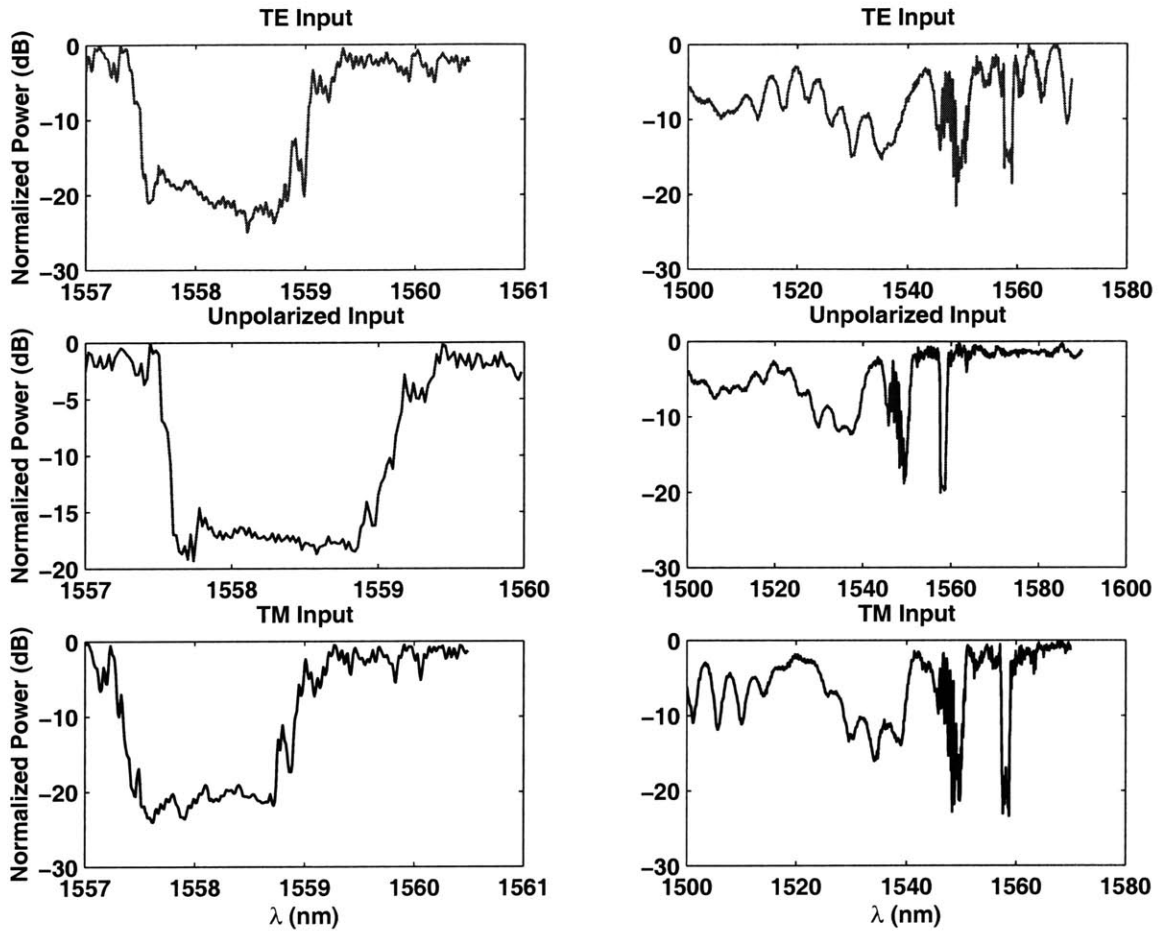
**Figure 6-12:** Transmission measurement on uniform Bragg grating; DBR device 3.
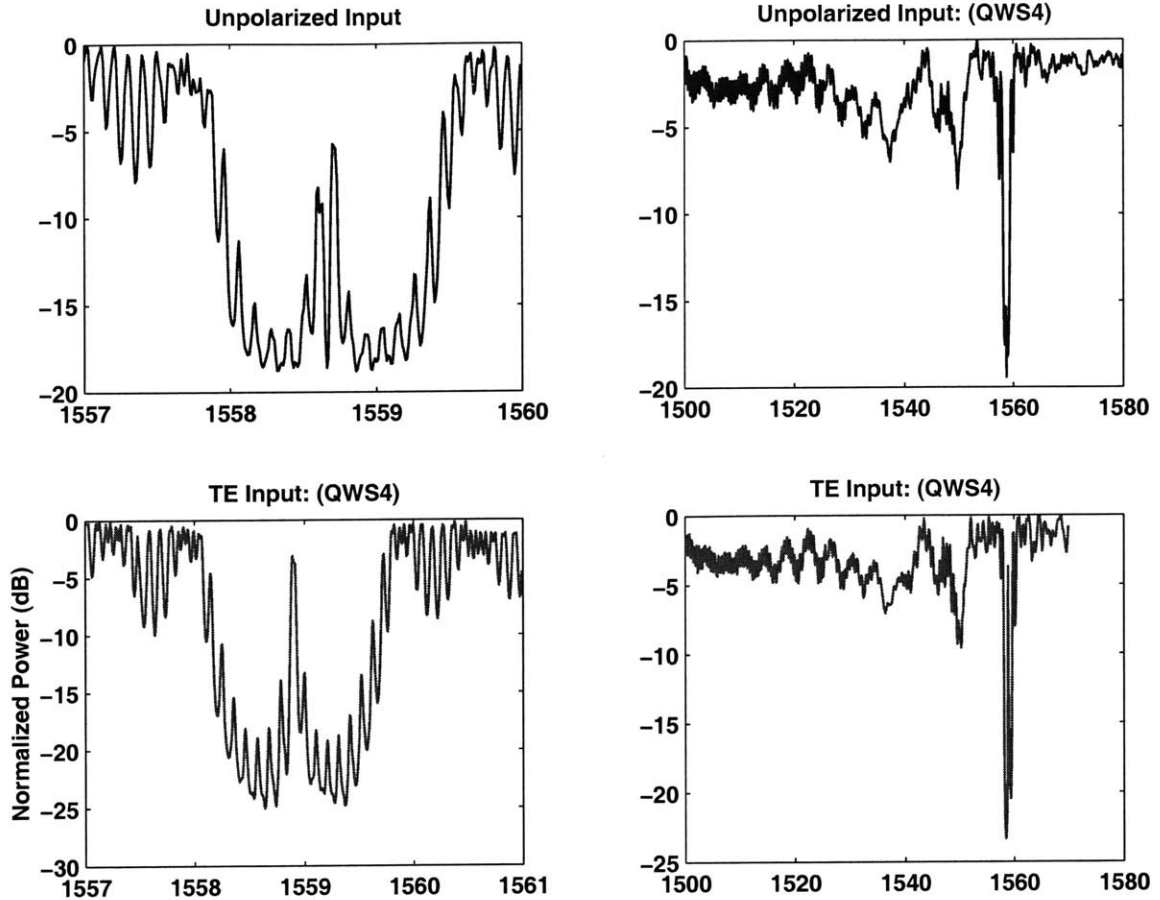
**Figure 6-13:** Transmission measurement on quarter-wave shifted grating; QWS-BR device 4.

loss in the above wavelength range suggests that these modes are probably some kind of guided modes; either they are slab modes which exist due to gradation in the index of the overgrown InP or they are higher order modes of the same guide.

## 6.5 Quarter-wave Shifted Bragg Grating Resonators (QWS-BR)

Five quarter-wave shifted grating structures were fabricated on the chip-set. However, a inspection of the mask revealed that the first three had large defects in the grating regions rendering them unmeasureable. The other two were measured and the results are presented below. As explained in chapter 3 , the quarter-wave shift in the center of the grating creates a transmission resonant state precisely in the center of the stopband at the Bragg wavelength, $\lambda_B$. Consequently we expect that as the wavelength is scanned, the transmission will be

suppressed strongly within the stopband except at the Bragg wavelength where we expect high transmission. An inspection of figs. (6-13) and (6-14) reveals the resonant transmission peaks in the center of the stopband. Measurements were performed with unpolarized and polarized input light. For the unpolarized input we observe two peaks within the stopband which correspond to the TE and TM modes. TE and TM modal shapes are slightly different for the gratings structures. Consequently these modes have different effective indices, $n_{eff}^{TE}$ and $n_{eff}^{TM}$ and resonant Bragg wavelengths which results in peaks at different locations in the stopband. Also since the two modes have different grating strength $\kappa$ the width of the resonance and how close it reaches to the zero dB level are different for the two peaks. This can be seen for both measured quarter-wave shifted devices. For the TE input we see that only one central peak is evident. The oscillatory nature of the spectral response is due to the superimposition of the Fabry-Perot modes on the grating response. AR coating the chip facets should remove these extra oscillations. We note that the resonant peak returns almost to the zero dB level. This indicates very low loss grating structures. This was expected based on the loss measurement done on the waveguide. The resonant peak of device QWS-BR 5 is considerably below the zero dB level. However, this device was designed with a bandwidth of 300 MHz which is extremely narrow. To some extent the tuning capability of the laser source is strained to measure this response. Moreover since the designe $Q$ of this device is so close to the expected radiation $Q_R$ of the grating structures, the slightest amount of loss has a significant impact on the height of the resonant transmission peak. The fact that the peak does not return to zero dB is partly due to loss and partly due to the fact that the chip is not AR coated and has Fabry-Perot resonances. The section comparing theory and measurement discusses in detail the loss estimates of these devices. On the broad wavelength scan we again notice lowered transmission on the low wavelength side caused due to coupling of guided modes to radiation modes as discussed earlier. Another interesting point to note is that the resonant peaks are very accurately centered in the stopband which indicates that the phase shift introduced in the grating is a very precise $\lambda/4$ phase shift.
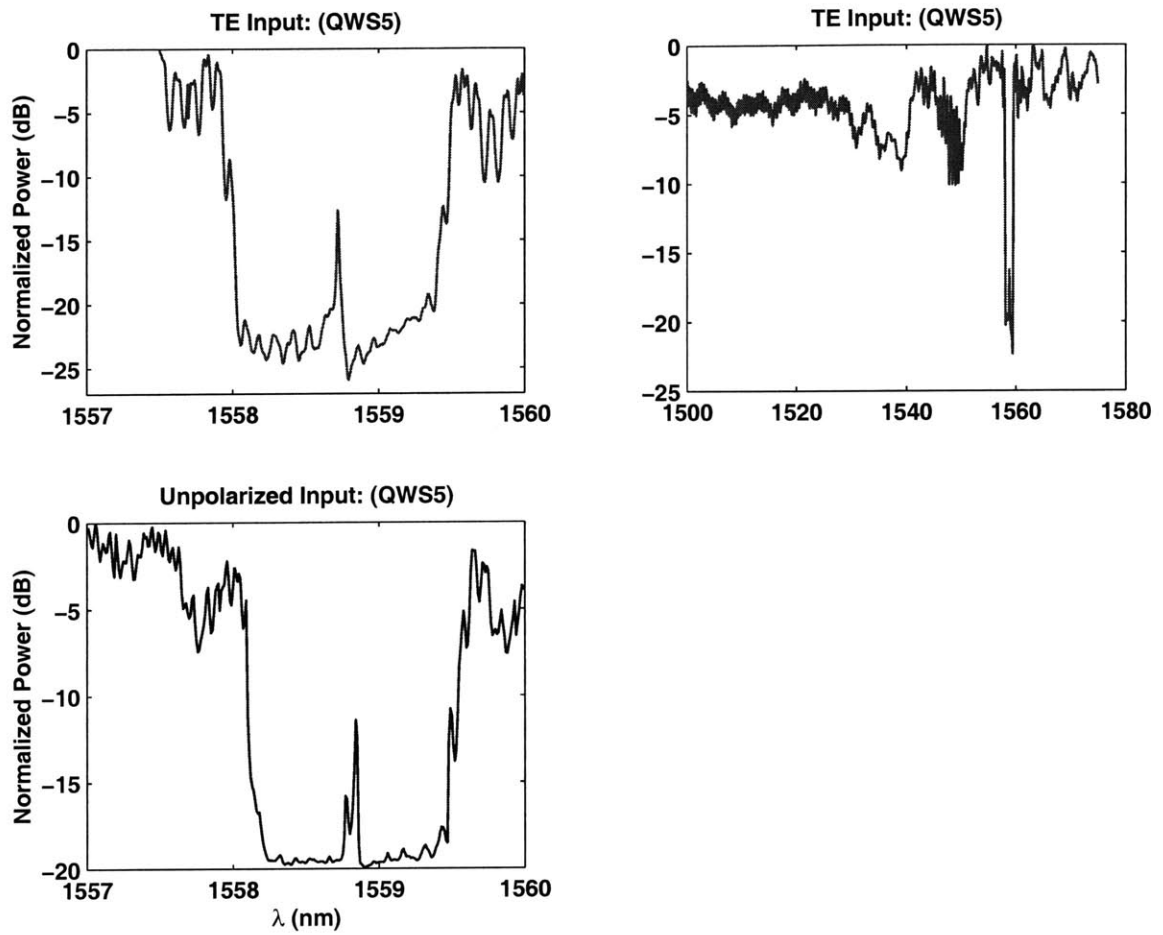
**Figure 6-14:** Transmission measurement on quarter-wave shifted grating; QWS-BR device 5.
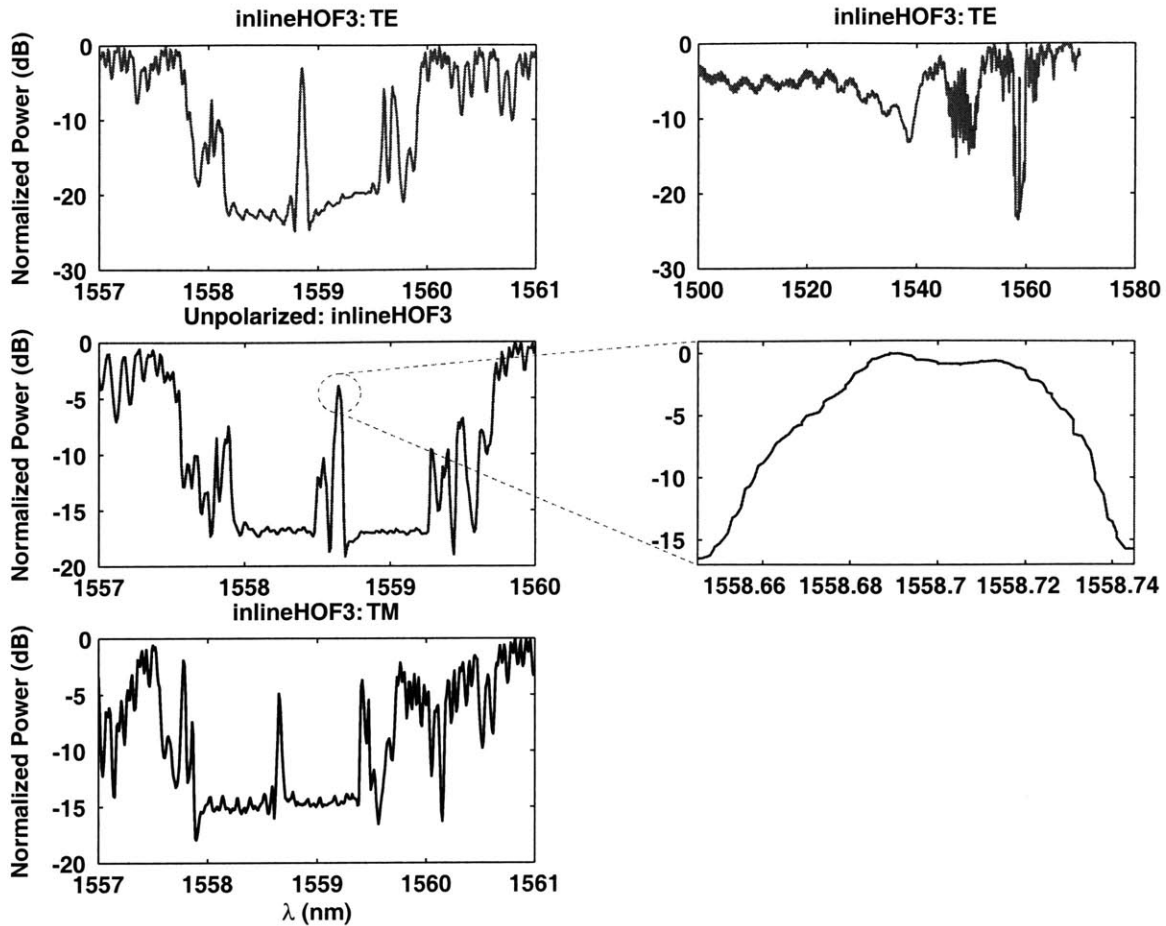
**Figure 6-15:** Transmission measurement on inline coupled Bragg resonators which form the third-order inline filter; device 3.

## 6.6  Inline Higher-Order Filters

Four higher-order inline filters (inline HOFs) were fabricated. A higher-order inline filter has multiple quarter-wave shifts where coupling between the different Bragg resonators can be engineered to give a desired spectral response. Three of the filters were third-order filters and the last one was a fifth-order filter with corresponding numbers of quarter-wave shifts. Higher order filters have a few spectral characteristics that easily distinguish them from a first-order, single quarter-wave shift structure. Firstly unlike first order filters, the resonant transmission peaks within the stopband can be shaped. All the inline filters were designed to yield maximally flat, Butterworth spectral responses in the center of the stopband. Secondly, the roll-off of the response with wavelength is much faster. For each added quarter-wave shift the roll-off with frequency increases by 20 dB/decade. Finally
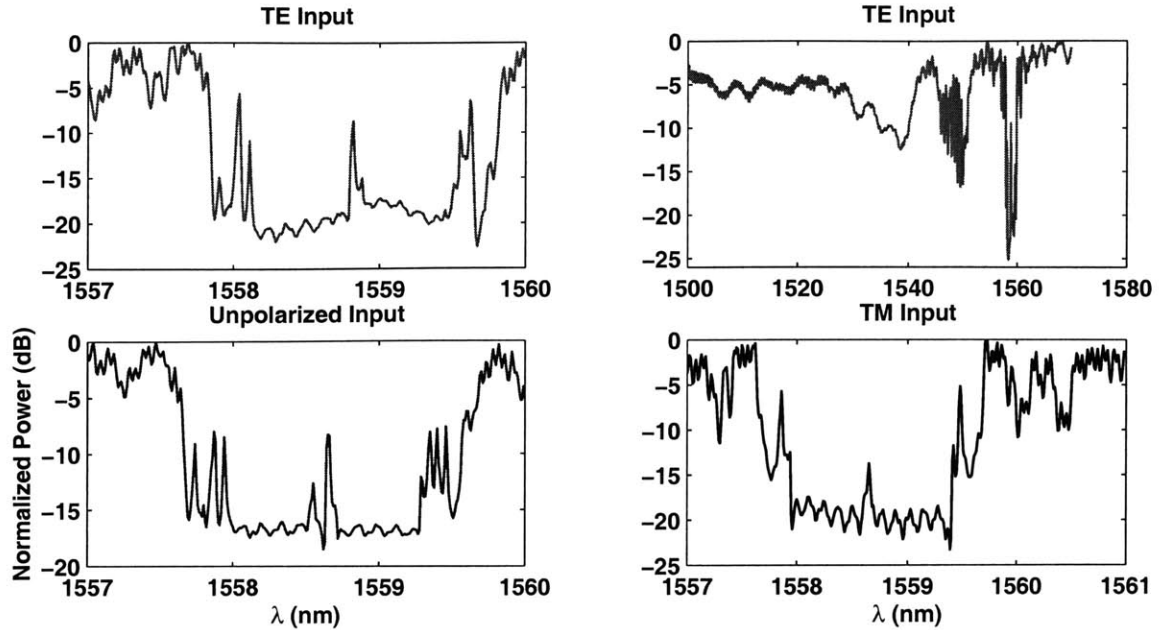
**Figure 6-16:** Transmission measurement on inline coupled Bragg resonators which form a third-order inline filter; device 2.

the coupling of the multiple Bragg resonator cavities creates additional resonances at the edge of the stopband, a feature which clearly distinguishes a higher-order filter from the first-order, single quarter-wave shift devices.

Two of the four higher order devices yielded good results. These are shown in Fig. (6-16) and Fig. (6-15). For unpolarized light we see two resonant states within the stopband as expected corresponding to the TE and TM responses. A very fine scan with a 1 pm stepsize was performed in the wavelength range of the peaks for inline HOF device 3 and is shown in the adjacent plot. We see a flattening of the top of the transmission peak. This is not a resolution-limited flattening as numerous points were taken in the vicinity of the transmission peak. The dip in the center of the resonant peak is again a Fabry-Perot artifact and would disappear if the chip facets were AR coated. We will return to this issue in the following section. In addition to the flattened response at the top, we see another idiosynchratic trait of higher-order filters; near the edge of the stopband we see additional resonances. Compare this to the response of the single quarter-wave shifted Bragg resonator response, Fig. (6-13). For the unpolarized input we see about four additional "spikes", two for the TE and TM states. For the TE input, we note that the TM peak in the center of the stopband is suppressed heavily; it drops from about 10 dB below the TE peak to

about 20 dB below. In addition, we see that the number of resonances near the edge of the stopband are also halved, as expected for the TE input. As in the case of the DBRs and QWS-BR-DBRs we notice coupling to radiation modes on the low wavelength side of the stopband.

## 6.7  Comparison of Measurement and Theory

In the previous section the measured data from various devices was presented. The data was used to estimate the optical parameters and we found that

$$\bar{n}_g \approx 3.4612 \tag{6.9}$$

$$\bar{\alpha} = 0.6388 \text{ cm}^{-1} \tag{6.10}$$

$$\bar{\kappa}_{TE} \approx 54.76 \text{ cm}^{-1} \tag{6.11}$$

$$\bar{\kappa}_{TM} \approx 56.85 \text{ cm}^{-1} \tag{6.12}$$

$$\tag{6.13}$$

where the overbar implies an averaged quantity based on measurements on multiple devices. We will now proceed to use these estimates to compare the measured data against theoretical predictions. The theoretical predictions are made using coupled mode theory in space which describes the coupling between backward and forward propagating waves caused by the grating in terms of the following familiar equations.

$$\frac{dA}{dz} = -j\delta A + \kappa B \tag{6.14}$$

$$\frac{dB}{dz} = j\delta B + \kappa A \tag{6.15}$$

$$\tag{6.16}$$

Note that coupled mode theory in this form only considers coupling between backward and forward propagating waves of a single guided mode. It does not take into account coupling between guided and radiation modes and so we do not expect good agreement between data and theory on the low wavelength side when we move far enough from the stopband. In addition to this, the above equations by themselves do not take into account the fact that the chip is not AR coated. For this we must include reflections from the chip facet and lengths from the edge of the grating devices to the chip facets. A transmission matrix formalism is used to incorporate these Fabry-Perot effects and to solve the above CMT equations. This formalism is discussed in section 3.1.1

**Figure 6-17:** Overlay of measured uniform Bragg grating data and coupled mode theory prediction for TE input. Fabry-Perot effects due to reflection from chip facets were taken into account.

## 6.7.1  DBR

Figure (6-17) shows the overlay of measured data and theory. The values of the optical parameters used in the theoretical simulations are given above. No attempt was made to optimize these parameter values to give some best-fit result. The values of $n_g$ and $\alpha$ were independantly estimated. Moreover the $\kappa$ values were calculated from a two point measurement on the dbr spectral response. Despite this we see an excellent fit between the measurement and the data. Particularly striking is the quality of the fit outside the stopband where the calculated Fabry-Perot modes line up very well with the measured data. For the purposes of calculating the Fabry-Perot effect it was assumed that the devices are precisely centered on the chip so the edges of the gratings are equidistant from the chip
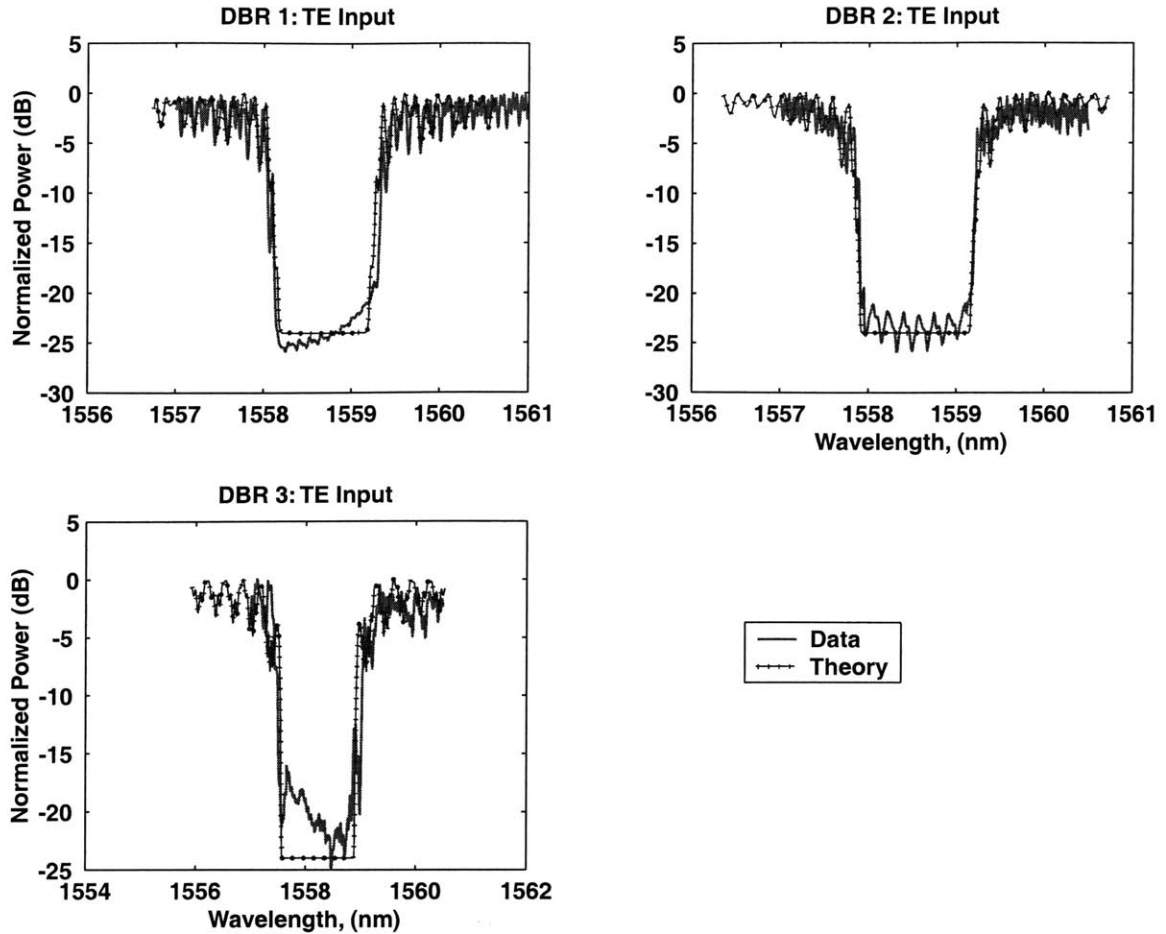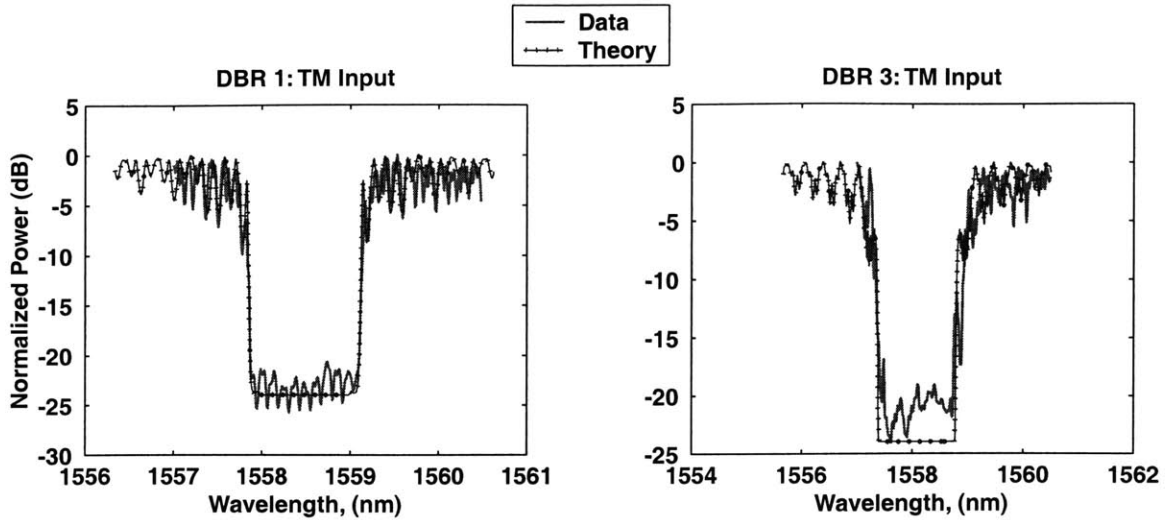
**Figure 6-18:** Overlay of measured uniform Bragg grating data and coupled mode theory prediction for TM input. Fabry-Perot effects due to reflection from chip facets were taken into account.

facets. Based on the length of the DBR structures, theoretically we predict suppression within the stopband in excess of -80 dB. However coupling of stray light travelling through the substrate into the output lensed fiber creates a noise floor. For this purpose a constant noise floor of -24 dB was assumed and was added to theoretical response for all the devices. One difference that we do notice between data and theory is the oscillations within the stopband. These are Fabry-Perot oscillations of the noise floor. In our calculations the noise floor was assumed to be constant. An inspection of the X-ray mask revealed that DBR device 3 had defects and unlike the other two devices, it does not have a clean response within the stopband. Even so the fit at the edges of the stopband and outside the stopband are very good. Figure (6-18) shows the comparison for the TM response. Again we get an excellent fit other than the oscillations within stopband which are dominated by Fabry-Perot modes of the stray light (cladding modes, etc.) and not the guided mode. Outside the stopband the agreement is excellent;

## 6.7.2 QWS-BR

Figure (6-19) shows on overlay of the theoretical prediction and the measured data. Once again, the optical parameters estimated independantly from the QWS-BR spectral response were simply used as inputs to the simulations. The fit is remarkable. Not only is the response outside the stopband predicted to a high degree of accuracy. Within the stopband, we see

**Figure 6-19:** Overlay of measured QWS-BR device 4 data and Coupled Mode theory prediction taking into acount Fabry-Perot effects due to reflection from chip facets.

that the Fabry-Perot oscillations are also predicted. The reason why these oscillations are visible here and not in the DBR theoretical response is due to the fact that the floor for the QWS-BR device is dominated by the guided mode which is taken into account by the simulation and not stray light. The length of the qws grating was such that the floor of the theoretical response was predicted to be near -30 dB (confirm). Once again a constant noise floor was added but it was not large enough to mask the Fabry-Perot oscillations of the guided mode. As mentioned earlier, the fact that the resonant transmission peak does not return to the zero dB level is partly due to waveguide loss and partly due to the fact that the chip facets are not AR coated. For QWS-BR device 4, an assumed loss value of $\bar{\alpha}$ in the theoretical simulation resulted in a theoretical peak falling short of the measured data. Consequently, the $\alpha$ used in the simulation was modified to yield a best fit. This value was 20 % of the minimum measured loss. This shows that indeed this device has extremely low loss. The measured $Q = \frac{\lambda_B}{\Delta\lambda}$ of this device is about 40000. For QWS-BR device 5 the designed bandwidth was 300 MHz. The loss value used to align the theoretical peak with the measured data for QWS-BR 5 was the minimum measured waveguide loss value, $\alpha_{min} = 0.43$ cm$^{-1}$. Because the designed Q of this device was so
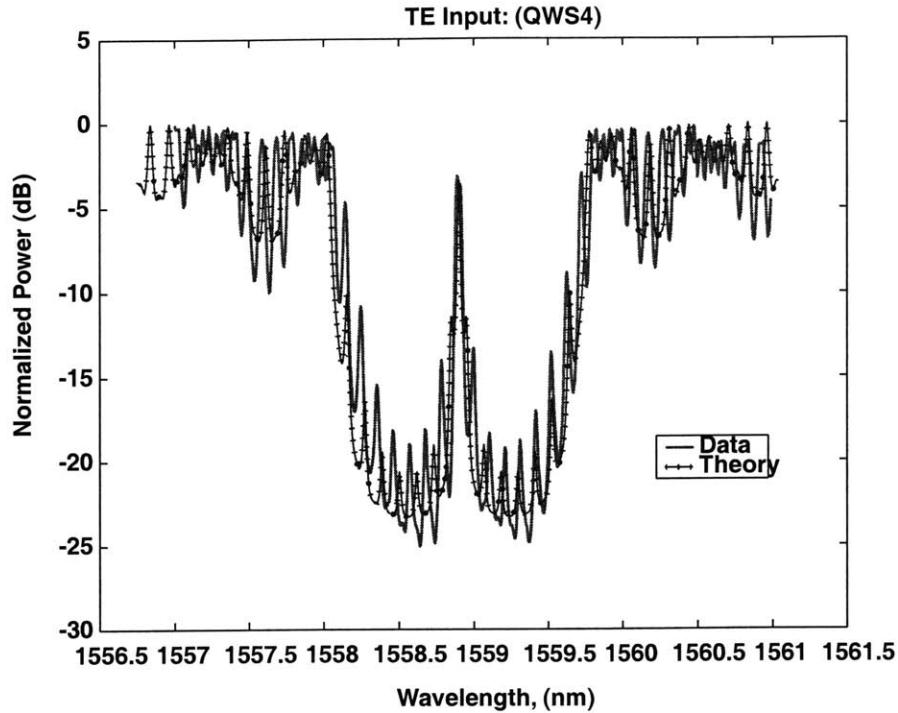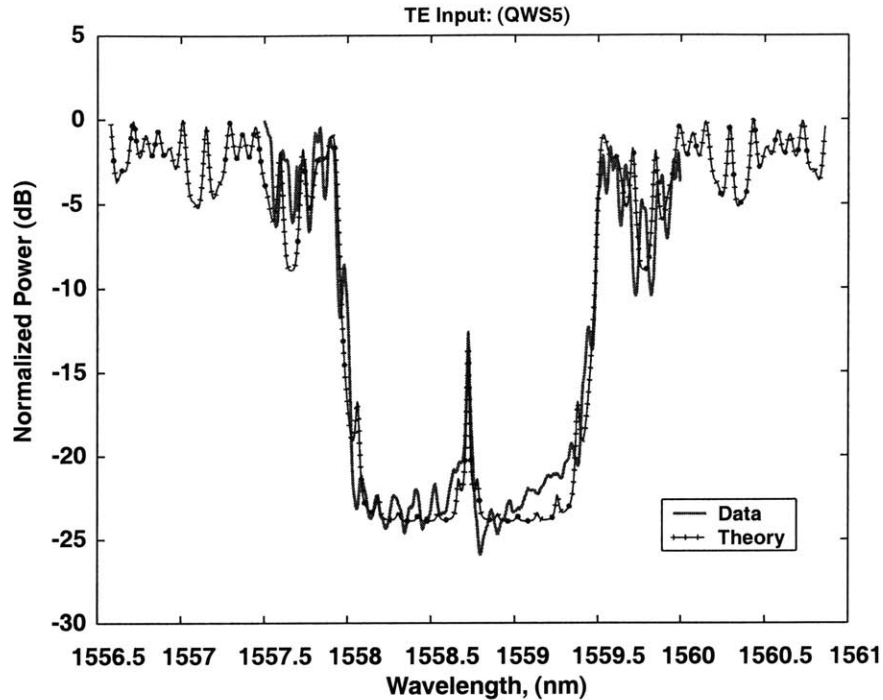
**Figure 6-20:** Overlay of measured QWS-BR device 5 data and coupled mode theory prediction taking into acount Fabry-Perot effects due to reflection from chip facets.

high the slightest loss produces a correspondingly larger impact on the maximum level that the resonant transmission peak attains, Fig. (6-20). An interesting point to note is that the simulations predict the behavior outside the stopband very well for both devices. The envelope and the modulations within them are well modelled. As mentioned earlier, the theoretical simulation assumed the gratings to be centered relative to the chip facet. The fit can be improved further by not making this assumption and adjusting the lengths to the chip facets to better match the Fabry-Perot modes. Also, the effective index can be adjusted to better match the modulation depth. However, since the theoretical predictions using the independently estimated optical parameters gave such a remarkable match to the data it was deemed unnecessary to adjust the optical parameters in a best-fit fashion.

### 6.7.3   Inline HOFs

Figures (6-21) and (6-22) shows the comparison of theory and measurements for the higher order filters. We see again that the data is modelled very well by the simulation both within and outside the stopband. As expected the simulation predicts the existence of the additional resonances near the edges of the stopband. For inline HOF device 3, the loss

**Figure 6-21:** Overlay of measured inline HOF device 3 data and Coupled Mode theory for TE input. Fabry-Perot effects due to reflection from chip facets were taken into account.
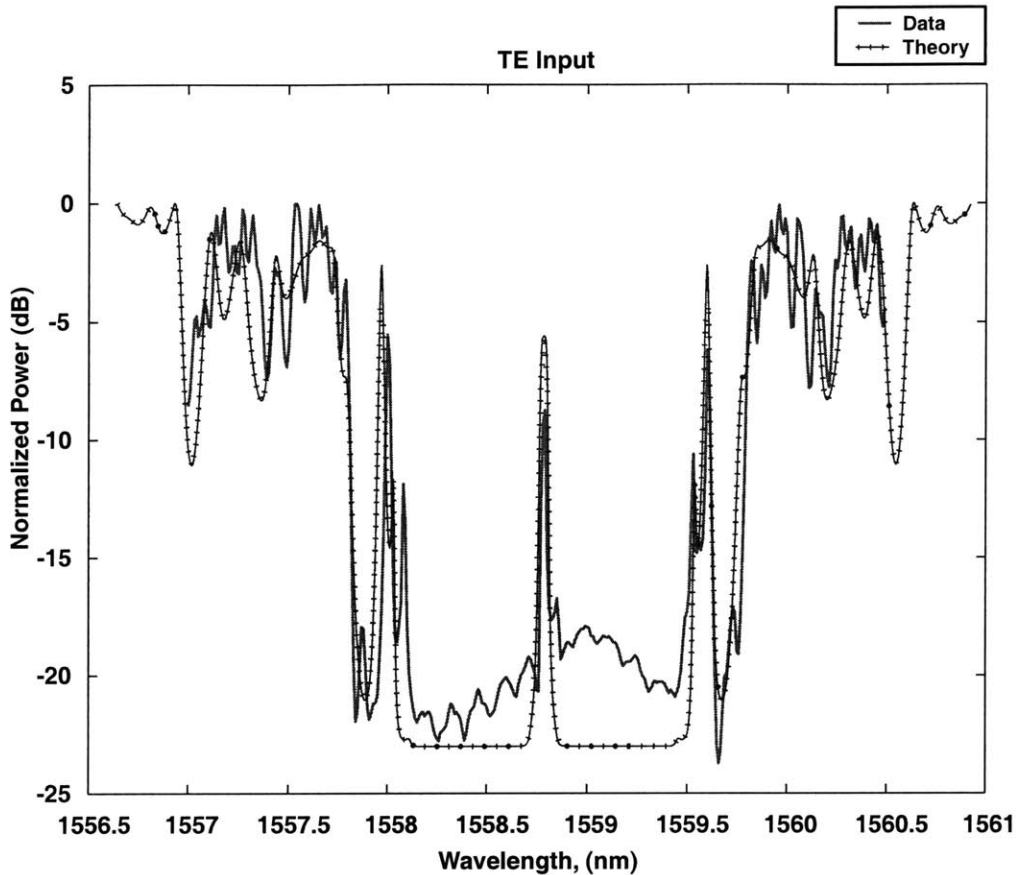
**Figure 6-22:** Overlay of measured inline HOF device 2 data and Coupled Mode theory for TE input. Fabry-Perot effects due to reflection from chip facets were taken into account.

value used to match the peak level of the resonant transmission peak within the band was 20% of the $\alpha_{min}$. For inline HOF device 2, $\alpha_{min}$ was used in the simulation.

## 6.8  Side-coupled Device

A variety of side-coupled devices including side-coupled recievers, first-order filters and higher-order filters were measured. The measurement involved exciting the bus waveguide at the input and measuring the throughput power. A common feature in all these devices is that measurement of the transmitted signal on the bus waveguide should reveal a sharp drop at and near the Bragg frequency. This drop corresponds to power that is either tapped to the adjacent resonator(s) or reflected on the bus due to interactions with the side-coupled Bragg resonators. However, this feature was not clearly observed in any of these devices. The measuement was complicated by the fact that the chip facets were not AR-coated
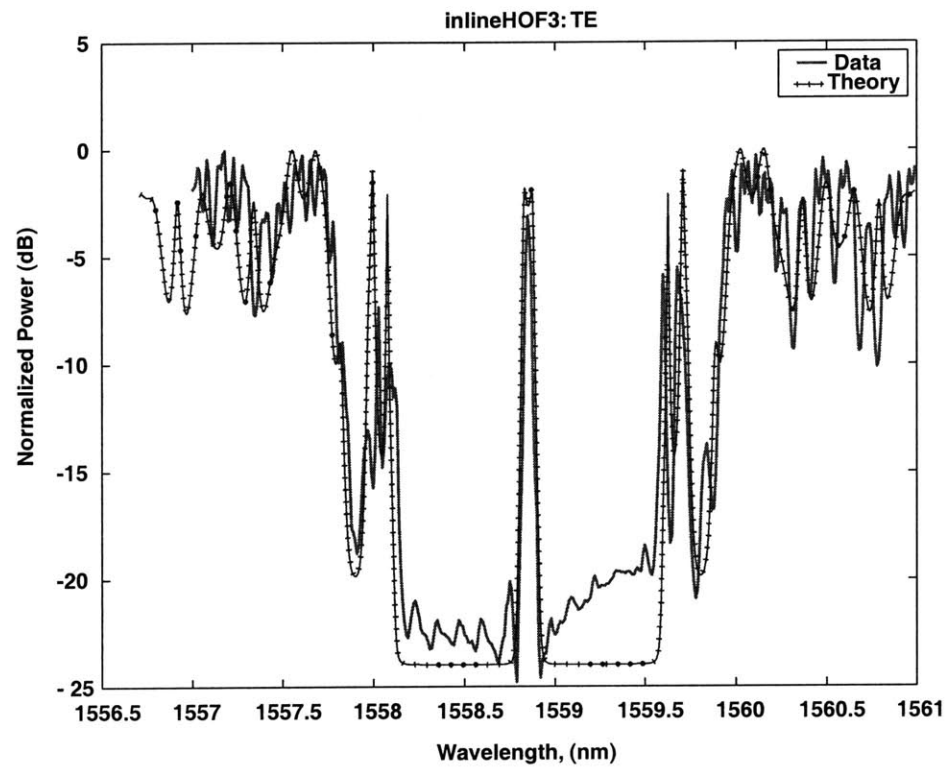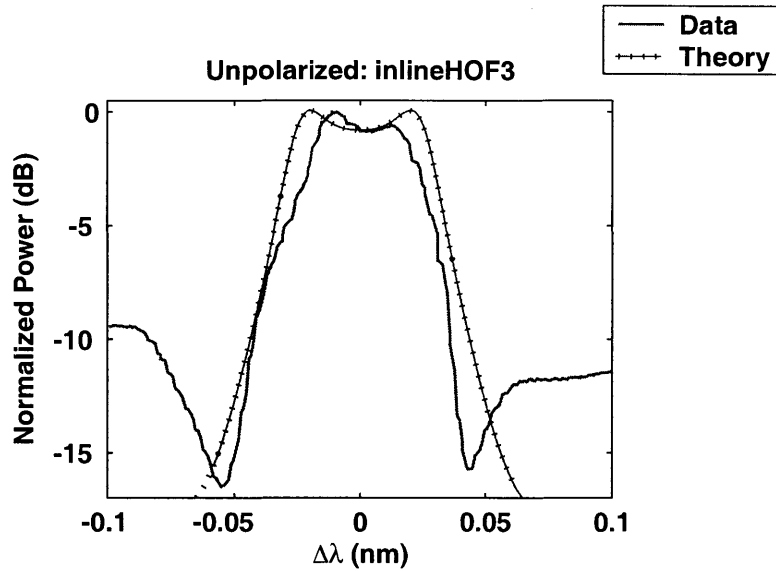
**Figure 6-23:** Overlay of measured inline HOF data and Coupled Mode theory for TE input. Fabry-Perot effects due to reflection from chip facets were taken into account.

which led to Fabry-Perot oscillations. These oscillations made the identification of the drop in transmitted signal corresponding to coupling to the adjacent resonator(s) hard to detect. Another reason for not detecting a clear discernible drop in the transmitted signal could be a mismatch in the propagation constants of the bus waveguide and the Bragg resonator guides. As mentioned earlier the Bragg resonator guides were made wider than the bus guides to produce synchronous guides. The widths of these guides were chosen on the basis of an assumed value of the InGaAsP, $n_{co}$. However, since $n_{co}$ after the growth of the core region is not well known its possible that the guides are mismatched. We saw in section 4.3.7) that a small $\Delta\beta \sim \kappa$ corresponding to $\Delta n_{eff} \sim 10^{-3}$ for the case when $\kappa \approx 60$ cm$^{-1}$ is enough to distort the response of the side-coupled devices significantly. In the presence of Fabry-Perot fringes the detection of the dropped channel is even more difficult. Figure (6-24) shows the calculated response of a side-coupled receiver filter with no AR-coating on the chip facet when there is a propagation mismatch corresponding to $\Delta n_{eff} = 2.0 \times 10^{-3}$. This is overlayed on a plot of the transmitted signal when the two guides are completely matched. We see that with a mismatch of this order it is easy to miss the drop in the transmitted signal. In the measured responses of all the side-coupled devices the Fabry-Perot oscillations were visible; however, no drop in the transmitted signal corresponding to interaction with the resonator(s) was clearly discernible. Consequently, we suspected that

**Transmitted Power in Bus (SCR)**
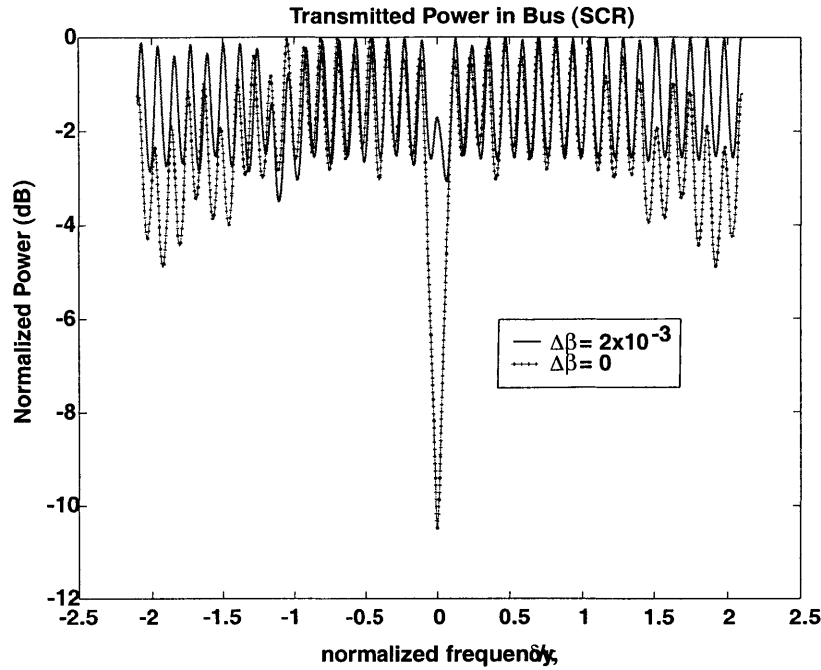


**Figure 6-24:** Presence of Fabry-Perot fringes exacerbates the $\Delta\beta$ mismatch issue making it difficult to detect a resonant drop in the transmitted signal.

the propagation constants of the bus waveguide and the resonator guides were mismatched. In a few cases of the side-coupled devices we were able to directly excite the resonators and observed that they did have clear resonance peaks. Hence the $\Delta\beta$ mismatch is the most likely reason for not having observed a drop in the transmitted power in the bus waveguide.

# Chapter 7

# Conclusions and Future Work

Integrated Bragg gratings and Bragg resonators are frequency selective elements that form the basic building blocks of various optical filters. We have looked at a variety of topologies in which these elements can be arranged to construct integrated optical add/drop filters . In this chapter we briefly summarize the salient features, issues and challenges associated with the use of Bragg gratings and Bragg resonators in the different topologies as add/drop filters.

## 7.1  Bragg Gratings and Resonators

### 7.1.1  Bragg Gratings

Integrated Bragg gratings reflect light strongly within their stopband, centered about the Bragg wavelength, allowing a band of frequencies to be separated out from a wide-band signal. The width of the frequency band, $\Delta\omega_{sb}$, that is reflected is related to the grating strength, $\kappa$, and the group velocity, $v_g$, of the grating guide. The grating strength, $\kappa$, is, therefore, determined by the requirement on the width of the reflected band. In InP material systems where the group index, $n_g \sim 3.5$, a grating strength, $\kappa \sim 35$ cm$^{-1}$ corresponds to a $\Delta\omega_{sb} \sim 100$ GHz. The peak reflected power or equivalently the peak transmission suppression in gratings is related to the $\kappa L$ product where $L$ is the total length of the grating. For a transmission suppression in excess of 25 dB, the $\kappa L$ product must be on the order 3.5. This constraint of $\kappa L \sim 3.5$ determines the length of the grating structure.

Uniform Bragg grating have high side-lobes, as we saw earlier. These side-lobes decay rather slowly and can lead to unacceptable cross-talk levels from adjacent WDM channels.

**Bragg Grating**

**Apodized Bragg Grating**

**Bragg Resonator**

**Inline Higher Order Filter**

**Apodized Grating Add/Drop Filter**

**Coupled Resonator Add/Drop Filter**
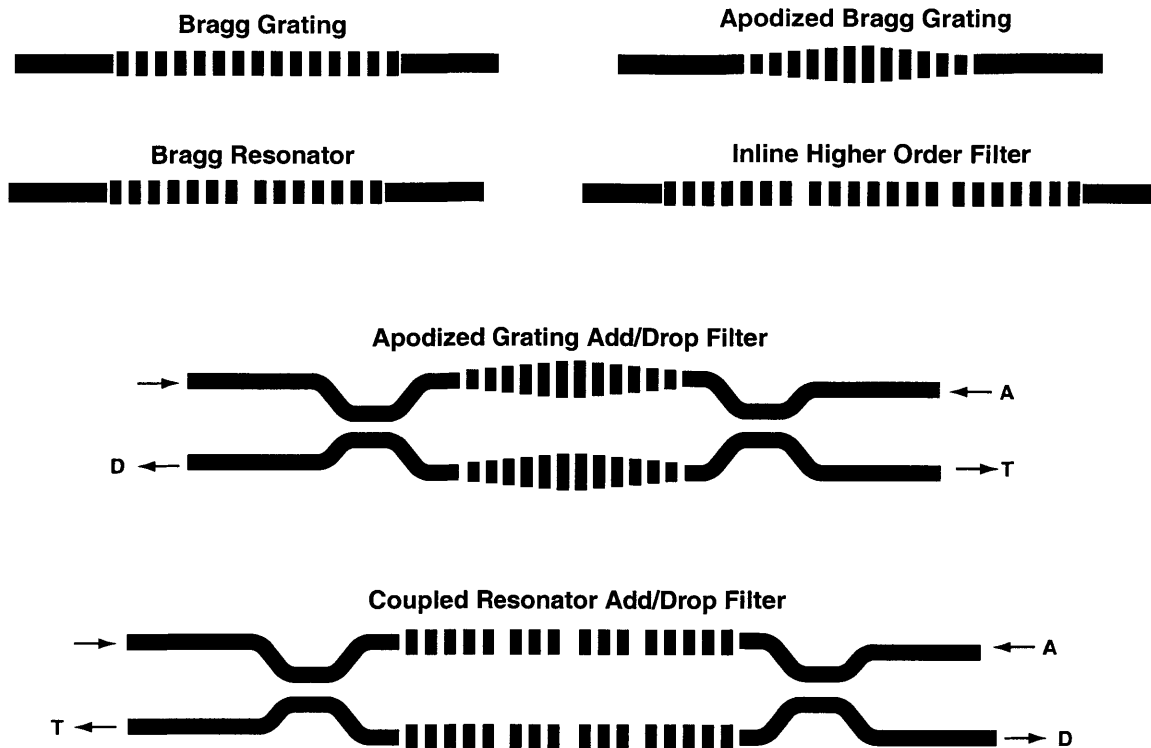
**Figure 7-1:** Bragg gratings and resonators form building blocks of add/drop filters. Both gratings and resonators can be put in the arms of a balanced Mach-Zehnder interferometer to form add/drop filters.

Therefore, if Bragg gratings are to be used in reflection it is necessary to apodize the gratings. The grating strength, $\kappa(z)$ must be tapered at its ends to reduce the side-lobe levels. Several apodization windowing functions can be used to reduce cross-talk levels. Given the current WDM channel spacings and required channel bandwidths, a uniform grating is unable to meet all specifications and apodizing the gratings becomes essential. Apodization reduces the average $\kappa$ of the grating structure; this means that grating lengths get longer in order to maintain $\langle \kappa L \rangle \sim 3.5$. For narrow WDM channels spacings of 50 GHz or less, the gratings can become several millimeters long. Fabricating long grating may be challenging due to introduction of chirp or accidental phase-shifts. As a result the use of Bragg gratings in reflection may be better suited to wider WDM channel spacings like 100 or 200 GHz.

### 7.1.2    Bragg Resonators

Bragg resonators, unlike gratings, have a resonant transmission state exactly in the center of the stopband. All frequencies within the stopband are strongly reflected; only the resonant transmission state at the Bragg wavelength propagates through. Consequently, the resonator forms a frequency selective element in which the desired channel is accessed in transmission. All the channels off resonance but within the stopband are reflected. However, outside the stopband the grating is no longer effective as a reflector and all frequencies outside the stopband are transmitted. As a result an inline Bragg resonator can only be used as a frequency selective element in systems where all the WDM channels are within the stopband of the grating. This constraint that all WDM channels are restricted to the grating stopband requires large grating strengths, $\kappa$, if high number of channels are to be accomodated. Large $\kappa$ gratings are difficult to fabricate and can suffer from high radiation losses.

Single Bragg resonators, near resonance, have Lorentzian responses with the associated roll-off with frequency. For most WDM applications, given the requirements on channel bandwidths, the roll-off of first-order Lorentzian filters is not adequate to meet cross-talk specifications. Consequently higher-order filters are needed. These can be achieved by inline coupling of multiple Bragg resonators as seen in Fig. (7-1). The coupling between these resonators can be chosen using the design methods discusses earlier to get appropriately flat-top, large bandwidth filters which have sufficiently fast roll-offs with frequency. Since, away from resonance, transmission within the stopband of the grating is heavily suppressed there is no need for apodization of gratings if Bragg resonators are used; there are no side-lobe issues to deal with inside the stopband. However, as mentioned above the use of inline Bragg resonators in add/drop filters restricts the WDM channels to within the stopband. Thus, use of coupled Bragg resonators offers the challenge of making high $\kappa$ gratings which do not suffer from high radiation losses to accomodate sufficient WDM channels.

### Mach-Zehnder Add/Drop Filter

The use of Bragg gratings or resonators in the balanced arms of a Mach-Zehnder provides an integrated approach to separating the input from the output and throughput channels. Either apodized Bragg gratings or coupled inline Bragg resonators can be used in the Mach-Zehnder configuration as shown in Fig. (7-1); each approach has its limitations as discussed

above. A key requirement on Mach-Zehnder based devices is that the two gratings or res-
onators must be perfectly aligned to each other to within a fraction of the optical wavelength,
$\lambda$. Misalignment on the order $\lambda/2$, for a Bragg grating (resonator) based Mach-Zehnder,
will introduce a $\pi$ phase mismatch that will reverse the add and throughput (drop) ports
and cause the drop (throughput) port to appear at the input port. Smaller misalignments
would make the two arms unbalanced and cause the throughput (drop) channels to appear
in both the add and throughput (drop) branches. Likewise the drop (throughput) channel
would appear partially at the input port. Thus, misalignements effectively produce inser-
tion losses and mix the outputs at the ports. They must be restricted to being much less
than the optical wavelength, $\lambda$. The 3 dB coupler regions of the Mach-Zehnder must be
designed such that they split the power evenly over the entire WDM wavelength range. This
requires designing wavelength-independant couplers which have been described in detail in
[41]. Managing bend losses for the coupler sections may require large bends. For weak
index contrast, moderate grating strength, $\kappa$, structures Mach-Zehnder devices tend to be
fairly large and bulky and can range from several millimeters to a centimeter measured
end-to-end.

## 7.2   Side-coupled Bragg Resonator and Push-Pull Filters

### 7.2.1   Side-coupled Bragg Resonator Filters

We saw in chapter 4 that Bragg resonators can be side-coupled to a bus waveguide to
form a receiver filter. However, complete power transfer requires two resonators where the
second resonator, placed with a $\lambda/4$-shift relative to the first, serves as a reflector forcing
complete power transfer to the receiver resonator. The simplest first-order side-coupled
add/drop filter, thus, requires two Bragg resonators staggered on opposite sides of the bus
guide. Near resonance it has a characteristic Lorentzian response. Again, for typical WDM
specifications, first-order filters are not adequate to meet specifications and one must design
higher-order filters. A systematic way to to design higher-order side-coupled receiver filters
using equivalent circuits was derived earlier. However, as in the case of a first-order filter,
a reflector is needed for complete power transfer. Higher-order filters capable of complete
power transfer require higher-order reflectors. There is no systematic way to design higher-
order reflectors using coupled Bragg resonators and one must rely on ad-hoc techniques
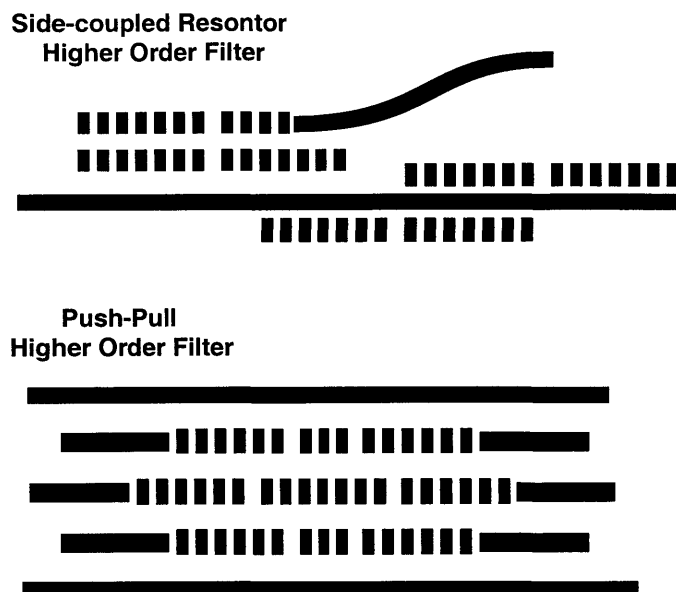
**Side-coupled Resontor
Higher Order Filter**

**Push-Pull
Higher Order Filter**

**Figure 7-2:** Bragg resonators side-coupled to a bus waveguide can be used as add/drop filters. Alternately coupled pairs of Bragg resonators can be side-coupled to one another and two waveguides to form push-pull add/drop filters.

for this topology. Figure (7-2) shows a side-coupled add/drop filter with the two Bragg resonators on the right side forming the higher-order reflector. In general an $n^{th}$-order filter requires $2n$ resonators to achieve complete power extraction of the dropped channel.

A limitation of using side-coupled Bragg resonator add/drop filters is that WDM channels are again constrained to be within the stopband. The reason, as before, has to do with the fact that the grating outside the stopband is not an effective reflector. Consequently, normal waveguide-to-waveguide coupling causes transfer of power from the bus guides to the resonator guides outside the stopband. This causes a reduction of throughput channel power if they lie outside the stopband. Moreover, the transfer of these channel powers to the drop port constitutes cross-talk to the dropped channel. Consequently, the WDM channels are restricted to the grating stopband.

Another issue that needs to be contended with in designing Bragg resonators side-coupled to waveguides is designing dissimilar waveguides with identical propagations constants. We discussed in section 4.3.7 the impact $\beta$-mismatch has on the performance of these devices. This applies to first and higher-order devices. What complicates the issue further is the absence of precise knowledge of the refractive index of the waveguide core. Mismatch in the propagation constants, $\Delta\beta$, on the order of the grating strength $\kappa$ can

destroy device performance. This problem is more severe for low or moderate $\kappa$ devices but is alleviated for high $\kappa$ structures due to the increased margin for error, i.e $|\Delta\beta| < \kappa$.

### 7.2.2 Push-Pull Filters

Push-pull filters use degenerately coupled Bragg resonators sandwiched between bus and access waveguides to form add/drop filters. As in the case of side-coupled filters, higher-order push-pull devices are needed to meet WDM specifications. Push-pull filters, however, offer the benefit of complete power transfer of the selected channel to the access guide for arbitrary filter orders. A systematic way to design the complete $2n$ resonator system to yield full-transfer higher-order filters was derived. This is a considerable advantage over using the side-coupled scheme where we have to rely on ad hoc techniques to the design the needed higher-order reflector. However, as in the case of the side-coupled Bragg resonator filters, WDM channels may be constrained to the grating stopband. This constraint can be alleviated to some degree by bending the bus and access guides away from the resonators as we discussed in section 5.3.1. The propagation constant mismatch, $\Delta\beta$, between the bus and resonator guides remains an issue for push-pull filters as well.

Another general observation about side-coupled or push-pull filters is that obtaining wide bandwidth filters may be challenging. Channel bandwidths are increased by lowering the external Q of the system. This requires stronger side-coupling between adjacent guides and resonators. The coupling, however, is limited by how close waveguides can be reliably fabricated. Moreover, higher side-coupling tends to deteriorate device performance outside the stopband.

## 7.3  Future Work

In chapter 6 we saw that on the short wavelength side gratings coupled guided modes to radiation modes. Coupled Mode theory in space (CMT-space) of Bragg gratings, as discussed in chapter 3 however, does not predict this radiation. The reason is that CMT-space only treats coupling between the two fundamental guided modes. It ignores interaction between any other modes by arguing the the grating pertubation does not provide phase-matched coupling between them. On the short wavelength side, however, as seen in section 6.4.1 there is phase-matched coupling between the forward-traveling guided modes and the backward-traveling radiation modes. To predict this coupling all the modes of the system

including radiation modes must be included. We are currently developing a transfer-matrix method that takes all guided and the first $N$ radiation modes into account and solves the scattering from an abrupt junction between the tooth and the trench. By concatening the abrupt junctions matrices with the intervening propagation matrices, it is possible to accurately model Bragg gratings taking into account interaction between all modes.

As we seen in the discussion above, making large $\kappa$ gratings is highly desireable when using Bragg resonator systems. Large $\kappa$ gratings have strong radiation losses. Creating a strong grating without strong coupling to radiation modes remains a challenge that needs to be overcome. Work is in progress to achieve this aim.

Control of $\Delta\beta$ remains a limitation which must be overcome. The problem lies in designing matched dissimilar guides in the absence of the precise values of the material indices. One way to overcome this constraint is to have a $\beta$ control mechanism that can tune the guides into synchoronous mode allowing add/drop filtering. Tuning the $\beta$ out of synch would turn off the add/drop filter. Ways to achieve this tuning by index control via current, fields and temperature are being explored.

# Bibliography

[1] R. Ramaswami and K. Sivarijan, "Optical Networks: A Practical Perspective,"2nd edition, Morgan Kaufmann Publishers, Oct. 2001

[2] Biwanth Mukherjee, "WDM Optical Communication Networks: Progress and Challenges," IEEE Journal on Selected Areas in Communications, Vol. 18, NO.10, October 2000.

[3] "International Telecommunication Union", http://www.itu.int/home/index.html

[4] Adrian Janssen, "The Evolution of Passive Devices in WDM networks," in Electronic Components and Technology Conference, 1999. 1999 Proceedings. 49th , 1999 pp. 13-18

[5] Adel A. M. Saleh, Jane M. Simmons, "Architectural Principles of Optical Regional and Metropolitan Access Networks," J. of Lightwave Tech, vol. 17, NO. 12, Dec. 1999.

[6] M. Kuznetsov, N.M. Foberg, S.R. Henion, H.G. Rao, J. Korn, K.A. Rauschenbach, E. Modiano, V.W.S. Chan, "A Next-Generation Optical Regional Access Network," IEEE Communications Magazine, Jan 2000, pp 66-72.

[7] J. Bautista, B. Shine, "Filter technologies vie for DWDM system applications," Fiber Optics Online Article. http://www.fiberopticsonline.com/content/news/article.asp?DocID=%7BCA3F5DC1-4843-11D4-8C54-009027DE0829

[8] K.O. Hill and G. Meltz, "Fibter Bragg Grating Technology Fundamental and Overview," *J. of Lightwave Tech* Vol. 15, NO. 8, August 1997.

[9] D. Pastor, J. Capmany, D. Ortega, V. Tatay and J. Marti, "Design of Apodized Linearly Chirped Fiber Gratings for Disperion Compensation," *J. of Lightwave Tech.*, vol. 14, no. 11, 1996.

[10] P. Bernasconi, C. Doerr, C. Dragone, M. Cappuzzo, E. Laskowski, A. Paunescu, " Large N x N waveguide grating routers," *J. of Lightwave Tech.* Vol. 18, NO. 7, July 2000 pps:985 -991

[11] Y.P Li and C.H. Henry, "Silica-based optical integrated circuits," *in Proc. IEE Optoelectronics* , Vol. 143 NO. 5 , Oct. 1996, pp: 263-280

[12] A. Kaneko, T. Goh, H. Yamada, T. Tanaka, I. Ogawa, "Design and Applications of Silica-based Planar Lightwave Circuits," *IEEE Jour. of Selected Topics in Quant. Elect.* Vol. 5, No. 5, Sept/Oct. 1999.

[13] B. Bennett, R.A. Soref and J.A. Del Alamo, "Carrier-Induced Change in Refractive Index of InP, GaAs, and InGaAsP", *IEEE Jour. of Quant. Elect.*, Vol. 26, No. 1, Jan. 1990.

[14] C. Thirstup, "Refractive Index Modulation Based on Excitonic Effects in GaAsIn-InP Coupled Asymmetric Quantum Wells", *IEEE Jour. of Quant. Elect.*, Vol. 31, No. 6, June 1995.

[15] B.J. Offrein, F. Horst, G.L. Bona, H.W.M. Salemink, R. Germann and R. Beyeler, "Wavelength Tunable 1-from-16 and Flat Passband 1-from-8 Add-Drop Filters", *IEEE Photonics Tech. Letters*, Vol. 11, No. 11, Nov. 1999.

[16] A. Kaneko, "Recent progress on arrayed-waveguide gratings for WDM applications," *in Digest of the LEOS Summer Topical Meetings*, 1999, pp: II29-II30

[17] D. Marcuse, *Theory of Dielectric Optical Waveguides*, 2nd Edition, Acamemic Press, Inc, Harcourt Brace Jovanovich, Publishers, 1991

[18] C. Vassallo, *Optical Waveguide Concepts*, Elsevier Science Publishers, 1991.

[19] A.W. Snyder, J.D. Love, *Optical Waveguide Theory*, Kluwer Academic Publishers, Nov. 1983.

[20] H. A. Haus, *Waves and Fields in Optoelectronics*, Prentice-Hall, Englewood Cliffs, NJ, 1984.

[21] A. Yariv, *Optical Electronics*, 4th Edition, Harcourt Brace Jovanovich College Publishers, 1991.

[22] H. A. Haus and W.-P. Huang, "Couple-Mode Theory", *Proceedings of the IEEE*, Vol. 79, No. 10 1991. pps:1505-1518

[23] H. A. Haus et. al., "Coupled-Mode Theory of Optical Waveguides," *J. of Lightwave Tech.*, vol. 5, pp 16-23, 1987.

[24] A. Yariv, "Coupled-Mode Theory for Guided-Wave Optics", *IEEE J. of Quantum Electron.*, vol. 9, pp. 919-933, 1973.

[25] H. Kogelnik and C. V. Shank, "Coupled-wave theory of distributed feedback lasers," *J. Appl. Phys., 43*, no. 5, 2328-2335, May 1972.

[26] G. Strang, *Linear Algebra and Its Applications* 3rd edition, International Thomson Publishing, 1998.

[27] B.E Little and C. Wu, "Window Functions for Ideal Response in Distributed Feedback Reflection Filters," *IEEE Photon. Technol. Lett.,* Vol. 9. No. 1 pp. 76-78, 1997.

[28] P.S. Cross H. Kogelnik, "Sidelobes Suppression in Corrugated-Waveguide Filters," *Optics Lett.,* Vol. 1 No. 1, pp. 43-45, 1997

[29] A.V. Oppenheim and R.W. Schafer, *Discrete-Time Signal Processing*, Prentice-Hall, Inc. Englewood Cliff, NJ, 1989.

[30] E.A. Lee and D.G. Messerschmitt, *Digital Communication*, 2nd Edition, Kluwer Academic Publishers, 1993.

[31] J.G. Proakis, *Digital Communications* 4th edition McGraw-Hill Higher Education; Aug. 2000

[32] J.A.R. Williams, I. Bennion, K. Sugden and N.J. Doran, "Fiber dispersion compensation using a chirped in-fibre Bragg grating," *Electron. Lett.*, Vol. 30, pp. 985-987, 1994.

[33] H. Kogelnik, "Filter Response of Nonuniform Almost-Periodic Structures," *The Bell System Technical Journal*, vol. 55, no. 1, pp. 109-126, Jan. 1976

[34] D.H. Staelin, A.W. Morgenthaler, J.A. Kong, *Electromagnetic Waves*, Prentice-Hall, Englewood Cliff, NJ, 1994.

[35] H.A. Haus, *Electromagnetic Noise and Quantum Optical Measurements* Springer-Verlag, 2000.

[36] H. A. Haus and Y. Lai, "Theory of Cascaded Quarter Wave Shifted Distributed Feedback Resonators," J. Quantum Electronics, vol. 28, no. 1, pp. 205-213, 1992.

[37] H. Suzuki, J. Kani, H. Masuda, N. Takachio, K. Iwatsuki, Y. Tada and M. Surnida, "1-Tb/s )(100 × 10 Gb/s) Super-Dense WDM Transmission with 25-GHz Channel Spacing in Zero-Dispersion Region Employing Distributed Raman Amplification Technology," *IEEE Photon. Technol. Lett.,* vol. 12, no. 7, pp.903-905, 2000.

[38] Y. Yamada, S. Nakagawa, K. Takashina, T. Kawazawa, H. Taga, K. Goto, "25 GHz spacing ultra-dense WDM transmission experiment of 1 Tbit/s (100 WDM/spl times/10 Gbit/s) over 7300 km using non pre-chirped RZ format," *Electron. Lett.'* , vol. 35 no. 25 , pp. 2212-2213, 1999.

[39] M.H. Lim, J. Ferrera, K.P. Pipe, H.I. Smith, "A Holographic Interferometry Technique to Measure In-Plane Distortion," *Jour. of Vac. Sci. and Tech. B,* November/December 1999, pp. 2703.

[40] K. Jinguji, N. Takato, A. Sugita, and M. Kawachi, "Mach-Zehnder Interferometer Type Optical Waveguide Coupler with Wavelength-Flattened Coupling Ratio," *Electron Lett.,* Vol. 26 No. 17, pp. 1326-1327, 1990.

[41] B.E. Little and T.E Murphy, "Design Rules for Maximally Flat Wavelength-Insensitive Optical Power Dividers using Mach-Zehnder Structure," *IEEE Photon. Texhnol. Lett.,* Vol. 9. No. 12, pp. 1607-1609, 1997.

[42] T.E Murply, "Design, Fabrication and Measurement of Integrated Bragg Grating Optical Filters", *PhD Thesis*, Dept. of Elec. Eng. and Comp. Sci, MIT, 2001.

[43] H. A. Haus and Y. Lai, "Narrow-band Distributed Reflector Design," J. Lightwave Technology, vol.9 , no. 6, pp. 754-760, 1991.

[44] H. A. Haus, Y. Lai, "Narrow-band optical channel-dropping filter", *J. Lightwave Technol.*, vol.10, no.1, p. 57-62, 1992

[45] J.N. Damask, "Integrated-Optic Grating-Based FIlters For Optical Communication Systems," *PhD Thesis*, Dept. Elec. Eng. and Comp. Sci., MIT, 1996.

[46] J-P. Weber, "Optimization of the Carrier-Induced Effective Index Change in In-GaAsP Waveguides - Application to Tunable Bragg Filters", *IEEE J. of Quant. Elec.*, Vol. 30, No. 8, Aug. 1994.

[47] D.A.B. Miller, A.C. Gossard, W. Wiegmann, T.H. Wood and C.A. Burrus, "Electric-Field dependence of optical absorption near the band gap of quantum-well structures", *Physical Review B*, Vol. 32, No. 2, July 1985.

[48] "Band-Edge Electroabsorption in Quantum Well Structures: The Quantum-Confined Stark Effect", *Physical Review Letters*, Vol. 53, No. 22, Nov. 1984.

[49] T.Kameda, H. Mori, S. Onuke, T. Kikugawa, F. Tsuchiya and H. Nagai, " A DBR Laser Employing Passive-Section Heaters, with 10.8 nm Tuning Range and 1.6 MHz Linewidth", *IEEE Phot. Tech. Lett.*, Vol. 5, No. 6, June 1993.

[50] A. B. Williams, *Electronic Filter Design Handbook*, McGraw-Hill Book Company, 1981.

[51] A. I. Zever, *Handbook of Filter Synthesis*, New York: Wiley, 1967.

[52] Ernst A. Guillemin, *Synthesis of Passive Networks*, John Wiley & Sons, Inc. 1957.

[53] H. Y.-F Lam, *Analog and Digital Filters: Design and Realization*, Prentice-Hall, Englewood Cliffs, NJ 1979.

[54] C. Dragone, C.A. Edwards, R.C. Kistler, "Integrated optics N*N multiplexer on silicon", *IEEE Photon. Technol. Lett.*, vol.3, no.10, p. 896-9, 1991

[55] B.E. Little, S. T. Chu, H. A. Haus, J. Foresi, J.-P. Laine, "Microring resonator channel dropping filters", *J. Lightwave Technol.*, vol.15, no.6, p. 998-1005, 1997

[56] B.E. Little, J.S. Foresi, G. Steinmeyer, E.R. Thoen, S.T. Chu, H.A. Haus, E.P. Ippen, L.C. Kimerling, W. Greene, W.Ultra-compact," $Si-SiO_2$ microring resonator

optical channel dropping filters," *IEEE Photonics Technol. Lett.,* vol. 10 no. 4 , pp.549-551 1998.

[57] C. Manolatou, M.J. Khan, S. Fan, P.R. Villeneuve, H.A. Haus, J.D. Joannopoulos "Coupling of modes analysis of resonant channel dropping filters", *IEEE J. Quantum Electron.,* vol. 35, no. 9, pp. 1322-1331, 1999.

[58] H. A. Haus, Y. Lai, "Theory of cascaded quarter wave shifted distributed feedback resonators", *IEEE J. Quantum Electron.,* vol.28, no.1, p. 205-13, 1992

[59] B. E. Little, J.-P. Laine, S. T. Chu, "Surface-roughness-induced contradirectional coupling in ring and disk resonators", 1997 *Opt. Lett.,* vol.22, no.1, p. 4-6,

[60] S. Fan, P. R. Villeneuve, J. D. Joannopoulos, H. A. Haus, "Channel drop tunneling through localized states", *Phys. Rev. Lett.,* vol.80, no.5, p. 960-3, 1998

[61] S. Fan, P. R. Villeneuve, J. D. Joannopoulos, H. A. Haus, "Channel drop filters in a photonic crystal", *Optics Express,* vol.3, no.1, p. 4-11, 1998.

[62] S. Fan, P. R. Villeneuve, J. D. Joannopoulos, M. J. Khan, C. Manolatou, H. A. Haus, "Theoretical analysis of channel drop tunneling processes", submitted to *Phys. Rev. B.*

[63] M.H. Lim, T.E. Murphy, J. Ferrera, J.N. Damask, H.I. Smith, "Fabrication Techniques for Grating-Based Integrated Optical Devices," , *Jour. of Vac. Sci. and Tech. B,* November/December 1999, pp. 3208.

[64] J. Ferrara, "Nanometer-scale placement in electron-beam lithography ", *PhD Thesis,* Dept. Elec. Eng. and Comp. Sci., MIT, 2000

[65] M. Lim, "" *PhD Thesis,* Dept. Elec. Eng. and Comp. Sci., MIT, 2001

[66] D. Marcuse, "Radiation Losses of Dielectric Waveguides in Terms of the Power Spectrum of the Wall Distortion Function," *Bell Syst. Tech. J.,* vol. 48, pp. 3233-3242, Dec. 1969.

[67] W.W. Rigrod, D. Marcuse, "Radiation Loss Coefficients of Asymmetric Dielectric Waveguides with Shallow Sinosoidal Corrugations," *IEEE J. of Quant. Elec.,* vol. QE-12, no. 11, 1976.

[68] W.-H. Lee and W. Streifer, "Radiation loss calculation for corrugated dielectric waveguides," *J. Opt. Soc. Am.* vol. 12, Dec. 1978.

[69] M. Matsumoto, "Analysis of radiation properties of channel-waveguide gratings," *J. Opt. Soc. Am. B,* vol. 8, no. 2, 1991.

[70] M. Kuznetsov and H.A. Haus, "Radiation Loss in Dielectric Waveguide Structures by the Volume Current Method," *IEEE J. of Quant. Elec.,* vol. QE-19, no. 10, Oct. 1993.